Study of Relativistic Electrons Generated from Ultra-intense Laser-Plasma Interaction relevant to Laser Wakefield Acceleration and Fast Ignition Laser Fusion

by

Mianzhen Mo

A thesis submitted in partial fulfillment of the requirements for the degree of

Doctor of Philosophy

in

Photonics and Plasmas

Department of Electrical and Computer Engineering

University of Alberta

Abstract

Ultra-intense ($> 10^{18}\ W/cm^2$) laser interaction with matter is capable of producing relativistic electrons which have a variety of applications in scientific and medical research. Knowledge of various aspects of these hot electrons is important in harnessing them for various applications. Of particular interest for this thesis is the investigation of hot electrons generated in the areas of Laser Wakefield Acceleration (LWFA) and Fast Ignition (FI).

LWFA is a physical process in which electrons are accelerated by the strong longitudinal electrostatic fields that are formed inside the plasma cavities or wakes produced by the propagation of an ultra-intense laser pulse through an under-dense plasma. The accelerating E-fields inside the cavities are 1000 times higher than those of conventional particle accelerators and can accelerate electrons to the relativistic regime in a very short distance, on the order of a few millimeters. In addition, Betatron X-ray radiation can be produced from LWFA as a result of the transverse oscillations of the relativistic electrons inside the laser wakefield driven cavity. The pulse duration of Betatron radiation can be as short as a few femtoseconds, making it an ideal probe for measuring physical phenomena taking place on the time scale of femtoseconds. Experimental research on the electron acceleration of the LWFA has been conducted in this

thesis and has led to the generation of mono-energetic electron bunches with peak energies ranging from a few hundreds of MeV to 1 GeV. In addition, the Betatron radiation emitted from LWFA was successfully characterized based on a technique of reflection off a grazing incidence mirror. Furthermore, we have developed a Betatron X-ray probe beamline based on the technique of K-shell absorption spectroscopy to directly measure the temporal evolution of the ionization states of warm dense aluminum. With this, we have achieved for the first time direct measurements of the ionization states of warm dense aluminum using Betatron X-ray radiation probing.

Fast Ignition (FI) is an advanced scheme for inertial confinement fusion (ICF), in which the fuel ignition process is decoupled from its compression. Comparing with the conventional central hot-spot scheme for ICF, FI has the advantages of lower ignition threshold and higher gain. The success of FI relies on efficient energy coupling from the heating laser pulse to the hot electrons and subsequent transport of their energy to the compressed fuel. As a secondary part of this thesis, the transport of hot electrons in overdense plasma relevant to FI was studied. In particular, the effect of resistive layers within the target on the hot electron divergence and absorption was investigated. Experimental measurements were carried out and compared to simulations indicating minimal effect on the beam divergence but some attenuation through higher atomic number intermediate layers was observed.

Preface

This thesis is an original work by Mianzhen Mo. Some of the work in this thesis was accomplished in collaboration with researchers from the University of Alberta, and some with researchers from other universities and institutes. The experiments described from Chapter 5 to 10 were carried out in the Advanced Laser Light Source (ALLS) facility, whereas the experiment in Chapter 11 was conducted in the Jupiter Laser Facility at the Lawrence Livermore National Laboratory. All of the experiments were performed under the guidance and supervision of Professor Robert Fedosejevs. The introduction in Chapter 1, physics background in Chapters 2 and 3, experimental methodologies in Chapter 4 and conclusions in Chapter 12 were written by myself and edited by Prof. Fedosejevs.

Chapter 5 has been published as: P. E. Masson-Laborde, M. Z. Mo, A. Ali, S. Fourmaux, P. Lassonde, J. C. Kieffer, W. Rozmus, D. Teychenné, and R. Fedosejevs, "Giga-electronvolt electrons due to a transition from laser wakefield acceleration to plasma wakefield acceleration", Phys. Plasmas **21**, 123113 (2014). I am the equivalent first author in this article. I was responsible for carrying out the experiment, analyzing and interpreting the experimental data, helping to interpret the simulation results and preparing the experimental part of the initial manuscript. The 3D PIC simulations and the analysis of the simulation results were carried out by Dr. Masson-Laborde who also prepared the major part of the initial manuscript. A. Ali assisted with the experiment and part of the data analysis. Dr. Fourmaux and P. Lassonde assisted with the experiment. Prof. Rozmus helped to interpret the simulation results. Prof. Fedosejevs designed the experiment, helped to interpret the experimental and simulation results and coordinated the collaboration that was involved in this work. All authors contributed to the discussion and writing of the manuscript.

Chapters 6 and 7 have been published as: M. Z. Mo, A. Ali, S. Fourmaux, P. Lassonde, J. C. Kieffer, and R. Fedosejevs, "Quasimonoenergetic electron beams from laser wakefield acceleration in pure nitrogen", Appl. Phys. Lett. **100**, 074101 (2012) and "Generation of 500 MeV - 1 GeV energy electrons from laser wakefield acceleration via ionization induced injection using CO_2 mixed in He", Appl. Phys. Lett. **102**, 134102 (2013) respectively. I was responsible for carrying out the experiments, analyzing and interpreting the experimental data, and drafting the initial manuscripts. A. Ali, Dr. Fourmaux and P. Lassonde assisted with the experiments. Prof. Fedosejevs designed the experiments, helped to interpret the data and edited the manuscripts. All authors contributed to the discussion and writing of the manuscripts.

Chapter 8 has been published as: M. Z. Mo, A. Ali, S. Fourmaux, P. Lassonde, J. C. Kieffer, and R. Fedosejevs, "Characterization of laser wakefield generated betatron X-ray radiation using grazing incidence mirror reflection", Eur. Phys. J. D **68**, 301 (2014). I was responsible for carrying out the experiment, analyzing and interpreting the experimental data, conducting the simulation to compare the experimental data and drafting the initial manuscript. A. Ali, Dr. Fourmaux and P. Lassonde assisted with the experiment. Prof. Fedosejevs designed the experiment, helped to interpret the data, advised on the simulation and edited the manuscript. All authors contributed to the discussion and writing of the manuscript.

Chapter 9 has been published as: M. Z. Mo, Z. Chen, S. Fourmaux, A. Saraf, K. Otani, J. C. Kieffer, Y. Y. Tsui, A. Ng and R. Fedosejevs, "Laser wakefield generated X-ray probe for femtosecond time-resolved measurements of ionization states of warm dense aluminum", Rev. Sci. Instrum. **84**, 123106 (2013). I was responsible for designing the experimental setup, leading the experiment, analyzing and interpreting the experimental data, conducting the simulation and drafting the initial manuscript. Dr. Chen assisted with the experiment and part of the data analysis, Dr. Fourmaux, A. Saraf, Dr. Otani

assisted with the experiment, Prof. Tsui helped to interpret the data, Prof. Ng suggested the problem that led to this experiment, Prof. Fedosejevs involved in designing the experimental setup, interpreting the data and editing the initial manuscript. All authors contributed to the discussion and writing of the manuscript.

Chapter 10 and Chapter 11 were written by myself and revised by Prof. Fedosejevs. For the research work presented in Chapter 10, I was responsible for leading the experiment, analyzing the experimental data, and conducting the theoretical calculations and simulations to interpret the experimental data. The experiment described in Chapter 11 was led by Prof. Fedosejevs and involved many collaborators from outside the university. I was responsible for setting up some of the X-ray diagnostics, conducting the experiment, analyzing and interpreting the X-ray results described in Chapter 11. The PIC simulations shown in Chapter 11 were conducted by Prof. Honrubia from Spain.

Acknowledgements

First and foremost, I would like to express the deepest appreciation to my academic supervisor, Professor Robert Fedosejevs, who has been a tremendous mentor for me. I would like to thank him for introducing me to the fascinating subject of ultra-intense laser plasma interaction, which has kept my Ph.D life extremely busy and will continue to do so for the rest of my life. His professional attitude, cultivated diligence, dogged persistence and unending dynamism demonstrated whenever attempting to unravel the mysteries behind the scientific hurdles have always impressed me and have helped my professional development in the physics field. I would like to thank him for unreservedly imparting me his expertise, which has helped me tackle a lot of seemingly impossible puzzles during my research. I would like to thank him for providing me opportunities to take part in many experimental campaigns at the most powerful laser facility (ALLS) in Canada as well as at one of the worlds' best laser facilities (LLNL).

This work could not have been completed without the expert support from the technicians at the Electrical and Computer Engineering Department of the University of Alberta and the laser facilities where our experiments were conducted. I would like to thank Blair Harwood, Steve Drake, Herbert Dexel and his team at the machine shop at the University of Alberta. I would like to thank the technical staff at the ALLS facility. Special appreciation is due to Philippe Lassonde, Mark O. Bussiere, Joel Maltais and G. Lebrun. I would like to thank the Jupiter Laser Facility staff for their support of our experiments, in particular Jim Bonlie, Rich Combs, Rob Costa and Bob Cauble.

I am grateful to all the colleagues and collaborators that I have worked

with throughout my Ph.D career. In particular, I would like to thank the staff scientist, Sylvain Fourmaux, at the ALLS facility for providing us with such a great platform for LWFA experiments as well as for spending many late nights with us in the experimental area. I would like to thank the staff scientist, Tony Link, at the LLNL for guiding me through each step of the process of running a proper LSP simulation and for his prompt response to my every single inquiry on the LSP simulations. I would like to thank Professor Wojciech Rozmus from the Department of Physics at the University of Alberta and Dr.Paul-Edouard Masson-laborde from CEA in France for conducting the PIC simulations for our LWFA experiments. I would like to thank Shaun Kerr and Zhijiang Chen, the two colleagues at UofA, for their generous support to my experiments as well as for being genuine friends in my Ph.D life. Many thanks goes out to Professor Ying Tsui, Dr.Henry Tiedje, Atif Ali, Raj Masud, Hal Friesen at UofA, Professor Andrew Ng from UBC, Mingsheng Wei from General Atomics, Gregory Elijah Kemp, Doulgass Wertepney and Shengjiang from OSU, Chris McGuffey, Charlie Jarrott, Sugreev Chawla, Anna Sorokovikova, and Professor Farhat Beg from UCSD and Arpit Saraf, Kazuto Otani and Professor Jean-Claude Kieffer from INRS-EMT.

Last but not least, I would like to thank my family. Words cannot express how grateful I am to my wife, Yelan Lao, for taking good care of our baby boy Ruirui and for encouraging me whenever I was frustrated by my Ph.D research. Without her unrelenting support, encouragement and understanding, I would not have advanced so smoothly on the road to realize my dream. A special thanks is given to my parents, Yijia Mo and Xuewen Huang, for giving birth to me in the first place and supporting me spiritually throughout my life.

Contents

List of Tables

List of Figures

List of Abbreviations

List of commonly used abbreviations

ASE	Amplified Spontaneous Emission
ALLS	Advanced Laser Light Source
CPA	Chirped-pulse Amplification
CCD	Charge-Coupled Device
CHS	Central Hot Spot
DT	Deuterium-Tritium
fs	femtosecond (10^{-15} of a second)
FI	Fast Ignition
FWHM	Full Width at Half Maximum
ICF	Inertial Confinement Fusion
INRS	Institut National de la Recherche Scientifique
LWFA	Laser Wakefield Acceleration
LLNL	Lawrence Livermore National Laboratory
OPCPA	Optical Parametric Chirped Pulse Amplification
ps	picosecond (10^{-12} of a second)
PW	Peta-watt (10^{15} watt)
TW	Tera-watt (10^{12} watt)
MA	Mega-ampere (10^{6} ampere)
MeV	Mega-electronvolt (10^{6} eV)
GeV	Giga-electronvolt (10^{9} eV)

Chapter 1

Introduction

Ever since the laser was invented by Maiman in 1960 [1], laser technology has advanced at an incredible rate, the pulse energy increasing from joules to mega-joules, the pulse duration shrinking from microseconds to femtoseconds (10^{-15} s), and the pulse power growing from watts to petawatts (10^{15} watt). The key to high and ultrahigh power laser intensity is the amplification of ultrashort pulses on the picosecond and femtosecond time scales. Laser pulses with durations in such an ultrashort regime can be achieved with mode locking, a well established technique developed at the beginning of the 1970s [2]. When propagating these ultrashort pulses through the amplifying media, the laser intensity becomes so high during amplification such that nonlinear processes such as self-focusing take place inside the media, consequently damaging the optical components of the amplifiers. This technical difficulty constrained the laser power of a single laser module to the gigawatt level for two decades until the invention of the chirped-pulse amplification (CPA) approach[3, 4].

As opposed to the direct amplification approach, the CPA technique, as illustrated in Fig.1.1, would stretch out the laser pulse in the time domain prior to amplification. This removes the limitation of damaging the gain medium through nonlinear processes that are inevitable in the direct approach. After amplification, the laser pules would be re-compressed back to the original pulse

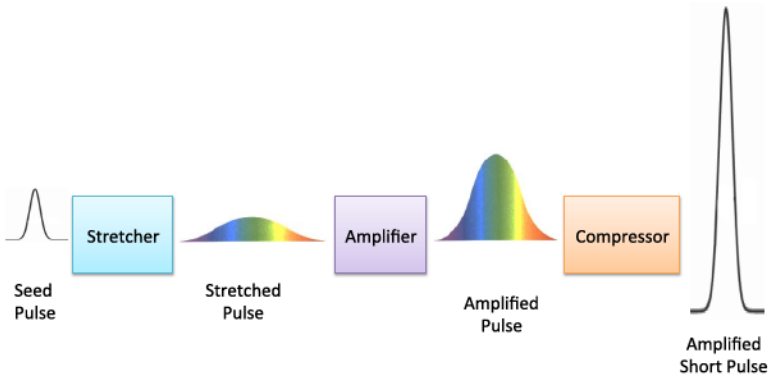

Figure 1.1: The schematic diagram of chirped pulse amplification.

duration, therefore allowing the laser pulse to reach the ultrahigh power regime. With this CPA technique, laser pulses with peak power of petawatts and pulse widths of multi-femtoseconds are readily available in many research facilities around the world. When focusing to micron spot sizes, these ultra-high power laser pules can give enormous peak intensities in excess of 10^{21} W/cm^2, corresponding to an electric field of approximately 0.1 PV/m in free space that is three orders of magnitude higher than the binding electric field of a hydrogen atom.

Given that the laser field strength exceeds the interatomic field by many orders of magnitude, relativistic effects come into play when the ultra-intense and short laser pulses interact with plasma, which have kept physicists busy for more than two decades and still require further experimental and theoretical investigations to be fully understood. There are many plasma related applications that aim to make use of these ultra-intense and short laser pulses, such as fusion energy using the concept of fast ignition [5], laser wakefield acceleration

(LWFA) [6], generation of coherent XUV radiation [7], hard and soft X-ray source generation[8] and the list goes on.

Among the many applications of high intensity laser plasma interaction, LWFA and fast ignition will be studied and constitute the main part of this thesis. Technically, laser wakefield acceleration concerns relativistic phenomena occurring in an underdense plasma region whereas fast ignition takes place in an overdense plasma region. These two plasma regions are defined based on the laser critical density, which is the density at which the laser light will be reflected while propagating inside a plasma and takes the form of:

$$n_c(cm^{-3}) = \frac{\omega_0^2 m_e \varepsilon_0}{e^2} \simeq 1.1 \times 10^{21}/\lambda_{\mu m}^2 \tag{1.1}$$

where ω_0 is the laser angular frequency in vacuum, m_e is the electron mass, ε_0 is permittivity of free space, e is the electron charge and $\lambda_{\mu m}$ is the laser wavelength in vacuum in units of μm. Given a laser wavelength of 0.8 μm, which is widely used in recent ultra-high power lasers, the critical density is calculated to be $n_c \simeq 1.72 \times 10^{21}\ cm^{-3}$. For laser wakefield acceleration, the working plasma density normally ranges from $10^{17}\ cm^{-3}$ to $10^{19}\ cm^{-3}$, which is 2 to 4 orders less than the critical density, thus referred to as underdense plasma. On the other hand, the plasma is defined as overdense plasma for fast ignition since the density involved ranges from critical density to compressed matter densities (on the order of $10^{26}\ cm^{-3}$), which is around 5 orders of magnitude higher than the critical density.

The relativistic laser plasma interaction is characterized by the laser normalized vector a_0 that is given by:

$$a_0 = v_{os}/c = eE/m_e\omega_0 c \simeq 0.85\sqrt{I_{18}\lambda_{\mu m}^2}, \tag{1.2}$$

where v_{os} is given by $v_{os} = eE/m_e\omega_0$ and represents the quiver velocity of the electron in the laser electric field E in the non-relativistic regime, c is the speed

of light in vacuum and I_{18} is the peak laser intensity in units of 10^{18} W/cm^2. When $a_0 \geqslant 1$, the quiver motion of the plasma electrons become relativistic. For laser pulses with $\lambda = 1\,\mu m$, a focused intensity of $\sim 1.4 \times 10^{18}$ W/cm^2 corresponds to the onset of the relativistic electron motion.

1.1 Laser Wakefield Acceleration

High energy particles that are in the relativistic regime are of great interest because of their widespread uses in a variety of areas, including applications in industrial and medical fields such as electron-beam material processing [9] and proton therapy for cancer treatment [10], as well as the applications in scientific research such as particle and nuclear physics. Besides, high energy particles such as electrons may be manipulated into emitting extremely bright and coherent beams of high energy X-rays via synchrotron radiation, which have numerous uses in the study of atomic structure, chemistry, biology, high energy density physics and so on. For applications such as chemistry and biology using the synchrotron radiation, electron bunches with energy ranging from a few hundreds of MeV to multi-GeV are required to produce X-ray photons with high enough photon energy and sufficient brightness. For particle physics at the next energy frontier, electrons and positrons at the TeV energy scale are required in order to search for new physics. Therefore, there is a great demand for particle accelerators at high energy and high intensity.

Conventionally, linear accelerators or linacs are widely used to generate high energy particles, which rely on a technique based on radio-frequency oscillating electric fields sustained in a metalic cavity. However, the accelerating gradients supplied by this technique are limited to approximately 100 MV/m, due in part to the electric breakdown that takes place on the cavity wall. Therefore, numerous acceleration modules have to be staged sequentially over a distance of many kilometers in order to reach the energy of interest for particle physi-

cists. For instance, the Stanford Linear Accelerator Center (SLAC), the world's longest electron accelerator, was built with a length of 3 kilometers in order to accelerate electrons to 50 GeV of energy.

In an effort to reduce the size of accelerators, plasma based accelerators have been investigated. Ionized plasmas can sustain electron plasma waves with electric fields in excess of $E_0 = cm_e\omega_p/e$ or

$$E_0(V/m) \simeq 96\sqrt{n_e(cm^{-3})}, \tag{1.3}$$

where $\omega_p = (n_e e^2/m_e\epsilon_0)^{1/2}$ is the electron plasma frequency and n_e is the ambient electron number density. For instance, a plasma density of $n_e = 10^{18}\, cm^{-3}$ yields $E_0 \simeq 96\, GV/m$, which is approximately three orders of magnitude greater than that achieved in conventional linacs. In addition, since the plasma is already ionized, breakdown issues such as those encountered in the conventional linear accelerators are not of concern in plasma-based accelerators. With such high accelerating gradient fields, plasma based accelerators can potentially accelerate the particles to the desired energy in a much shorter distance than conventional accelerators. Therefore, plasma based accelerators have the potential to become the next generation of compact accelerators.

Plasma waves in plasma based accelerators can be excited by intense laser pulse(s) or by energetic particle beams. Comprehensive overviews of plasma based accelerators can be found in Refs.[11, 12]. The approach of interest in this thesis is driving the plasma waves with an ultra-intense laser pulse, which is normally referred to as laser wakefield acceleration (LWFA). The concept of LWFA was first proposed by Tajiama and Dawson in 1979 [6]. In LWFA, a traveling intense laser pulse in underdense plasma excites a plasma wave or wake with a phase velocity close to the speed of light. The excited plasma wave is essentially a density modulation of the plasma electrons by which strong longitudinal E-fields were developed in the electron depleted region where the local

charge is greatly unbalanced. Electrons trapped in the plasma wave with sufficient initial energy can be accelerated by the established longitudinal E-field for a long time and gain a significant amount of energy. The trapped electrons tend to bunch up in phase space as they are accelerated in the plasma wave, resulting in monoenergetic bunches with narrow energy spread. In addition, the spatial length of the accelerated electron bunch is constrained by the period of the plasma wave, making the electron bunch extremely short with a pulse duration on the order of a few femtoseconds [13].

Remarkable progress has been achieved in making high-quality energetic electrons with the LWFA scheme. Much of this development is due to the rapid development of CPA laser technology, making compact sources of intense, high power, ultrashort laser pulses readily available. In recent years, LWFA researchers have been able to produce low divergence[14, 15], energy-tunable[16, 17], MeV-to-GeV scale [18, 19, 20] electron bunches with good stability. These beams are of great interest as a driver for various free-electron X-ray sources[21]. For instance, by colliding the laser-wakefield relativistic electrons with an intense laser pulse, a bright narrow-band X-ray pulse tunable from $\sim$ 70 keV to $>$ 1 MeV is generated through a mechanism known as Thomson scattering [22]. This new generation of tunable ultrashort hard X-ray radiation can be used in many X-ray radiological applications[23, 24].

The plasma wave in LWFA not only has a strong accelerating field but also has strong focusing fields. These focusing fields can cause the trapped electrons to oscillate transverse to their acceleration direction, in "betatron orbits". This motion generates X-ray radiation, so called Betatron radiation, which can have a peak brightness comparable to that obtained with conventional "3rd generation" light sources [25]. This is in part due to the ultra-short-pulse nature of the Betatron radiation that is expected to have the same temporal duration as the laser excited electron bunch, i.e.: a few femtoseconds. In addition, Betatron radiation has other attractive properties such as broad bandwidth,

narrow divergence and accurate synchronization with the laser source pulse. Such X-ray sources can be used in a wide range of studies into the structure of matter.

As the major part of this thesis, the aim of my Ph.D studies are:

- to study the electron acceleration with the LFWA scheme. Of particular interest are achieving stable generation of monoenergetic GeV-level electrons with different injection mechanisms, studying the scaling of the electron energy with plasma density and optimizing the charge of the accelerated electrons.

- to characterize the Betatron radiation by using the X-ray reflection off a grazing incidence mirror.

- to employ the Betatron radiation to temporally resolve the ionization states of warm dense aluminum.

1.2 Inertial confinement fusion and Fast ignition

Fusion reactions combine lighter nuclei, such as hydrogen, together to form a heavier one. According to Einstein's mass-energy relationship, i.e.: $E = mc^2$, a nuclear reaction in which the total mass of the final products is smaller than that of the initial reacting nuclei releases energy that is proportional to such a mass difference. Another way to interpret this is through the nuclear binding energy, which is the energy one must invest to disassemble the nucleus into its component neutrons and protons. For fusion reaction, the heavier nucleus in the final state has a stronger nuclear force to bind the nucleons to a lower potential state, thus releasing energy that is given by the difference between the final and initial binding energies of the interacting nuclei.

Of many potential fusion reactions, the easiest one to target for terrestrial power production is the DT reaction:

$$D + T \rightarrow \alpha\,(3.5MeV) + n\,(14.1MeV) \tag{1.4}$$

due to its large fusion cross-sections (1-5 barns[1]) achievable at relatively modest collision energies (25 - 300 keV) [26]. In the above equation, D and T represent deuterium and tritium (isotopes of hydrogen), and α and n stand for an alpha particle (or helium nucleus ${}^{4}_{2}He$) and neutron respectively. The DT reaction is the goal for many clean-energy minded scientists. The DT reaction implies that most of the energy emerges primarily as neutrons. For applications such as the production of electricity, one has to convert the kinetic energy from the neutrons to heat in order to make use of the energy. For other uses, the neutrons produced in the DT reactions can be used as breeders of fuel for power plants using nuclear fission or to burn up radioactive waste produced from fission reactors.

To combine two positively charged nuclei together, one has to overcome the strong coulomb repulsive barrier. One way to achieve this is to confine the reaction nuclei in the form of plasma with sufficiently high temperature, on the order of 10 keV. Under the thermal equilibrium condition, the Coulomb collisions just redistribute the kinetic energy among plasma particles, and fusion reactions will occur primarily for particles in the high energy tail of the distribution function. This approach is referred to as thermonuclear fusion. For the fusion to occur, the plasma has to be maintained for a sufficient period of time and at a certain level of temperature and density.

Currently, there are two major approaches to confine such a fusion plasma, magnetic and inertial confinement. The magnetic confinement approach takes advantage of the nature of plasma as charged particles. Charged particles such

[1] 1 barn $= 10^{-24}\ cm^{-2}$

as the fuel ions follow the magnetic field lines. The fusion fuel can therefore be trapped in devices with appropriate magnetic field configurations. Examples are Tokamaks[27] and Stellarators[28]. Inertial confinement involves no external means of confinement, but exclusively relies on mass inertia. Suppose a fusion plasma has been assembled in a spherical volume. The mass inertia then keeps it together for a short period of time given by the time a sound wave takes to travel from the surface to the center. The fusion burn has to occur in this period of time. The approach of interest in this thesis is related to inertial confinement fusion (ICF), therefore, the rest of this section will be limited to ICF.

Because of the short confinement time in ICF, typically one tenth of a nanosecond, to burn a considerable part of the fuel, one has to confine the fuel plasma to extremely high densities to achieve high reaction rates. According to the Lawson criterion that defines the ignition condition for fusion reactions, $n\tau > 10^{14}\ s/cm^3$ [29], where n and τ are the number density for the reaction nuclei and confinement time respectively, the DT fuel for ICF has to be compressed to about a thousand times its solid density.

Compression in ICF is achieved through implosion of an ultra-smooth hollow spherical fuel shell of ~ 2 mm diameter. The shell itself has an outer layer of Be, C or polymer to form an ablator with a region of DT ice on its inner surface. The inside of the shell is filled with DT gas. The potential driver can be a high power laser or ion beam. The method of interest in this thesis is to use an array of short energetic laser pulses, delivering enough energy to heat and compress the fuel. This is known as laser fusion.

There are two primary approaches through which the laser pulses generate the required energy flux and pressure for the implosion, i.e. direct drive and indirect drive, as presented in Fig.1.2. In the direct dive scheme, the lasers irradiate directly the fuel capsule surface, ablating the outside layer and driving a strong implosion. In indirect drive, the lasers are directed on the inner wall

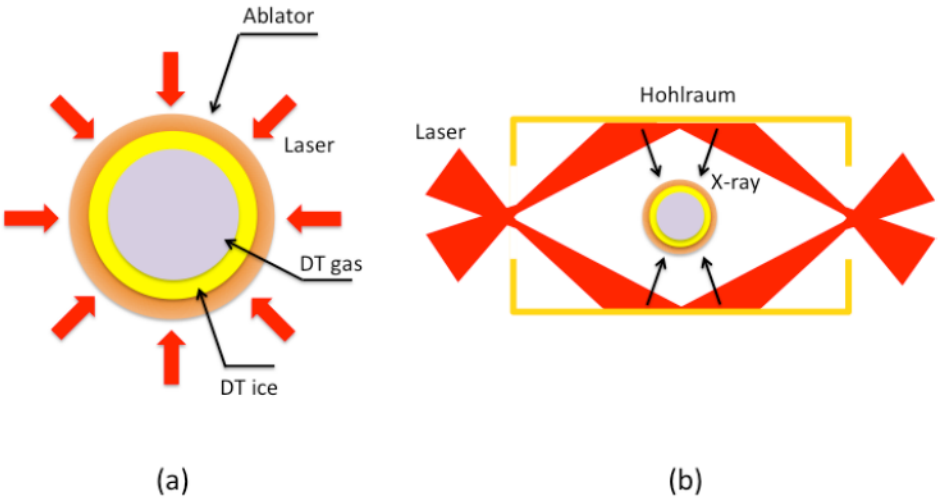

Figure 1.2: Comparison of direct-drive (a) and indirect-drive (b) compressing the fuel in ICF.

of a hohlraum that contains the fuel capsule, producing X-rays that irradiate the fuel. The hohlraum is a canister with laser entrance holes at each end and is made of gold or other high-Z materials such that the generated plasma re-radiates most of the absorbed laser energy in the form of X-rays. In both direct and indirect drive, intense radiation of the capsule ablates the front layer and the consequent rocket-like reaction pressure from the ablated plasma drives the implosion of the fuel, creating a central hot spot (CHS) for igniting the DT fuel.

Of these two methods, the direct drive is more efficient in energy coupling. However, indirect drive allows for a more symmetric drive because X-rays emitted from the hohlraum are uniform and isotropic. Furthermore, the radiation-driven implosion from the indirect drive is more stable with respect to hydrodynamic instabilities [26]. For both schemes, the global efficiency of the compression is limited by the implosion asymmetries, which mainly come from the defects of the capsule manufacture and the uniformity of the laser irradiation. Moreover, the ignition of these two schemes relies on the formation of a central hot spot, which requires good control of hydrodynamic instabilities

during implosion. These issues with the above two CHS ignition schemes necessitate a high-precision drive. Fast Ignition (FI) is designed to separate the compression and ignition processes and thus reduce the stringent requirements on the implosion drive somewhat.

The idea of FI is to decouple the fuel ignition process from its compression. Firstly, fuel is imploded to produce a high-density configuration without a hot spot. Secondly, the imploded fuel is brought to ignition by use of an external energy source: e.g.: a hot electron beam with relativistic energies produced by one or more high-power laser pulses interacting with the fuel. In the FI scheme, the hot spot required for ignition can be created by hot electrons depositing energy in an off-center small area of the imploded fuel. More details of FI are given in Chapter 3.

Fast ignition presents many distinct advantages in comparison with the CHS schemes, and offers the possibility to achieve ignition at lower total laser energies. Examples of the advantages for FI are lower ignition threshold, higher gain and lower sensitivity to the hydrodynamic instabilities. In particular, the low sensitivity to hydrodynamic instabilities relaxes significantly the requirements on the smoothness of the target surface and the spherical uniformity of the drive.

The success of the FI scheme relies on efficient energy coupling from the heating laser to the hot electrons and subsequent transport of this energy to the compressed fuel. In particular, the transport involves relativistic electron beams with currents on the order of 100 MA. And they have to cross an overdense plasma region with thickness of some 100 μm to deposit an energy of $\sim$ 20 kJ in a small area with diameter of $\sim$ 40 μm. As it turns out, transport of such currents through plasma is a complex problem. First of all, the hot electrons are born with large angular divergence, requiring special target designs for beam collimation. Secondly, the hot electrons are subject to beam filamentation and energy dissipation by collective mechanisms [30]. These challenges

have to taken into account and overcome before the Fast Ignition concept can be put into practical use.

My research related to FI was to study hot electron transport relevant to the fast ignition, and in particular, to investigate the effect of resistive layers within the target on the hot electron divergence and absorption.

1.3 Outline of the Thesis

Chapter 2 provides a detailed background of the physics of the electron acceleration and Betatron radiation generation related to the laser wakefield acceleration. Regarding the electron acceleration, an overview of the acceleration mechanism is given first, followed by a detailed introduction of some important nonlinear processes that are involved in LWFA. With respect to Betatron radiation, the physics of the radiation generation along with the theory concerned with some important features of Betatron radiation is described in detail.

Chapter 3 presents some basic background related to Fast Ignition and absorption mechanisms that allow the the energy of ultra-intense laser pulse to be transferred to the plasma. In addition, the temperature scaling of the hot electrons and the physics of the return current for neutralizing the hot current is discussed.

Chapter 4 gives an overview of the 200 TW laser system at the Advanced Laser Light source (ALLS) located at INRS at Varennes, Quebec and the Titan laser beamline in the Jupiter Laser Facility at Lawrence Livermore National Laboratory. The LWFA experiments described in this thesis were conducted with the 200 TW laser at ALLS and the FI experiments with the Titan laser. Also presented in this chapter are some diagnostics that were used during the experiments.

Chapter 5 discusses a LWFA experiment where electron energy enhance-

ment was observed at relatively high plasma density, which was due to a non-linear transition from LWFA to plasma wakaefield acceleration (PWFA) as verified by 3D Particle-in-Cell (PIC) simulations.

Chapter 6 demonstrates another LWFA experiment where mono-energetic electron bunches with peak energy as high as 0.5 GeV were achieved with pure nitrogen gas.

Chapter 7 illustrates the experimental results of GeV electrons from LWFA achieved with ionization injection using CO_2 mixed in He.

Chapter 8 describes a new diagnostic technique through which the critical energy of the Betatron radiation can be measured based on emission in the 5-10 keV range. This technique is based on the X-ray reflection off a grazing-incidence mirror.

Chapter 9 presents the characterization of a Betatron X-ray probe beam-line, which was developed to temporally resolve the ionization states of Warm Dense Aluminum. With this Betatron X-ray probe, the ionization state of the Warm Dense Aluminum was successfully measured. The experimental results along with the simulation results for interpreting the measurements are given in **Chapter 10**.

Chapter 11 is dedicated to Fast Ignition related measurements. This chapter discusses an experiment in which the resistive effect from a high-Z material layer on the hot electron divergence and absorption was studied. Electron transport simulation with a kinetic electron transport code was conducted and the results compared with the observations from the experiments.

Chapter 12 summarizes the work and its impact and proposes further steps to expand upon the work herein.

Chapter 2

Physics of Laser Wakefield Acceleration

2.1 Electron acceleration

The mechanism of laser wakefield acceleration, as illustrated in Fig.2.1, can be understood by the following scenario: Consider an ultra-intense short laser pulse, $> 10^{18}\ W/cm^2$, propagating into an underdense plasma. The electrons are expelled from the beam axis by the ponderomotive force (pressure of the light wave, see Sec.2.1.1) of the laser pulse and form a sheath surrounding the ions, which remain immobile due to the heavy mass. A cavity void of electrons is therefore set up behind the laser pulse. The resulting cavity, termed as 'wake' or 'bubble', travels with the light pulse at a phase velocity close to the speed of light. It is worthwhile mentioning that in plasma-based wakefield acceleration, a regime which involves the complete expulsion of the plasma electrons from some region about the axis behind the driver is commonly referred to as a bubble or blowout regime. Inside the wake in the bubble regime, the longitudinal electric field can reach a magnitude on the order of 100's of GeV/m, which is able to accelerate electrons to strongly relativistic energies in very short distances.

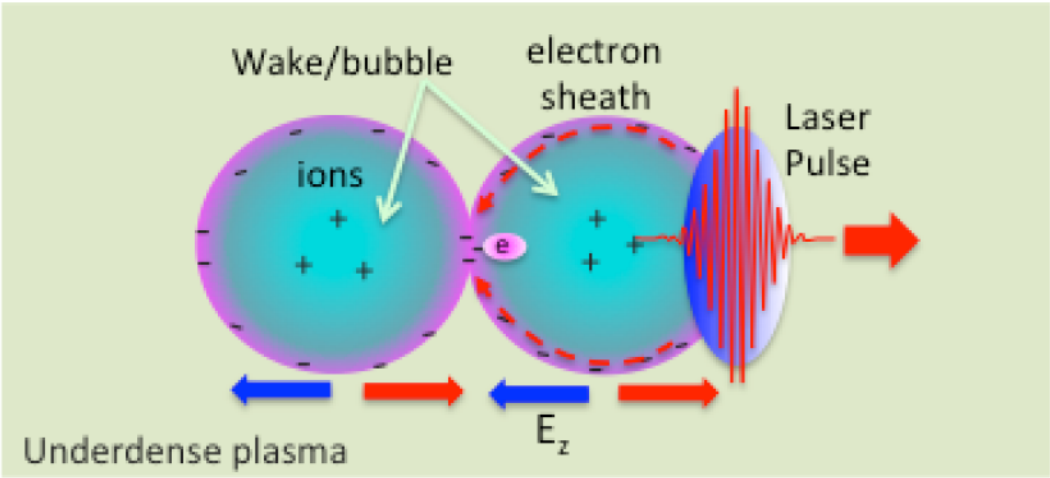

Figure 2.1: Schematic diagram showing the process of laser wakefield acceleration.

Due to the coulomb force from the space charge, electrons from the sheath will be accelerated back to axis at the tail of the wake and some of the electrons can be injected into the wake if they gain sufficient energy to catch up with the wake before slipping into the deceleration phase [31]. Loading of the injected electrons into the wake weakens the wakefield amplitude (beam loading), reducing the field gradient below the injection threshold and consequently terminating the injection, thus producing a group of monoenergetic electrons. The injected electrons can be accelerated until they overrun the wake, after which electrons will experience deceleration and lose energy accordingly. This process is commonly referred to as electron dephasing and the corresponding acceleration distance is defined as dephasing length. While traveling inside the underdense plasma, the laser pulse is subject to energy dissipation that is dominated by erosion of the pulse leading edge and energy expended in the plasma wakes formation[32]. As a result, the laser will completely deplete in energy after propagating a certain length, namely the pump depletion length, and can't drive the wakefield any longer after this length. The required intensity to drive the wakefields is achieved by tight focusing of the high power laser

pulse and subsequent relativistic self focusing of the laser pulse. However, the leading edge of the laser pulse tends to diffract more rapidly before the self focusing sets in, leading to continuous erosion of the leading edge of the pulse, which will slowly reduce the laser intensity so as to terminate the driving of the bubble. Fortunately, the self-focusing of the laser pulse that takes place during the propagation cancels out the inherent diffraction effect for the majority of the laser pulse length, allowing the laser pulse to travel many Rayleigh lengths with high intensity. This nonlinear process is referred to as self-guiding and plays a significant role in achieving high energy electrons for the LWFA scheme.

As described above, LWFA involves a number of nonlinear phenomena that can effect the electron acceleration and can determine the characteristics of the final electron bunch such as the peak energy, beam divergence and the monochromaticity. Therefore, it is vital to understand the underlying physics of these nonlinear processes.

2.1.1 Ponderomotive Force

Light waves have radiation pressure. In general, this pressure is so weak as to be difficult to measure. However, in the high laser intensity regime, this pressure becomes substantial and when applied to the plasma can transform to a strong nonlinear force, known as Ponderomotive force (PMF) [33], that can couple to the particles.

To derive this nonlinear force, we start with the equation of motion for an electron in the presence of oscillating $\mathbf{E}$ and $\mathbf{B}$ fields of a wave [33]:

$$m\frac{d\mathbf{v}}{dt} = -e[\mathbf{E}(\mathbf{r}) + \mathbf{v} \times \mathbf{B}(\mathbf{r})] \tag{2.1}$$

According to the linear theory, dependent variables can be decomposed into two parts, an equilibrium part indicated by a subscript 0 and a perturbation part indicated by a subscript 1: $\mathbf{E} = \mathbf{E}_0 + \mathbf{E}_1$, $\mathbf{B} = \mathbf{B}_0 + \mathbf{B}_1$, $\mathbf{v} = \mathbf{v}_0 + \mathbf{v}_1$.

In the equilibrium state, we can assume the electron is at rest and the $\mathbf{E}$ and $\mathbf{B}$ fields are absent, therefore, one can have: $\mathbf{E}_0 = 0$, $\mathbf{B}_0 = 0$ and $\mathbf{v}_0 = 0$. Apparently, the nonlinearity only comes from the perturbations, i.e.: $\mathbf{v}_1 \times \mathbf{B}_1$ and $\mathbf{E}_1$ since all of the equilibrium parts vanish. Since the perturbations are small in amplitude, any terms containing higher power than the product of two perturbation quantities will be neglected.

Assume a wave electric field taking the form of:

$$\mathbf{E} = \mathbf{E}_s(\mathbf{r})\ cos\ \omega t \tag{2.2}$$

where $\mathbf{E}_s(\mathbf{r})$ contains the spatial dependence. To first order, we may neglect the $\mathbf{v} \times \mathbf{B}$ term in Eqn.2.1 and evaluate the $\mathbf{E}$ at the initial position $\mathbf{r}_0$. We have

$$m\frac{d\mathbf{v}_1}{dt} = -e\mathbf{E}(\mathbf{r}_0) \tag{2.3}$$

$$\mathbf{v}_1 = -(e/m\omega)\mathbf{E}_s\ sin\ \omega t = d\mathbf{r}_1/dt \tag{2.4}$$

$$\mathbf{r}_1 = (e/m\omega^2)\mathbf{E}_s\ cos\ \omega t \tag{2.5}$$

Going to second order, we expand $\mathbf{E}(\mathbf{r})$ about $\mathbf{r}_0$ in Tyler series:

$$\mathbf{E}(\mathbf{r}) = \mathbf{E}(\mathbf{r}_0) + ((\mathbf{r} - \mathbf{r}_0) \cdot \nabla)\mathbf{E} \mid_{r=r_0} + ... \tag{2.6}$$

where $((\mathbf{r} - \mathbf{r}_0) \cdot \nabla)\mathbf{E} \mid_{r=r_0} = \mathbf{E}_1$, and $\mathbf{r} - \mathbf{r}_0 = \mathbf{r}_1$. And now we have to account for the cross term in Eqn.(2.1), $\mathbf{v}_1 \times \mathbf{B}_1$, and $\mathbf{B}_1$ is given by Maxwell's equation:

$$\nabla \times \mathbf{E} = -\partial B/\partial t \tag{2.7}$$

$$\mathbf{B}_1 = -(1/\omega)\nabla \times \mathbf{E}_s \mid_{r=r_0}\ \sin\ \omega t \tag{2.8}$$

Considering the contribution only from the perturbation, Eqn.(2.1) can be

recast as:

$$m\frac{d\mathbf{v}_1}{dt} = -e[((\mathbf{r}-\mathbf{r}_0)\cdot\nabla)\mathbf{E} + \mathbf{v}_1 \times \mathbf{B}_1] \tag{2.9}$$

Substituting Eqns.2.4, 2.5 and 2.8 into the above equation and averaging over time, one can get:

$$\mathbf{f}_{NL} = m\left\langle \frac{d\mathbf{v}_1}{dt} \right\rangle = -\frac{1}{2}\frac{e^2}{m\omega^2}[(\mathbf{E}_s\cdot\nabla)\mathbf{E}_s + \mathbf{E}_s \times (\nabla \times \mathbf{E}_s)] \tag{2.10}$$

where $\langle\ \rangle$ represents the time averaging operator. The prefactor of $\frac{1}{2}$ comes from the equality: $\langle \sin^2\omega t\rangle = \langle cos^2\omega t\rangle = 1/2$. Applying the identity of cross product of $\mathbf{a}\times(\mathbf{b}\times\mathbf{c}) = \mathbf{b}(\mathbf{a}\cdot\mathbf{c}) - \mathbf{c}(\mathbf{a}\cdot\mathbf{b})$ to the above equation, the term $(\mathbf{E}_s\cdot\nabla)\mathbf{E}_s$ will vanish, and what remains is:

$$\begin{aligned}\mathbf{f}_{NL} &= -\frac{1}{2}\frac{e^2}{m\omega^2}\nabla\left\langle \mathbf{E}_s^2(\mathbf{r})\right\rangle \\ &= -\frac{1}{4}\frac{e^2}{m\omega^2}\nabla\mathbf{E}_s^2\end{aligned}$$

Here, another factor of $1/2$ comes in because of the independent variable $\mathbf{r}$, which is a cosine function of time. This is the effective nonlinear force that is exerted on a single electron. By multiplying this force with the electron density n_e, which can be written in terms of plasma angular frequency of ω_p, as well as using the equality of $\mathbf{E}_s^2 = 2\left\langle \mathbf{E}^2\right\rangle$, one can achieve the formula of ponderomotive force in unit of N/m^3:

$$\mathbf{F}_{NL} = -\frac{\omega_p^2}{\omega^2}\nabla\frac{\left\langle \epsilon_0\mathbf{E}^2\right\rangle}{2} \tag{2.11}$$

From the above equation, one can tell that ponderomotive force is a result of spatial gradient of the laser intensity, therefore, it exists in both the transverse and longitudinal directions when laser propagates in a plasma. In the case of underdense plasma, transversely, this force tends to push the electrons away from high intensity area, whereas, longitudinally, this force snow plows the

electrons forward, forming a narrow plasma density spike that in turn can erode the leading edge of the laser pulse.

After further derivation, one can get the radiation pressure p_{pmf} resulting from the PMF as a function of laser peak intensity I_p, which is given by:

$$p_{pmf} = \frac{1}{2}\frac{I_p}{c} \tag{2.12}$$

For instance, given an ultrahigh laser intensity on the order of $10^{18}\ W/cm^2$, the above equation gives a radiation pressure as high as 10^8 atmospheres, which is approximately two orders of magnitude higher than the pressure in the core of the earth.

2.1.2 Self-guiding

To maintain the strong longitudinal field over distances required to achieve highly energetic electrons, the laser must be sustained at ultra-high intensity over several Rayleigh lengths. This requirement for sustained high laser intensity can be satisfied by the self-guiding of the laser pulse itself where the inherent diffraction is balanced by the self-focusing of the laser pulse. Self-focusing occurs in the relativistic regime due to an increase in refractive index of the plasma with intensity due to the relativistic increase in the electron mass. A threshold power for self focusing to balance diffraction is given by the critical power P_c, which is given by:

$$P_c(GW) = 17\frac{\omega_0^2}{\omega_p^2} = 17\frac{n_c}{n_e} \tag{2.13}$$

where ω_0 is the laser angular frequency in vacuum, ω_p is the plasma frequency, given by $\omega_p = \sqrt{n_e\, e^2/(m_e \epsilon_0)}$, n_e is the plasma density and n_c is the critical density for the incident laser frequency as given in Eqn.1.1.

A laser beam can be approximated by a Gaussian profile in which the trans-

verse electric field or intensity distributions are given by Gaussian functions. When a Gaussian beam is focused by a lens, at the focal position, the intensity distribution is given by $I(r) = I_0\, e^{-2r^2/W_0^2}$, where I_0 is the peak intensity, r is the radial distance from the center axis of the beam and W_0 is the focal spot radius at which the intensity drops to $1/e^2$ of the peak value. In LWFA, a stable self-guiding of the laser pulse is achieved when the self-focused laser spot size, W_0, matches with the bubble radius, R_b, by the approximate relation[34]:

$$W_0 \sim R_b = \frac{2\sqrt{a_0}}{k_p} \propto n_e^{-1/2} \tag{2.14}$$

where a_0 is the laser normalized vector as given by Eqn.1.2, k_p is the plasma propagation constant given by $k_p = 2\pi/\lambda_p$, and λ_p is the plasma wavelength.

2.1.3 Wavebreaking and Self-Injection

As previously mentioned, the advantage of plasma-based acceleration is that plasmas are capable of supporting large amplitude electrostatic waves with phase velocities close to the speed of light . The maximum electric field strength is reached when all the plasma electrons are oscillating with the same wave number $k_p = \omega_p/c$, where ω_p is the plasma frequency. In the linear regime ($a < 1$), the plasma waves are assumed sinusoidal, and the maximum field strength is given by:

$$E_{WB0}[V/cm] = cm_e\omega_p/e \simeq 0.96\sqrt{n_e(cm^{-3})} \tag{2.15}$$

which is known as the cold nonrelativistic wave breaking field [35]. The wave-breaking limit is reached when the local fluid velocity in the wave equals the wave velocity and particles can start to be trapped and accelerated by the wave. The most familiar analogy to the wave breaking is the breaking of water surface waves on a coastline. When a wave reaches the coast, its wave crest steepens as

the amplitude increases due to the horizontal component of the fluid velocity associated with the wave motion. As the amplitude reaches to the point that the wave crest overruns the wave, the wave starts to spill forward or the wave starts to break.

In the nonlinear regime, the maximum electric field could be potentially higher due to the additional nonlinear behavior of the plasma waves. In the one-dimensional nonlinear regime ($a_0 > 1$), the maximum amplitude of a single period plasma wave is given by [36]:

$$E_{WB} = \sqrt{2}(\gamma_p - 1)^{1/2} E_{WB0} \tag{2.16}$$

which is referred to as the cold relativistic wave breaking field, where $\gamma_p = (1 - v_p^2/c^2)^{-1/2}$ is the relativistic Lorentz factor associated with the phase velocity v_p of the plasma wave. In the three-dimensional nonlinear regime ($a_0 > 2$), this maximum amplitude differs and is approximated as $E_{max} \simeq \sqrt{a_0}\, E_{WB0}$ [34]. For instance, given the currently available ultra-high power lasers and large numerical aperture focusing optics, a_0 can reach as high as 10 [18], which gives $E_{max} \simeq 3E_{WB0}$.

When the plasma waves are excited far beyond the wave breaking limit, the wave structure is destroyed and a large amount of charge can be accelerated to high energy but with a broad energy spread. However, with appropriately shaped laser pulses, this normally catastrophic process of wave breaking can be tamed to produce high quality beams of electrons. What happens is that when the wave is close to the wave breaking limit, some electrons from the electron sheath can be trapped into the wake without destroying the wave structure. This trapping process takes place at the tail of the bubble and is normally referred to as self-trapping or self-injection. For the self-injection to occur, electrons at the tail of the bubble must be able to catch up with the wake. For this to happen, the following physical conditions have to be satisfied [34]:

- the bubble radius is large enough. This provides sufficient distance for the electrons that drift backward on the sheath to gain enough longitudinal momentum to move in the forward direction with a speed close to the speed of light by the time they reach the tail of the bubble. Note that the electrons in the sheath are accelerated by the bubble fields.

- the trajectory of crossing electron beams created by the laser ponderomotive force gives birth to a narrow sheath at the rear part of the ion channel with the highest accelerating and focusing fields.

To date, a number of experimental and theoretical studies have been conducted to fully understand the dynamics of this self-injection process [34, 37, 38, 39, 40, 41]. Many of the experiments and simulations consistently show that it requires laser intensity a_0 of approximately 3 - 4 to reach the threshold of self-injection [34, 38, 39]. Based on the size matching condition required for self-guided propagation as shown in Eqn.2.14, one can find that this threshold intensity $a_0 > (3-4)$ is equivalent to stating that the minimum normalized bubble size $(k_p R_b)$ for self-injection is $(k_p R_b)_{min} \sim (3.5-4)$, independent of plasma density.

In contrast, a recent paper that analytically studied the electron trajectories in a plasma bubble derived an approximate threshold equation for self-injection in which the minimum normalized bubble size $(k_p R_b)$ is dependent on the plasma density and is given by [40]:

$$k_p R_b > 2\sqrt{\ln(2\gamma_p^2) - 1} \tag{2.17}$$

where $\gamma_p \simeq \frac{1}{\sqrt{3}}\omega_0/\omega_p$ [32] is the Lorentz factor associated with the phase velocity of the bubble in the 3D nonlinear regime. Equation 2.17 was obtained by solving for the trapping condition in which the maximum distance an electron slips back relative to the bubble center is shorter than the bubble radius. Based on this equation, Mangles et al. derived an analytical model that finds the

plasma density threshold for self-injection by using the relation between the bubble radius and the laser pulse energy and duration, $k_p R_b = 2\sqrt{2}(\alpha E/\tau P_c)^{1/6}$ [34], where α is the fraction of the energy contained in the FWHM of the laser focal spot, E is the total energy of the laser pulse, P_c is the critical power for self-focusing, τ is the laser pulse duration. The final expression of the plasma density threshold for self-injection takes the form of [37]:

$$\alpha E > 8P_c \left[\ln(\frac{2n_c}{3n_e}) - 1\right]^3 \tau(l) \tag{2.18}$$

where $\tau(l)$ is the pulse duration after a propagation length l and is given by $\tau(l) \simeq \tau_0 - (n_e l)/(2cn_c)$, where τ_0 is the original pulse duration of the laser before interacting with the plasma. Apparently, this model requires the knowledge of initial laser pulse energy, laser pulse duration and plasma interaction length to predict the density threshold. To give an example, given $\alpha E = 1$ J, for a 30 fs and 800 nm laser pulse, this model predicts a density threshold for self-injection of $\sim 7 \times 10^{18}\ cm^{-3}$ for an effective laser plasma interaction length of 2 mm.

2.1.4 Ionization Injection

The drawback of self-injection is the relatively high laser intensity ($a_0 > 3-4$) that is required to initiate the injection, increasing the difficulty of achieving high energy electrons. However this intensity threshold can be reduced to $a_0 > 1.6$ [31, 42] when using the ionization injection approach instead, in which injection relies on tunnel ionization of the inner shell electrons by the most intense part of the laser field. Note that tunnel ionization is a process in which bound electrons escape the atomic potential barrier holding them to the nucleus due to suppression by the strong electric field of a laser pulse. The threshold laser intensity or appearance intensity for onset of tunnel ionization

Table 2.1: Appearance Intensities of selected ions for tunnel ionization according to Eqn.2.19.

Ion	$E_{ion}(eV)$	I_{app} (W/cm^2)
He^{+}	24.59	1.46×10^{15}
He^{2+}	54.42	8.77×10^{15}
N^{5+}	97.9	1.47×10^{16}
N^{6+}	552.1	1.03×10^{19}
N^{7+}	667.0	1.62×10^{19}
O^{6+}	138.1	4.04×10^{16}
O^{7+}	739.3	2.44×10^{19}
O^{8+}	871.4	3.60×10^{19}

is given by [43]:

$$I_{app}(W/cm^2) \simeq 4 \times 10^9 (\frac{E_{ion}}{eV})^4 Z^{-2} \tag{2.19}$$

where E_{ion} is the ionization potential of the ion or atom with charge (Z-1). For convenience, we tabulated the threshold laser intensities for a few ions of interest in laser wakefield acceleration experiments, as shown in Table 2.1.

In ionization injection, atoms with large difference in the ionization potential between outer and inner shell electrons, for instance nitrogen and oxygen as indicated in Table 2.1, are introduced as the interaction medium instead of uniformly ionized atoms like He and H_2 that are used in self-injection. The outer shell electrons (for example N^{1+} to N^{5+}) are ionized by the leading edge of laser and are subsequently expelled by the laser ponderomotive force to form the electron sheath. Whereas the inner shell electrons (N^{6+} and N^{7+}) residing in the wake created by the outer shell electrons are only ionized by the peak of laser. These inner shell electrons that are born inside the wake are initially at rest. As a result, in the frame of the laser pulse, they slip back but simultaneously feel the established longitudinal field and Ponderomotive field and therefore gain energy. Once they gain enough energy to reach the phase velocity of the wake, they will turn around and move in the forward direction with

respect to the wake and will be accelerated to higher energy. Because of the net potential difference between the bubble edge and its interior, these injected electrons are born with a higher initial potential energy compared with their counterparts in the self-injection scheme, thus requiring less intensity to inject them into the wake.

2.1.5 Maximum Energy Gain

Once the electrons are injected into the bubble either through self-injection or ionization injection, they will be accelerated by the longitudinal electric field until they cross the middle of the bubble, after which they will be out of phase with the wake and start to decelerate. The distance that electrons travel until they become out of phase with the wake is called the dephasing length, L_d, which is given by[34]:

$$L_d \cong \frac{4}{3}\frac{\omega_0^2}{\omega_p^2}\frac{\sqrt{a_0}}{k_p} = \frac{4}{3}\frac{n_c}{n_e}\frac{\sqrt{a_0}}{k_p} \tag{2.20}$$

where ω_p is the plasma frequency, k_p is the propagation constant of the plasma wave, n_e is plasma density and a_0 is the laser normalized amplitude. As previously mentioned, the laser pulse is subject to energy dissipation that is dominated by erosion of the pulse leading edge and the plasma wake formation during propagation inside the plasma. In other words, the laser pulse will be depleted after some distance, which is called the pump depletion length, given by [34]:

$$L_{pd} \simeq \frac{\omega_0^2}{\omega_p^2} c\tau_{FWHM} \tag{2.21}$$

where τ_{FWHM} is the laser pulse duration at FWHM.

Where electron acceleration is dominated by the dephasing length, the maximum energy gain is simply the product of the dephasing length and the average longitudinal electric field inside the wake. The peak longitudinal electric field inside a 3D nonliear wake is [34] $E_{z,max}(V/m) = mc\omega_p\sqrt{a_0}/e =$

$96\sqrt{n_e(cm^{-3})}\sqrt{a_0}$, and because the wakefield is roughly linear, the average wakefield is half of the $E_{z,max}$, i.e.: $E_{LW}(V/m) = 48\sqrt{n_e(cm^{-3})}\sqrt{a_0}$. Under the laser self-guiding condition, the peak intensity reaches a stationary value giving a laser normalized amplitude of [34]:

$$a_0 \simeq 2(P/P_c)^{1/3} \tag{2.22}$$

where P is the laser power and P_c is the critical power as given by Eqn.2.13. By multiplying the dephasing length L_d with the average wakefield E_{LW} and replacing a_0 with Eqn.2.22, one will achieve the following equation for the maximum energy gain [34]:

$$\Delta E_{max}(GeV) \cong 1.7(\frac{P[TW]}{100})^{1/3}(\frac{10^{18}}{n_e\,[cm^{-3}]})^{2/3}(\frac{0.8}{\lambda_0\,[\mu m]})^{4/3} \tag{2.23}$$

where $P[TW]$ is laser power in TW, n_e is the electron density in cm^{-3} and λ_0 is the laser wavelength in μm. For a given laser wavelength, the maximum energy gain increases with the laser power but decreases with the electron density, which in part is due to the fact that the depahsing length becomes shorter with increasing density. Normally, for most of the LWFA experiments, Ti:sapphire lasers with a central wavelength of 0.8 μm were employed. Therefore the dependency on the wavelength in the last term is normally neglected. However, it is clear that shorter wavelengths should lead to higher energies.

So far, a large number of LWFA experiments have demonstrated the production of monoenergetic electron beams using both self-injection[18, 19, 37, 44, 45, 46, 47, 48] and ionization-induced injection[20, 31, 49, 50, 51]. A summary of the measured peak electron energies reported in the literature is plotted in Fig.2.2 against the predicted peak energies given by Eqn.2.23. The measured energies include the results from both self-injection and ionization injection schemes. As indicated, most of the experimental results agree reasonably well with the predicted energies from the scaling law, Eqn.2.23, regardless of injec-

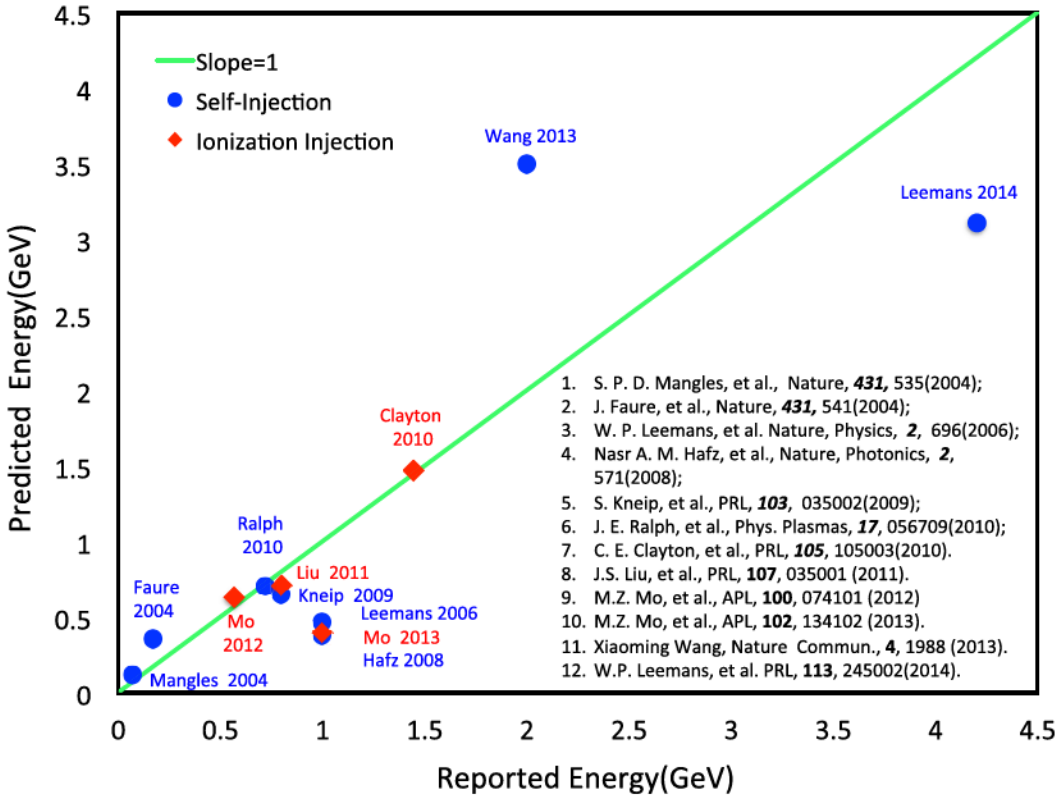

Figure 2.2: Plot of reported peak electron energies obtained in LWFA experiments versus the predicted peak energies achieved with Lu's scaling law as given in Eqn.2.23. Blue solid circles represent electrons that were produced with self-injection scheme whereas red diamonds with ionization injection scheme. The green line indicates reported energies equal to predicted energies.

tion scheme. However there are some cases where the experiments observed energies more than double of the predicted ones. Furthermore, electrons with energies in GeV level have been routinely achieved by many research groups using both self-injection and ionization injection schemes. It is encouraging to point out that the maximum peak electron energies achieved to date have reached as high as 2 GeV, which was recently reported by the research group at University of Texas at Austin [18] and 4 GeV by the research group at University of California at Berkeley [19] using Petawatt-class lasers. With the continuing advancement of the high power laser technology seen today, these records will be certainly broken in the near future.

2.1.6 Beam Loading

Relativistic charged particles such as electrons moving through plasma can excite wakefields in a fashion similar to that of an intense laser pulse. This process is normally referred to as plasma wakefield acceleration (PWFA) [52], and is commonly used in experiments carried out at the Stanford Linear Accelerator Center (SLAC) using GeV electron beams to drive nonlinear plasma waves [53]. For a laser driver, the wake is initiated by the ponderomotive force of the laser pulse which expels the electrons, whereas for a relativistic electron bunch, the plasma wake is excited by the coulomb force of the relativistic electron bunch. In a plasma-based accelerator, the wake resulting from the accelerated bunch is out of phase with that is excited by the driver beam, therefore causing an adverse effect on the original wake. The process by which the wake produced from the accelerated bunch significantly interferes with the field of the original wake from the driver bunch is called beam loading [12]. Beam loading is an inevitable process in plasma-based accelerators and can largely affect the characteristics of the accelerated particle bunch, such as the total charge and energy spread, and therefore the efficiency of the plasma-based accelerators.

To be able to excite a plasma wave, the length of the electron bunch has to

be small enough and satisfy the condition: $k_p\sigma_z \leq 1$ [12], where σ_z is the bunch length. In the linear regime, the issue of beam loading can be addressed by assuming the final accelerating field is a linear superposition of the wakefield generated by the trailing bunch with that of the driver bunch [54]. The maximum number of loaded beam electrons or beam loading limit was evaluated by finding the number of the electrons required to produce a wakefield that will cancel out the accelerating field, which is given by:

$$N_{max} \simeq 5 \times 10^5 \sqrt{n_e(cm^{-3})} A_b(cm^2) \frac{E_z}{E_0} \tag{2.24}$$

assuming $k_p\sigma_z < 1$ and $E_z/E_0 < 1$, where E_0 is the cold nonrelativistic wave breaking field as given in Eqn.2.15, E_z is the longitudinal electric field, n_e is the background plasma density in cm^{-3} and A_b is the cross-sectional area of the bunch in cm^{-2}. For an ultrashort unshaped bunch that contains N electrons, the wake-induced energy spread scales as N/N_{max} and the efficiency of converting wake energy to accelerated electron energy scales as $N/N_{max}(2 - N/N_{max})$. As N approaches N_{max}, the efficiency approaches 100% but at the same time the energy spread approaches 100% as well. Therefore, there is a trade-off between the efficiency and the energy spread for the accelerated electron bunch that is constrained by the beam loading effect.

The beam loading effect has been studied for plasma-based wakefields in the nonlinear 3D bubble regime [55, 56]. Particularly, in Ref.[56], a theoretical model on how the beam loading develops in a nonlinear 3D bubble regime was established and described in great detail. This model is generalized and is applicable to laser driven wakefield acceleration. An analytical solution for the beam loaded charge was derived and is given by:

$$Q(nC) \simeq 0.047 \left(\frac{eE_z}{mc\omega_p}\right)^{-1} \sqrt{\frac{10^{16} cm^{-3}}{n_e}} (k_p R_b)^4 \tag{2.25}$$

where E_z is the axial electric field at the position where the beam loading starts. This equation also illustrates the trade-off between the number of particles that can be accelerated and the accelerating gradient. For a laser wakefield accelerator, assuming matched-beam, self-guided laser propagation, $k_p R_b = 4$ to ensure operation above the self-injection threshold and $n_e = 5 \times 10^{18}\ cm^{-3}$, and choosing $\frac{eE_z}{mc\omega_p} = \frac{k_p R_b}{2} = 2$ [34], one can obtain $Q \simeq 0.3\ nC$. Note that the bunch profile used in deriving the Eqn.2.25 was optimized to be trapezoidal (high charge in front), providing a constant axial field across the bunch to minimize the energy spread in contrast to that of the 1D linear wake case where the axial field scales with N/N_{max} for an unshaped bunch. Therefore, a loaded beam bunch with a trapezoidal shape is favorable for achieving high beam-loading efficiency while minimizing energy spread. While the shape of the accelerated beam bunch cannot be controlled at will, it is possible to minimize beam energy spread by injecting a driver particle bunch with an initial energy chirp or using a monoenergetic trapezoidal bunch to compensate for the modified axial fields from the beam loading effect[56]. Technically, shaping the injected bunch to a trapezoidal shape is relatively easy to implement and is therefore a common technique to achieve high beam-loading efficiency for plasma wakefield acceleration experiments[57].

2.2 Betatron Radiation

The laser induced wakefield not only provides a large longitudinal field on a compact scale for accelerating electrons, but it also offers an ideal system for producing synchrotron-like X-ray radiation.

Recall that in the process of laser wakefield acceleration, the high intensity laser pulse traveling in an underdense plasma expels the plasma electrons from the propagation axis through the ponderomotive force, leaving behind a positively charged bubble void of electrons. Electrons from the perimeter of the

bubble can be injected into the bubble and be accelerated to highly relativistic energies by the strong axial electric field. If injected off axis, the trapped electrons feel a transversal focusing force from the space charge in addition to the strong axial E-field. Because of the transversal focusing force, the electrons undergo betatron oscillations while they are accelerating inside the cavity[21, 58]. The oscillation motion of the electron in the cavity is given by [59]:

$$\frac{d\mathbf{p}}{dt} = -m\,\omega_p^2\,\frac{\mathbf{r}_\perp}{2} + \alpha\frac{m\,c\,\omega_p}{e}\mathbf{u}_z = \mathbf{F}_\perp + \mathbf{F}_\parallel \tag{2.26}$$

where $\mathbf{p}$ is the relativistic momentum of the electron, m is the electron mass at rest, c is the speed of light, ω_p is the plasma frequency, $\mathbf{r}_\perp$ is the transverse position of the electron and $\mathbf{u}_z$ is the unit vector in the axial direction z. The term $\mathbf{F}_\perp$ is the linear restoring force that drives the transverse oscillation of the electron and the term $\mathbf{F}_\parallel$ is responsible for the electron acceleration in the longitudinal direction. α is the factor to account for the difference of the longitudinal E-field strength in different regimes, e.g. in the 3D bubble regime, $\alpha = \sqrt{a_o}/2$ [34].

2.2.1 Emission Spectrum

Due to its relativistic motion, the electron emits synchrotron-like radiation, so called betatron radiation, that is related to the electron trajectory as described in Eqn.2.26. The energy spectrum of the radiation by a single electron following an oscillatory trajectory $\mathbf{r}(t)$ with a normalized velocity $\boldsymbol{\beta}(t)$ is given by[58]:

$$\frac{d^2I}{d\omega\,d\Omega} = \frac{e^2\omega^2}{4\pi^2 c}\,\Big|\int_{-T/2}^{T/2} dt\,[\mathbf{n}\times(\mathbf{n}\times\boldsymbol{\beta})]\exp[i\,\omega\,(t-\mathbf{n}\cdot\mathbf{r}/c)]\Big|^2 \tag{2.27}$$

where $d^2I/d\omega\,d\Omega$ is the energy radiated per frequency ω per solid angle Ω, during the time T, and $\mathbf{n}$ is the unit vector pointing in the direction of observation. The resultant radiation spectrum from the oscillating electron is characterized

by the betatron strength parameter [59], which reads

$$K = \gamma\, r_\beta\, \omega_\beta / c = 1.33 \times 10^{-10} \sqrt{\gamma\, n_e [cm^{-3}]}\, r_\beta\, [\mu m] \tag{2.28}$$

where γ is the relativistic Lorentz factor of the electron, r_β is the amplitude of the electron oscillation, ω_β is the betatron oscillation frequency that is given by $\omega_\beta = \omega_p / \sqrt{2\gamma}$, c is the speed of light and n_e is the plasma density.

The strength parameter K is correlated with the spectral characteristics of the radiation. For the highly relativistic electrons generated by LWFA, the range of interest for the strength parameter is K much larger than unity where the plasma acts like a wiggler and numerous high harmonics are produced leading to a broadband spectrum. The on-axis spectral intensity caused by a single electron can be described by the synchrotron radiation function [60, 61]:

$$\frac{dI}{dE} \cong \frac{1}{4\pi\epsilon_0} \sqrt{3} \frac{e^2}{c} \gamma \frac{E}{E_c} \int_\xi^\infty K_{5/3}(\xi')\, d\xi' \tag{2.29}$$

where $\xi = E/E_c$, and $E_c(keV) \cong 5 \times 10^{-24} \gamma^2 n_e(cm^{-3}) r_\beta(\mu m)$ is the critical energy [59]. Half of the energy will be radiated below E_c and half above E_c. $K_{5/3}$ is a modified Bessel function of the second kind. Because of the strongly relativistic motion of the electrons, the betatron radiation is confined to a narrow cone with half opening angle of $\theta \simeq K/\gamma$. Fig.2.3 plots the betatron spectral intensity as a function of E/E_c according to Eqn.2.29. Two things can be found from the graph. Firstly, the betatron spectrum has a broad bandwidth that extends a few times E_c. Experimentally, betatron radiation up to a few hundreds of keV has been observed [62]. Secondly, the spectral intensity peaks around $0.3\, E_c$, after which the intensity drops exponentially.

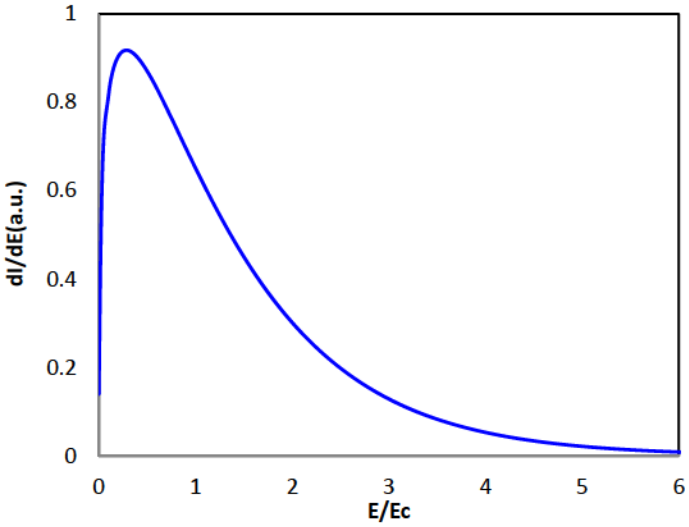

Figure 2.3: Typical spectrum of betatron radiation according to Eqn.2.29.

2.2.2 Emission Brightness

The total number of photons N_{ph}, with mean energy of E_c, radiated by N_e electrons that undergo betatron oscillations inside the wake, is estimated to be [63]:

$$N_{ph} \simeq N_e \frac{2\pi}{9} \frac{e^2}{\hbar c} N_0 K \simeq 5 \times 10^{-3} N_e N_0 K \tag{2.30}$$

where N_0 is the number of betatron oscillations. The number of betatron oscillations performed by an electron inside the wake can be calculated as a ratio of the time needed for the electron to pass through the bubble and the period of the betatron oscillations, which is given by:

$$N_0 \simeq \frac{L/(c - v_\phi)}{2\pi/\omega_\beta} = \frac{\omega_0^2 L}{3\pi\sqrt{2\gamma}\,\omega_p c} \tag{2.31}$$

where L is the bubble length, v_ϕ is the phase velocity of the wake, which is given by $v_\phi \simeq v_g - v_{etch} \simeq c[1 - 3\omega_p^2/(2\omega_0^2)]$ for 3D bubble regime [34], where v_g and v_{etch} are the group velocity of laser light in underdense plasma and the pulse etching velocity respectively. Unlike the Equation 81 in Ref.[63] where

the phase velocity of the wake was treated to be equal to the group velocity of the laser, our expression of N_0 is more appropriate for 3D nonlinear bubble regime. Using the matched beam size condition as shown in Eqn.2.14, one can approximate the bubble length as $L \simeq 4\sqrt{a_0}/k_p$. With this approximation and $k_p = \omega_p/c$, Eqn.2.31 can be rewritten as:

$$N_0 \simeq \frac{\sqrt{2\,a_0}}{3\,\pi\,\sqrt{\gamma}}(\frac{\omega_0}{\omega_p})^2 \tag{2.32}$$

Eqns.(2.30) and (2.32) can be used to estimated the total number of X-ray photons produced from Betatron radiation. Taking the Betatron radiation measurements reported in Ref.[64] as an example, the experimental conditions were $a_0 = 4.7$, $n_e \simeq 1 \times 10^{19}\ cm^{-3}$, $\lambda = 0.8\ \mu m$, $\tau_L = 30\,fs$, the measured electron energy was approximately 200 MeV, corresponding to $\gamma \simeq 391$, the charge of the electrons was measured to be approximately 200 pC, corresponding to $N_e \simeq 1.3 \times 10^9$ and the measured average betatron divergence $\theta \sim 8.5$ $mrad$, corresponding to $K \sim 3.3$ with $K = \theta\gamma$ for 200 MeV electrons. Based on these parameters, from Eqn.2.32 one can obtain $N_0 \sim 2.2$. Substituting N_0 and other necessary parameters into Eqn.2.30, one can get the total emitted photon number $N_{ph} \sim 4.5 \times 10^7$, which is in close agreement with the measurement of around 5×10^7. Knowing the total photon number, one can estimate the brightness at any particular energy E, which is given by:

$$B_X(E) \simeq \alpha(E)\frac{\Delta E}{E}\frac{N_{ph}}{\tau_b\,\theta^2\,A_b^2} \tag{2.33}$$

where τ_b and A_b are the pulse duration and the area of the betatron source respectively, $\alpha(E)$ is the fraction of the number of photons within a bandwidth of ΔE centered around the energy E over the total number of photons emitted, which in principle can be calculated by Eqn.2.29. At $E = E_c$, $\alpha \simeq 0.4$ [63]. From the brightness number given in Ref.[64], one can estimate $B_X \sim 4 \times 10^{21}$ photons/(s $mrad^2$ mm^2 0.1%BW) for X-rays at a photon energy of 30

keV, which is the measured critical energy in that experiment. Such a peak brightness is comparable to currently existing third-generation conventional light sources such as the BESSY U-49 beamline in Germany, which has a peak brightness of $\sim 5 \times 10^{21}$ photons/(s $mrad^2$ mm^2 0.1%BW) for photons with energy of 30 keV [65].

2.2.3 Pulse Duration

In addition to the narrow beam divergence and ultrahigh brightness, another striking feature of the Betatron radiation is its ultrashort pulse duration, on the order of femtoseconds. As we mentioned previously, for laser wakefield acceleration, the injected electrons inside the cavity are accelerated within the rear half of the bubble that has a radius of approximately λ_p. As a result, for dephasing length dominated wakefield acceleration, the electron bunch is mainly constrained in the rear half of the bubble. Therefore, one would expect the electron bunch to be ultrashort, $\tau < \lambda_p/c$, e.g., a duration $\tau < 30$ fs for $n_p = 10^{19}$ cm^{-3}. This simple minded estimation on the pulse duration of the electron bunch was justified by the experiment done by Lundh et al.[13], in which the pulse duration of the electron bunch was measured to be on the order of 1-2 femtoseconds for $n_p = 10^{19}$ cm^{-3} using the technique of coherent radiation transition. Since the Betatron X-ray radiation is a result of oscillation of electron bunch, in principle it should have the same temporal profile as the electron bunch, i.e. femtosecond pulse duration.

2.2.4 Other Properties

Other properties of laser wakefield generated Betatron radiation includes small source size, on the order of microns, and temporal synchronization with the laser pulse. The source size of betatron radiation can be measured using the technique of Fresnel edge diffraction caused by the spatial coherency of the

source. Measurements using this technique showed a source size of $\sim 1-2$ μm [64, 66]. Since electrons emit X-rays incoherently in the betatron mechanism, the source size determines the degree of spatial coherence, the length of which is given by $L_c = \lambda d/(2\pi w_b)$, where λ is the X-ray wavelength, d is the distance from the object to the source and w_b is the source size. For instance, in Ref.[66], L_c was found be to be ~ 10 μm for 10 keV Betatron X-rays and an object placed at $\sim$ 1 m away from the source. Therefore, betatron X-ray radiation is a suitable source for phase contrast imaging that can be used in biological, medical and geological studies. In addition, the betatron radiation is intrinsically synchronized to the laser pulses, enabling pump-probe applications.

Chapter 3

Physics of Fast Ignition

As an alternative approach to inertial confinement fusion (ICF), Fast Ignition is radically different from the traditional approach in that it separates the fuel ignition from the compression phase [5, 67]. Fast Ignition (FI) is designed based on the four phases as presented in Fig.3.1. Fast Ignition can be considered as a four stage process. First of all, the millimeter-scale fuel pellet consisting of deuterium and tritium is imploded as in the traditional way to produce a high-density configuration without an ignition hot spot. Secondly, at the moment of maximum compression, a first short laser pulse (100's ps) with power of (0.1 - 1.0) petawatt (10^{15} W) is employed to drill a channel via the ponderomotive force through the coronal plasma composed of the ablated material that surrounds the fuel. Thirdly, after the channel is formed, a second shorter pulse (20 ps) with a power of $\sim$ 10 pW is directed into the channel, converting part of its energy to hot or suprathermal electrons at the relativistic critical density surface. These hot electrons propagate through the relativistic critical density surface and deposit their energy in the high density core of the fusion pellet, creating a hot spot with a high enough temperature to ignite fusion reactions. Lastly, once a critical threshold deposited energy is reached, ignition occurs and causes a thermalnuclear burn wave to propagate throughout the whole compressed fuel.

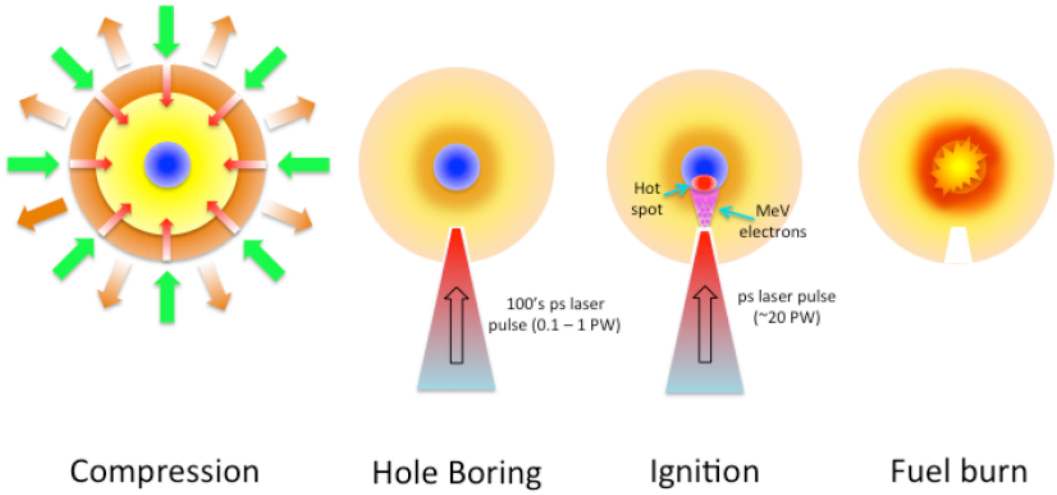

Figure 3.1: The four phases of the Fast Ignition concept.

The success of the FI scheme relies on the conversion efficiency to hot electrons and the electron source characteristics. The electrons must be energetic enough to propagate into the most compressed parts of the fuel, where the density ranges from 200 to 400 g/cm^3. Meanwhile, to form a hot spot small enough for significant heating, the energy deposition must be constrained in a local spot, typically on the order of 20 μm radius. Furthermore, the electrons must have sufficient energy, typically on the order of MeV, to penetrate into the high density fuel to heat it to an ignition temperature of approximately 10 keV.

3.1 Isobaric and Isochoric Models

Fig.3.2 compares the density and temperature profiles of the compressed fuel produced in FI and the conventional central hot spot (CHS) ICF approaches. In the CHS scheme, the fuel undergoes isobaric (constant pressure) compression by the implosion, resulting in two parts, a relatively low density and high temperature hot spot, surrounded by a high density and low temperature main fuel. On the other hand, in the FI scheme, the fuel experiences isochoric

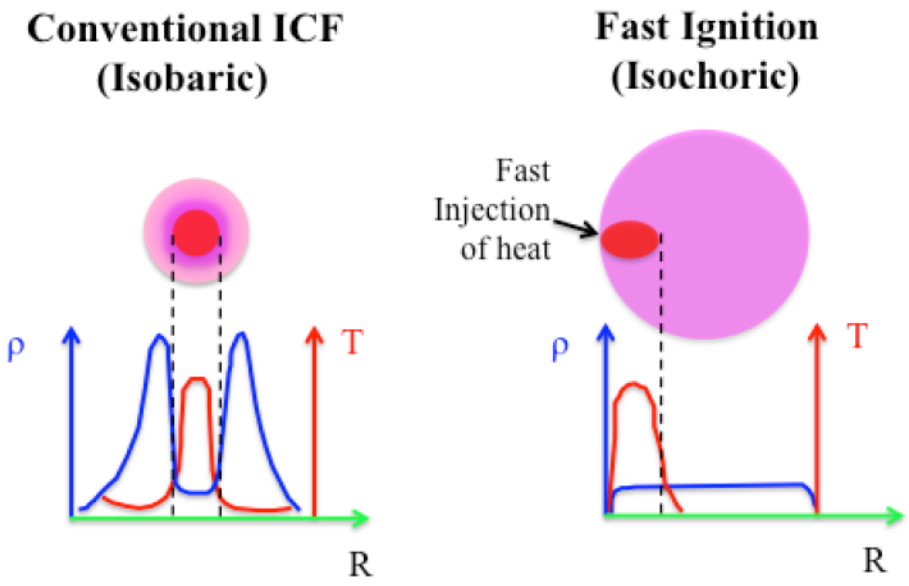

Figure 3.2: Density and temperature profiles of the compressed fuel in conventional central hot spot ICF and fast ignition schemes.

(constant density) compression, and the hot spot is formed in an off-center small area of the fuel heated by an external source, i.e: hot electron beams generated by ultra-intense laser pulses. Fast ignition presents many distinct advantages in comparison with the CHS scheme, and offers the possibility to achieve ignition with current technological means. One advantage of FI is that the density and pressure requirements for the compressed core are less than those for CHS ignition, so in principle fast ignition will allow lower compression laser energy and some relaxation of the need to maintain precise, spherical symmetry of the imploding fuel capsule. In addition, FI provides an improved energy gain higher than that of the CHS approach. These two models, isobaric and isochoric, have been studied through 2D numerical simulations by Atzeni and his colleagues in which energy is injected into pre-compressed D-T fuel [67]. The simulations found that the ignition energy from the isochoric configuration was approximately 5 times greater than that for isobaric ignition.

3.2 Ignition Requirements

In nuclear fusion research, the Lawson criterion is an important general measure of the system that defines the conditions needed for a fusion reactor to reach ignition. The general expression for the Lawson criterion is in the form of product of density n and confinement time τ, which also specifies the condition for D-T reaction to result in net generation of energy[29]:

$$n\,\tau > 10^{14}\,s/cm^3 \tag{3.1}$$

However, in inertial confinement fusion, since the confinement time is proportional to the hot spot radius, it is more useful to write the Lawson criterion in a different way, which is related to the product of the mass density ρ and radius R of the ignition hot spot, so called areal density. Lawson criterion in this case is given by:

$$\rho\,R \geqslant 0.4\,g/cm^2 \tag{3.2}$$

For FI scheme, numerical 2D radiation-hydrodynamic models have been used to describe the ignition process with good accuracy [67]. The work has established the appropriate ignition condition for fast ignition, where the areal density and temperature should satisfy:

$$\rho\,R_h \geqslant 0.5\,g/cm^2 \tag{3.3}$$

$$T_h \geqslant 10 - 12\,keV \tag{3.4}$$

Where R_h and T_h are the radius and temperature of the hot spot. The numerical simulations also found the threshold values of the deposited beam energy, power and intensity to reach ignition, which read:

$$E_{ig}(kJ) = 140(\frac{\rho}{100\,g/cm^3})^{-1.85}, \tag{3.5}$$

$$W_{ig}(W) = 2.6 \times 10^{15} (\frac{\rho}{100\, g/cm^3})^{-1}, \tag{3.6}$$

$$I_{ig}(W/cm^2) = 2.4 \times 10^{19} (\frac{\rho}{100\, g/cm^3})^{0.95}. \tag{3.7}$$

The pulse duration t_b and the radius r_b of the hot electron beam can be derived based on the two relations $E_{ig} = W_{ig} t_b$ and $W_{ig} = \pi r_b^2 I_{ig}$, which are given by:

$$t_b(ps) = 54\, (\frac{\rho}{100\, g/cm^3})^{-0.85} \tag{3.8}$$

$$r_b(um) = 60\, (\frac{\rho}{100\, g/cm^3})^{-0.97} \tag{3.9}$$

Generally, a compressed density of roughly 300 g/cm^3 has been recognized as optimum for fast ignition. Substituting the optimum density into Eqns.3.5 to 3.9, one can obtain a set of minimum requirements for fast ignition: $E_{ig} \simeq 18.3\, kJ$, $W_{ig} \simeq 8.7 \times 10^{14}\, W$, $I_{ig} \simeq 6.8 \times 10^{19}\, W/cm^2$, $t_b \simeq 21.2\, ps$ and $r_b \simeq 20.7\, \mu m$. To match the minimum areal density of 0.5 g/cm^2 for the hot spot required for ignition, one would expect the hot electron bunch have a penetration depth of the same order of 0.5 g/cm^2 inside the compressed DT fuel. Such a penetration depth can be obtained by relativistic electrons with energy of approximately 1 MeV [68]. Therefore, in fast ignition scheme, hot electrons with energy on the order of 1 MeV are of most interest in creating the necessary hot spot to initiate the ignition.

3.3 Collisionless absorption

Energy transfer from the laser pulse to hot electrons for fast ignition involves a number of laser absorption mechanisms that occur near the critical density. Here only collisionless absorption mechanisms such as resonance absorption, vacuum heating and $J \times B$ heating are introduced since collision absorption becomes ineffective in high temperature plasma generated by laser pulses with intensities above 10^{15} W/cm^2 [43, 69].

3.3.1 Resonance Absorption

Resonance absorption occurs when plasma oscillations are excited at the critical density region when an obliquely p-polarized light wave impinges on a plasma density gradient [70]. For p-polarized light, the electric field oscillates in the plane of incidence. In this case, a component of electric field lies in the direction of the density gradient, i.e.: $\mathbf{E} \cdot \bigtriangledown n \neq 0$. As a result, this electric field component tunnels through to the critical density from the lower density region where the light turns around and is reflected. The electrons oscillate along the density gradient direction, thus building up a resonant electron plasma wave (at the critical density, the plasma frequency is resonant with the laser frequency). However, for s-polarized light, since the electric field is perpendicular to the plane of incidence ($\mathbf{E} \cdot \bigtriangledown n = 0$), there is no coupling between the electromagnetic wave and the longitudinal electron plasma wave. Fractional absorption of the incident light wave due to the resonance absorption depends on a variable given by $\tau = (\omega L/c)^{2/3} sin^2\theta$, where ω is the laser frequency in vacuum, L is the plasma scale length, c is the light speed and θ is the angle of incidence of the light wave. Detailed numerical calculations for a linear density profile demonstrated that a peak absorption of ~ 0.5 can be achieved at an optimum angle of incidence given by $\tau \sim 0.6$ [71]. For example for 45^o angle of incidence, this would correspond to a density scale length of $0.2\lambda_0$, where λ_0 is the vacuum wavelength of the incident light. The absorbed energy will contribute to the suprathemal tail of the electron velocity distribution function [70, 71].

3.3.2 Vacuum Heating

Resonance absorption breaks down in a very steep density gradient since the oscillation amplitude of the electron plasma wave near the critical density is longer than the plasma scale length. In this case, another absorption mechanism named vacuum heating or Brunel heating comes into play.[72] To describe

the vacuum heating, we consider a case with the plasma scale length approaching zero, e.g. a sharp plasma-vacuum interface, in which the electrons within a skin depth near the edge of the material will be directly exposed to the electric field. A thermal electron arriving near the interface at the right moment with respect to the laser cycle will be pulled out strongly into the vacuum by the laser electric field. As the electric field reverses its direction, the electron turns around accordingly and travels back to the plasma. Since the plasma is overdense, the laser electric field diminishes rapidly and only penetrates through a distance of the skin depth. Thereby the electron travels deeper into the plasma free of the deceleration force of the laser field, and deposits its energy by colliding with other particles.

An analytical model based on the capacitor approximation was developed by Brunel to study the Vacuum heating [72]. In this model, the magnetic field of the wave is ignored and the laser electric field is assumed to have a component normal to target surface such that it will pull the electrons back and forth across their equilibrium position that is near the surface. Assuming the oscillating electrons are all lost to the solids, this model predicts the laser absorption coefficient scale as following:

$$\eta_a = \frac{4}{\pi} a_0 \frac{sin^3\theta}{cos\theta} \tag{3.10}$$

where $a_0 = v_{os}/c$ is the laser normalized vector where $v_{os} = eE/m\omega$, and θ is the incident angle of the light wave. According to this expression, more absorption is expected at larger incident angles and with higher laser intensity ($I\lambda^2 \propto a_0^2$). In fact, the above expression predicts absorption over 100% in that it ignores the fact that the electric field amplitude is reduced due to imperfect reflectivity as well as that the return velocities of electrons may become relativistic at intensities over $1 \times 10^{18}\ W/cm^2$. After taking into account the above two factors, in the strongly relativistic regime ($a_0 \gg 1$), the dependence on the

intensity disappears and the absorption coefficient can be reformulated by the following expression [43]:

$$\eta_a = \frac{4\pi\alpha'}{(\pi + \alpha')^2} \tag{3.11}$$

where $\alpha' = sin^2\theta/cos\theta$, which suggests a peak absorption of 100% at incident angle of 73^o.

The pitfall of this capacitor model is that it neglects the influence from the magnetic field, which become comparable to the electric field at relativistic intensities, part of which can be induced by the DC currents set up on the surface of the target besides that from laser wave. This additional magnetic field can deflect the fast electrons and prevent them from returning to the plasma, resulting in a smaller absorption coefficient than that predicted by the capacitor model. This problem was pointed out by Gibbon and Bell [73], who simulated the vacuum heating using a $1\frac{1}{2}$ D particle-in-cell code. The simulation indicated that vacuum heating dominates over resonant absorption for plasma scale length $L/\lambda < 0.1$, and is most efficient when $v_{os}/c \simeq 3.1(L\backslash\lambda)^2$. In addition, the simulation also suggested that the absorption tends to peak at 45^o instead of 73^o as mentioned early on for the capacitor model. Finally, it was found that at an incident angle of 45^o, for $L/\lambda = 0.04$, the absorption rate saturates at around 10%-15% for high laser intensity ($I\lambda^2 > 10^{17}\ Wcm^{-2}\mu m^2$).

3.3.3 $J \times B$ heating

Physically, $J \times B$ heating is very similar to vacuum heating in that the electrons are directly accelerated into a step-like plasma profile by the laser electromagnetic field, which penetrates a skin depth into the overdense plasma. The major difference is that the driving force for $J \times B$ heating is the oscillating component of the Ponderomotive force instead of the laser electric field. For a linearly polarized wave $E = E_0(x)\sin\omega t$, it will generate a ponderomotive force in the

longitudinal direction:[74]

$$f_p = -\frac{m}{4}\frac{\partial^2 v_{os}(x)}{\partial x^2}(1 - \cos 2\omega t) \tag{3.12}$$

The first term on the right hand side is the usual DC Ponderomotive force, which tends to push the electrons inward. The second term, oscillating at twice the laser frequency, leads to the heating in the same manner as the electric field does in resonant absorption. $J \times B$ heating is valid for any polarization except circular, where the second term vanishes. The absorption of $J \times B$ heating is demonstrated to be around 10%-15% for $I\lambda^2$ on the order of $10^{18}\ Wcm^{-2}\mu m^2$, and drops significantly as the laser intensity reduces below this and increases at intensities above this [74].

3.4 Hot electron generation and temperature scaling

All of the aforementioned collisionless absorption mechanisms will one way or another superheat some fraction of the electrons to temperatures T_h much hotter than the bulk plasma temperature T_e. The energy distribution of resulting hot electrons takes the form of a Maxwellian, which superimposes with the existing one for the bulk electrons, thereby forming a Bi-Maxwellian distribution with two characteristic temperatures, i.e. T_h and T_e. The determination of T_h and its fractional energy content poses one of the most important issues in short-pulse laser-solid interactions. Particularly, the fast ignition scheme relies crucially on the highest possible conversion efficiency of the laser energy into hot electrons of a specific energy.

In addition, the above three mechanisms indicate that hot electron generation depends strongly on parameters such as laser intensity, target material and geometry, prepulse contrast ratio and so on. To date, a number of expressions

for scaling of the hot electron temperature with laser intensity have been found based on either experimental findings or theoretical models.

Experiments carried out by Beg [75] in which a picosecond laser pulse impinges on planar solid targets found that the hot temperature scales as:

$$T_h(keV) = 215(I_{18}\lambda_{\mu m}^2)^{1/3} \tag{3.13}$$

where I_{18} is the laser intensity in units of $10^{18}\ W/cm^2$, $\lambda_{\mu m}$ is the laser vacuum wavelength in units of μm. Beg's scaling law applies for laser intensities up to $10^{19}\ W/cm^2$, and can be attributed to resonance absorption and vacuum heating.

For laser intensities exceeding $10^{18}\ W/cm^2$, simulations done by Wilks [76] show that the plasma is driven relativistically by the laser, and the dominant absorption comes from the Ponderomotive force driven $J \times B$ heating, which gives the scaling law as following:

$$T_h(keV) = 511[(1 + 0.73I_{18}\lambda_{\mu m}^2)^{1/2} - 1] \tag{3.14}$$

Recently, a fully relativistic model based on the conservation of momentum and energy was developed by Haines [77] and demonstrated that in an overdense plasma hot electrons only interact over a distance of collisionless skin depth, which is much shorter than the laser wavelength. In other words, the electrons do not see the full ponderomotive potential as they did in Wilks' model, resulting in a smaller temperature given by:

$$T_h(keV) = 511[(1 + 1.21\sqrt{I_{18}\lambda_{\mu m}^2})^{1/2} - 1] \tag{3.15}$$

The hot electron temperatures obtained with the above three scaling laws are plotted against those measured in recent experiments [78, 79, 80, 81] in Fig.3.3. It should be noted that laser peak intensities were used in computing

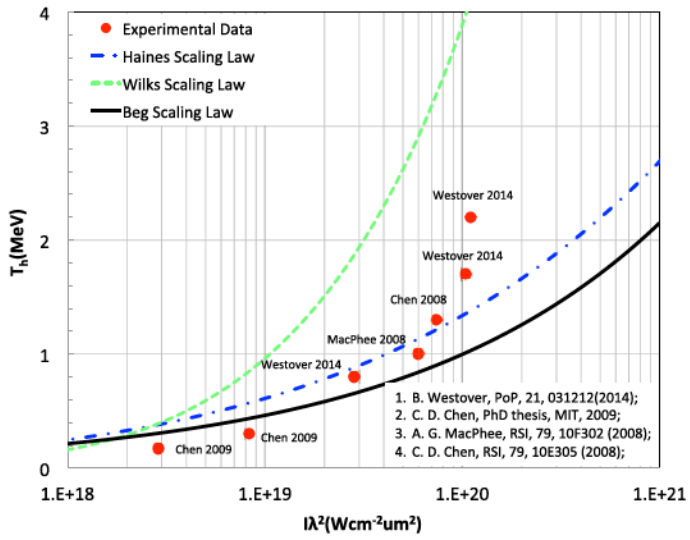

Figure 3.3: Plots of hot electron temperature versus $I\lambda^2$ obtained with Beg's scaling law (black solid line) as given by Eqn.3.13, Wilks' scaling law (green dashed line) as given by Eqn.3.14 and Haines' scaling law (blue dash-dotted line) as given by Eqn.3.15. For comparison, the measured hot electron temperatures from the literature are also plotted in the graph, as indicated by the red solid dots.

the $I\lambda^2$ for the experimental data and for the three scaling laws. As indicated, for the $I\lambda^2$ ranging from 10^{18} $Wcm^{-2}\mu m^2$ to 10^{21} $Wcm^{-2}\mu m^2$, it appears that Beg's experimental scaling law predicts the lowest hot electron temperature whereas Wilks' ponderomotive scaling law gives the highest. Comparing the experimental data with the scaling results, it is found that, for $I\lambda^2$ below 10^{19} $Wcm^{-2}\mu m^2$, the measured temperatures are below all of the scaling results and Beg's scaling gives the closet values to the measurements, for $I\lambda^2$ between 10^{19} $Wcm^{-2}\mu m^2$ and 10^{20} $Wcm^{-2}\mu m^2$, the measured results seem to agree the best with the results from the Haines' scaling law and are slightly higher than Beg's scaling results, for $I\lambda^2$ above 10^{20} $Wcm^{-2}\mu m^2$, the measured temperatures are much higher than the results from Beg's and Haines' scaling laws. Over the $I\lambda^2$ range covered by the experimental data, it appears that the measured temperatures are significantly colder than what Wilks' ponderomotive scaling predict with the laser peak intensities.

3.5 Cold return current

In previous sections, we have learned that hot electrons or fast electrons are an inevitable consequence of ultra-intense laser interacting with solid surfaces. Theoretically, as these energetic electrons propagate inside the target, a large magnetic field, on the order of a Gigaguass, will be induced by the hot electron current according to Ampere's law. Suppose that this magnetic field is produced along the whole length of the hot electron trajectory or the penetration depth of the hot electron. The resulting magnetic energy contained in the cylinder of the fast moving electrons can be estimated and was shown to to be significantly higher than the energy carried by the hot electron bunch alone [82]. Such a significant discrepancy in energy implies that the fast electron current can not be maintained. It must be opposed by an inductively or electrostatically generated electric field which confines the fast electrons near the surface of the target, or else the background thermal plasma must supply a balancing return current [82]. Local charge neutrality requires that the hot current j_h and the cold return current j_c should satisfy: $j_{total} = j_h + j_c \simeq 0$.

Since there is a finite resistivity with the cold solid-density background plasma, an electric field will be rapidly induced, slowing the propagation of the fast electrons and coupling energy to the cold return current electrons. The magnitude of this electric field is given by:

$$j_c = -j_h = \sigma_e E \tag{3.16}$$

where σ_e is the electrical conductivity in the background plasma for the cold return current electrons. In other words, instead of streaming freely inside the cold solid target, the fast electrons would experience deceleration and eventually refluxing at a certain point due to the potential gradient associated with the electric field from the cold return current.

The continuity equation for fast electrons, combined with Eqn.3.16, is given

by:

$$\frac{\partial n_h}{\partial t} = \nabla \cdot (\frac{j_h}{e}) = -\nabla \cdot (\frac{\sigma_e}{e} E) \tag{3.17}$$

Assuming the fast electron distribution is Maxwellian and is confined by the induced electric field, $E = -\nabla\phi$, the density of the hot electrons can be described by: $n_h = A \exp(\phi/T_h)$ [33]. Based on this equation, one can obtain:

$$E = -\frac{T_h}{n_h} \nabla n_h. \tag{3.18}$$

Substituting this equation into Eqn.3.17, gives:

$$\frac{\partial n_h}{\partial t} = \nabla \cdot (\frac{\sigma_e T_h}{e n_h} \nabla n). \tag{3.19}$$

This is the diffusion equation for the hot electrons and the diffusion factor $D = \sigma_e T_h / e n_h$ is inversely proportional to the hot electron density.

Since for the hot electrons of our interest, the electron collisional loss time is larger than the laser pulse-length, one can assume the hot-electron temperature is constant during the laser pulse, the conductivity of the background plasma is constant and uniform and the adiabatic losses are negligible[82]. With these assumptions, the solution to the diffusion equation in one-dimension during the laser pulse is given by [82]:

$$n_h = n_0 (\frac{t}{\tau_{laser}}) (\frac{z_0}{z + z_0})^2 \tag{3.20}$$

where

$$n_0 = \frac{2 I_{abs}^2 \tau_{laser}}{9 e T_h^3 \sigma_e} \quad and \quad z_0 = \frac{3 T_h^2 \sigma_e}{I_{abs}} \tag{3.21}$$

where I_{abs} is the absorbed laser intensity, τ_{laser} is the laser pulse length and z is the distance away from the surface of the target. In practical units, the above

two quantities can be recast as [82]:

$$n_0 = (\frac{I_{abs}}{10^{18}\,W cm^{-2}})^2(\frac{\tau_{laser}}{ps})(\frac{T_h}{200\,keV})^{-3}(\frac{\sigma_e}{10^6\,\Omega^{-1}\,m^{-1}})^{-1}\,1.7\times10^{22}\,cm^{-3} \tag{3.22}$$

$$z_0 = (\frac{T_h}{200\,keV})^2(\frac{\sigma}{10^6\,\Omega^{-1}\,m^{-1}})(\frac{I_{abs}}{10^{18}\,W cm^{-2}})^{-1}12\,\mu m. \tag{3.23}$$

To give an example, considering a 1 μm laser pulse with peak intensity of $I_0 = 10^{20}\ W/cm^2$ impinging onto a 10 eV aluminum target with density close to solid. Assuming 40% of the laser energy is transferred to hot electrons[75], which is reasonable for a combination of resonance absorption, vacuum heating and $J \times B$ absorption, one can have $I_{abs} = 4\times10^{19}\ W/cm^2$. From Beg's scaling law as shown in Eqn.3.13, one can estimate $T_h \sim 1\,MeV$. The conductivity σ_e for Al at $T_e = 10\,eV$ is around $10^6\ \Omega^{-1}\,m^{-1}$ [83]. Substituting the above numbers into Equation 3.23, one can obtain that the 1 MeV hot electrons can penetrate a distance of approximately 8 μm into the target during the laser pulse, significantly less than the collisional range R_e of approximately 1 mm for 1 MeV electrons traversing inside aluminum [84]. It implies that the hot electron transport is inhibited by the induced electric field set up by the cold return current from the background plasma.

The threshold laser intensity for the resistively inhibited transport can be estimated by equating z_0 and R_e, and is given by [82]:

$$I_{inhib} > (\frac{T_{cold}}{100\,eV})^{3/2}(\frac{Z}{13})^{-1/2}(\frac{\rho}{2.7\,g/cm^3})10^{17}\,W/cm^2 \tag{3.24}$$

where T_{cold} is the plasma temperature of the background plasma, Z is the ionization state of the material and ρ is the density of the material.

Chapter 4

Methodologies

In this chapter, we present methodologies employed for the LWFA and FI experiments, including the laser systems and the diagnostic setups for the experiments. The LWFA experiments were performed with the 200 TW laser system at the Advanced Laser Light Source (ALLS) facility at the Institut National de la Recherche Scientifique (INRS) in Varennes, Québec[85, 86]. Whereas the FI experiments were carried out with the Titan laser beamline [87] at the Jupiter Laser Facility at the Lawrence Livermore National Laboratory (LLNL) in Livermore, California. The contents of this chapter will be arranged in the order of experiments carried out.

4.1 LWFA experiments

4.1.1 ALLS 200 TW Laser System

The ALLS 200 TW laser system is a compact laser system based on Ti:Sapphire technology and CPA technique. This laser system is a commercial prototype built by Amplitude Technologies that can be operated at 10 Hz with a central wavelength of 800 nm. The schematic layout of the laser system is presented in Fig.4.1. The seed pulse of the laser system is generated with a broad spectral

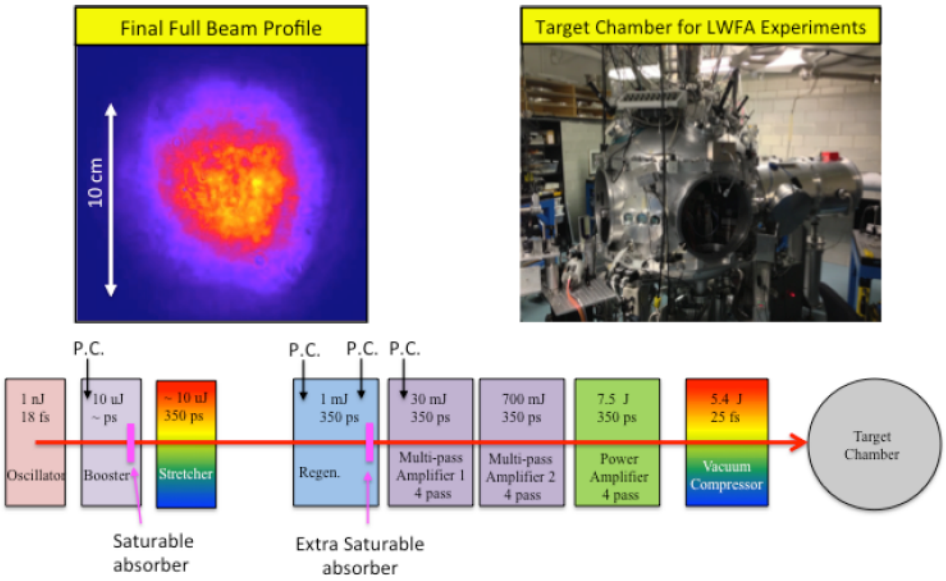

Figure 4.1: Schematic diagram showing the 200 TW Laser System at ALLS. The inset shown on the top left is the near-field image of the final full beam profile and the image on the top right is the target chamber image for LWFA experiments. P.C. represents Pockels Cell.

bandwidth of 100 nm by an oscillator that is operated at 64.1 MHz repetition rate (corresponding to 15.6 ns round trip time). The output energy and the pulse width of the seed pulse are 1 nJ and 18 fs respectively. The seed pulse then passes through a booster that consists of a 14-pass ring amplifier and a solid state saturable absorber to amplify and clean the laser pulse. The laser pulse after the booster has an energy of approximately 10 μJ with a pulse width broadened to $\sim$ 1 ps. This amplified and broadened laser pulse is further stretched in pulse width by a grating based stretcher, which increases the pulse width to $\sim$ 350 ps (FWHM). After the stretcher, the laser pulse is relayed into a regenerative amplifier with an amplification factor of 10^3. After the regenerative amplifier, the pulse is further amplified to a final maximum energy of 7.5 J by two multi-pass amplification stages together with a power amplification stage that is pumped by fourteen YAG Pro-pulse pump lasers (16 J total pumping energy). The amplified laser pulse is re-compressed in a

vacuum compressor down to a pulse duration of 25 fs with an energy of around 5.4 J. The final beam is approximately 9 cm in diameter and the beam profile is a quasi-flattop as indicated in the inset in Fig. 4.1. The output beam from the compressor travels over several meters in a vacuum beam tube before entering the dedicated target chamber, as shown in Fig.4.1, in which the laser is focused by an off-axis parabola onto the target.

Four Pockels cells in total were employed throughout the laser system to isolate the main pulse and increase the laser pulse contrast ratio. As shown in Fig.4.1, the first one in the oscillator was used to bring down the laser repetition rate to 10 Hz, the second one at the entrance of the regenerative amplifier was used for seeding and the third one at the exit of the regenerator for switching the pulse out of the regenerative amplifier and the forth one between the regenerative amplifier and the first multi-pass stage was for reducing the prepulse level.

One of the drawbacks of the CPA technique is the presence of a temporal pedestal or prepulse prior to the main pulse, which is primarily due to the Amplified Spontaneous Emission (ASE) and the leakage of the main laser pulse due to the imperfect matching of optical elements in the laser chain. The ASE, also known as superluminescence, occurs when the laser gain medium is pumped to the state of population inversion. The resulting spontaneous emission will pass through the same amplification stages designed for the main pulse and become amplified. Since the chirping in the laser system is optimized for the main pulse, the ASE normally manifests itself as a plateau-shaped pedestal in front of the main pulse with a time duration on the order of nanoseconds. Generally, in most of ultra-fast laser systems, the leakage of the main pulse is mainly from the Pockels cells that were normally used in combined with polarizers to manipulate the switching in and out of the light inside optical amplifier cavities. The leakage normally has a pulse duration comparable to the main laser pulse and comes nanoseconds earlier than the main pulse depending on

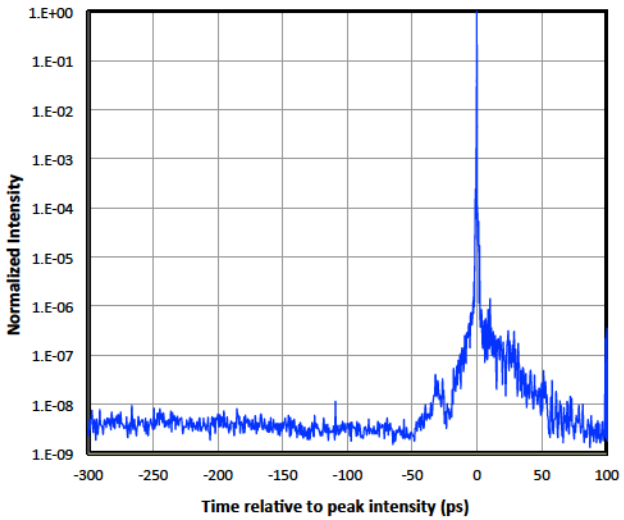

Figure 4.2: Typical laser pulse contrast of the ASE in picosecond time scale for ALLS's 200 TW laser.

the round trip time of light inside the cavity where the leakage occurs. If the prepulse is intense enough it will create a preplasma in front of the target that can potentially change the laser-matter interaction mechanism. Therefore, in high-intensity laser-matter applications, the laser pulse contrast ratio (LPCR), the ratio of main pulse intensity over prepulse intensity, is a crucial parameter that should always be taken into account.

For the 200 TW ALLS laser, a cleaning technique based on high energy transmission through saturable absorbers before power amplification was applied to enhance the laser pulse contrast ratio [86]. As indicated in Fig.4.1, the extra saturable absorber for this purpose was installed at the exit of the regenerative amplifier. This technique was demonstrated to improve the LPCR to better than 10^{10} with only a 30% energy loss at a 10 Hz repetition rate [86]. With this technique, the pulse contrast for the leakage was maintained above 10^{8} in intensity during the experiments and the contrast for the ASE in terms of laser beam intensity was measured to be between 10^{8} and 10^{9}, as indicated in Fig.4.2.

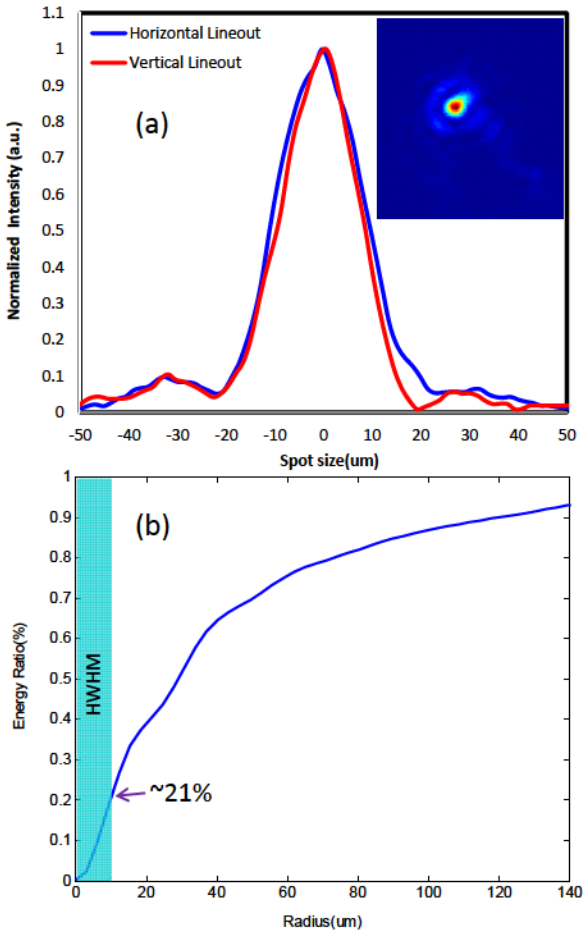

Figure 4.3: (a) Lineouts of the typical laser focus (shown in the inset) employed in LWFA experiments. (b) Equivalent energy ratio versus the radius for the laser focus shown in (a).

4.1.2 Laser focal spot

For the LWFA experiments carried out for this thesis, the 9-cm-diameter laser pulses arriving at the target chamber were focused onto the gas jet targets by a 150-cm focal length off-axis parabola (OAP). The laser pulses were linearly polarized with average energy of approximately 2.4 J at target and pulse width of 30 fs FWHM. The lineouts of a typical focal spot in vacuum obtained during the experiments are shown Fig.4.3 along with the contained equivalent energy fraction as a function of radius.

The lineouts in Fig.4.3(a) imply that the FWHM's of the focus are $20\,\mu m \times 18\,\mu m$ in the horizontal and vertical directions. The peak intensity for this focal spot is measured to be $7.3 \times 10^{18}\ W/cm^2$, corresponding to a normalized vector potential a_0 of 1.8. From the breakdown of the contained energy ratio versus radius as plotted in Fig.4.3(b), one can obtain that the energy contained within the FWHM of the focal spot is only 20% of the total energy, which corresponds to 48% of the energy within the central lobe of an Airy function focal spot. The rest of the energy is spread out to the halo that surrounds the central spot due to the aberrations associated with the grating compressor and the OAP and the wavefront distortion due to self-phase modulation.

4.1.3 Electron Spectrometer

The energy spectra of the electrons achieved from the LWFA experiments were measured with electron spectrometers. An electron spectrometer normally consists of a permanent dipole magnet to disperse the electrons according to their energies and a detector to observe the electrons. In our experiments, to be able to resolve electrons with energy at the GeV level, we used two separate magnet dipoles of identical length of 10 cm with magnetic field strengths of 1.12 T and 0.84 T respectively. The detector of our spectrometer is a Lanex fluorescent screen that was placed 20 cm after the exit of the second magnet. The fluorescence emitted from the Lanex film was collected by an f/2.8 aperture lens system and imaged onto a 12 bit CCD camera (Point Gray).

The motion of a relativistic electron with velocity $\vec{\mathbf{v}}$ traveling in a magnetic field $\vec{\mathbf{B}}$ can be described by:

$$\frac{d\vec{\mathbf{p}}}{dt} = -e(\vec{\mathbf{v}} \times \vec{\mathbf{B}}) \tag{4.1}$$

where $\vec{\mathbf{p}} = \gamma m \vec{\mathbf{v}}$ is the relativistic momentum of the electron, γ is the relativistic Lorentz factor and is given by $\gamma = 1/\sqrt{1-(v/c)^2}$. Since the magnetic field

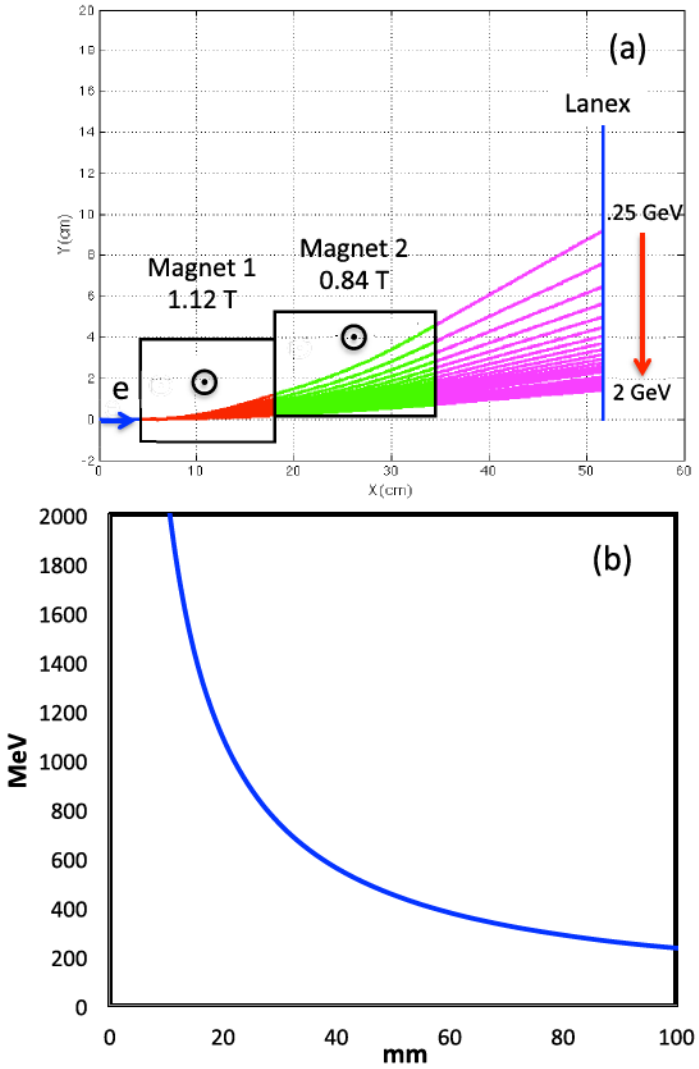

Figure 4.4: (a) Simulated trajectories of electrons with energies from 250 MeV to 2000 MeV in 50 MeV per step passing through the electron spectrometer employed in our LWFA experiments. Colors on the trajectories represent different areas that electrons pass through before arriving at the Lanex screen. The two black boxes stand for the areas of the magnetic field from the two magnet dipoles. The energy increasing from the top to bottom on the Lanex screen corresponding to the geometrical setup in our simulation. (b) Corresponding dispersion curve of the electron spectrometer. The distance in mm represent the deviation of the electrons on the screen in the energy dispersion direction from the reference position when no magnets are present.

does no work on the electrons, γ of the electron will be constant throughout the magnetic field. The assumption of constant γ together with the motion equation implies that the electron will experience circular motion inside the magnetic field with the gyration frequency given by: $\omega_0 = \frac{eB}{\gamma m}$. Once exiting the magnetic field, the electron will travel in linear motion again and the position of the electron can be easily tracked.

Fig.4.4 (a) plots the simulated trajectories of the electrons with energy ranging from 250 MeV to 2 GeV in our electron spectrometer system based on Eqn.4.1. From this graph, one can see that the curvature of the electron's trajectory inside the magnetic field is decreasing with the energy since the gyroradius is proportional to the electron momentum. Because of that, the electrons with different energies will hit different positions at the Lanex screen, which results in a dispersion curve of the electron spectrometer as indicated in Fig.4.4 (b).

4.1.4 Interferometry

For LWFA experiments, the under-dense plasma background for bubble formation and electron acceleration can be obtained by laser ionization of a gas jet [50, 51], laser ionization of a gas cell [20] or gas-filled capillary discharge waveguide [45]. For the LWFA experiments performed for this thesis, gas jets formed by supersonic conical nozzles were selected as the targets. A commercial Parker Valve solenoid (Model 009-181-900) was employed to switch on the gas flow through the nozzle for about 12 ms and was controlled with a home made electronic pulser system. The conical nozzles, as shown in Fig.4.5, were made in the Electrical and Computer Engineering Department's machine shop and are similar to those characterized in Ref.[88]. The D_{crit} of all of our nozzles is 0.8 mm and the D_{exit} varies from 2.4 mm to 10 mm to provide different ranges of gas densities.

Plasma density can be measured through interferomtry. The measurement

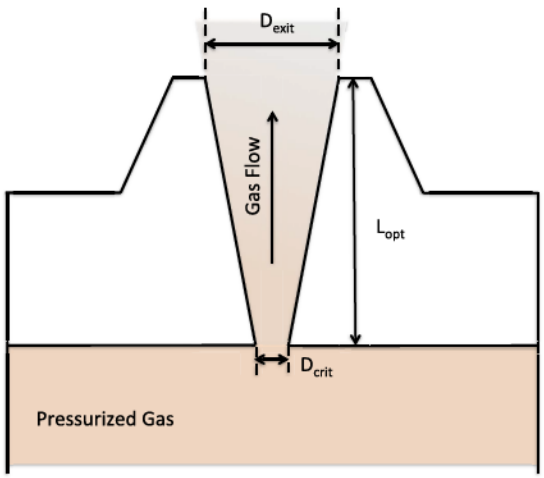

Figure 4.5: The schematic diagram showing the supersonic conical nozzle used for LWFA experiments.

depends on the fact that the refractive index difference between the plasma and the reference material, normally vacuum, would induce a phase shift in the measurement beam and after the two beams of the interferometer are combined, interference fringes are produced where the measurement beam has passed through the plasma. For our LWFA experiments, we had an online polarization based interferometer system to monitor the plasma density. This polarized light interferometer is based on a Wollaston polarizing prism as the beam splitter and it is normally referred to as a Nomarski interferometer [89]. The principle of the Nomarski interferometer is presented in Fig.4.6.

A Wollaston prism has two orthogonal calcite prisms cemented together to form two right triangle prisms with perpendicular optical axes. Because of that, it separates unpolarized light into two orthogonal linearly polarized outgoing beams with the angle of divergence determined by the prisms' wedge angle, the birefringence of calcite and the wavelength of the light. Normally, the Wollaston prism was used in combination with polarizers to give interference fringes. As shown in Fig.4.6, the first polarizer P1 was used to select the polarization of the light to give equal components on the two orthogonal direc-

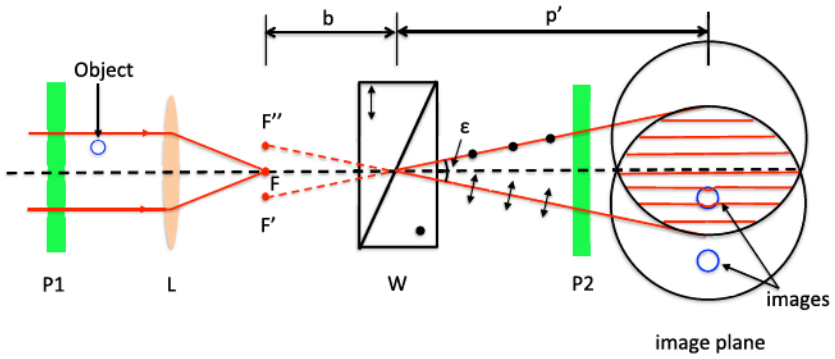

Figure 4.6: The schematic diagram showing the principle of the Nomarski Interferometer. P1 and P2 stand for polarizers, L means lens and W represents Wollaston prism.

tions of the prism. The second polarizer, normally 45^o to the two orthogonal optical axes, was used to select the same components of the two orthogonal light with equal polarization and intensity to overlap at the image plane to produce the interferogram. Notice that the insertion of the Wollaston prism doubles the focal spot F of a collimated beam after the lens L and creates the two virtual sources F' and F". These are responsible for the double images and the inference phenomenon. Since the two beams leaving the Wollaston have a phase difference that is proportional to their distance from the mid-plane (equal geometrical paths in both prism halves) of the prism, the interference fringes at the image plane are straight lines that are parallel to the apexes of the prism. The spacing i of the two adjacent fringes at the detector for a given wavelength is given by [89]:

$$i = (\lambda/\epsilon)(p'/b) \tag{4.2}$$

where ϵ is the angular separation of the two polarizations in radians, and p' and b are distances defined in Fig.4.6.

Therefore, for Nomarski interferometer, the fringe separation can be altered by changing the distance between lens focus and the Wollaston prism without

changing the magnification of the lens system. Furthermore, the orientation of the fringes can be changed by rotating the polarizers. The tricky part of the Normarski interfeormeter is that one has to make sure that one of the images of the object must overlap with an undisturbed region of the field of view, which can be done by choosing a prism with proper ϵ, setting up an appropriate distance b and using a large enough probe beam diameter. This would guarantee that the Nomarski inerferometer behaves as a normal interferometer such that the distortions of the fringes at the image position are directly from the refractive index change along the optical path covered by the object.

Comparing with other commonly-used interferometers such as Mach-Zehnder and Michelson interfeormters, the advantages of the Nomarski interferometer are the following:

1) Straight line arrangement of the system components, i.e.: light source - object - lens - Wollaston - detector. Therefore, it saves space for installation and is the best option when diagnostic space is constrained in the target area.

2) The alignment is relatively easy and is free of stability problems.

3) The interfeormeter has equal optical path lengths for the two separated beams after the prism that form the interferogram. Therefore, there is no additional effort to achieve this as in other interferometers that normaly require very precise adjustment of path lengths.

4)It is easy to achieve straight line fringes that are preferential for extracting the phase shift information. For other interferometers, the line fringes may be subject to a certain level of curvature due to wavefront distortion from optical misalignment and therefore requiring sophisticated alignment strategies for the optics.

4.1.5 Abel Inversion

Once the interferogram where the plasma density is embedded is obtained, one has to apply some inversion algorithm to extract the density from the measured

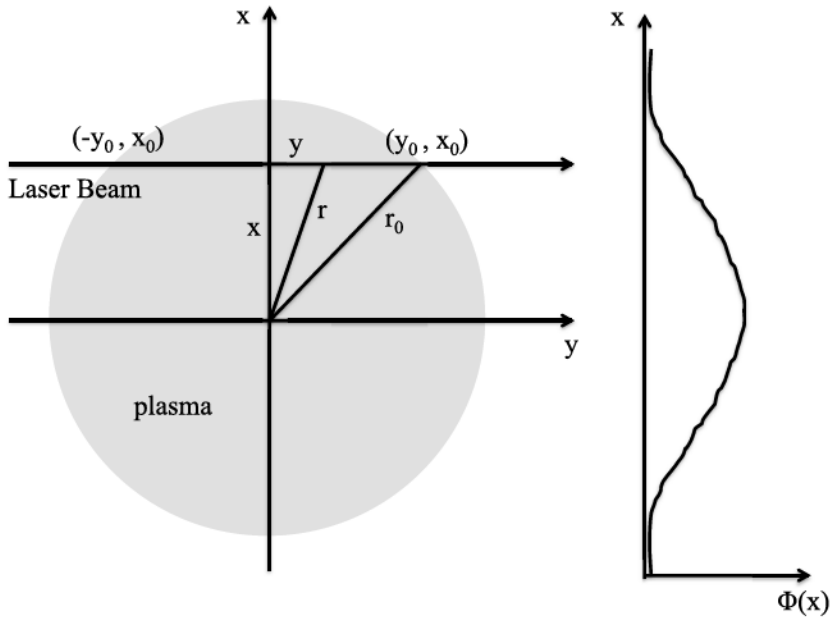

Figure 4.7: Schematic diagram showing the Abel transformation. The plasma is circularly symmetric with respect to the direction perpendicular to the paper.

phase shift. This problem is similar to that of calculating the emissivity of an optically thin plasma from the measured intensity profile [90] and is normally referred to as Abel inversion.

In Abel inversion, the plasma is assumed to be cylindrically symmetric. Fig.4.7 shows the principle of the Abel inversion and corresponding coordinate system. Consider the phase shift variation experienced by a laser beam with wavelength λ_0 passing through the two coordinates of the plasma, $(-y_0,\ x_0)$ and $(y_0,\ x_0)$, as indicated in Fig.4.7. It is apparent that the phase shift of interest is the integration of the refractive index difference between plasma and vacuum along the line $x = x_0$. In 2-D Cartesian coordinate, without losing the generality, the phase shift Φ at any value of x is given by:

$$\Phi(x) = \int_{-y_0}^{y_0} k(\eta_r(y) - 1)dy = \frac{4\pi}{\lambda_0}\int_0^{y_0} (\eta_r(y) - 1)dy \tag{4.3}$$

where $k = 2\pi/\lambda_0$ and η_r is the refractive index of the plasma. In cylindrical

coordinates, the above equation can be recast as:

$$\Phi(x) = \frac{4\pi}{\lambda_0} \int_x^{r_0} \frac{(\eta_r(r) - 1) r dr}{(r^2 - x^2)^{1/2}} \tag{4.4}$$

By using a mathematical transformation, this equation can be also written as:

$$\frac{2\pi(\eta_r(r) - 1)}{\lambda_0} = -\frac{1}{\pi} \int_r^{r_0} \frac{\Phi'(x) dx}{(x^2 - r^2)^{1/2}} \tag{4.5}$$

where $\Phi'(x) = d\Phi(x)/dx$. The integral on the right hand side can be solved with a matrix summation as described in Ref. [90]. Accordingly, from the phase shift Φ_k along the x-axis x (parallel to the laser propagation axis) for n equidistant values $x_k = kr_0/n$ (for $k = 0, ..., n-1$), the value of refractive index corresponding to $r_j = jr_0/n\,(j = 0, 1, ..., n-1)$ can be given by the simple relation:

$$\eta_j(r_j) - 1 = \frac{\lambda_0}{2\pi r_0} \sum_k a_{jk} \Phi_k(x_k), \tag{4.6}$$

where a_{jk} are coefficients tabulated in Ref. [90].

In interferogram analysis, the phase shift of a distorted fringe can be converted to an equivalent quantity called fringe shift by the following relation: $\Phi = 2\pi\delta_i/i$, where δ_i is the spatial shift of the fringe from original position, i is the fringe spacing and the ratio of δ_i/i is namely fringe shift. Practically, it is easier to figure out the fringe shift than the phase shift given an interferogram with distorted fringes. Therefore, Eqn.4.6 is rewritten as as a function of fringe shift:

$$\eta_j(r_j) - 1 = \frac{\lambda_0}{r_0} \sum_k a_{jk} \frac{\delta_i(x_k)}{i}, \tag{4.7}$$

Knowing the refractive index, one can derive the plasma density through the following relation: $\eta_r = \sqrt{1 - n_e/n_c} \simeq 1 - n_e/(2n_c)$, where n_e is the plasma density and n_c is the critical density for laser. With this relation, Eqn.4.7 can

be rewritten to as:

$$n_e(r_j) \simeq -\frac{2\lambda_0 n_c}{r_0} \sum_k a_{jk} \frac{\delta_i(x_k)}{i}. \tag{4.8}$$

So far, we have learned that the Abel inversion procedure can be used to derive the plasma density based on the phase shift or fringe shift information achieved with interferometry for a cynlindrically symmetric plasma. However, as mentioned previously, this algorithm is based on the assumption that the plasma is cylindrically symmetric, which may not be the case for practical measurements. A modified Abel inversion, so called weighted asymmetric inversion [91, 92] was therefore proposed to take care of plasma with asymmetric density distribution. The detail of this modified Abel inversion was described in Ref.[91]. In this modified inversion, the asymmetry of the fringe shifts is weighted and introduced into the final plasma density distribution, which is assumed to have a $cos\theta$ transverse asymmetry contribution. As given in Ref.[91], Equation 4.8 for the final plasma density will be broken into two parts, one accounts for the density in the positive x side:

$$n_{xj} = \frac{2\lambda_0 n_c}{r_0} \left\{ \sum_{k=1}^{N} a_{jk} \left[f_k(\frac{r_k + r_j}{2r_k}) + f_{-k}(\frac{r_k - r_j}{2r_k}) \right] + a_{j0} \left[f_0 + r_j(\frac{f_1 - f_{-1}}{2r_1}) \right] \right\}, \tag{4.9}$$

and the other one for negative x side:

$$n_{x-j} = \frac{2\lambda_0 n_c}{r_0} \left\{ \sum_{k=1}^{N} a_{jk} \left[f_k(\frac{r_k - r_j}{2r_k}) + f_{-k}(\frac{r_k + r_j}{2r_k}) \right] + a_{j0} \left[f_0 + r_j(\frac{f_{-1} - f_1}{2r_1}) \right] \right\}, \tag{4.10}$$

where $f_{\pm k} = \delta_i / i$ are the fringe shift measurements on the positive and negative sides of the x-axis respectively. At $x = 0$, the plasma density can be recovered by averaging both sides of values along the x-axis, i.e.: $n_{yj} = (n_{xj} + n_{x-j})/2$.

A matlab GUI app called "Frinedit" based on the Abel inversion algorithm was developed to derive the plasma density from the interferograms achieved from the LWFA experiments. In this software, fringe shifts of the interferogram

are first computed by tracing the trajectories of the fringes. The fringe shifts are then passed to Eqn.4.8 or Eqn.4.9 and Eqn.4.10 to calculate the density of symmetric or asymmetric plasma target. Details of this software is given in Appendix A.

4.2 FI experiments

4.2.1 Titan Laser System

Titan laser is one of the beamlines in Jupiter Laser Facility at the Lawrence Livermore National Laboratory located at Livermore California. The Titan laser is a 1053 nm Nd:glass laser which combined the techniques of CPA and optical parametric amplification (OPA) [93] in its front end system in what is called Optical Parametric Chirped Pulse Amplification (OPCPA) to deliver clean laser seed pulses. These are then amplified in glass laser rods and disk amplifiers up to 150 J and recompressed to 500-700 fs (FWHM) pulses on target. With the f/3 off-axis parabola available in the target chamber, the focused peak intensity of the Titan laser can exceed $1 \times 10^{20}\ W/cm^2$.

Fig.4.8 presents the schematic layout of Titan laser system. The seed pulses with pulse duration of 200 fs and wavelength of 1053 nm are generated by a commercial GLX-200 master oscillator (made by Time Bandwidth Products Inc.). The seed pulses are then sent to the Offner Pulse Stretcher to expand the pulse width up to 1.6 ns. The stretched pulses are firstly amplified to a few mJ by a two stage OPCPA, the front-end pre-amplifier. The pump laser pulses for the OPCPA, coming out from a CW oscillator modulated at 5 Hz with wavelength of 1053 nm, are amplified to 1.5 J by a regenerative amplifier together with a 4-pass amplifier, the gain medium of which are a 3 mm Nd:YLF rod and two 12.7 mm Nd:YLF rods respectively. The amplified pulses are then frequency doubled by a BBO (β-barium borate) crystal to 526 nm before pumping the OPCPA. After the OPCPA, the pre-amplified pulse is sent to the

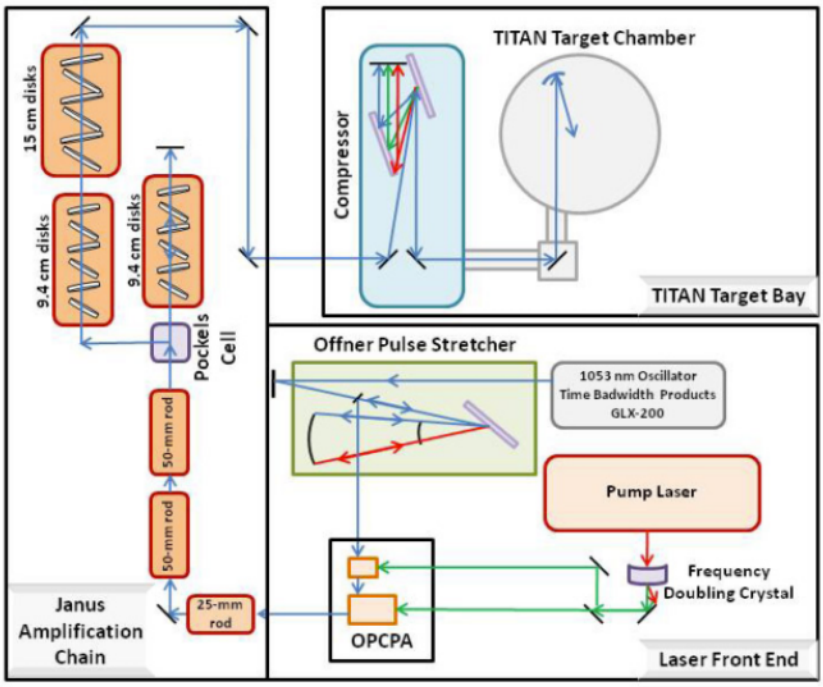

Figure 4.8: Schematic layout of Titan Laser System. (Image courtesy of Cliff Chen)

Janus Amplification Chain for power amplification. It passes through a 25-mm diameter flashlamp pumped rod amplifier and two 50-mm diameter flashlamp pumped rod amplifiers giving a laser pulse output energy of ~5 J. The beam then makes a double pass through a series of 9.4 cm disk amplifiers, then is switched out by a Pockels Cell to another amplification stage that consists of two separate sets of 9.4 cm and 15 cm disk amplifiers to reach its full energy of ~ 150 J. After the amplification stages, the beam is recompressed back to a pulse length of $\sim (500 - 700)$ fs by the compressor located at the Titan target room. This short pulse beam with diameter of 25 cm is then redirected by two turning mirrors before being focused down to the target chamber center (TCC) with an off-axis dielectric coated parabola.

To minimize the preplasma effect on the laser matter interaction, for the Fast Ignition experiments conducted in this thesis, the second harmonic generation (SHG) of the Titan laser was employed. Since SHG is a nonlinear process such that the output signal strength is proportional to the square of the input laser intensity, the low intensity prepulse from the 1ω laser won't be converted as efficiently as the main pulse, hence resulting in a much higher laser pulse contrast with the 2ω laser pulse. The second harmonic crystal used was a 2-mm-thick KDP crystal that was installed inside the vacuum compressor. The conversion efficiency of 2ω laser was measured to be approximately $40 - 60\%$ during the experiments. The KDP crystal was smaller in diameter than the full laser beam and thus an apodized beam beam of 20 cm diameter was employed, which gave an average energy of around 50 J at target for the 2ω laser.

4.2.2 Laser Diagnostics

The shot to shot laser diagnostics for monitoring the equivalent focal spot at TCC, pulse length and prepulse were set up by using the leakage light through the last two turning mirrors before the parabola. The leakage light from the turning mirror in the compressor would be used for the prepulse

monitor and the autocorrelator for measuring the pulse length. The prepulse monitor consisted of a water breakdown cell that has a nonlinear response to protect the sensitive photodiode from damage by the high laser intensities. The leakage through the last turning mirror, $\sim 10^{-5}$ of the main pulse energy, was used for an equivalent plane monitor (EPM). While the best focus at the target plane in vacuum was established at the beginning of the experiments by optimizing the parabola with low laser power looking at the focus imaged by an objective attached to a CCD camera, the EPM is then able to record the intensity distribution of subsequent system shots with full power at an equivalent target plane. With the EPM, one can characterize the effects of pump induced distortion and non-linear optical refractive index on the full power focal spot. Regarding the layout of the EPM, it is a single lens system that consists of a full aperture f = 6.3 m lens and necessary optics to relay the focus to a 16 bit CCD camera. Because of the difference in f/number, the spatial dimension of the EPM system scales as the focal length ratio of the lens and the parabola.

Fig.4.9 plots the typical prepulse profiles of the Titan 2ω laser with and without injected prepulses. For comparison, the 1ω prepulse digitized from Ref.[78] is also plotted. The injected prepulse came from a second long pulse beam available in the Titan facility and was injected coaxially with the short pulse beam that is discussed here. The energy of the intrinsic prepulse for the 2ω laser pulse was measured to be less than 10 μJ, while the energy of injected prepulse is controllable and can be adjusted from a few mJ to hundreds of mJ. Notice that the injected prepulse, as indicated in the graph, starts around 2 ns before the main pulse. The intensity contrast ratio of the prepulse for 2ω laser was measured to be as low as 10^{-11}, which potentially prevents any preplasma formation during the experiments. Comparing with the intrinsic prepulses between 1ω and 2ω, one finds that the laser pulse contrast ratio of the 2ω laser was increased by approximately three orders of magnitude, a huge

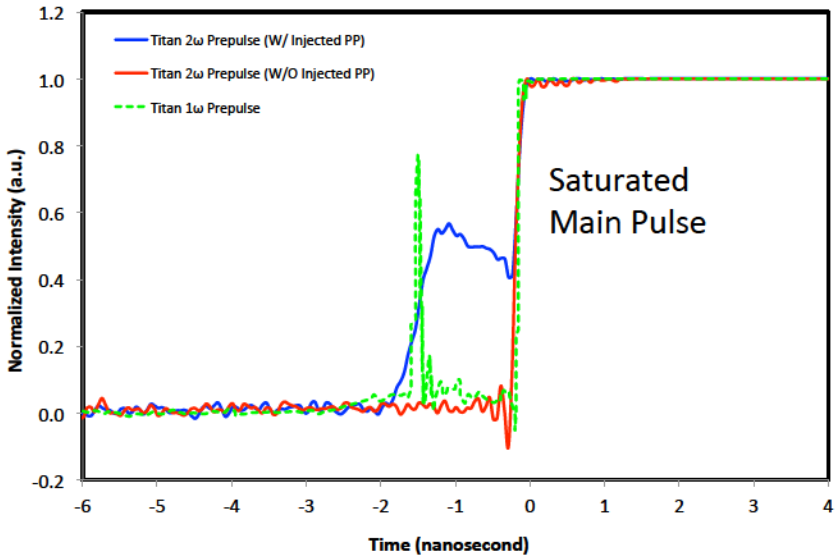

Figure 4.9: Typical prepulse profiles of Titan 2ω Laser with (blue solid curve) and without (red solid curve) injected prepulse. The energy of injected prepulse was measured to be 2 mJ while the one of intrinsic prepulse was less than 10 μJ. For comparison, the typical prepulse profile for Titan 1ω digitized from Ref.[78] is plotted in dashed green. In this particular 1ω prepulse, the ASE was measured to be 13 mJ while the leakage or replica of the main pulse was 8 mJ. Note that the y-axis scale is different for the different curves plotted.

benefit when using the 2ω laser.

Fig.4.10 (a) shows the typical best focus of the Titan 2ω laser at the target plane in the Titan 2011 September Campaign led by the University of Alberta. The best focus was achieved by optimizing the f = 60.19 cm off-axis parabola using the milijoule OPCPA light. As shown, the focal spot manifests itself as an ellipse with FWHM sizes of 3.5 μm by 8.0 μm in the vertical and horizontal axes. The elliptical focal spot was mapped into a circle spot with equal area, indicating that the energy fraction within a diameter of 6 μm (the equivalent FWHM size) is $\sim 20\%$, as seen in Fig.4.10 (b). Fig.4.10 (c) plots the integrated energy fraction as a function of the intensity for the same spot, in which the laser energy and pulse duration (FWHM) were normalized to 50 J and 1.1 ps

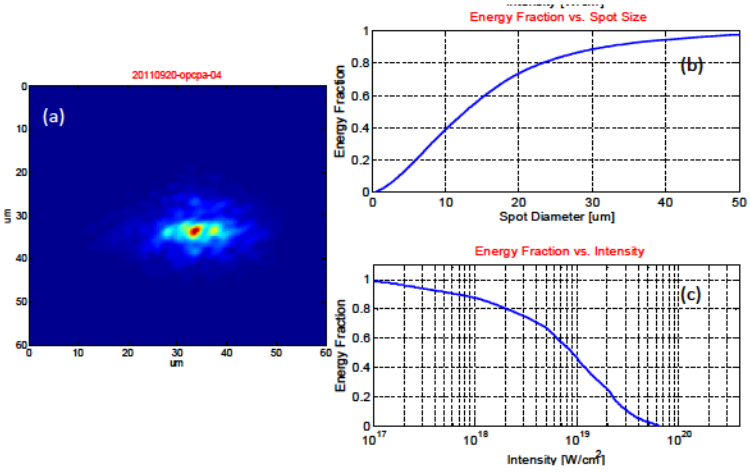

Figure 4.10: (a) Typical image of the best focus of Titan 2ω laser achieved in the Titan 2011 September Campaign. This focus was achieved with the low power laser light that only experienced the amplification by OPCPA. (b) Energy fraction versus diameter of equivalent circular spot. (c) Energy fraction versus instantaneuous intensity for the focal spot shown in (a) that was normalized to 50 J and 1.1 ps. Note that 50 J and 1.1 ps were the average laser energy at target and average pulse duration measured in the Titan 2011 September Campaign, respectively.

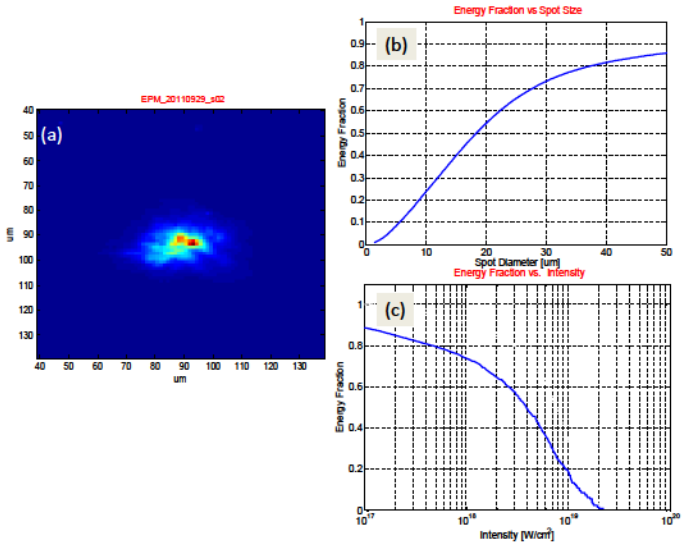

Figure 4.11: (a) A sample image of the EPM focus for the Titan 2ω laser achieved in the Titan 2011 September Campaign. (b) Energy fraction versus diameter of equivalent circular spot. (c) Energy fraction versus instantaneuous intensity. The laser energy and pulse duration were measured to be 44.5 J and 1.1 ps for this data shot.

respectively[1]. It is demonstrated that 10%, 50% and 80% of the available power are delivered above 3.2×10^{19}, 9.0×10^{18} and 2.0×10^{18} W/cm^2, respectively. Note that the peak intensity is approximately 6.5×10^{19} W/cm^2.

A sample image of the EPM focus of a system shot achieved at the best focus position in the Titan 2011 September Campaign is shown in Fig.4.11 (a), in which the spatial dimension was corrected by the focal length ratio (10.5) as discussed previously. The energy and pulse duration for this shot were measured to be 44.5 J and 1.1 ps. The same processing methods as those in analyzing the image of Fig.4.10 (a) were applied to this focal spot and the results are plotted in (b) and (c). One can see that the EPM focus is also an ellipse with FWHM sizes of 7.7 μm and 15.3 μm in the vertical and horizontal directions. The energy fraction within the equivalent FWHM size is around 25%, as indicated in (b). From (c), it shows that the peak intensity is 2.3×10^{19} W/cm^2, and 10%, 50% and 80% of the available power are delivered above 1.3×10^{19}, 3.9×10^{18} and 4.7×10^{17} W/cm^2, respectively.

Discrepancies are clearly seen between the focal spot measured at the target plane with the OPCPA and the one measured with EPM in full laser power. Possible reasons are given as follows: 1) the full beam profiles would be slightly different with and without the power amplification. When the laser is engaged in full power, the nonlinear refraction index change of the gain medium and the thermal effect of the pumping system will modify the wavefront of the beam profile. Therefore, the focus achieved with OPCPA is not fully representing the actual focus at target during system shots; 2) the EPM is a single lens system, the optical astigmatism is not the same as that of the parabola. 3) there is some degree of B-integral effect that takes place inside the 10-cm-thick combination of mirror substrate, window and lens combined when the laser is at full power, which deteriorates the focal profile of the EPM. Based on these

[1] 50 J and 1.1 ps are the average laser energy and pulse length achieved in the Titan 2011 September Campaign

possible reasons, one can average the intensity distributions of the OPCPA and EPM focii to reconstruct an intermediate focal spot, which is taken to represent better the actual focus and was used for benchmarking simulations.

4.2.3 X Ray Diagnostics

As seen in Fig.3.3, generated hot electrons can reach a temperature of a few hundreds of keV to an MeV with 1 μm laser intensity around 10^{19} W/cm^2. With such a high temperature, hot electrons are capable of knocking out the K-shell (most inner shell) electrons from the target atoms, and as a result, the electrons from a higher energy level fill up the vacancies and X-ray photons are emitted accordingly. This physics process is called K-alpha ($K\alpha$) emission, which is normally used to infer hot electron properties. Copper is one of the standard tracer materials that is inserted into the target to produce the desired $K\alpha$ emission. A number of X ray detection techniques that utilize X ray crystals have been developed and are being used in the fast ignition experiments. Those that were used in my PhD research include Cu $K\alpha$ Bragg crystal Imagers, Highly Oriented Pyrolytic Graphite(HOPG) Spectrometers and Kirkpatrick-Baez (KB) Microscopes, all of which are designed specifically to look at X rays near 8.048 keV (1.541 $\mathring{A}$), the Cu $K\alpha$ emission line.

Cu $K\alpha$ Imager

The crystal utilized in the Cu $K\alpha$ Imager is a spherically bent quartz crystal (also called Bragg crystal), the lattice system of which is hexagonal with a Miller index of $21\bar{3}1$. The Bragg crystal has a 2d lattice spacing of 3.082 $\mathring{A}$ and reflects X-rays according to the Bragg diffraction condition [94]:

$$2d \sin\theta_B = n\lambda \tag{4.11}$$

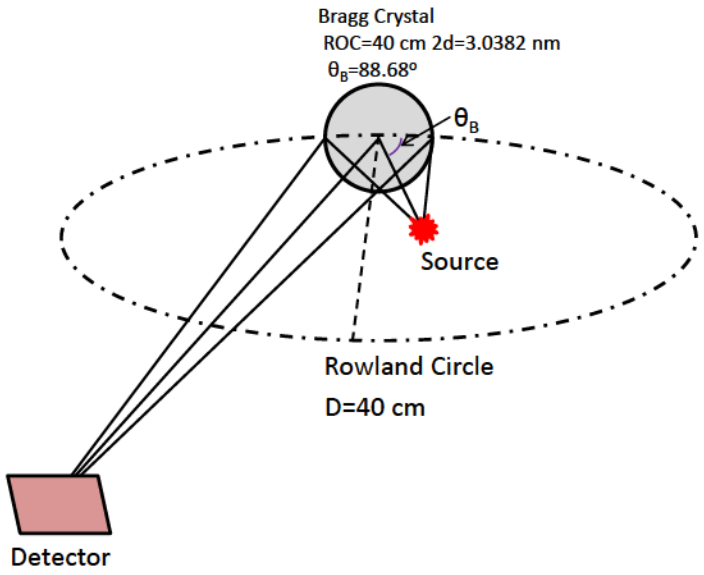

Figure 4.12: Cu $K\alpha$ imager

where θ_B is the Bragg angle (relative to the surface of crystal), n is an integer representing the diffraction order and λ is the wavelength of the incident X-rays.

The Bragg crystal that we used has a diameter of 4 cm and radius of curvature of 40 cm. The normal setup for the Cu $K\alpha$ Imager is illustrated in Fig.4.12. The x-ray source is placed within a Rowland circle whose diameter is equal to radius of curvature of the crystal, and the emitted X-rays are reflected and focused to a position that is outside the Rowland circle by a Bragg crystal that is mounted on the Rowland circle. The imaging properties of spherically bent Bragg crystal are similar to those of spherical mirrors, and thus can be understood with normal geometric optics. The lens formula that applies to the Cu $K\alpha$ imager is given by:

$$\frac{1}{p} + \frac{1}{q} = \frac{1}{f} = \frac{2}{Rsin\theta_B} \tag{4.12}$$

where p is the object distance, q is the image distance, f is the focal length and is given by $f = Rsin\theta_B/2$, and R is the radius of curvature of the Bragg crystal. In order to minimize the astigmatism that is inevitable with the off-axis imaging

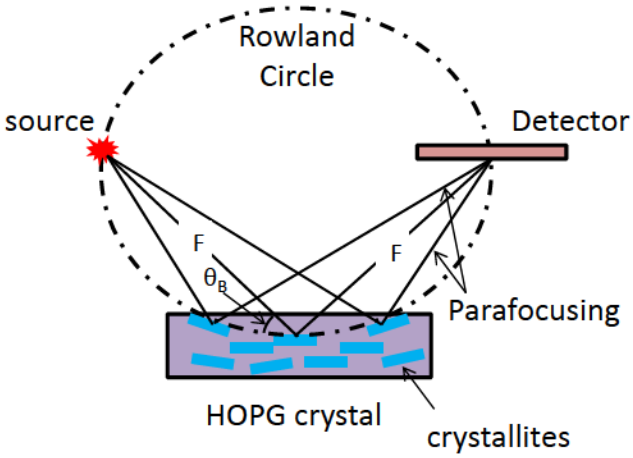

Figure 4.13: HOPG Spectrometer

system, the Cu $K\alpha$ imager is operated with incident angle close to normal, and the diffraction order is picked as 2 for fulfilling the Bragg diffraction condition that is given by Eqn.4.11. For the second order diffraction, the Bragg angle is set as 88.68^o for measuring Cu $K\alpha$ X ray.

The Cu $K\alpha$ Imager is capable of giving 2-D time-integrated, spatially resolved information of the hot electron flux by detecting and imaging the X-ray radiation within a narrow bandwidth around the Cu $K\alpha$ wavelength. However, the Cu $K\alpha$ spectral line shifts and broadens with increasing target temperature [95], and shifts out of the narrow bandwidth of Bragg crystal once it is sufficiently heated (on the order of 100 eV). The collection efficiency of Cu $K\alpha$ Imager is thus dependent on the temperature of target, and a correction needs to be made for the loss of signal due to target heating.

Highly Oriented Pyrolytic Graphite Spectrometer

Highly Oriented Pyrolytic Graphite (HOPG) is a mosaic crystal, which consists of a large number of small crystallites [96] with orientations close to that of the main crystal axis. The angular distribution of the crystallites, with plane orientations slightly off the normal axis to the surface, is called the mosaic

spread. Mosaicity makes it possible that even for a slightly different angles of incidence to the crystal surface, an energetic distribution of photons can be reflected, because each photon of this energetic distribution can find a crystallite plane with the right Bragg angle. Therefore, the mosaicity is responsible for the higher integral reflectivity of HOPG crystal in comparison to perfect crystals.

A typical setup of a HOPG spectrometer is shown in Fig.4.13. Generally, the HOPG is operated at the first order of diffraction for Cu $K\alpha$, the corresponding Bragg angle of which is 13.4^0. The rays emitted by a point source are focused onto a line in the image plane if the crystallites are lying on the Rowland circle. This parafocusing occurs in 1:1 magnification geometry, for which the distances F between source and crystal and crystal and image plane are equal. Due to crystal mosaicity, the rays further along the crystal surface would also find other well aligned crystallite planes, thus are reflected and reach the image plane. This means, the effective depth, from which diffraction in mosaic crystals occurs, is much larger as compared to an ideal crystal. A HOPG spectral imager is an essential diagnostic to run in conjunction with the Cu $K\alpha$ Imager because its broad bandwidth response consistently permits all the $K\alpha$ line radiation to be collected, and therefore is not sensitive to shifting of the line wavelength due to temperature.

Kirkpatrick-Baez Microscope

The KB microscope was first proposed by Kirkpatrick and Baez in 1948 [97], and it consists of two orthogonal mirrors that are placed in succession, which is depicted in Fig.4.14 (a). These two mirrors are super-polished to a RMS roughness down to a few angstroms in order to minimize the scattering of short wavelength X-rays caused by the surface irregularity. On top of the super-polished mirror is a high Z material coating layer, which provides a refractive index step profile from the ambient air or vacuum. Typical choices of coatings

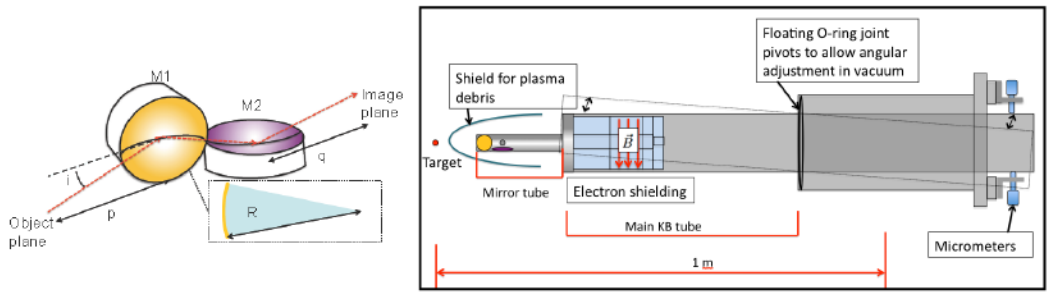

(a) (b)

Figure 4.14: (a)Two spherical mirrors placed in series in KB microscope, (b) KB microscope Setup. (Image courtesy of Hal Friesen [H.J. Friesen, MSc thesis, University of Alberta, 2011])

are nickel, platinum, gold and iridium. The X-rays will be reflected if it arrives at a incident angle(relative to normal) larger than the critical angle θ_c that is derived from the total internal reflection condition:

$$\theta_c = asin\frac{n_1}{n_2} \tag{4.13}$$

where n_1 is the refractive index of the coating layer, and n_2 is the refractive index of the air. Normally, the KB microscope works in grazing incidence due to the fact that the x ray reflectivity in this case is high enough to give a visible image for data recording.

We already developed a KB microscope with Pt coated X ray mirrors at the University of Alberta, as presented in Fig.4.14 (b). The KB setup is a re-entrant module designed to mount on a chamber flange, made up of two tubes connected with an O-ring seal to allow slight pivoting of the inner tube for alignment purpose. The entire hardware is made out of aluminum to minimize the activation that is generated by the hard X-ray radiation and MeV particles generated in the Fast Ignition experiments. Inside the central tube, there are an X-ray collimator and magnet shields against incoming charged particles. This

central tube is free to pivot about the central O-ring over a range of angles, and is controlled by micrometers at the outside end of the tube.

Since in theory the KB mirrors are achromatic and are able to reflect whatever X-ray wavelength comes in as long as they meet the total internal reflection requirement, the KB microscpe is actually a broad band x ray imager. Thus it is resistant to the temperature shift of the Kα emission. The KB microscope is also capable of observing hard x ray Bremsstrahlung in the 6-8 keV range, which the Cu $K\alpha$ imager and HOPG Spectrometer cannot view.

Chapter 5

GeV electrons due to a transition from laser wakefield acceleration to plasma wakefield acceleration*

We show through experiments that a transition from laser wakefield acceleration (LWFA) regime to a plasma wakefield acceleration (PWFA) regime can drive electrons up to energies close to the GeV level. Initially, the acceleration mechanism is dominated by the bubble created by the laser in the nonlinear regime of LWFA, leading to an injection of a large number of electrons. After propagation beyond the depletion length, leading to a depletion of the laser pulse, whose transverse ponderomotive force is not able to sustain the bubble anymore, the high energy dense bunch of electrons propagating inside the bubble will drive its own wakefield by a PWFA regime. This wakefield will be able to trap and accelerate a population of electrons up to the GeV level during

*The contents of this chapter have been published in the article: P.E. Masson-Laborde, M.Z. Mo, et al., Phys. Plasmas **21**, 123113 (2014). The first two authors contributed equally to this work.

this second stage. Three dimensional particle-in-cell simulations support this analysis and confirm the scenario.

5.1 Introduction

The pioneering work of Tajima and Dawson [6] in 1979, based on the fact that an ultrashort terawatt (TW) laser propagating through an underdense plasma will excite strong plasma wakes that may trap and accelerate electrons up to high energies, has led to the development of the laser wakefield accelerator (LWFA) concept. Since then, a tremendous amount of progress has been made in improving the quality and energy of the generated electron beams, with the goal to reach the GeV-level. Finally, in the past decade, prior to which time most of the experimental accelerated electrons were characterized by an exponential energy distribution [98, 99], high quality monoenergetic electron beams were reported by many groups [20, 44, 46, 47, 51, 100, 101, 102, 103]. Most of these experiments, were conducted in the so-called blowout regime or "bubble" regime, identified in many simulations and theoretical analyses [12, 34, 38, 104, 105, 106, 107, 108] where the electrons are expelled radially from the beam axis by the transverse ponderomotive force of the laser, which creates a three dimensional (3D) cavity (the "bubble") empty of electrons. This bubble, full of ions, is surrounded by a sheath of relativistic electrons, and some of them can be self-trapped and then accelerated to high energy leading to a monoenergetic bunch of electrons of high quality. This acceleration of the electrons by the strong electric field inside the bubble will be limited by the dephasing length, resulting in a maximum energy gain that can be estimated from the laser and plasma parameters [34]:

$$E_{max}(GeV) \cong 1.7(\frac{P}{100TW})^{1/3}(\frac{10^{18}cm^{-3}}{n_e})^{2/3} \tag{5.1}$$

where P is laser power and n_e is plasma density.

Relativistic electron bunches can also be used to generate the full expulsion of the electrons and to create the accelerating cavity. This process called the plasma wakefield accelerator (PWFA), is known for years [52, 109], and is commonly used in experiments carried out at the Stanford Linear Accelerator Center (SLAC) using GeV electron beams to drive nonlinear plasma waves [53, 57, 110]. In the PWFA regime, the ponderomotive force of the laser is replaced by the space charge force of the electron beam in the radial expulsion of the electrons. In the PWFA regime, the phase velocity of the wake is the same as that of the electron bunch, and therefore will be independent of the plasma density. Consequently, dephasing between the accelerated electrons and the driver only occurs when the accelerated bunch obtains higher energies and velocities than the driving bunch and reaches the center of the bubble. This is not the case in LWFA, where high-energy electrons can outrun the field that moves at the group velocity, depending on the plasma density. This difference is an important advantage of the PWFA regime compared to LWFA.

There are indications in a few laser wakefield acceleration experiments to date of peak electron energies above those that would be predicted by the scaling law given by Eqn.5.1, leading to the generation of hundreds of MeV to GeV class electrons under higher density conditions [46, 51, 103, 111, 112]. Such an energy enhancement was also observed in one of the earliest 3D PIC simulations of the laser wakefield process by Tsung et al. [38] where it was observed that a second bunch of electrons was accelerated to 0.84 GeV. Hafz et al. [46] also compare their results to PIC simulations but neither Hafz et al. or Tsung et al. gave clear explanations as to the mechanisms causing the enhanced electron energies. Recently Hidding et al. [113] proposed the combination of the LWFA process with the PWFA process in separate plasmas to create and then accelerate quasi-monoenergetic electron bunches, carrying out PIC simulations indicating that a secondary 10 pC bunch of 500 MeV electrons could be accelerated up to 1 GeV by a 100 pC primary bunch of 500 MeV

electrons. Pae et al. [114] proposed that there can be a mode transition from the LWFA process to the PWFA process within a single interaction plasma, demonstrating in a 3D PIC simulation the acceleration of a 16 pC secondary bunch of electrons up to 320 MeV by a 200 pC primary bunch of electrons with peak energy of 380 MeV. In this case no energy enhancement was demonstrated. In a more recent experiment [115] a step density gas jet was employed to obtain injection at $7.5 \times 10^{18}\ cm^{-3}$ and then acceleration over 6 mm of plasma at $3.5 \times 10^{18}\ cm^{-3}$ producing a continuum of accelerated electrons up to 1.5 GeV in energy. Analysis of the results using 2D PIC simulations indicated that a secondary bunch of electrons was accelerated with peak energies up to 1.8 GeV in a mechanism they describe as phase locking with the plasma wake. However, there was no discussion as to why this phase locking occurs and no indication of a quasi-monoenergetic bunch.

In this chapter, we will report the experimental results on laser wakefield driven electron generation achieved with the 200 TW beamline at the Advanced Laser Light Source (ALLS) facility located at INRS, Varennes [85], which is a platform developed for high intensity relativistic laser-plasma interaction studies and for laser wakefield acceleration studies [50, 51, 79, 116]. In the experiment, GeV electrons have been observed with self-injection in relatively high density plasma, on the order of $1 \times 10^{19}\ cm^{-3}$, produced by an ultraintense laser pulse interacting with a single-stage gas jet. We will show from 3D particle-in-cell (PIC) simulations, that the level of energy obtained and the characteristics of the electron beams can be understood as a two-stage process, where in the first stage the LWFA will accelerate a dense bunch of high energy electrons, and then after the complete depletion of the laser pulse, this bunch will create a wakefield in the PWFA regime, which is able to accelerate electrons close to GeV level. The PIC simulation analysis implies that these GeV electrons can be seen as experimental observation of the two-stage process describe by Ref.[113], indicating that the single-stage hybrid plasma wakefield

acceleration is a feasible approach to achieve energetic electron beams.

The chapter is organized as follows. Section 5.2 and 5.3 present the experimental setup and the experimental results respectively. Section 5.4 presents the simulation results of the experiment and their interpretation. Section 5.5 and 5.6 summarize our discussions and conclusions respectively.

5.2 Experimental Setup

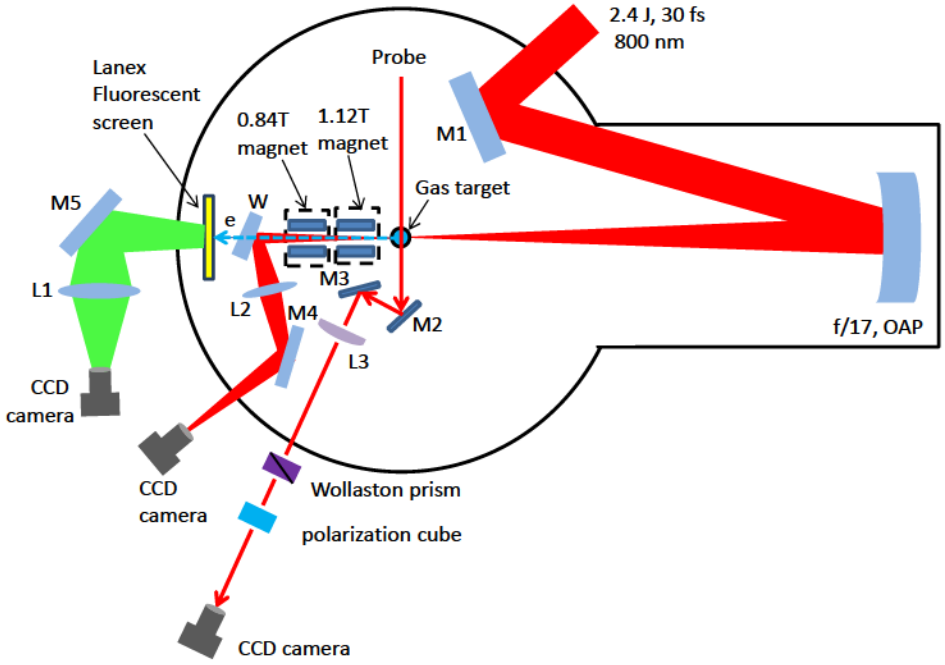

Figure 5.1: Schematic diagram of the experimental setup for the laser wakefield acceleration experiments. M1 - M5: reflective mirrors; OAP: off-axis parabola; L1 - L3: lenses; W: beam splitter glass wedge.

The experiments were performed with the 200 TW laser system located at the Canadian Advanced Laser Light Source(ALLS) facility at INRS, Varennes [85]. The 200 TW laser system is a compact laser system based on Ti:Sapphire technology and chirped pulse amplification (CPA) technique with a central operating wavelength of 800 nm in a horizontal polarization. For typical data

shots during the experiments, the facility delivered laser pulses with energy of 2.4 J and pulse duration of 30 fs at full-width half-maximum (FWHM) onto the gas target. As shown in Fig.5.1, the 9-cm-diameter laser pulses were focused by a 150 cm focal length off-axis parabola (OAP) onto the gas target. The vacuum focal spot measured with a single-lens imaging system shows a full-width at half maximum (FWHM) diameter of approximately 22 μm, within which area it contains $\sim 25\%$ of the total energy. The focused peak intensity in vacuum was measured to be approximately $7.0 \times 10^{18}\ W/cm^2$, corresponding to a laser normalized vector a_0 of 1.7.

The generated electron beams were dispersed by two separate 10-cm-long dipole magnets with magnetic field strengths of 1.12 T and 0.84 T onto a Lanex fluorescent screen that was placed 20 cm after the last magnet. The fluorescence emitted from the Lanex screen was collected by an f/2.8 aperture lens system and imaged onto a 12-bit charge coupled device(CCD) camera. A side-view Nomarski interferometer based on a Wollaston prism as the beam splitter [89] was employed to monitor the plasma density. The probe beam for the side-view interferometry came from the zero-order diffraction of the first grating in the compressor, which was then compressed with an extra compressor down to 40 fs. The path length of the probe beam is adjustable to get various delays relative to the main pulse. The side scattered light emitted from the laser plasma interaction region at an angle normal to the plane spanned by the laser polarization direction and the propagation direction was collected by a top-view imaging system to monitor the plasma channel formation.

The gas jet was formed by a 5-mm-diameter supersonic conical nozzle connected to a pulsed solenoid valve (Parker Valve). The nozzle design was similar to that of Semushin et al.[88] with a critical throat diameter of 0.8mm and length of 10.5mm. The working gas during the experiments was pure helium. The density of the helium plasma was calculated by use of a modified Abel inversion algorithm[91], where the asymmetry of the fringe shifts is weighted

and introduced into the final plasma distribution, assuming a $\cos\theta$ transverse asymmetry contribution. The uncertainty of the measured electron energy was estimated according to an electron beam shot to shot divergence of 9.8 mrad, which is derived based on the standard deviation of the positions of the straight through reference shots when both magnets were removed, leading to an error of (+311 MeV\-196 MeV) at 1 GeV.

5.3 Experimental Results

The electron energy spectra obtained at different plasma densities: 4.70×10^{18} cm^{-3}, 1.05×10^{19} cm^{-3} and 1.16×10^{19} cm^{-3} using a 5-mm gas jet with a laser power of 80 TW are shown in Fig.5.2(a). The electron energy is dispersed in the horizontal direction while the vertical profile shows the lateral deflection and divergence of the electron beams. The corresponding dN/dE electron energy spectra integrated over the full width for each spectral image normalized to unity is plotted in Fig.5.2(b). Pronounced monoenergetic peaks ranging from 0.15 to over 1 GeV have been observed in different shots as shown in Fig.5.2(a). More distinct monoenergetic features were observed at the lower electron density of 4.70×10^{18} cm^{-3}, while multiple bunches and quasi-continuous injection start to dominate as the electron density was increased to 1.05×10^{19} cm^{-3} and 1.16×10^{19} cm^{-3}.

The top image of Fig.5.2(a) shows a typical electron image at plasma density of 4.70×10^{18} cm^{-3}. From the image, one can see that there is merely one monoenergentic electron bunch in the spectrum, which has a prominent peak at 345 MeV with energy spread of 10%, a total charge of 7.3 pC and $1/e^2$ beam divergence of 12 mrad. When increasing the plasma density to 1.05×10^{19} cm^{-3}, as shown in the middle image of Fig.5.2(a), three separated electron bunches of different characteristics are observed. To the high energy end, a relatively weak monoenergetic electron bunch, having a total charge of 0.4 pC, peaks

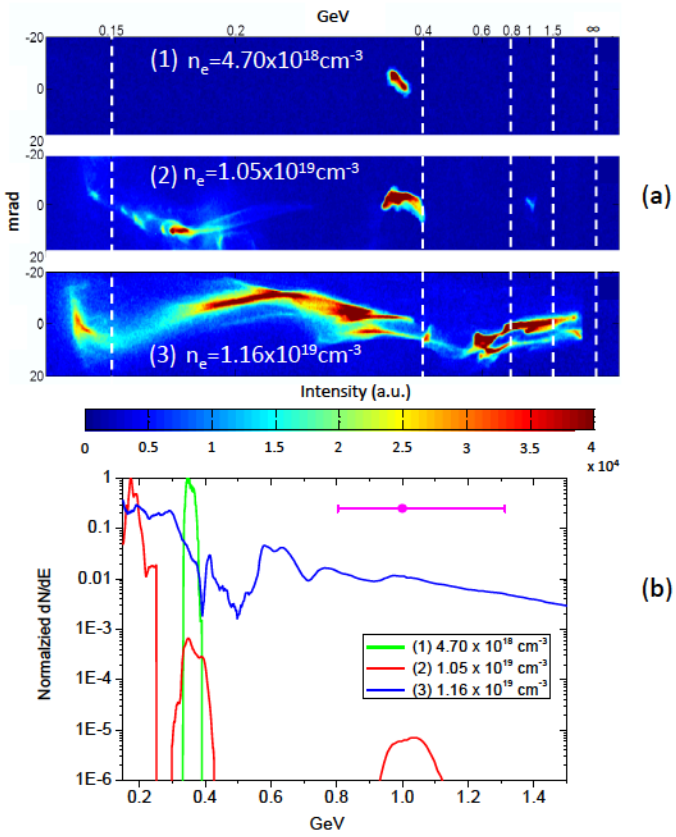

Figure 5.2: (a) Energy resolved images of the electron bunches for pure helium at plasma densities, (1) $4.70 \times 10^{18}\ cm^{-3}$, (2) $1.05 \times 10^{19}\ cm^{-3}$, (3) $1.16 \times 10^{19}\ cm^{-3}$; All the images are plotted in the same color range where the brightness represents the flux of the electrons in arbitrary units. (b) Corresponding normalized electron number density per electron energy; Note that the y axis is plotted in a logarithmic scale; Representative uncertainty of measured electron energy at 1 GeV is indicated by the magenta circular dot and attached bars at the top of the plot.

around 1.03 GeV. The $1/e^2$ beam divergence of this GeV bunch was measured to be less than 6 mrad. The second bunch to the left, peaking around 350 MeV, is also monoenergetic and has a total charge of 11.7 pC. Compared to the first two electron bunches, the third one peaking around 175 MeV spreads more in divergence but contains a larger total charge of 36.6 pC. At an electron density of $1.16 \times 10^{19} cm^{-3}$, as shown in the bottom image of Fig.5.2(a), more continuous injection was observed with high energy electrons extending up to $1.5^{+0.8}_{-0.4}$ GeV. These features can clearly be seen in the lineout plots of electron

number density per unit energy in Fig.5.2(b). The total charge contained in this shot is measured to be around 245 pC. Note that the calculated charge for these electron images is based on the manufacturer's specifications for the camera response and the imaging system optical efficiency. It is estimated that the accuracy of this result is within a factor of 2.

Comparing the maximum peak energies achieved for these three particular shots, one may notice that higher energy bunches of electrons appear at the higher densities which is contrary to the expected decreasing dephasing length and lower maximum energy obtained with increasing density. Also, applying Lu's scaling law for maximum energy gain as shown in Eqn.5.1, one would expect a peak electron energy of 350 MeV at the plasma density around 1.1×10^{19} cm^{-3} for a laser power of 80 TW as employed in this experiment. However, the measured GeV peak energies around this density as depicted in the bottom two images in Fig.5.2(a) are more than double of the expected value, which as we will demonstrate using PIC simulations is due to an energy boost mechanism introduced by the transition from LWFA to PWFA occurring at high plasma density. The details will be discussed in Sec.5.4. Energy spectra shown in Fig. 5.2 illustrate transition from the LWFA mechanism to PWFA with increasing plasma density. As the PWFA becomes more efficient at higher background densities the energy spread of accelerated electrons also becomes larger consistent with a theory of PWFA [12].

For each shot the maximum energy peak was determined where a distinct peak in the energy spectrum was observed. This is called the maximum peak energy. Fig.5.3 plots the average of the maximum peak energies achieved at different plasma densities. The green diamonds represent the average of all the maximum peak energies achieved at identical plasma density. An average of 60 shots at each density were taken to conduct the statistics of the maximum peak energies. The blue dots represent the average of the top three maximum peak energies for each density. For comparison, the predicted average maxi-

mum energy gain at each density according to Eqn.5.1 with input laser power of 80 TW is also plotted in the graph. Looking at the average of all the maximum peak energies, one can see that the peak energy agrees approximately with the prediction when the plasma density is above $6 \times 10^{18}\ cm^{-3}$, below which the measurement starts to deviate from the prediction. This phenomena was observed and reported previously [50] and is attributed to the violation of bubble matching condition which is needed to self guide the laser propagation inside the plasma. However, in relatively high plasma density region, i.e. around $1 \times 10^{19}\ cm^{-3}$ and above, occasionally there are some shots that generate electrons more than double of the prediction, particularly in the region near $1.1 \times 10^{19}\ cm^{-3}$, in which GeV electrons were observed. A 3D Particle-in-cell (PIC) simulation was conducted to understand the physics behind this energy doubling phenomena and the details will be given in Sec.5.4.

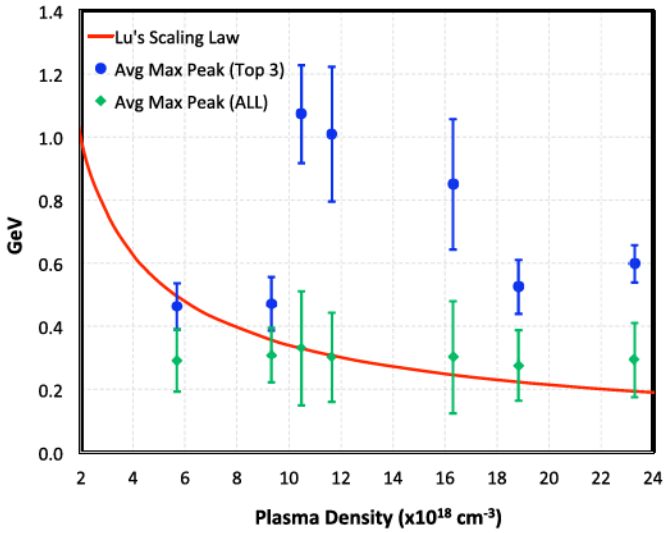

Figure 5.3: Energy of the highest energy peak in the electron distribution measured at each electron density for pure helium. The blue dots stand for the average of the top three maximum achieved peak energies at each density. The green diamonds are the averages of all the energies of the highest energy peaks for shots at identical density. The error bars are obtained from the standard deviation of the given number of measurements. The red line represents the predicted energies at a given laser power of 80 TW using the nonlinear scaling law given by Eqn.[5.1]

The laser propagation in the plasma can be experimentally studied by looking at the side scattered light emitted from the plasma, which is due to the combined effect of Thomson scattering [117, 118] and Raman scattering [119, 120]. To aid in the understanding of the physics behind the observed energy boosting phenomena, the plasma channel images were captured during the experiments and are shown in Fig.5.4, which plots two typical side scattered images achieved at the same plasma density of $1.16 \times 10^{19}\ cm^{-3}$ for pure He. Among them, the top one is the plasma channel image corresponding to the GeV shot (the bottom image) as shown in Fig.5.2(a). As indicated, the plasma channels appear around 0.25 mm before the laser focus and last for less than 2 mm due to the pump depletion. Particularly, for the GeV shot achieved at this density as shown in the Fig.5.2(a), the plasma channel is around 1.3 mm in length. At the density of $1.16 \times 10^{19}\ cm^{-3}$, the plasma wavelength is estimated to be $9.82\ \mu m$ by using the formula: $\lambda_p[\mu m] = 3.34 \times 10^{10}/\sqrt{n_e(cm^{-3})}$, and the pump depletion length, approximated by [34] $L_{pd} = c\tau_L(\omega_0/\omega_p)^2$, where c is the light speed in vacuum and τ_L is the laser pulse duration, and ω_0 and ω_p are the laser and plasma angular frequencies, is estimated to approximately 1.4 mm. The estimated pump depletion length agrees approximately with the length of plasma channel that we observed here. The critical power for self-focusing, given by $P_c(GW) = 17 n_c/n_e$, where n_c is the critical density given by $n_c = \omega^2 m\varepsilon_0/e^2$ (ε_0 is the permittivity in free space), is calculated to be ~ 2.6 TW at the density of $1.16 \times 10^{19}\ cm^{-3}$, which gives a ratio of P/P_c of 31 for 80 TW laser. With the laser power greatly in excess of the critical power for self-focusing, the modulated structures of the side scattered images, as shown in Fig.5.4, come about as a general response to the self-oscillations of beam propagating in a nonlinear medium.[117, 118]

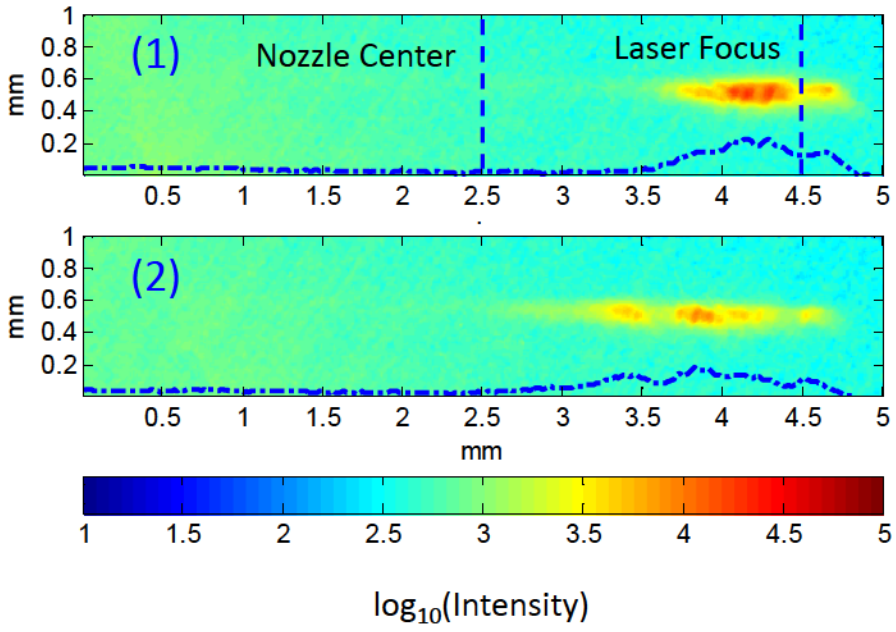

Figure 5.4: (1)-(2) Side scattered images of the plasma channels formed at identical density of $1.16 \times 10^{19}\ cm^{-3}$ achieved with the top-view imaging system. Note that the false color in all of the images is plotted in base 10 logarithmic scale to present clearer features of the plasma channel. Lineouts of the plasma channels after taking logarithm are rescaled and overlaid with the images. The nozzle center and the laser focus position are marked with blue dashed lines. The laser propagated from right to left.

5.4 Simulations results

To understand the physics behind the energy doubling phenomena that we observed, we use the 3D fully relativistic PIC code SCPIC [121], which is a successor of the code MANDOR [122, 123] already used in many laser-plasma applications. This code uses a well-known Yee scheme for solving Maxwell equations and the Boris scheme for equations of motion of the macroparticles. The laser pulse propagates in the x-direction in a fully ionized plasma (y and z being transverse directions). Parameters are the same as those used in the experiment, the laser wavelength is $\lambda_0 = 0.8\ \mu m$, the pulse duration is $\tau_L = 30$ fs at full-width-half-maximum (FWHM), and the laser focal spot is $w_0 = 22$

μm at FWHM. The laser pulse peak intensity is $I = 7 \times 10^{18}\ W/cm^2$, corresponding to a normalized vector potential $a_0 = 1.7$. The laser is propagating in a 5-mm-long plasma, with a homogeneous density of $n_e = 1.1 \times 10^{19}\ cm^{-3}$, corresponding to a normalized density of $n_e/n_c = 5.7 \times 10^{-3}$ with n_c the laser critical density. In our study, we use a moving window and the simulation window size is $125\lambda_0 \times 78\lambda_0 \times 78\lambda_0$, and the total number of macroparticles used is about 1.2×10^8. Based on our experimental conditions, the pump depletion length [34] is $L_{pd} = c\tau_L(\omega_0/\omega_p)^2 \approx 1.43\ mm$, and the dephasing length is $L_d = (2/3)\sqrt{a_0}(\omega_0/\omega_p)^2\lambda_p/\pi \approx 0.9\ mm$, both are much smaller than the total length of the plasma, so we may expect that the laser will not be able to maintain sufficient power to accelerate electrons up to the total 5mm length long. Note that the estimate of the pump depletion length, L_{pd}, is consistent with the side scattered image shown in Fig.5.4 where the strong scattered light signal extends over the distance comparable with L_{pd}. We will show that, in agreement with Ref.[114], two regimes can be identified in our simulations: an early stage takes place when $t < t_{pd} \approx L_{pd}/c \approx 5\ ps$, during which period the main acceleration mechanism is attributed to LWFA, and the second stage with mechanism due to PWFA comes into play when $t \gg t_{pd}$. As we will discuss later, the transition from the LWFA to PWFA occurs because the laser is fully depleted and cannot sustain the bubble anymore.

5.4.1 LWFA regime

In the first stage of the propagation, before the pump depletion length, the laser will undergo strong self-focusing (here we have $P/P_c \simeq 30$), and consequently the normalized peak amplitude a_0 will grow up to large value, reaching a maximum around $a_0 \simeq 7$ (Fig.5.5(a)). At the same time, the radius of the focal spot will be significantly reduced. Many useful diagnostics of the pulse evolution can be found in Ref.[124], and some of them were employed here to study the pulse evolution during the propagation. As can be seen in

Fig.5.5(b), which shows the normalized intensity weighted laser radius given by: $< w^2 >= \frac{\int y^2 E_y^2 dy}{\int E_y^2 dy}$,[124] the laser radius decreases to a very small value as its amplitude is growing (Fig.5.5(a)) in the first 500 um's of propagation. The transverse ponderomotive force of the laser expels the electrons and creates an ion channel. When the Coulomb force from the ion channel, which tends to pull back the expelled electrons, is equal to the radial ponderomotive force, a stable bubble shape is reached. From this equality, we can estimate the blowout radius given by $R \simeq 2\sqrt{a_0}/k_p \simeq 10\lambda_0$, where k_p is the plasma wavenumber, given by $k_p = (2\pi/\lambda_0)\sqrt{n_e/n_c} \simeq 0.6\ \mu m^{-1}$. Fig.5.6(a) illustrates, after a propagation distance of $L = 1.2\ mm$: (i) the electron density n_e/n_c in the 2D plane (x-y, z=0) (top picture), (ii) a lineout of electron density and longitudinal electric field E_x (middle picture) and (iii) the electron normalized momentum $p_x/m_e c$ (bottom picture). As indicated, electrons are trapped in this cavity and are accelerated up to 250 MeV, and the total charge for these electrons is around 300 pC. The laser continues to propagate and electrons are injected and accelerated as long as the bubble still exists. However, after a propagation of $L = 2.2\ mm$, as seen in Fig.5.6(b), the bubble is elongated in the longitudinal direction due to the injection of a large number of electrons, along with the fact that electrons injected inside the cavity start to dephase, despite the fact that the accelerating field is not yet affected too much by the beam loading [56, 125] and keeps a sharp profile along the longitudinal direction. The onset of the electron injection during LWFA regime, is related to the succession of self-focusing and defocusing periods during the laser propagation [126]. As depicted in Fig.5.5(b) and (d), which show the laser radius and the number of macroparticles above 20 MeV as a function of propagation distance respectively, the injection and acceleration starts when the minimum laser radius is reached, at which time the laser becomes self-guided.

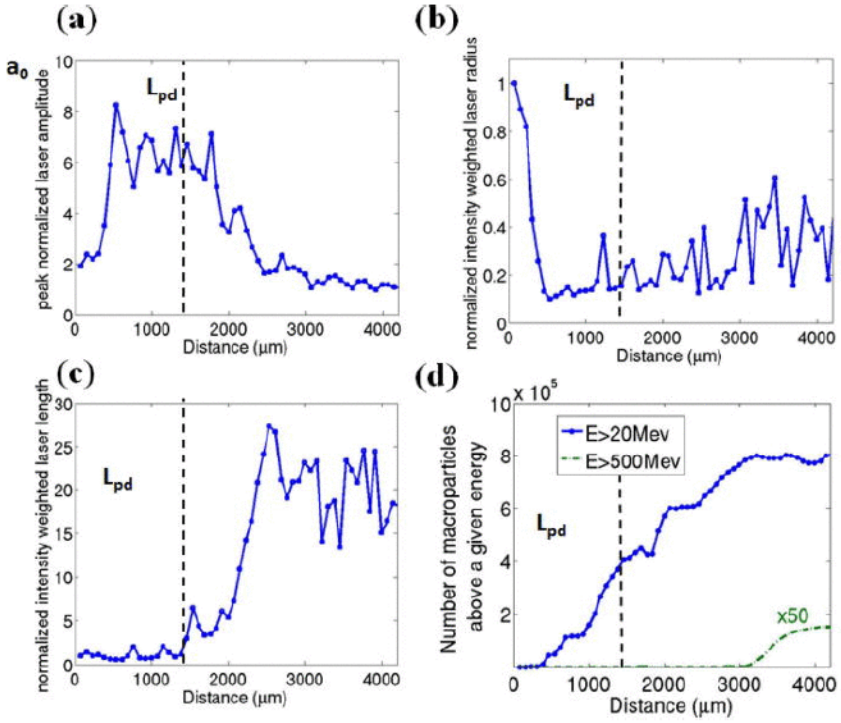

Figure 5.5: (a) Normalized laser peak amplitude as a function of propagation, (b) normalized intensity weighted laser radius as a function of propagation, (c) normalized intensity weighted laser length as a function of propagation, (d) number of macroparticles with energy larger than 20MeV (solid line) and larger than 500MeV as a function of propagation (dashed line, multiplied by 50 in order to fit in linear scale with the 20MeV curve). The pump depletion length L_{pd} is illustrated in all curves with the dashed line.

5.4.2 Transition from LWFA regime to PWFA

As we can see in Fig.5.5(a), beyond the distance of laser pump deletion, the laser pulse peak amplitude begins to strongly decrease from its maximum value obtained during self-focusing. For a propagation distance of $L = 2.2\ mm$ (corresponding to Fig.5.6(b)), the peak amplitude is back to its initial value. After this distance of propagation, the shape of the pulse is strongly modified from its initial shape due to group velocity dispersion and self-steepening [32, 127, 128, 129, 130]. Again, following Ref.[124], we can look at the normalized pulse length given by: $< L_x^2 >= \frac{\int (x-x_{max})^2 E_y^2 dx}{\int E_y^2 dx}$, where x_{max} is the position

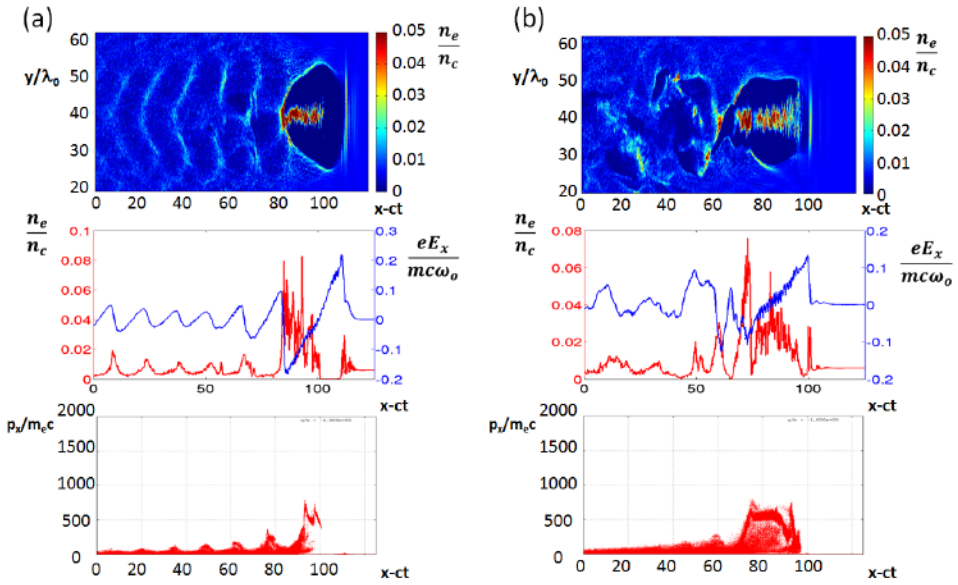

Figure 5.6: (a) At time t=4 ps, corresponding to a propagation distance of 1.2 mm (LWFA regime): (from top to bottom) 2D map (x-y plane) of electron density (normalized to ρ_c); On-axis lineout of the longitudinal electric field (blue curve) and electron density (black curve); Electron normalized momentum p_z/mc. (b) Same pictures but for time t=7.5 ps, or a propagation distance of 2.2 mm (end of LWFA regime). Both 2D maps are scaled to $n = 0.05n_c$

(longitudinal) of the maximum amplitude of the laser pulse. This quantity is illustrated in Fig.5.5(c), and we can clearly see that after 2 mm of propagation the depletion of the pulse occurs, leading to a broadening of the pulse length.

From this moment, as can be seen in Fig.5.7(a) showing the density, longitudinal electric field and phase space after a propagation distance of L = 2.7 mm, the electrons are dephased, and despite the low quality of the transverse electric field, the bubble is maintained. However, the longitudinal electric field does not have a sharp profile any more but also is affected by a beam loading effect. The loaded charge Q and the accelerating field modified by Q satisfy

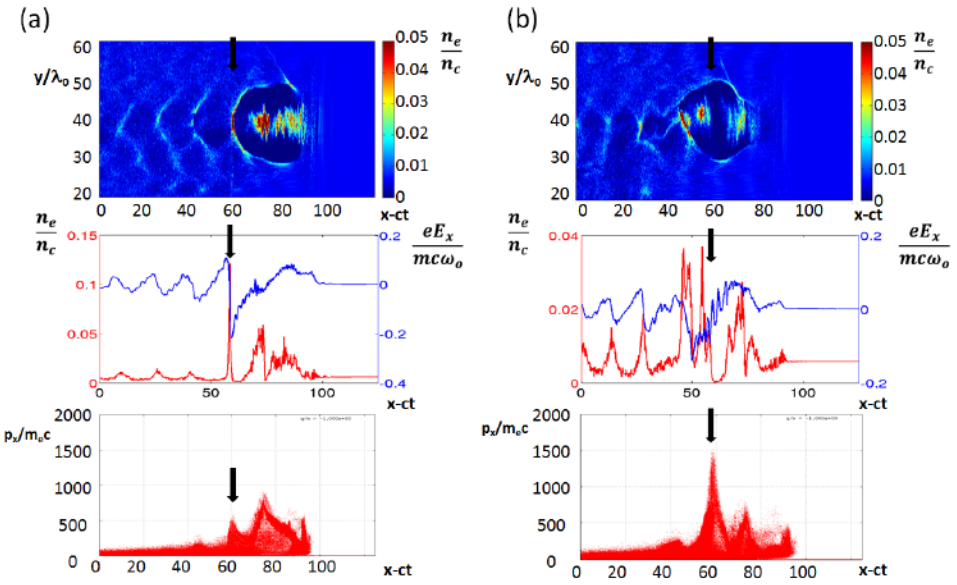

Figure 5.7: (a) For time t=9 ps, at a propagation distance of L=2.7 mm (beginning of the PWFA regime): top: 2D map (longitudinal-transverse plane) of electron density (normalized to ρ_c), middle: on-axis line out of the longitudinal electric field (blue curve) and electron density (black curve) and bottom: electron normalized momentum p_z/mc. (b) same pictures but for time t=12 ps, so a propagation distance of L=3.6 mm (PWFA regime). All the 2D map are scaled to $n = 0.05n_c$. The black arrow in the pictures indicates the position of the electrons injected during the PWFA regime.

the following relation [56]:

$$Q(nC) > 1.5 \times 10^{-3}\sqrt{1.1 \times 10^{19} cm^{-3}/n_c}(k_p R_b)^4(\frac{eE_x}{mc\omega_0})^{-1}, \qquad (5.2)$$

which illustrates the balance between the number of accelerated electrons and the field, E_x, produced by the original bunch. This is characteristic for the PWFA and the interaction between loaded charge and the accelerating bunch [56]. Here, for our parameters, we find that beam loading will become significant for $Q > 1nC$, which is very close to the total charge of the electrons

injected inside the cavity up to this propagation distance in the LWFA regime. The shape of the longitudinal electric field shows evidence that the first leading bunch of electrons inside the cavity, previously injected during LWFA regime, is now driving the acceleration by playing the role of the wakefield driver. Comparisons between longitudinal and transverse electric field at this time and the time corresponding to Fig.5.6(a), are illustrated respectively in Fig.5.8(b) and (a). We can see that, while initially the laser pulse is driving the wakefield, at late time, the position of the electric field indicates that the remaining pulse is no longer the driver of the wakefield. Furthermore, we can observe that, as already indicated by Fig.5.5, the laser pulse is fully depleted and broadened. In order to be sure that the laser is not driving the wakefield, we made PIC simulations using as an initial condition, the laser as it is at the end of the LWFA regime. Our simulations confirm that, because of the effective length and amplitude of the pulse, no wakefield can be generated at this time.

At this point we see another population of electrons (position $x - ct \simeq 60$ on Fig.5.7(a) and (b) indicated by the black arrow) is being accelerated by the longitudinal electric field which is now driven by the primary bunch of electrons.

5.4.3 PWFA regime

When the transition to plasma wakefield acceleration regime occurs, we can try to estimate the spatial features of the main electron bunch now driving the wakefield. By assuming a bi-Gaussian profile for the leading electron bunch such that $n_b = n_{b0} \exp(-x^2/2\sigma_x^2) \exp(-r^2/2\sigma_r^2)$, with $r^2 = y^2 + z^2$, we can obtain for the time corresponding to Fig.5.7(a), some estimates of the FWHM radius along the longitudinal axis: $\sigma_x \simeq 5\lambda_0$, such that $k_p\sigma_x \simeq 2$, and also estimates along the transverse direction: $\sigma_r \simeq 1.2\lambda_0$, such that $k_p\sigma_r \simeq 0.6$. At this particular moment, when the second injection occurs boosted by the longitudinal electric field created by the bunch, the bunch density can be estimated

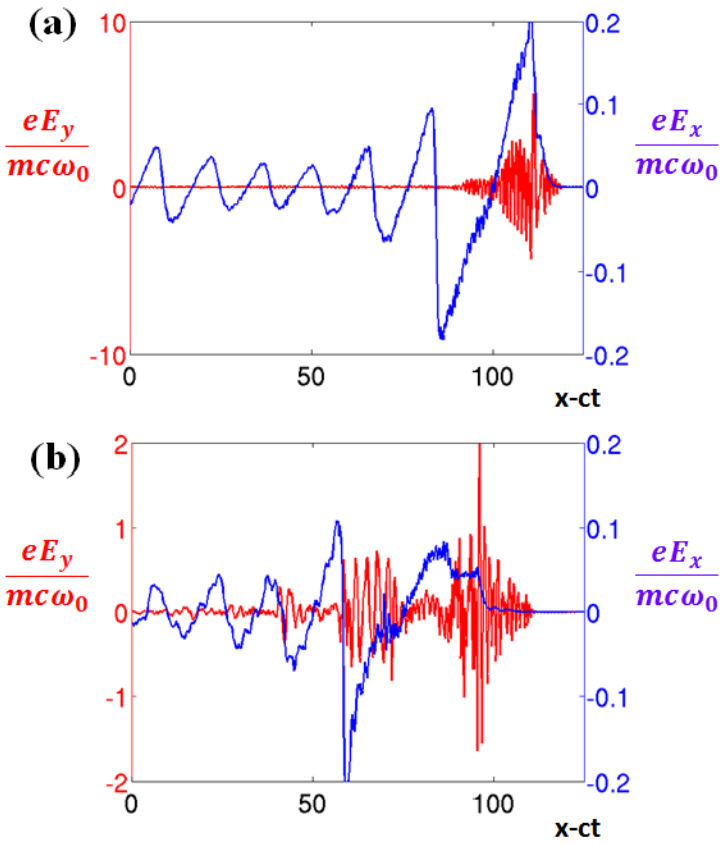

Figure 5.8: On-axis lineout of the longitudinal electric field (black curve) and transverse electric field (blue curve) as a function of the propagation distance for: (a) t=4 ps, at a propagation distance of L=1.2 mm (top picture) and (b) for time t=9 ps, at a propagation distance of L=2.7 mm.

as $n_{b0}/n_e \simeq 7$. Some values estimated at different times during propagation can be found in Table 5.1.

Table 5.1: Estimates of FWHM radius σ_x and σ_r along longitudinal and transverse directions for different times, and leading electron bunch density estimates n_{b0}/n_e.

Time (ps)	L (mm)	$k_p\sigma_x$	$k_p\sigma_r$	n_{b0}/n_e
8	2.4	2.3	0.6	7
10.5	3.1	1.9	0.47	4.5
12	3.6	0.94	0.66	3
12.5	3.8	0.8	0.8	2

The electron bunch will be able to excite a nonlinear plasma wake if the bunch length is approximately the same order as the plasma period, e.g. $k_p\sigma_x \leq 1$ according to the theory developped by Lu *et al* [106]. As we can see, after more than 2.4 mm of propagation, when the laser is fully depleted, this condition is satisfied. Also, the transverse gradient in the bunch profile is always such that $k_p\sigma_r << 1$, and the bunch density is such that $1 < n_{b0}/n_e < 10$. According to linear theory[106], which is valid for narrow short electron beams such that $k_p\sigma_r << 1$ and $n_{b0}/n_e < 10$, the accelerating field in the blow-out regime is maximized for $k_p\sigma_x \simeq \sqrt{2}$ and is given by:

$$\frac{eE_x}{mc\omega_0} \equiv \sqrt{\frac{n_e}{n_c}} 1.3 \frac{n_{b0}}{n_e} k_p^2 \sigma_r^2 \ln \frac{1}{k_p\sigma_r} \tag{5.3}$$

Using the estimates from above, we can find that once we enter into the regime of PWFA, the theoretical value of maximum field is given by $\frac{eE_x}{mc\omega_0} \approx 0.12$, which is close to results from PIC simulation as we can seen on Fig.5.8(b).

During the PWFA regime, as observed on Fig.5.7(b), the transverse shape of the bubble has changed and the radius around the leading bunch is not the same as the radius in the middle, which is a typical behavior of the PWFA regime. In the blow-out regime of PWFA, the blow-out radius is no longer given by the matching with the laser driver $k_pR \simeq 2\sqrt{a_0}$, but in this case it is given by [106]

$k_p R_{th} \simeq 2\sqrt{\frac{n_{b0}}{ne}}(k_p\sigma_r) \equiv 2\sqrt{\Lambda}$, where Λ is the normalized charge per unit length. Based on the values in Table 5.1, we can estimate the theoretical values for the bubble radius in the PWFA regime for two different times: at t=8 ps (L=2.4 mm), we find $R_{th} \simeq 8.5\lambda_0$, and at t=12 ps (L=3.6 mm) $R_{th} \simeq 6\lambda_0$. In Fig.5.9(a) and (b) the transverse cross-section of the electron density is illustrated for two different times: for t=4 ps in the LWFA regime and for t=12 ps in the PWFA regime, and we can see that despite the fact that the bubble is maintained, its radius decreases. In Fig.5.9(c) is illustrated a line-out of the cross-section of the electron density (here normalized to background density) for different times corresponding to (i) the LWFA regime (L=1.2 mm), (ii) the beginning of the PWFA regime (L=2.4 mm) and (iii) later in time during the PWFA regime (L=3.6 mm). The observed values of the bubble radius at these times in the LWFA and PWFA regimes are consistent with theoretical predictions, based on the amplitude a_0 for the first case, and the estimates given above for the second case depending on the radius and density of the leading bunch.

As can be seen in Fig.5.8 and discussed previously, the laser pulse at this time is fully depleted and is strongly distorted from its initial shape. It is modified by self-phase modulation, resulting in pulse steepening and pulse compression and is also subject to a frequency red-shifting. The density variations in an accelerating structure, in particular in the central region between the driving bunch and the beam load where electron density is decreasing provide a dynamic dielectric response resulting in the red-shifting of the laser light frequency [131]. This longer wavelength can be seen in Fig.5.8(b) but appears to be separated from the front of the pulse. This is due to the bunch of electrons injected inside the bubble driven in the PWFA regime (Fig.5.7(a)). Indeed, this longer wavelength of the laser can be estimated to be around $\lambda_0' \simeq 3\lambda_0$, resulting in a critical density around $n_c' \simeq 2 \times 10^{20} cm^{-3}$, while the bunch of

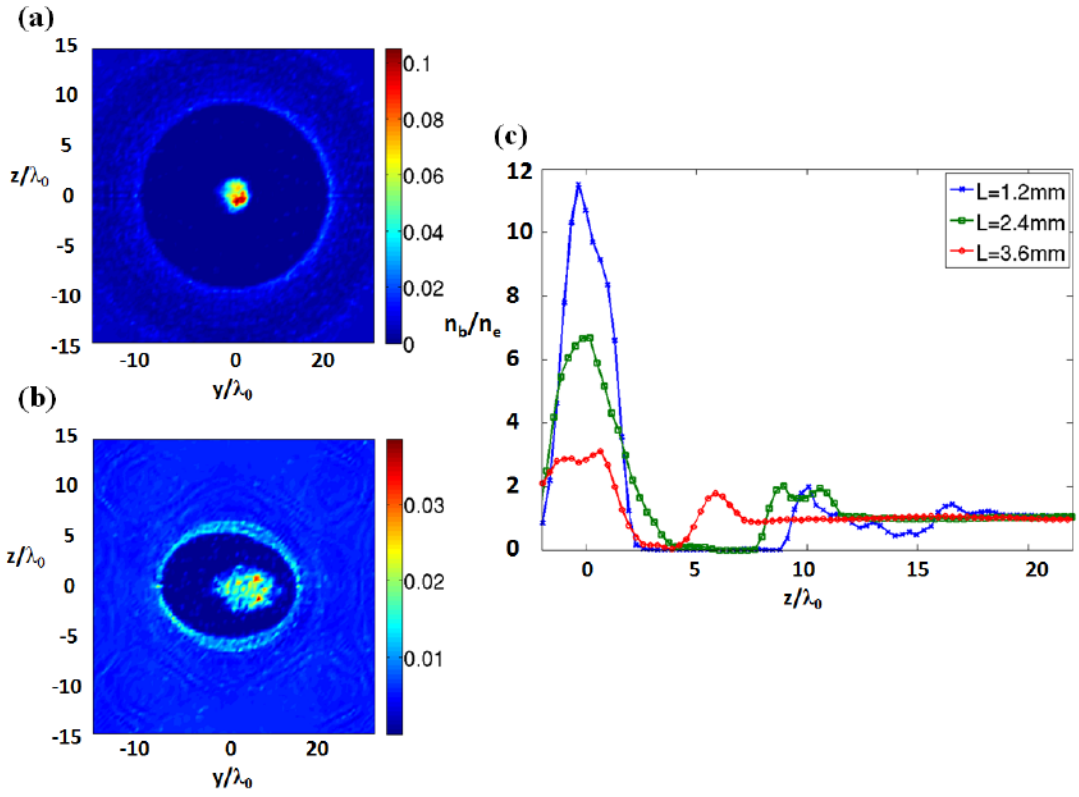

Figure 5.9: (a) and (b) Transverse cross-section of electron density, taken in the middle of the bubble in the longitudinal direction, in the LWFA regime (t=4 ps, at a propagation distance of L=1.2 mm) and in PWFA regime (t=12ps, at a propagation distance of L=3.6 mm). (c) line-out of the electron density (normalized to the background density n_e) along the transverse direction for different propagation distances $L = [1.2; 2.4; 3.6]mm$.

injected electrons inside the bubble as can be seen in Fig.5.7(a) may have a density around $n_e \simeq 1.8 \times 10^{20} cm^{-3}$ ($0.1n_c$ defined at $\lambda_0 = 0.8\mu m$). Consequently, this bunch of electrons will be overcritical for the longer wavelength of the laser resulting in a 'trapped' radiation pulse separated from the front of the pulse as can be seen in Fig.5.8(b).

The time sequence of the electron normalized momentum p_z/mc for 4 different times during the PWFA regime, showing the growth in energy of the

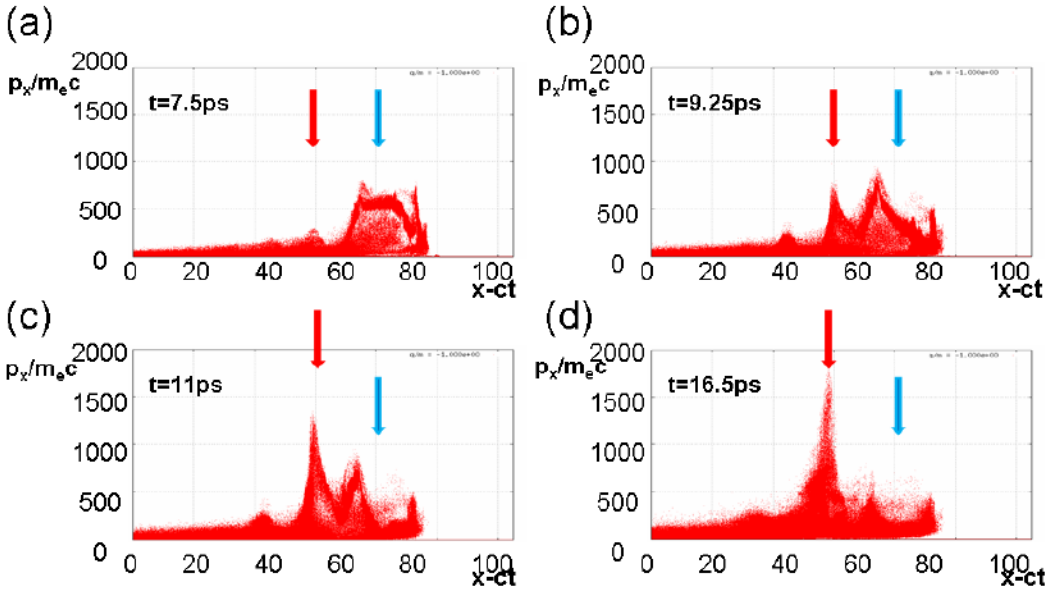

Figure 5.10: Time sequence of the electron normalized momentum p_z/mc for 4 different times during the PWFA regime, showing the growth in energy of the secondary bunch as well as the decrease in energy of the leading bunch. Pictures are for the following times: (a) t=7.5 ps, (b) t=9.25 ps, (c) t=11 ps, (d) t=16.5 ps.

secondary bunch as well as the decrease in energy of the leading bunch is illustrated in Fig.5.10. Once we enter in the PWFA regime, the secondary bunch of electrons (indicated by the red arrow), already accelerated by the laser in the LWFA regime to almost 150 MeV, is then accelerated during the PWFA regime. At the same time, the leading bunch (indicated by the blue arrow) driving the bubble is losing energy.

At late time, electrons that are accelerated will finally obtain $\gamma \simeq 1500$ or almost 750MeV. As can be seen on Fig.5.11, showing the distribution function dN/dE, the boosting effect due to the transition to PWFA is apparent. Initially, in the LWFA regime, the energy of the injected electrons can be esti-

mated from the scaling law as shown in Eqn.5.1. This gives for our parameters a maximum electron energy around $E \simeq 270MeV$, which is close to what we obtain in the LWFA regime (blue dashed curve in Fig.5.11). Nevertheless, the boosting effect due to the transition to PWFA, while the laser is depleted, can clearly be observed and will accelerate some electrons up to 750 MeV, with an estimated charge around 8 pC for a peak energy of $700 \pm 100MeV$. In our simulations, with the resolution we were able to use, we have not been able to reproduce the experimental GeV level. To obtain a more realistic simulation of the experimental observations, a better resolution (in terms of number of particles) will be needed, because only a small number of electrons will be accelerated to this level. Also, small variations in the density of the plasma could change the initial laser propagation and consequently the injection/acceleration process during LWFA, and thus the evolution of the leading electron bunch. Changing the density of the bunch will result in a different PWFA regime, and could increase the maximum energy obtained in the simulation. In other words, the physical mechanism that can explain the high energies (larger than scaling due to LWFA in bubble regime) identified in our simulation, appears to be very sensitive to the characteristics of the first injected bunch during LWFA.

Finally, the PWFA stage finishes and the acceleration of electrons stops, when the leading bunch of electrons outrun the rest of the laser field. The electrons end up oscillating in the small, but still present laser field, and won't be able to sustain the bubble anymore, which stops the acceleration in the PWFA regime. Because of these oscillations in the laser field, the electrons from the leading bunch transfer this oscillatory motion to the entire bubble, which is oscillating transversely, as we can see in Fig.5.12, showing the normalized distribution dN/dE as function of the angle θ defined as $\theta \equiv p_y/p_x$, and the γ factor. We can only see oscillations of the bubble in the plane of polarization of the laser (here along y) and nothing can be seen in the z-plane, which clearly indicates that this is oscillation of the leading bunch in the laser field

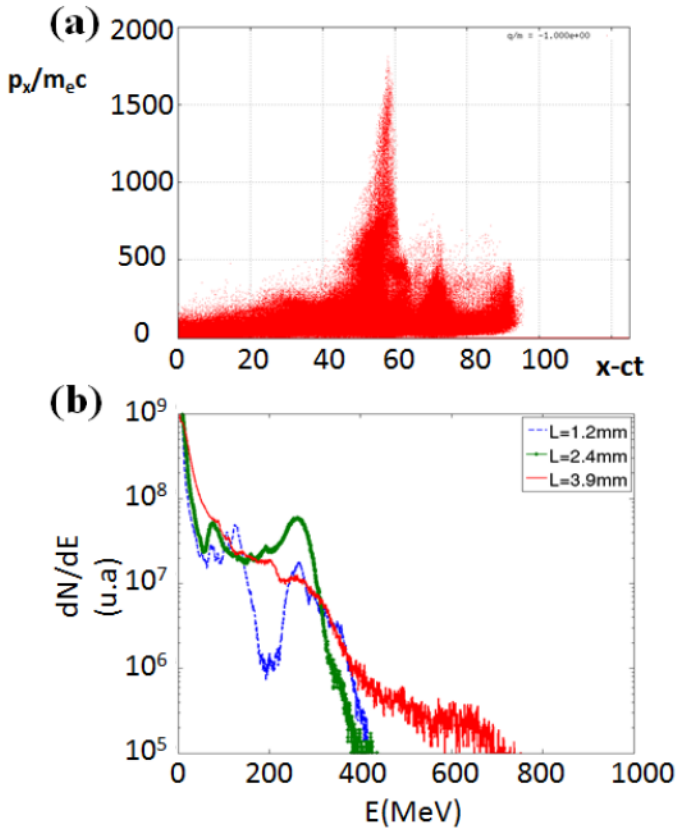

Figure 5.11: (a) Electron normalized momentum p_x/mc after a propagation distance of L=4.3mm and (b) distribution function of electrons dN/dE as a function of energy in MeV for three propagation distance corresponding to the LWFA regime (1.2 mm), beginning of PWFA (2.4 mm) and later in PWFA regime (3.9 mm).

which creates these large oscillations of the entire cavity. These oscillations of the accelerating cavity lead to acceleration of electrons off-axis, resulting in betatron oscillations inside the bubble of these accelerated electrons [61, 62, 132, 133, 134, 135].

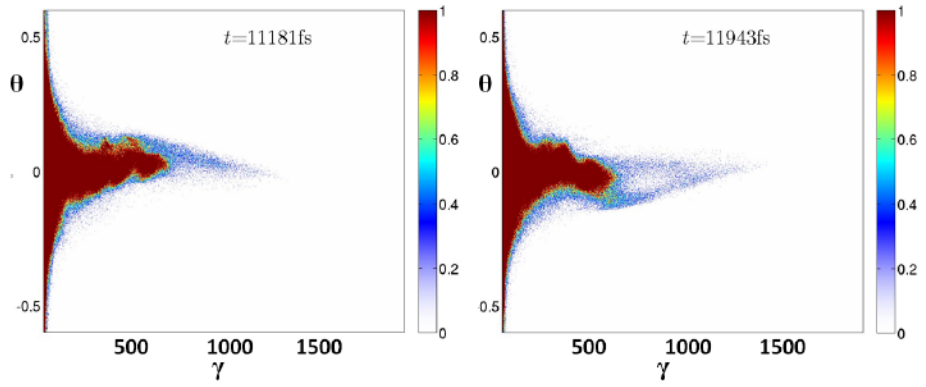

Figure 5.12: Normalized distribution of electrons as a function of energy (γ factor), and the angle θ (in radians) defined as $\theta \equiv p_y/p_x$ for two different propagation distances L=3.3 mm (left) and L=3.5 mm showing the large transverse oscillations.

5.5 Discussion

We now discuss the generation of the GeV electrons in Helium. This high level of energy, which is in disagreement with bubble wakefield scaling laws, can now be explained in view of the analysis using 3D PIC simulations by means of a two-stage process where an initial laser wakefield acceleration regime is followed by a plasma wakefield acceleration regime. The experimental observations are consistent with a number of signatures of this two step process which can be derived both from the analytical scaling laws and from the 3D simulation results presented.

Firstly, the pump depletion length is expected to be of the order of 2 mm, much less than the length of the gas jet. At the densities of the current exper-

iments, 10^{19} cm^{-3} the depletion of the laser pump beam occurs quite rapidly and there is not enough laser power to drive the acceleration of the bubble across the full length of the gas jet. Indeed this can be seen when looking at the side scattered light from the interaction process which is only observed of over the first 1 to 2 mm of the interaction process as shown in Fig. 5.4. In addition, the dephasing length for the LWFA process is similar, of the order of 2 mm, and thus even if the laser pulse were not depleted the electrons would start to dephase and lose energy at this point. However, if the electron bunch has a large enough charge it will start to perturb the bubble field (beam loading) and as the laser pulse dies it will take over as the driver of the bubble. During the transition from laser driven to electron driven bubble the perturbation in the bubble shape and plasma dynamics can potentially aid in the injection of a second electron bunch.

Once a secondary bunch of electrons is injected into the tail of the cavity it can then be accelerated throughout the remaining length of the gas jet system to energies which are much higher than those of the driving electron bunch as has already been observed in pure plasma wakefield accelerator experiments. From the 3D PIC simulation it is observed that the second bunch reaches an energy of approximately double that of the driving electrons. Because there is no longer a dephasing length limit the resultant energy could in principle be even greater than this, depending on the stength of the charge of the driving bunch and the length of interaction distance available. In the simulations of Pae et al.[114] it appears that in the case where the electron density was slightly lower, 7×10^{18} cm^{-3}, the primary bunch of electron only had a charge of 200 pC and only led to acceleration of the secondary bunch up to 320 MeV, a similar energy to that of the primary bunch. In the present simulation the larger charge in the primary bunch, of the order of 1nC, allowed for the much stronger acceleration of the secondary bunch up to double the driver electron energy.

As the primary electron bunch overtakes the laser pulse, the oscillatory EM field of the laser pulse is still sufficient to penetrate into the cavity and start to perturb the secondary acceleration process. The laser pulse at this point is strongly distorted due to self phase modulation and self steepening. As can be seen in Fig.5.8(b) the leading edge is compressed while the tail of the pulse stretched to a lower frequency of approximately 1/3 of the initial frequency. Due to this redshift, the radiation is now trapped within the tail region of the bubble because of its much lower critical density. This residual field has the effect of inducing transverse oscillations in the bubble structure and in the secondary electron bunch which in turn could lead to betatron oscillations and enhanced betatron emission. At the same time it perturbs the acceleration process and leads to a termination of the strong acceleration phase.

From the above, one would conclude that the combined LWFA/PWFA process requires a number of conditions in order to lead to effective enhancement of the electron energies above those obtained by pure LWFA in a similar system. Firstly, a large charge bunch of primary electrons must be produced in order to drive the secondary PWFA process. This requires good injection and fairly high electron density in order to create such a bunch. It would be expected that this charge bunch should be of the order of charge that would cause significant beam loading effects since this bunch eventually should create a field strong enough to take over driving the wakefield bubble by itself. Secondly, the pump depletion length should be approximately equal to the dephasing length so that just as the pump starts to fade away the primary electron bunch reaches the front of the bubble to start driving the wake itself. These lengths should be significantly shorter than the gas jet length in order for the subsequent plasma wakefield process to be effective in accelerating a secondary bunch of electrons. Both of these conditions would indicate that the observation of significant PWFA acceleration would require higher density plasmas setting a lower density limit for observing significant enhancements. Indeed, looking at the experimental

results shown in Fig.5.3 it appears that the enhancements are seen for electron densities above approximately $8 \times 10^{19}\ cm^{-3}$. On the other hand as one goes to much higher densities the initial wakefield acceleration process no longer would produce distinct electron bunches and would lead to the heating of a broad distribution of electron energies instead, thus dispersing the primary electron bunch and reducing its effectiveness in driving the PWFA acceleration process. This is compounded by the fact that as the density increases, an even higher charge density will be required to effectively drive the process in the higher density plasma. At the same time, at the higher densities the initial peak electron energy reduces with density and thus the boosted electron energies will also drop accordingly. Thus, one might expect that the combined process becomes less effective at higher densities. These two conditions lead to a window of densities where one could obtain the maximum boosted energies for a given laser power, wavelength and focal geometry. In our case as can be seen from Fig.5.3 it appears that this density range is approximately $8 \times 10^{18}\ cm^{-3}$ to $2 \times 10^{19}\ cm^{-3}$.

5.6 Conclusion

In this chapter, we have presented experimental results of wakefield acceleration, showing the generation of GeV electrons in Helium. These high electron energies, which are approximately double those from analytical laser bubble wakefield scaling laws can be understood as a laser wakefield process followed by a plasma wakefield process. The characteristics of this two stage process are clearly identified in the 3D PIC simulations under conditions similar to those of the experiment. The key components of the process include the creation of a large primary electron charge bunch, a pump depletion length approximately equal to the dephasing length so that the primary bunch can take over driving the plasma wake just as the laser pulse loses its driving strength and suffi-

cient remaining plasma length for the plasma wakefield acceleration to boost a second bunch of electrons up to GeV energies. These conditions can be met within a range of densities which in the case of the current experiment is approximately in the range of $8 \times 10^{18}\ cm^{-3}$ to $2 \times 10^{19}\ cm^{-3}$. The present results indicate that attainment of energies approximately double those from LWFA alone can be achievable under well controlled conditions. Clearly, further work is required both experimentally and theoretically to understand the detailed characteristics of this two stage process.

Chapter 6

Quasimonoenergetic electron beams from laser wakefield acceleration in pure nitrogen*

Quasimonoenergetic electron beams with maximum energy > 0.5 GeV and 2 mrad divergence have been generated in pure nitrogen gas via wakefield acceleration with 80 TW, 30 fs laser pulses. Long low energy tail features were typically observed due to continuous ionization injection. The measured peak electron energy decreased with the plasma density, agreeing with the predicted scaling for electrons. The experiments showed a threshold electron density of 3×10^{18} cm^{-3} for self-trapping. Our experiments suggest that pure Nitrogen is a potential candidate gas to achieve GeV monoenergetic electrons using the ionization induced injection scheme for laser wakefield acceleration.

*The contents of this chapter have been published in the article: M.Z. Mo, et al., Appl. Phys. Lett. **100**, 074101 (2012).

6.1 Introduction

The proposal of laser driven electron acceleration [6] and invention of the chirped pulse amplification [136] have enabled the development of compact laser based accelerators. In the past few years, significant advances have been made in laser driven plasma based accelerators with accelerating gradients exceeding 100 GeV/m [20, 45, 46, 47]. Experiments with electron energies of near and over 1 GeV have been reported to date using gas jets,[39, 46, 47, 48] gas cells [48, 20] and capillary discharge waveguides.[45] In the traditional self injection Laser Wakefield Acceleration(LWFA) scheme, pure helium gas has generally been used as interaction medium for self-injection with lower densities used to extend the dephasing length distance over which acceleration occurs to gain higher electron energies. In self-injection LWFA using gas-jet targets [39, 46, 47, 48] the energy of electrons was limited by dephasing length to the range of 0.7 to 1 GeV. Longer interaction lengths using even lower densities can be obtained using capillary discharge waveguides to accelerate high quality electron pulses with energies of up to and over 1 GeV [45].

Recently, ionization induced injection [137, 138] has been introduced by mixing controlled amounts of N_2 [31, 42] or CO_2 [20] with He to produce electron bunches with acceleration close to the maximum dephasing length to give electron energies up to 1.45 GeV [20], with increase in charge and decrease in divergence [31] as compared to self injection conditions. Experiments and simulations [42] demonstrate that ionization induced injection has a lower intensity threshold $a_0 \sim 2$, where $a_0 = (eE)/(m\omega c)$ with e the electron charge, E the electric field, m the electron mass, ω the angular frequency and c the light speed, as compared to self injection which requires higher laser intensity of the order of $a_0 \geq 4$ [38].

The addition of higher Z gases is capable of generating electron beams with high charge and low emittance required for applications such as x-ray genera-

tion through compton scattering [139] or betatron oscillation [140]. However, the use of higher Z gases for wakefield acceleration has not been extensively explored due to the expectation that ionization induced defocussing will compete with the relativistic self focusing required for wakefield acceleration.[141] A few experiments [79, 142, 143, 144] have reported quasimonoenergetic electron beams in the range of 7 to 50 MeV using $\sim 2-10$ TW laser pulses focused on pure nitrogen gas-jets. Recent PIC simulations have predicted that quasi-continuous, low divergence monoenergetic electron beams with peak energy in the range of 10 MeV can be generated by using ultra-short, KHz repetition rate mJ laser pulses [145], and quasimonoenergetic collimated GeV electrons can be produced by focusing into pure Nitrogen gas and using ionization injection [146]. Thus it is of interest to study wakefield acceleration in pure N_2 under self-injection condition. These previous results have motivated the current experimental investigations of ionization induced injection in pure Nitrogen for LWFA at higher laser powers.

In this chapter we report that pure nitrogen can be used to excite a uniform plasma to accelerate electrons over 0.5 GeV in the ionization injection regime using 80 TW laser pulses.

6.2 Experimental Setup

The experiments were carried out at the Canadian Advanced Laser Light Source(ALLS) facility located at INRS, Varennes [85] and the experimental setup was similar to the one shown in Fig.5.1. A linearly-polarized 800nm laser pulse with an energy of 2.4 J and pulse duration of 30 fs at full-width half-maximum (FWHM) is focused onto a supersonic gas jet target. The 9-cm-diameter laser pulses were focused by a 150 cm focal length off-axis parabola (OAP) onto the nitrogen gas target. The FWHM of the focal spot was measured to be 20 μm. The energies contained in the spot diameters of 20 μm, 40

μm and 60 μm are 20%, 36% and 72% of the total energy respectively. The Rayleigh range based on the $1/e^2$ intensity radius of $w_0 = 17\mu m$, $Z_r = \pi w_0^2/\lambda$, is estimated to be around 1 mm, where λ is the vacuum wavelength. The focused peak laser intensity and the corresponding normalized vector potential, a_0, are around 7.2×10^{18} W/cm^2 and 1.8 respectively in our experiments. Generated electron beams were dispersed by two separate 10-cm-long dipole magnets with magnetic field strengths of 1.12 T and 0.84 T onto a Lanex screen placed 20 cm away. The fluorescence emitted from the Lanex screen was collected by an f/2.8 aperture lens system and imaged onto a 12 bit charge coupled device(CCD) camera.

The gas jet was formed from an 1-cm-diameter supersonic conical nozzle fed from a pulsed solenoid valve (Parker Valve). Assuming the charge state of Nitrogen is 5+ [141], the electron density is estimated to range from 2.2×10^{18} cm^{-3} to 1.1×10^{19} cm^{-3} for backing pressures of the jet from 200 to 1000 Psi.

6.3 Experimental results and discussions

Fig.6.1.a shows typical quasimonoenergetic electron images obtained at different plasma densities. The electron energy is dispersed in the horizontal direction while the vertical profile shows the lateral deflection and divergence of the electron beams. Fig.6.1.b presents the corresponding lineouts of the electron images , which have been deconvolved to give electron number per MeV. Note that the bright features visible at the highest energy as seen in Fig.6.1.a manifest themselves as peaks in Fig.6.1.b. Also observed are the long lower energy tails following the high energy peaks, indicating the continuous injection and the acceleration of liberated K-shell electrons from Nitrogen. Such electron bunches with long-tail features occurred in 55% of the total shots where electrons were observed, whereas the rest are broad electron clouds with

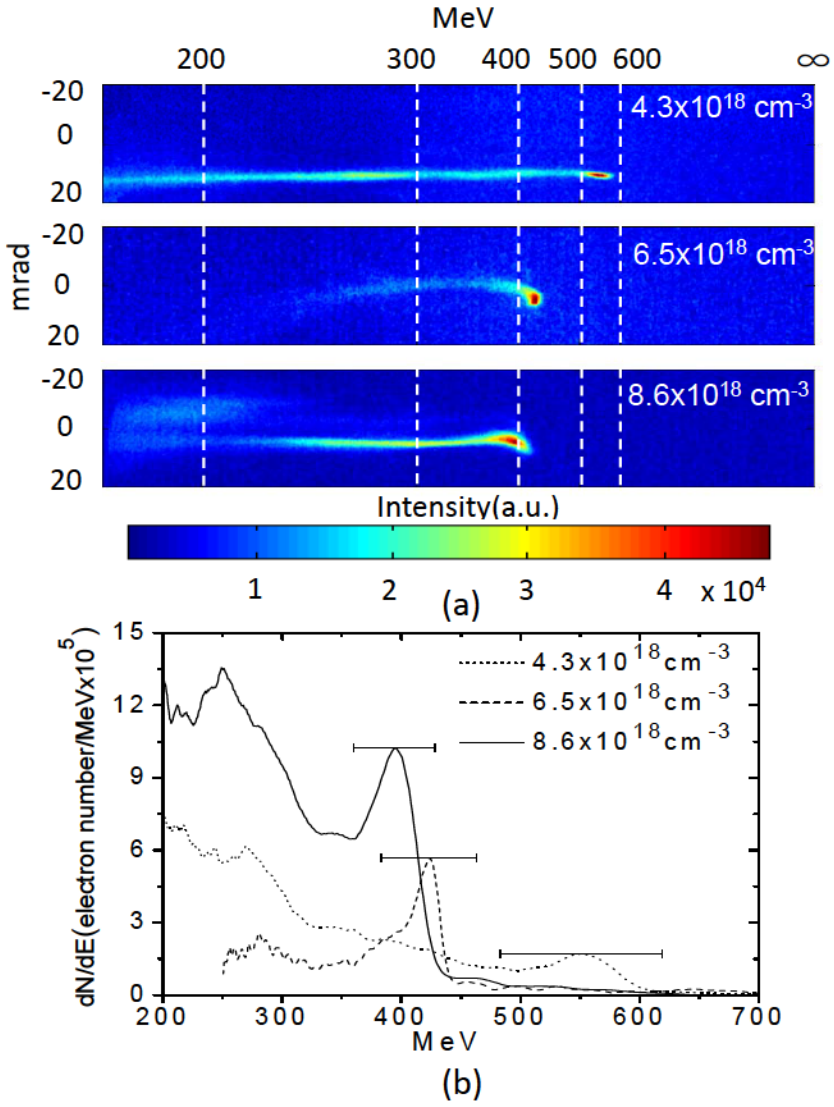

Figure 6.1: (a) Typical images of quasimonoenergetic electron bunches generated from pure Nitrogen at different electron densities. From top to bottom, $n_e = 4.3 \times 10^{18}\ cm^{-3}$, $6.5 \times 10^{18}\ cm^{-3}$ and $8.6 \times 10^{18}\ cm^{-3}$ respectively. (b) Corresponding electron number density per MeV.

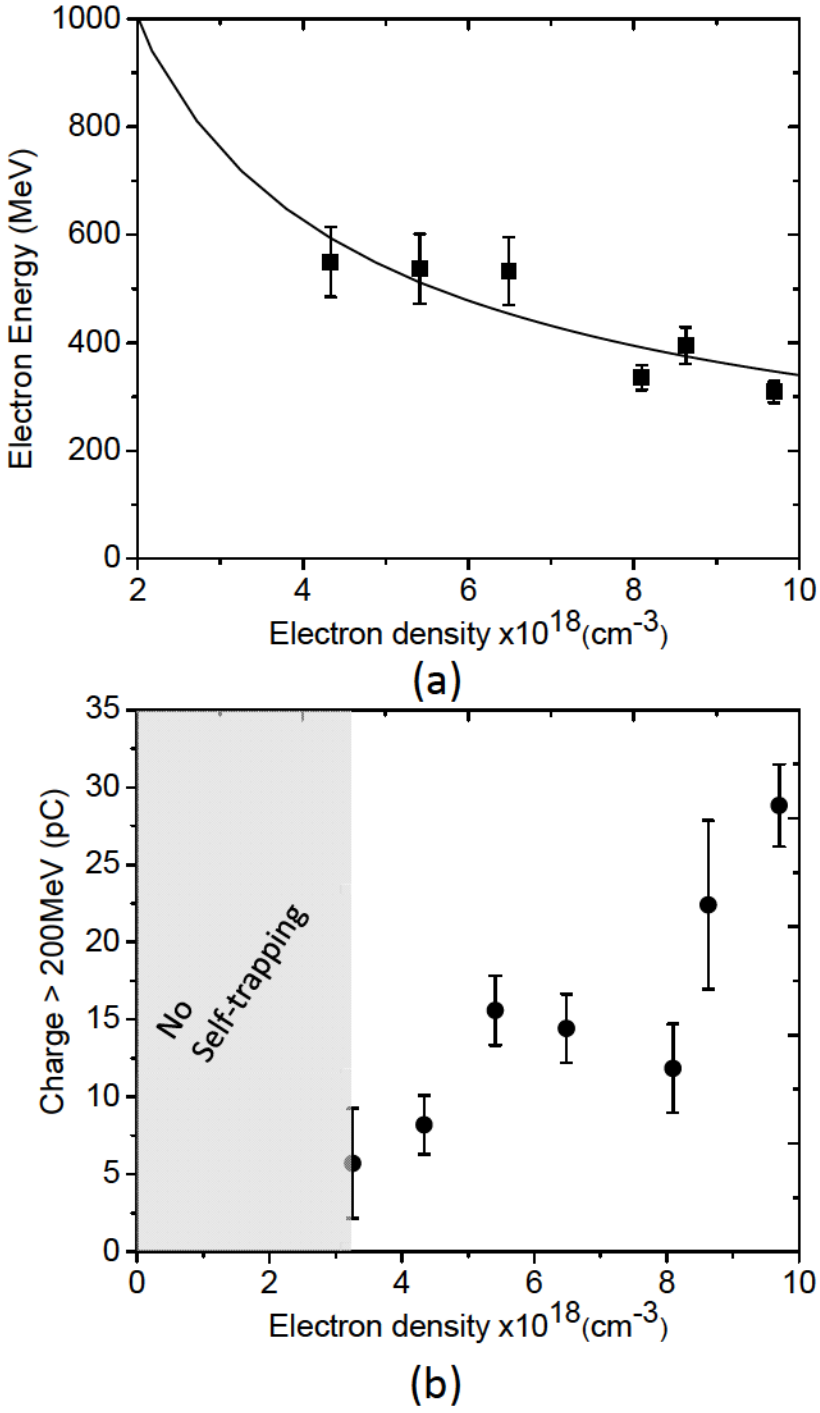

Figure 6.2: (a) Energy of the quasimonoenergetic electron peak as a function of the electron density. Solid squares stand for the measured peak electron energies, while the solid curve represents the predicted maximum electron energy versus density for a given laser power of 80 TW using Lu's scaling law as shown in Eqn.7.1. (b) Measured charge of electrons with energies > 200 MeV versus the electron densities. Below a threshold of $n_e = 3.3 \times 10^{18} cm^{-3}$, no electrons were accelerated to above 200 MeV, which is indicated by the shaded area.

random lateral distributions. Similar features were also reported in Ref. [42], where a mixture of He and N_2 (9:1) was used as the gas target. As shown in Fig.6.1, the maximum peak electron energy of 550 ± 70 MeV was measured at $n_e = 4.3 \times 10^{18}\ cm^{-3}$, with an $1/e^2$ divergence angle of 2 ± 0.1 mrad. The error bar of the energy was estimated based on the standard deviation of the positions of the straight through reference shots when both magnets were removed. Measurements show that around 20% of total shots observing electrons gave such quasimonoenergetic electron peaks with energy greater than 400 MeV.

Fig.6.2.a shows the maximum peak electron energies that were measured over a range of plasma densities. Note that the measured electron energy decreases with the plasma density, which agrees with the dephasing length becoming shorter and overall acceleration less with increasing the density. The observed trend agrees with the predicted maximum energy gain of electron, which is given by [34] $E_{max}(GeV) = 1.7(P/100TW)^{1/3}(n_e/10^{18}cm^{-3})^{-2/3}$.

Fig.6.2.b shows the total charge of electrons with energies greater than 200 MeV as a function of electron density. The charge here was calculated by taking the average of all shots that showed electron signals above 200 MeV at the same gas density. The calculated charge is based on the manufacturer's specifications for the camera response and the imaging system optical efficiency. It is estimated that the accuracy of this estimate is within a factor of 2. The charge drops from 28 pC to 5 pC as the electron density is reduced from $1 \times 10^{19}\ cm^{-3}$ to $3 \times 10^{18}\ cm^{-3}$, below which no electrons were seen on the Lanex screen above 200 MeV. The observation of such a minimum threshold density for $>$ 100 MeV electrons has previously been reported for helium [48]. Averaging over all the shots at different densities gives a mean beam charge of 15 pC for electron energy $>$ 200 MeV. Assuming a mean electron energy of 350 MeV, the conversion efficiency from laser to the fast electrons is on the order of 2×10^{-3}.

The observed density threshold for the self injection and trapping could be explained by the combination of self-focusing and ionization induced injection.

The required long acceleration lengths, several Rayleigh lengths, is achieved by relativistic self-focusing of the propagation beam. Stable self guiding is achieved when the laser spot size is matched to the bubble radius, R_b, by the approximate relation: $w_0 \sim R_b = 2\sqrt{a_0}/k_p \propto n_e^{-1/2}$, where w_0 is the gaussian laser e-folding field amplitude spot radius and k_p is the propagation constant of the plasma wave. [34] As the plasma density decreases, the bubble increases in size and eventually exceeds the laser spot size in the case of low density, thus violating the optimum guiding condition. Because of the large difference in ionization potential between K-shell electrons (552 eV and 667 eV for N^{6+} and N^{7+} respectively, requiring $I_L \sim 10^{19}\ W/cm^{-2}$ to ionize) and L-shell electrons (98 eV for N^{5+}, requiring $I_L \sim 2\times10^{16}\ W/cm^{-2}$ to ionize), the L-shell electrons are preionized by the leading front of the laser pulse and form the electron sheath of the bubble, whereas the K-shell electrons are produced at the peak of the laser pulse and circulate around to the inside back edge of the bubble, resulting in electron trapping and acceleration inside the bubble. For the case of low density, the larger bubble and beam size result in a laser intensity that is too low to ionize the K-shell electrons, thus turning off the ionization-injection.

6.4 Conclusion

In conclusion, the experiments have demonstrated that quasimonoenergetic electron beams with peak energies > 0.5 GeV and divergence as low as 2 mrad can be achieved with a 1-cm-long pure nitrogen gas jet at a plasma density of $4.3 \times 10^{18}\ cm^{-3}$. Long-tail features were also observed in the electron beams due to continuous injection. The measured peak electron energy decreased with the increasing plasma density, which agrees with the predicted maximum energy gain scaling for electrons. Experiments also show a threshold density of $3 \times 10^{18}\ cm^{-3}$ for self-trapping. Our experiments suggest that by using higher laser power and lower densities, pure Nitrogen is a potential candidate gas to

achieve GeV level monoenergetic electrons in the ionization induced trapping scheme for laser wakefield acceleration.

Chapter 7

Generation of 500 MeV - 1 GeV Energy Electrons from Laser Wakefield Acceleration via Ionization Induced Injection using CO_2 mixed in He*

Laser wakefield acceleration of 500 MeV to 1 GeV electron bunches is demonstrated using ionization injection in mixtures of 4 to 10% of CO_2 in He. 80 TW laser pulses were propagated through 5 mm gas jet targets at electron densities of $0.4 - 1.5 \times 10^{19}\ cm^{-3}$. Ionization injection led to lower density thresholds, a higher total electron charge and an increased probability of producing electrons above 500 MeV in energy compared to self-injection in He gas alone. Electrons with GeV energies were also observed on a few shots and is indicative of an additional energy enhancement mechanism.

*The contents of this chapter have been published in the article: M.Z. Mo, et al., Appl. Phys. Lett. **102**, 134102 (2013).

7.1 Introduction

Laser wakefield acceleration (LWFA) [6] is a promising approach to realize table-top accelerators because of the extremely high accelerating gradients which can be achieved. In LWFA, an ultra-intense laser is applied to drive an underdense plasma, creating a positively charged wake or 'bubble' due to the fact that electrons are expelled from the beam axis by the ponderomotive force of the laser and form an electron sheath surrounding the immobile ions. Electrons will be injected into the bubble if they gain sufficient energy to catch up with the bubble before they fall back on axis in the tail in the wake.[31] The injected electrons can then be accelerated by the strong electric field within the bubble until they reach the center of the bubble over a propagation distance of the dephasing length. The maximum energy gain for the electrons is simply the product of the average longitudinal electric field inside the wake and the dephasing length, which is given by Lu's scaling law [34]:

$$E_{max}(GeV) \cong 1.7(P/100TW)^{1/3}(10^{18}cm^{-3}/n_e)^{2/3} \tag{7.1}$$

where P is laser power and n_e is plasma density. To ensure the maximum electric field needed for generating these energetic electrons, stable laser self-guiding inside the plasma is required, which can be satisfied once the laser spot size is matched to the bubble radius, R_b, by the approximate relation:[34] $w_0 \sim R_b = 2\sqrt{a_0}/k_p \propto n_e^{-1/2}$, where w_0 is the gaussian laser e-folding field amplitude spot radius, $k_p = 2\pi/\lambda_p$ where λ_p is plasma wavelength, $a_0 = (eE)/(m\omega c)$ with e the electron charge, E the electric field, m the electron mass, ω the laser angular frequency and c the speed of light.

The injection process into the wakefield bubble to some extent determines the charge, divergence, energy gain as well as the energy distribution of the accelerated electrons. Traditionally, self injection using pure helium [39, 46, 47, 48, 100] or hydrogen [45] gas as the interaction medium was employed to

accelerate the electrons. However, very high laser powers or high densities are required to initiate the self injection and the energy gain is limited by dephasing length to the range of 0.7 to 1 GeV [39, 46, 47, 48]. Recently, a new technique, ionization induced injection, which takes advantage of the large ionization potential difference between the outer and inner shell electrons of trace atoms in the plasma, has been proposed and demonstrated to perform better than self-injection in a few respects, i.e. generating energetic electrons at lower threshold laser powers,[42] increasing the beam charge and reducing the beam divergence.[31] Recently, Clayton and his colleagues [20] found that, under the matched and self-guiding conditions, ionization injection can trap electrons inside the bubble with plasma density below $1.5 \times 10^{18} cm^{-3}$ using a 1.3-cm long gas cell, producing electrons with energy up to 1.45 GeV. The idea of ionization injection was also employed in a cascaded laser wakefield accelerator where the electron injection and acceleration are separated and manipulated in two different gas cells, generating near GeV quasimonoenergetic electron beams with plasma densities of approximate $5.7 \times 10^{18}\ cm^{-3}$ and $2.5 \times 10^{18}\ cm^{-3}$ in the first and second gas cell respectively.[49]

In this chapter, we investigate the ionization injection in interaction lengths shorter than 5 mm and at higher plasma densities ranging from $4 \times 10^{18}\ cm^{-3}$ to $1.5 \times 10^{19}\ cm^{-3}$ using 80 TW laser pulses. By adding 4% CO_2 into He, 300 MeV to GeV energy electron bunches were generated at higher charge density and with higher probability of obtaining electrons above 500 MeV than self injection in He alone. Such improved performance can be useful in the actual application of LWFA in electron generation and acceleration.

7.2 Experimental setup

The experiments were conducted at the Advanced Laser Light Source (ALLS) facility located at INRS, Varennes.[85] In these experiments, 800nm laser pulses

with energies of 2.4 J and pulse durations of 30 fs at full-width half-maximum (FWHM) were employed. A 150 cm focal length off-axis parabola (OAP) located inside the target vacuum chamber was used to focus the 9-cm-diameter laser pulses onto the gas target. The FWHM of the focal spot was measured to be 24 μm. The energy contained in the spot diameter of 24 μm is 30% of the total energy. The Rayleigh range based on the $1/e^2$ intensity radius of $w_0 = 20\mu m$, $Z_r = \pi w_0^2/\lambda$, is estimated to be around 1.5 mm, where λ is the vacuum wavelength. Based on the measured focal spot intensity distribution, the peak focused laser intensity and the corresponding normalized vector potential, a_0, are approximately 7.3×10^{18} W/cm^2 and 1.9 respectively in our experiments. A side-view Normarski interferometer [89] based on a Wollaston prism as the beam splitter was employed to probe the plasma formation and its density. The probe beam for the side-view interferometry was obtained by splitting the main laser pulse before compression and its path length was adjustable to obtain various delays relative to the main pulse. The gas was pulsed from a commercial Parker Valve (Model 009-181-900) connected to a 5-mm-diameter supersonic conical nozzle. The density of the plasma was calculated by use of modified Abel inversion algorithm[91, 92], where the asymmetry of the fringe shifts is weighted and introduced into the final plasma distribution, assuming a $\cos\theta$ transverse asymmetry contribution. The accuracy of the calculated density is estimated to be within $\pm 15\%$, which applies to all the density values hereafter. In order to investigate the electron generation via ionization injection, two partial pressures (4% and 10% by pressure) of CO_2 in the gas mixture were selected for the experiments.

The generated electron beams were dispersed by two separate 10-cm-long dipole magnets in series with magnetic field strengths of 1.12 T and 0.84 T onto a Lanex screen placed 20 cm beyond the exit of the second magnet. The fluorescence emitted from the Lanex film was collected by an f/2.8 aperture lens system and imaged onto a 12 bit CCD camera (Point Gray). The charge

of electrons is calculated based on the manufacturer's specifications for the camera response and the imaging system optical efficiency. It is estimated that the accuracy of this value is within a factor of 2. The uncertainty of the measured electron energy was estimated according to a shot-to-shot pointing stability of 10 mrad, which is derived based on the standard deviation of the pointing positions of reference shots when both magnets were removed. This leads to an error of (+300 MeV \ −200 MeV) at 1 GeV and significantly lower errors at smaller energies.

7.3 Experimental results and discussions

Fig.7.1 (a)-(c) show energy resolved images of the electron beams with 4% CO_2 for plasma densities of $8 \times 10^{18}\ cm^{-3}$ and $1.1 \times 10^{19}\ cm^{-3}$. The corresponding dN/dE electron energy spectra integrated over the full width for each spectral image normalized to unity is plotted in Fig.7.1 (d). Fig.7.1 (a) and (b) show the typical electron energy spectra observed at the density of $8 \times 10^{18}\ cm^{-3}$, where an isolated high energy bunch with narrow divergence and narrow energy spread is accompanied by a separate low energy tail typically with one or more peaks. These two separate bunches are of different characteristics, the high energy bunches in the two cases have peak energies of 860^{+220}_{-150} MeV and 760^{+160}_{-120} MeV, with FWHM lateral divergence of 2.8 mrad and 4.4 mrad, and total charges of 7 pC and 15 pC respectively; In the first case, the second bunch has a uniform shape but with a single peak energy at 450 MeV, and a total charge of 263 pC above 140 MeV. The lower energy tail of the second case as shown in Fig.7.1 (b) has three distinct peaks (168 MeV, 223 MeV and 311 MeV), and has a total charge of 258 pC above 140 MeV. It is possible that the observed long tail feature is due to the quasi-continuous injection via ionization of the inner K-shell of oxygen. Similar features have been previously reported [50] and also seen elsewhere [42, 48].

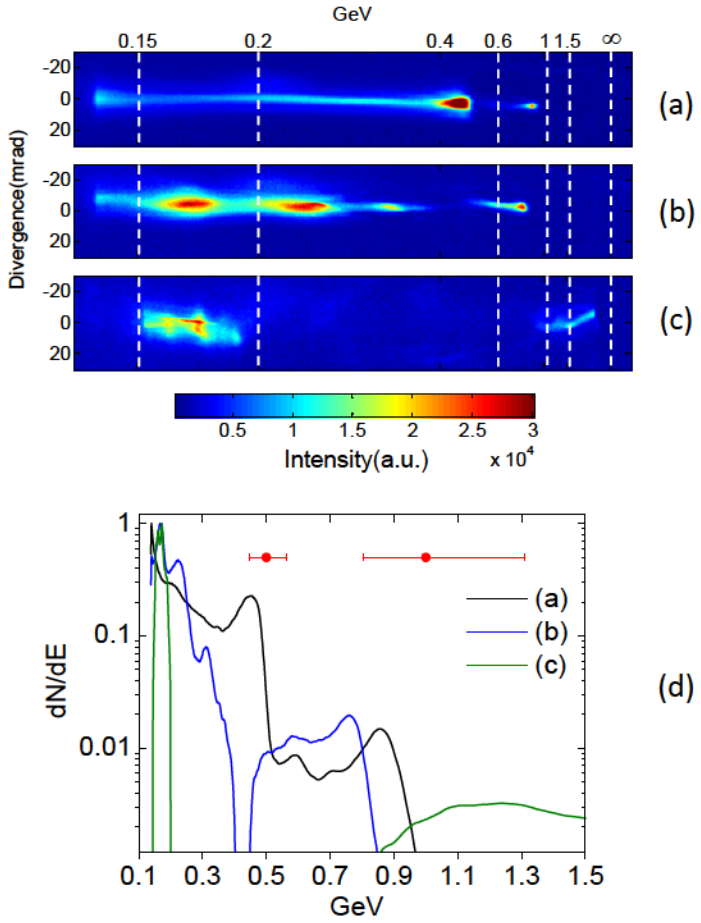

Figure 7.1: (a)-(c) Energy resolved images of the electron bunches for a ratio of 4% of CO_2 at plasma densities, (a) $8 \times 10^{18} cm^{-3}$, (b) $8 \times 10^{18} cm^{-3}$, (c) $1.1 \times 10^{19} cm^{-3}$; All the images are plotted in the same color range where the brightness represents the flux of the electrons in arbitrary units. (d) Corresponding normalized electron number density per electron energy; Note that the y axis is in logarithmic scale; Representative uncertainties of measured electron energy at 0.5 GeV and 1 GeV are indicated by the red circular spots and attached bars at the top of the plot.

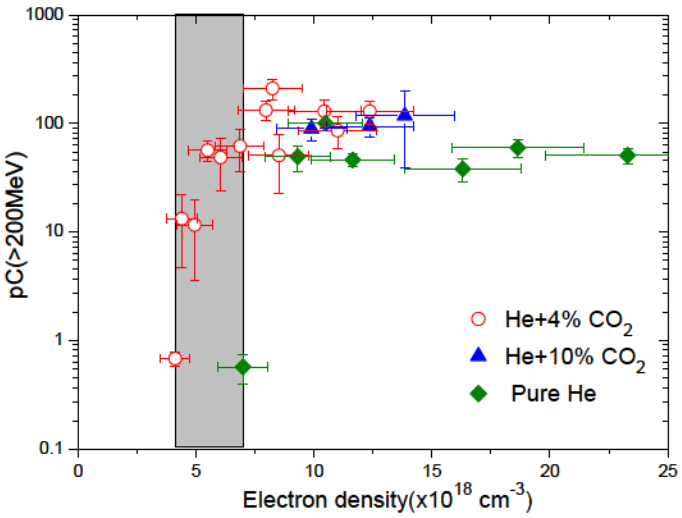

Figure 7.2: Measured charge of electrons with energy higher than 200 MeV versus the plasma density. Red empty circles are data points for the He mixed with 4% CO_2, while blue triangles for the He mixed with 10% CO_2, and green diamonds for pure He. The greyish shaded region represents the region that is below the injection threshold of 7×10^{18} cm^{-3} for pure He to the injection threshold of 4×10^{18} cm^{-3} with the addition of 4% CO_2. Note that due to the lack of data points at low enough density to observe the injection cutoff, the injection threshold for He mixed with 10% CO_2 is not determined here.

Fig.7.1 (c) depicts the electron image obtained at plasma density of 1.1×10^{19} cm^{-3}, where two widely separated bunches are observed. Note that the higher energy bunch reaches above 1 GeV and exceeds the resolution limit of 1.5 GeV of the electron spectrometer, above which electrons can't be measured accurately. The charge contained in this GeV bunch is around 10 pC, as compared to that of 74 pC for the lower energy bunch that peaks at around 170 MeV. Considering the theoretical energy gain based on Lu's peak energy scaling law, one would expect a peak electron energy of 350 MeV at the plasma density of 1.1×10^{19} cm^{-3} for a laser power of 80 TW as employed in this experiment. The observed GeV energy of the second bunch electrons as shown here is more than double of the predicted one. The physics behind this energy enhancement will be discussed later.

The total charges of electrons with energy higher than 200 MeV are plotted in Fig.7.2 as a function of the plasma density for three cases: pure He, He mixed with 4% CO_2 and He mixed with 10% CO_2. The charge here was calculated by taking the average of all shots that showed electron signals above 200 MeV at the same gas density in the same experimental day. When looking at the density thresholds for pure He and its mixture with CO_2, one finds that the addition of 4% CO_2 brings down the threshold from approximately $7 \times 10^{18}\ cm^{-3}$ to approximately $4 \times 10^{18}\ cm^{-3}$, indicating that ionization injection scheme allows wakefield acceleration in a lower density region relative to self injection, potentially providing a longer dephasing length for electrons to accelerate to higher energy. Due to the large number of electrons in each molecule of CO_2, a mixture ratio of 10% of CO_2 will double the electron density in theory relative to pure helium gas at the same pressure after being fully ionized by the ultra-intense laser. Such a high degree of ionization per atom aggravates the ionization-induced defocusing effect[42, 141, 147], leading to the failure to achieve laser wakefield acceleration at high density above $n_e \simeq 1.5 \times 10^{19}\ cm^{-3}$ for He+10% CO_2. What also can be seen from Fig.7.2 is an increase of the peak charge obtained when adding 4% CO_2 into pure He. As the density increases, the measured charge for pure helium tends to saturate at a level of approximate 50 pC. However, this number increases to $\sim$ 100 pC after mixing 4% CO_2 into the helium gas. The observation of a lower density threshold together with a higher charge saturation level reveals that ionization induced injection is advantageous in generating a large number of energetic electrons when compared with the self-injection approach. Statistics on the peak energies for all densities for both pure He and He mixed with 4% CO_2 have been compared. For an electron density range of $4 \times 10^{18}\ cm^{-3}$ to $1.5 \times 10^{19}\ cm^{-3}$, the probability of producing electrons with peak energy higher than 500 MeV with ionization injection is $\sim$ 37%, comparing to that of $\sim$ 5% for self-injection. This significant difference in probability of generating energetic electrons again illustrates the

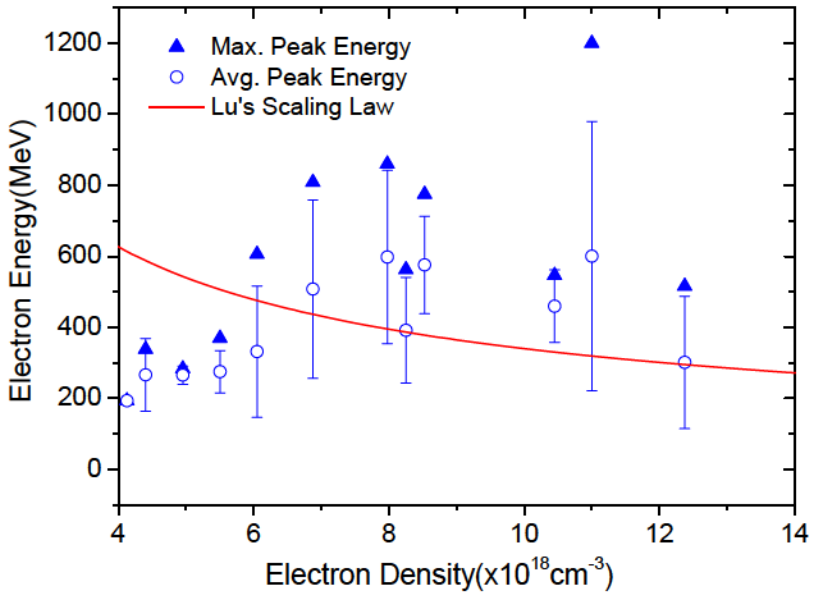

Figure 7.3: Energy of the highest energy peak in the electron distribution measured at each electron density for He mixed with 4% CO_2. The solid triangles are the single maximum achieved peak energies at each density. The empty circles are the averages of the energies of the highest energy peaks for shots at identical density, the standard deviation of which is considered as the error bar. The red line represents the predicted energies at a given laser power of 80 TW using the nonlinear scaling law given by Eqn.[7.1]

increased ease in generating more energetic electrons using ionization injection.

Fig.7.3 plots the dependence of average peak energy of electron (empty circles) versus the electron density. The maximum single peak energy (solid triangle) observed at each of the electron densities and the theoretically predicted energy scaling (red line) using the nonlinear scaling law given in Eqn.[7.1] for a given laser power of 80 TW are also plotted in the graph. The average peak energies indicate an approximate agreement with the scaling law in the density region higher than $6 \times 10^{18}\ cm^{-3}$. Below this density the scaling law predicts higher electron energies than observed. The deviation between the measurements and the predictions at low density can be explained by the fact that the matching condition is violated in that the increased optimum bubble

size at low density is larger than the self-focused laser spot size and injection is becoming more difficult with decreasing density.[47] In addition, as indicated by the observed maximum peak electron energy, at some density points such as at $n_e = 1.1 \times 10^{19}\ cm^{-3}$, as shown in Fig.7.1 (c), electrons inside the wake appear to experience enhanced wakefield acceleration leading to an energy double or more, compared with the scaling law as given by Eqn.[7.1]. This energy enhancement compared to the prediction of Eqn.[7.1] was observed with pure helium gas in similar plasma density as shown in Chapter 5 and also observed experimentally by a few other groups [46, 47]. The mechanism for this energy enhancement was identified as a transition to PWFA after the laser pulse depletion by the 3D-PIC simulations as discussed in Chapter 5.

7.4 Conclusion

In conclusion, electron bunches with average energies of the order of 500 MeV have been produced with ionization induced injection under the self-guiding condition of laser wakefield acceleration using 80 TW laser pulses. These results are in approximate agreement with the bubble wakefield scaling laws, particularly at densities above $6 \times 10^{18}\ cm^{-3}$. The use of ionization injection leads to improved performance in regards to increased electron charge, by a factor of two, lower injection threshold electron densities of $4 \times 10^{18}\ cm^{-3}$ as compared to $7 \times 10^{18}\ cm^{-3}$ and much higher probability of producing electrons above 500 MeV as compared to self injection in He gas alone under the same conditions. These results were obtained with shorter acceleration lengths and higher densities than typically reported previously. In a few shots, energies of approximately double the average values, up to the GeV energy range, were obtained indicative of some additional acceleration mechanism, which was due to a transition to PWFA after the laser pulse depletion.

Chapter 8

Characterization of Laser Wakefield Generated Betatron X-ray Radiation using Grazing Incidence Mirror Reflection*

We have developed a new approach to characterize betatron X-ray radiation that is excited by the wiggling of relativistic electrons inside laser wakefield driven cavities. This approach can measure the average critical energy, E_c, of the betatron radiation by using the reflection off a grazing incidence mirror (ROGIM). This technique relies on the reflectivity change of a high-Z-coated mirror with the grazing angle of incidence for the betatron X-rays. The average Ec measured with this approach is in agreement with the one measured with a photon-counting X-ray CCD. This approach suggests that grazing incidence mirrors coupled to X-ray detectors can be used as online monitors of E_c in betatron applications.

*The contents of this chapter have been published in the article: M.Z. Mo, et al., Eur. Phys. J. D **68**, 301 (2014).

8.1 Introduction

In the past decade, remarkable advances have been made in producing energetic electrons through the scheme of Laser Wakefield Acceleration (LFWA), which takes advantage of extremely strong electrostatic fields developed in a plasma wake following an intense laser pulse. To date, GeV-class electrons have been successfully demonstrated with the LWFA approach by a number of research groups around the world [18, 20, 45, 46, 47, 51, 115]. At the same time, the synchrotron-like Betatron X-ray radiation is emitted from the transverse oscillations of the relativistic electrons inside the plasma cavities. This X-ray emission is attracting increasing attention due to its attractive properties of femtosecond pulse duration, temporal synchronization, narrow divergence and high brightness. Thanks to these benefits, this Betatron X-ray radiation is a promising candidate to serve as an X-ray probe in investigating the structural dynamics of matter under warm dense states [148] or extreme states of temperature and pressure [149], which normally require ultrafast X-ray diagnostics.

In LWFA, an ultra-short laser pulse when focused to intensities $> 10^{18}$ W/cm^2 in a gas target creates an underdense plasma. The ultra-intense laser pulse interacts with the underdense plasma through the nonlinear ponderomotive force of the laser pulse. This force pushes the electrons away from the propagation axis forming an electron deficient region tailing the laser pulse surrounded by an electron sheath. The ions remain since they are too heavy to move. As a result, a series of ion cavities or "bubbles" traveling with a phase velocity close to the speed of light are formed behind the laser pulse. Electrons from the sheath will be dragged inward by the strong Coulomb force at the rear side of the bubble and can be drawn into the bubble if they have sufficient energy to match the speed of the bubble, a process referred to as injection. If injected off axis, the trapped electrons feel a transverse focusing force in addition to the strong longitudinal electrostatic field. Because of the transverse

focusing force, the electrons undergo Betatron oscillations while they are accelerating inside the cavity. The frequency of the Betatron oscillation is given by $\omega_\beta = \omega_p/\sqrt{2\gamma}$, where ω_p is the plasma frequency and γ is the relativistic Lorentz factor of the electron. The oscillating electrons radiate electromagnetic waves and the resulting radiation spectrum is characterized by a strength parameter given by [59], $K \simeq \gamma\theta = \gamma r_\beta \omega_\beta/c = 1.33 \times 10^{-10}\sqrt{\gamma n_e[cm^{-3}]}r_\beta[\mu m]$, where θ is the peak angular deflection of the electron trajectory, r_β is the oscillation amplitude, c is the speed of light, and n_e is the electron density.

The strength parameter K is correlated with the spectral characteristics of the radiation. For the highly relativistic electrons generated by LWFA, the range of interest for the strength parameter is K much larger than unity where the plasma acts like a wiggler and numerous high harmonics are produced leading to a broadband spectrum. The on-axis spectral intensity of the Betatron radiation can be described by the synchrotron radiation function [60, 61]:

$$\frac{dI}{dE} \cong \frac{1}{4\pi\epsilon_0}\sqrt{3}\frac{e^2}{c}\gamma\frac{E}{E_c}\int_\xi^\infty K_{5/3}(\xi')\,d\xi' \tag{8.1}$$

where $\xi = E/E_c$, and $E_c(keV) \cong 5 \times 10^{-24}\gamma^2 n_e(cm^{-3})r_\beta(\mu m)$ is the critical energy which divides the radiation energy into two equal energy spectral halves. $K_{5/3}$ is a modified Bessel function of the second kind of order 5/3. Because of the strongly relativistic motion of the electrons, the Betatron radiation is confined to a narrow cone with half opening angle of $\theta \simeq K/\gamma$. In addition, the Betatron radiation should have the same temporal duration as the laser excited electron bunch, which is on the order of a few femtoseconds [13].

The critical energy E_c is the main parameter which defines the Betatron radiation as it determines the shape of the spectrum. So far, a number of X-ray diagnostic techniques have been employed to characterize the spectrum of the Betatron radiation, including Ross filters [150], an X-ray diffraction crystal [59], photon counting CCDs [151] and an X-ray spectrometer with stacked

differential filters [62]. The Ross filter technique utilizes a pair of differential filters that have identical transmission coefficients except for a narrow energy window between the K-edges to sample a certain energy range of the X-rays. By assuming a synchrotron-like spectral function and fitting the detected X-ray signal obtained from a number of filter pairs to the predicted X-ray emission, one can deduce the E_c in a single laser shot. Regarding the second technique, the Betatron radiation was spectrally resolved using an X-ray Bragg crystal but with a narrow spectral window relative to the broad bandwidth of the Betatron Radiation. To obtain a reasonable bandwidth to retrieve the value of E_c, multiple crystals with different lattice spacings have to be used in addition to tuning the angles of the crystal to give a larger detection range. This approach measures the average E_c of the Betatron radiation as it requires a number of shots to reconstruct the spectrum. The photon counting method can directly measure the absolute spectral distribution of a single shot over a much larger spectral window than the previous two methods by counting the single-pixel events produced by X-ray photons striking the X-ray CCD. However, the cost of the X-ray CCD is expensive and requires postprocessing to isolate emission from single X-ray photons in order to accurately measure the photon flux. For the last approach, a series of filters with increasing atomic number were stacked in series with interleaving image plates as detectors to spectrally resolve the broadband Betatron radiation up to 80 keV range. In addition to the spectral information, this method can simultaneously reveal the angular dependence of the Betatron radiation in a single shot mode. However, it does require the post processing readout of the image plates after the Betatron emission measurement.

In this chapter, we propose another approach to measure the average E_c of the Betatron radiation by using the technique of Reflection off a Grazing Incidence Mirror (ROGIM). A grazing incidence mirror with a high-Z coating is capable of reflecting X-ray radiation over a broad bandwidth and has been

widely used in many X-ray diagnostics such as grazing incidence toroidal mirror imaging systems and Kirkpatrick-Baez (KB) microscopes. For instance, the KB micropscope consists of two orthogonal grazing incident mirrors mounted in succession that focus the X-rays in the two orthogonal planes. The ROGIM technique relies on the change in reflectivity of the high-Z coating mirror with the grazing angle of incidence of the X-rays. By fitting the measured reflectivities at different grazing angles to the corresponding theoretical reflectivities calculated assuming a synchrotron-like Betatron spectrum, the average E_c of the Betatron radiation can be determined. Recently, we have reported the characterization of a KB microscope to focus the Betatron radiation designed to probe the ionization states of warm dense aluminum pumped by the synchronized optical laser pulse [152]. In addition to the 2-dimensional X-ray focus, the KB microscope can be configured to view the 1-dimensional line foci of the two individual mirrors. With the ROGIM technique, one can directly characterize the E_c of the Betatron radiation by measuring the integrated intensity of one of the two line foci compared to the straight through intensity. In the experiment that was described in Ref.[152], an optical imaging system was installed to measure the 2D KB focus by observing the optical emission from a Lanex fluorescent film. Using the ROGIM technique to measure the E_c in this case does not require extra optical components and can be carried out during the pre-shot setup. Such a Lanex screen could be configured to be left in the system to observe the single reflection and straight through radiation without interfering with the propagation of the imaged probe beam. In other words, for such pump-probe experiments using the ultrafast Betatron radiation, the ROGIM technique can be used as an online E_c monitor from one of the grazing incidence mirrors while it is being used for X-ray focusing or imaging.

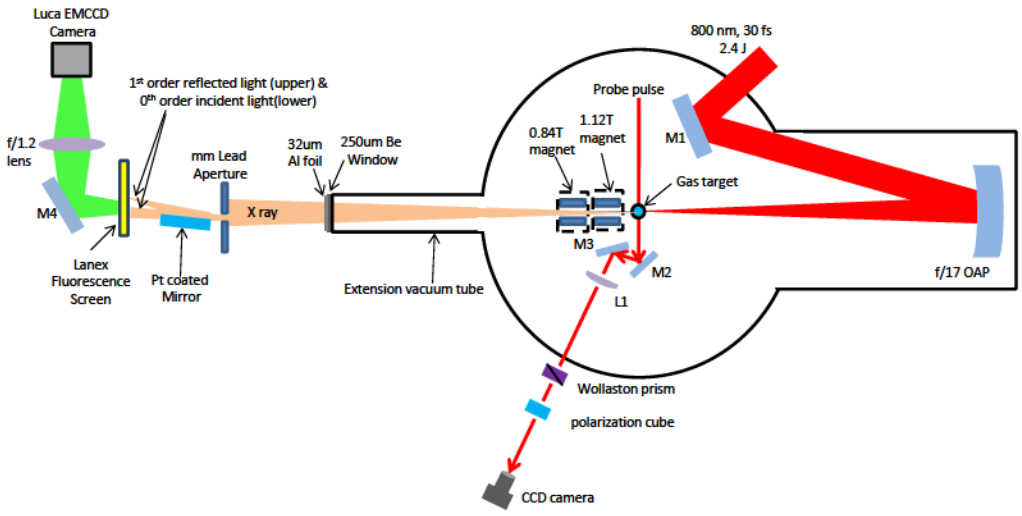

Figure 8.1: Schematic diagram of the experimental setup for measuring the Betatron X-ray radiation produced from laser wakefield acceleration.

8.2 Description of Experimental Setup

The experiments to characterize the betatron radiation were conducted at the Advanced Laser Light Source (ALLS) facility [85], and the setup diagram is shown in Fig.8.1. To create the plasma wakefield that generates the Betatron radiation, linearly polarized 800nm laser pulses with energy of 2.4 J and pulse duration of 30 fs (FWHM) were focused by an f/17 off-axis parabola (OAP) onto a gas jet target. The FWHM of the vacuum focal spot was measured to be 24 μm and the peak vacuum intensity was approximately 7.0×10^{18} W/cm^2. A side-view Normarski interferometer [89] based on a Wollaston prism as the beam splitter was employed to probe the plasma formation and its density. The probe beam for the side-view interferometry was obtained from the partial transmission of the main laser pulse through one of the mirrors. Helium was used as the gas target and was pulsed from a commercial Parker Valve (Model 009-181-900) connected to a 5-mm-diameter supersonic conical nozzle. The density of the plasma was calculated by use of modified Abel

inversion algorithm[91], where the asymmetry of the fringe shifts is weighted and introduced into the final plasma distribution, assuming a $\cos\theta$ transverse asymmetry contribution. A cylindrical plasma along the axis of the incoming laser beam was assumed for the analysis assuming a nonuniformity correction along the gas flow axis away from the nozzle. During the experiments, the gas pressure was fixed and the plasma density was measured to be approximately $1.2 \times 10^{19}\ cm^{-3}$.

The generated electron beams were measured by an electron spectrometer made with two separate dipole magnets in series with magnetic field strengths of 1.12 T and 0.84 T. Along the Betatron propagation axis, an extension vacuum tube was added to the target chamber to shorten the air path length that the Betatron X-rays experience before reaching the grazing incident mirror that was placed in the air. Extra filters that were inserted in the beam path of the Betatron included a 32-um Al foil along with the 250-um Be window that was used to seal the chamber. The grazing incident mirror, coated with platinum, was a 25 mm diameter spherically curved mirror, having radius of curvature (ROC) of 20 m. This grazing incident mirror was placed around 2.3 m away from the gas jet center and was mounted on a rotational stage to adjust the grazing angle of the X-rays. The X-rays incident upon the platinum mirror were focused in the meridional plane and reflected onto a Lanex fluorescent screen (Kodak Regular Lanex) after the mirror. The emitted fluorescence from the rear surface of the Lanex screen was collected by an f/1.2 lens system and imaged onto an Electron Multiplying CCD (Andor Luca EMCCD, Model: S658M) camera.

A thick lead aperture was set in front of the platinum mirror to prevent the direct X-ray beam from washing out the reflected X-ray beam on the Lanex screen. By measuring the separation between the 1D focused line and the unreflected line, one can determine the grazing angle of the X-rays impinging on the Platinum mirror. An average of 5 shots were taken to average the

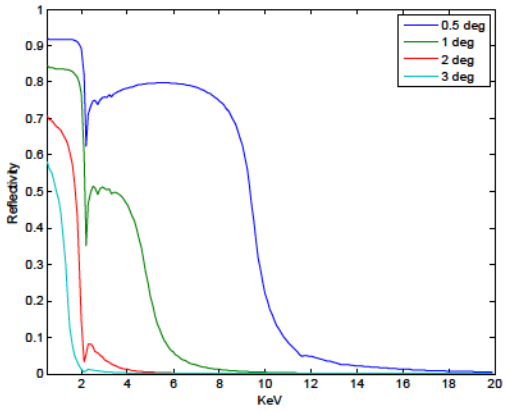

Figure 8.2: Theoretical reflectivity of platinum coated mirror as a function of X-ray energy for different grazing angles. The reflectivity was calculated with the Fresnel theory using scattering factors from NIST tables.

measured Betatron signal for each data point over a range of grazing incident angles.

8.3 E_c Measurement with the ROGIM technique

X-ray reflection off a grazing incidence mirror with high-Z coating can be understood as total internal reflection from an interface to a lower index of refraction material leading to reflection below a certain grazing angle. The theoretical reflectivity of the grazing incident mirror can be calculated using the Fresnel theory with the index of refraction given by the complex atomic scattering factors of the material that are readily available in NIST [153]. Fig.8.2 plots the theoretical reflectivity of the platinum coated mirror as a function of the X-ray

energy at different grazing angles. The reflectivity curves indicate that at a given grazing angle the reflectivity falls off with photon energy above a certain critical photon energy. The cutoff photon energy is given by the energy that has a critical angle for total internal reflection equal to the incident grazing angle. Comparing the reflectivity curves for different angles, one can find that increasing the grazing angle reduces the cut-off photon energy and the reflectivity. Therefore, while using the grazing mirror to reflect the Betatron radiation, increasing the grazing angles shrinks the bandwidth of the reflection spectrum and decreases the intensity of the reflection. Since the Betatron radiation is broadband the reflected signal represents the integrated X-ray intensity below the cutoff photon energy for a given grazing angle. By computing the theoretical integrated reflectivity for different values of E_c one can match the measured integrated reflectivity, and thus determine the value of E_c for a given Betatron source spectrum. The details of this procedure are presented below.

A single spherically curved grazing-incident mirror can be treated as a cylindrical lens in that X-rays in the meridional plane are focused with the focal length given by $f_m = R\sin\theta_g/2$, where R is the radius curvature of the mirror and θ_g is the grazing angle, whereas in the sagittal plane the focal length is given by $f_s = R/(2\sin\theta_g)$, which can be taken as infinity to first order.

Fig. 8.3 illustrates the X-ray focusing geometry of the Pt coated mirror in the meridional plane. As seen in Fig. 8.3, a 2 mm wide slit aperture made of 6 mm thick lead with one edge aligned close to the grazing mirror surface direction is used to define the angular range (typically 200 μrad) measured from the Betatron emission. The measurement samples the uniform central part of the emission which typically has a total angular divergence of 10-20 mrad. Part of the beam passes by the edge of the mirror giving a measure of the total X-ray emission strength.

As shown in Fig.8.4, the measured X-ray intensity distribution in the y or non-focused direction is fairly uniform, therefore the intensity function of the

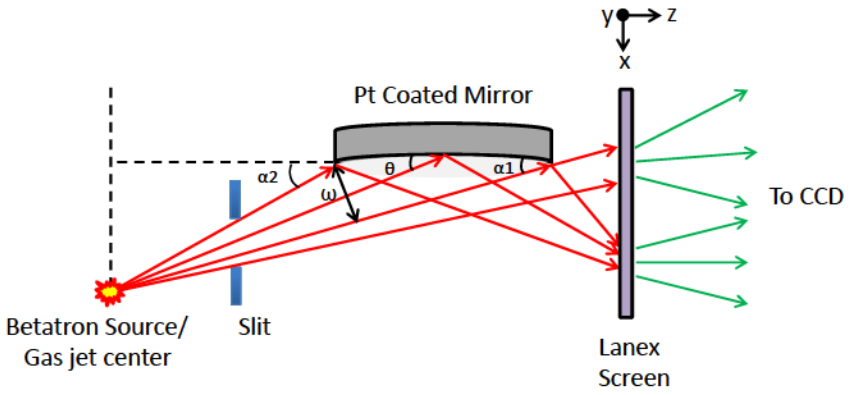

Figure 8.3: Schematic diagram showing the X-ray focusing of the Pt coated mirror in the meridional direction (spatial scale is exaggerated to show more clearly allocations of the variables for analysis). At the Lanex screen the X-ray focusing direction is defined as x direction while the non-focusing direction is y direction.

X-rays on the Lanex fluorescent screen can be reduced to be a function that has only one spatial variable x transverse to the line image by averaging the signal over a fixed length in the y direction. The images from the Lanex screen are recorded by imaging the fluorescence onto a CCD camera.

The total intensity function $\eta_t(\theta_g, x)$ of the X-rays on the Lanex screen, indicated by the lineouts as shown in Fig.8.4, consists of incident direct radiation function $\eta_i(\theta_g, x - x_{c1})$ and the reflected light function $\eta_r(\theta_g, x - x_{c2})$, where x_{c1} and x_{c2} are the central positions for the incident and reflected radiation and θ_g is the grazing angle at the center of the mirror. We assume a linear response of Lanex screen to X-ray energy deposited, which is reasonable for the X-ray energies in the keV range which are fully absorbed in the fluorescent detection region of the film. The response curve of the same Lanex screen was measured by Trauernicht et al. [154], indicating fairly uniform response. The measured integrated reflectivity at a given grazing angle of θ_g is given by:

$$R_m(\theta_g) = \frac{\int \eta_r(\theta_g, x - x_{c2})dx}{\int_{x_{c1}-0.5w}^{x_{c1}+0.5w} \eta_i(\theta_g, x - x_{c1})dx} \tag{8.2}$$

where w, as shown in Fig.8.3, is the effective angular aperture width spanned by the mirror in the focusing direction, x, relative to the gas jet center. The total X-ray energy accepted by the Pt mirror can be approximated by integrating the incident light function η_i symmetrically about x_{c1} with an angular width of w.

The opening angle in the focused direction subtended by the mirror relative to the gas jet center is less than 0.1 mrad for the selected grazing angles (0.3^o-0.7^o), which is small relative to the full divergence of the emitted betatron beam (10-20 mrad). Over such a small angular range, the betatron radiation intensity can be treated as constant and is thus given by the on-axis formula as shown in Eqn.[8.1]. Multiplying the Betatron spectrum with the filter transmission (including the air path) T(E) and the reflectivity R_{pt} of Pt mirror,

the theoretical integrated reflectivity at a central grazing angle of θ_g can be calculated:

$$\begin{aligned} R_{th}(\theta_g) &= \frac{\int_{\alpha_1}^{\alpha_2} \int \frac{dI}{dE} T(E) R_{pt}(\alpha, E) dE d\alpha}{\int_{\alpha_1}^{\alpha_2} \int \frac{dI}{dE} T(E) dE d\alpha} \\ &= \frac{\int_{\alpha_1}^{\alpha_2} \int \frac{dI}{dE} T(E) R_{pt}(\alpha, E) dE d\alpha}{|\alpha_2 - \alpha_1| \int \frac{dI}{dE} T(E) dE} \end{aligned} \tag{8.3}$$

where α_1 and α_2 are the grazing angles at the two ends of the mirror in the focused direction, which are indicated in Fig.8.3. Because the distance from the source to mirror ($\sim$ 2.3 m) is much larger that the size of the mirror (25.4 mm), the following approximate relationship $\alpha_1 \simeq \alpha_2 \simeq \theta_g$ holds true, which allows Eqn.8.3 to be simplified to the following:

$$\begin{aligned} R_{th}(\theta_g) &= \frac{\int_{\alpha_1}^{\alpha_2} \int \frac{dI}{dE} T(E) R_{pt}(\theta_g, E) dE d\alpha}{|\alpha_2 - \alpha_1| \int \frac{dI}{dE} T(E) dE} \\ &= \frac{\int \frac{dI}{dE} T(E) R_{pt}(\theta_g, E) dE}{\int \frac{dI}{dE} T(E) dE} \end{aligned} \tag{8.4}$$

The reflectivity of a metallic coated mirror is also sensitive to the surface roughness which can scatter a significant part of the incident X-ray flux [155]. Therefore, an additional factor that accounts for the scattering loss due to the surface roughness should be included when computing the mirror reflectivity. The mirror reflectivity including the surface roughness is given by [156]:

$$R = R_0 \exp(-\frac{16\pi^2 \sigma_{rms}^2}{\lambda^2} sin^2\psi) \tag{8.5}$$

where the R_0 is the reflectivity for a perfectly smooth surface, σ_{rms} is the root-mean-square roughness, λ is the X-ray wavelength and ψ is the grazing angle of incidence.

Looking at Eqn.8.4, one can see that to calculate the theoretical reflectivity,

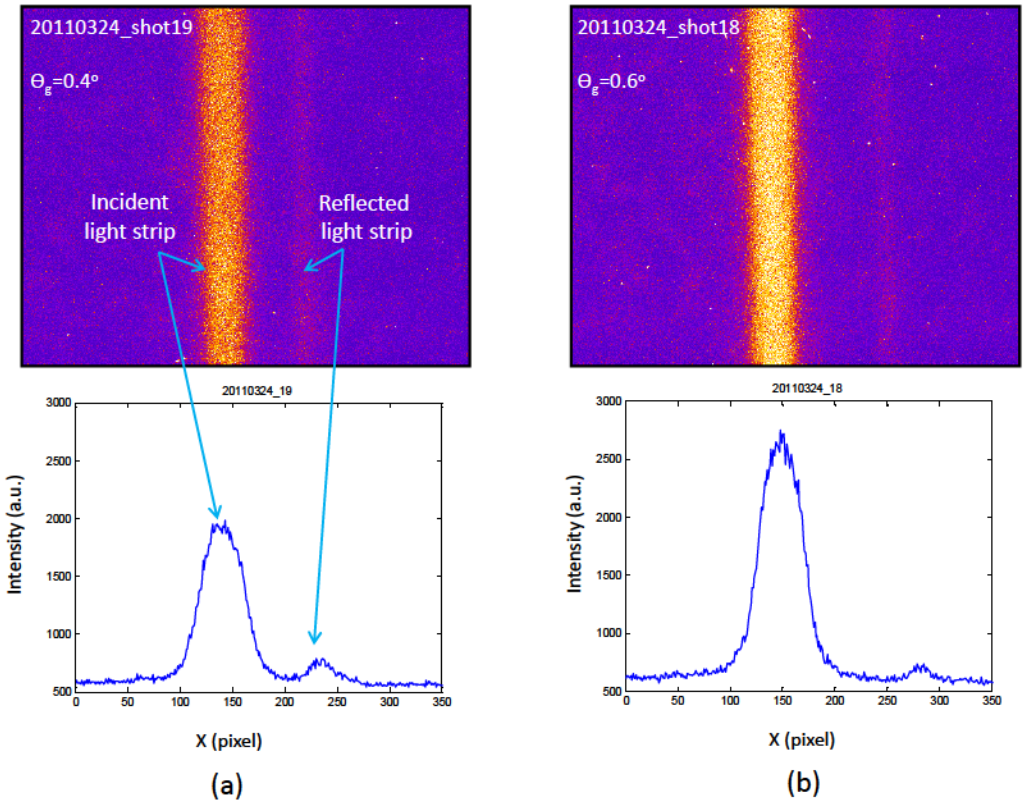

Figure 8.4: Measured Betatron reflections using a single Pt coated mirror at grazing incident angles of (a) 0.4^o (b) 0.6^o. The horizontal lineouts crossing the direct and the reflected light strips are plotted at the bottom of the images respectively.

the only unknown parameter is E_c of the Betatron spectrum since the absolute amplitude cancels out when taking the ratio of reflected to the incident signals. E_c can be determined from every laser shot by matching the measured value of reflectivity. If the reflectivity is measured at multiple angles of incidence, an average value of E_c can be determined by minimizing the sum of the rms errors squared $\Sigma_\theta(R_{th} - R_m)^2$ where R_{th} and R_m are the theoretical and the measured reflectivities at each angle respectively.

8.4 Results and Discussions

Typical images of the Betatron reflection from the platinum mirror at two different grazing angles are shown in Fig.8.4. A wide bright band from the directly incident radiation is clearly observed along with a separate narrower strip of weak reflected radiation. Notice that the horizontal axis of the image is the x-direction or the direction in which the incident X-rays are focused. Fig.8.5(a) shows the measured integrated reflectivities (discrete triangles) at different grazing angles of the Pt mirror and the theoretical curve corresponding to the minimum rms error using Eqn.8.4 with a value of E_c of 7.5 keV (solid blue curve). The error bar of the E_c is estimated to be around 1.3 keV from the uncertainties of the measured integrated reflectivities. In computing the theoretical reflectivities of the Pt mirror the surface rms roughness σ_{rms} was set to 7 $\AA$, which was determined by fitting Eqn.8.5 to the measured reflectivity for the mirror in previous studies [157]. Note that the additional scattering effect from this roughness leads to a reduction in the mirror reflectivity of the order of 10% to 20% at intermediate angles, which in turn results in a $\sim$ 15% reduction in magnitude for the best fit E_c when comparing to the case where the mirror surface is assumed to be perfectly smooth. For comparison, theoretical curves with E_c's of 6.2 keV (green dashed curve) and 8.8 keV (red dash-dotted curve) are also plotted in Fig.8.5(a). It should be noted that there are variations in Betatron emission intensity from shot to shot, but these will not affect the calculated E_c since it is only dependent on the ratio of reflected to transmitted signals. We would also expect minor variations of E_c from shot to shot but what we report here is the average E_c for our conditions. Knowing the E_c, we can calculate the relative intensity distribution of the Betatron source by substituting the E_c into the Eqn.8.1. The relative intensity distribution of the Betatron radiation with E_c of 7.5 keV is plotted in Fig.8.5(b). From this curve, one can see that the radiation intensity peaks at $\sim 0.29E_c$ (2.2 keV) and drops

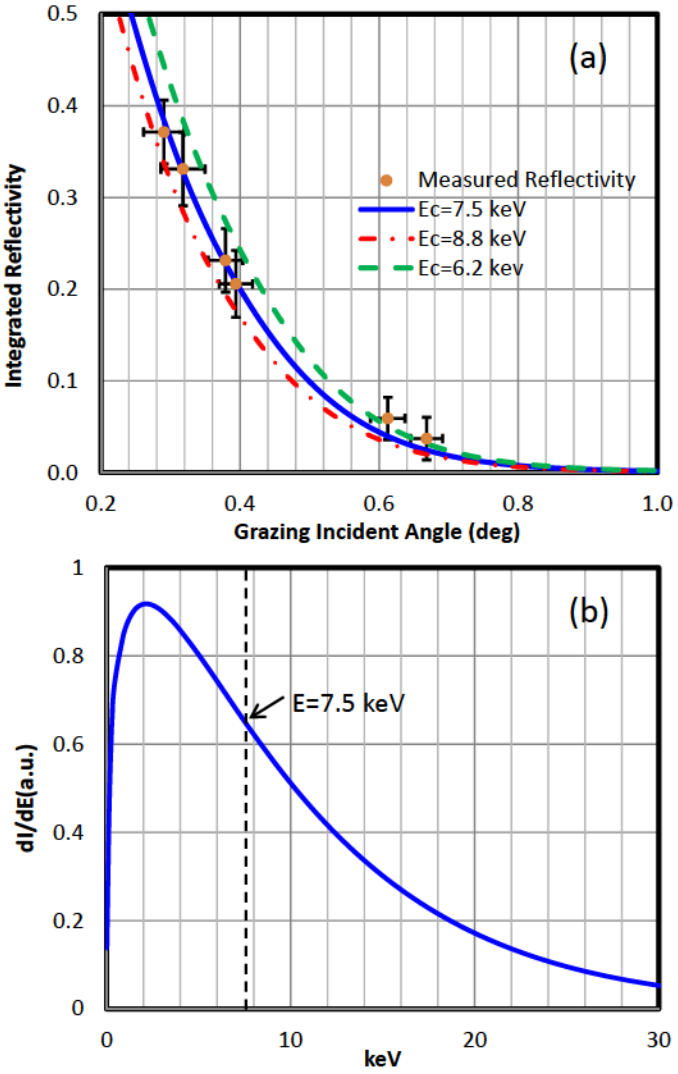

Figure 8.5: (a) Measured integrated reflectivities (triangles) of the reflected Betatron vs. grazing angles of the Pt mirror. Curves are the theoretical values calculated from Eqn.[8.4] for three different E_c: 6.2 keV (green dash), 7.5 keV (blue solid) and 8.8 keV (red dash-dot). (b) Simulated Betatron Spectrum with E_c of 7.5 keV, the dash vertical line indicates the X-ray energy of 7.5 keV.

approximately exponentially to zero above E_c.

To confirm the E_c of the Betatron source that was achieved with the ROGIM technique, an X-ray photon counting technique with a CCD cameara was used to measure the spectrum of the Betatron source produced in a separate experiment under the same experimental conditions. This technique is described in detail in Fourmaux et al. [151]. Knowing the CDD calibration in counts per eV and the CCD quantum efficiency, the calibrated experimental spectrum can be recovered. An X-ray CCD camera (Princeton Instruments, model: PI-LCX) which is cooled with liquid nitrogen was used. This is a deep-depletion CCD with 1340 $\times$ 1300 pixels with a pixel size of 20 μm $\times$ 20 μm. The X-ray CCD was positioned 3.1 m away from the gas jet in order to do the photon counting. The signal was also attenuated using an Al filter with 458 μm thickness.

Fig. 8.6(a) displays the measured experimental spectra of Betatron X-rays by photon counting for two typical shots (data1 and data2) recorded under the same experimental conditions used for the ROGIM measurement. We also present for each data set the best fit corresponding to a synchrotron distribution (see Eqn.[8.1]). Moreover, we illustrate the precision of this fit by showing the synchrotron distribution corresponding to $E_c = 9 \pm 1.5$ keV for data1 and $E_c = 8.5 \pm 1.5$ keV for data2. The critical energy averaged over ten successive shots and the corresponding statistical standard deviation is $E_c = 8.75 \pm 1.13$ keV. This average distribution is plotted in Fig. 8.6(b). Thus, the result obtained with the photon counting technique is in agreement with the ROGIM technique result within approximately one standard deviation. This is a significant result since the ROGIM technique measures the photon distribution below 10 keV photon energy while the photon counting technique measures photon energies above 10 keV. The agreement indicates that the emitted spectrum is indeed synchrotron-like over a large spectral range.

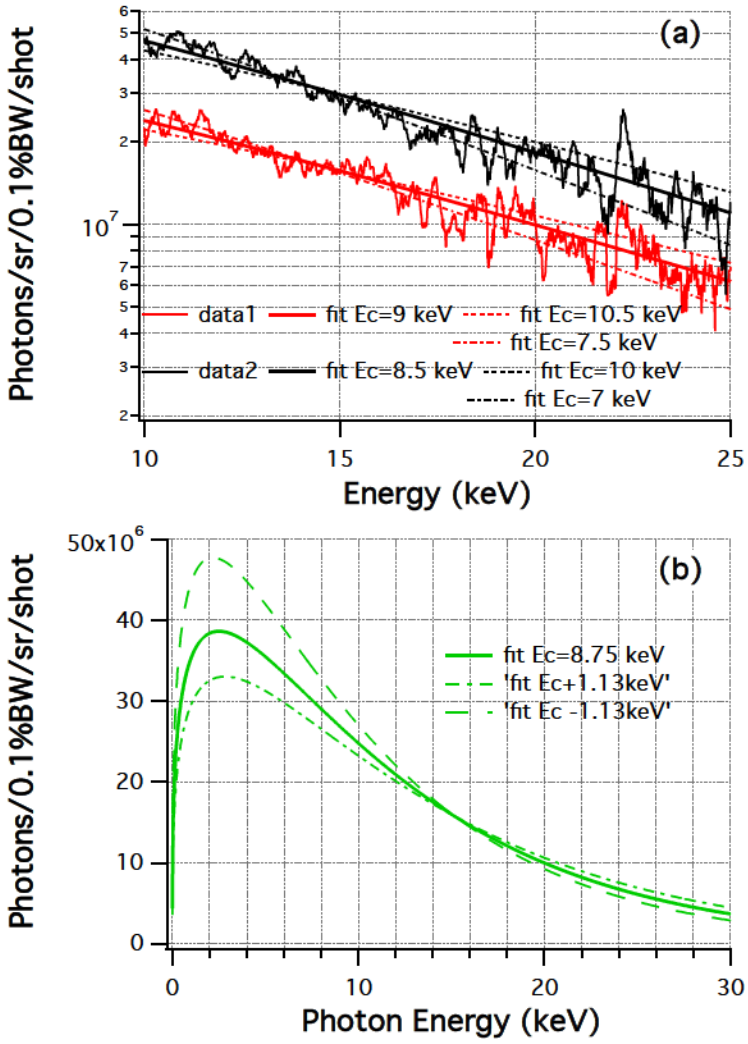

Figure 8.6: (a) Measured experimental spectra using the photon counting technique. We show the experimental data (line), the corresponding best fit (bold line), and to illustrate the precision of the fit we show the fit corresponding to $E_c \pm 1.5$ keV (dotted and semi dotted lines). (b) Simulated Betatron Spectrum corresponding to the critical energy averaged over ten shots with $E_c = 8.75 \pm 1.13$ keV.

8.5 Conclusion

In conclusion, we have developed a new approach to measure the average critical energy E_c of the laser wakefield generated Betatron X-ray radiation with the technique of Reflection off a Grazing Incidence Mirror (ROGIM). In this approach a grazing incidence mirror with high-Z coating reflects the Betatron X-ray radiation at different grazing angles. Part of the radiation bypasses the mirror giving a reference signal at the detector surface which in this case is a fluorescent screen imaged onto a CCD camera. Assuming a synchrotron-like spectrum of the Betatron radiation, one can determine the value of E_c for the Betatron radiation from every single shot. This measurement was carried out with several grazing angles in the range of 0.3^o to 0.7^o for a Pt mirror and an average value of E_c of 7.5 ± 1.3 keV was determined. This E_c is in reasonable agreement with the value measured with a photon-counting X-ray CCD under the same experimental conditions, indicating a uniform synchrotron-like spectrum over a large photon energy range of a few keV to 25 keV. Such a grazing incidence mirror measurement can be used as an online E_c monitor in Betatron application experiments by sampling a small part of the beam where a simple fluorescent screen together with CCD camera readout can be used. Specifically, for KB microscope applications the straight through radiation and single mirror reflection radiation could be used for this measurement without interfering with the main image spot of the KB microscope.

Chapter 9

Laser Wakefield Generated X-ray Probe for Femtosecond Time-resolved Measurements of Ionization States of Warm Dense Aluminum*

We have developed a laser wakefield generated X-ray probe to directly measure the temporal evolution of the ionization states in warm dense aluminum by means of absorption spectroscopy. As a promising alternative to the free electron excited X-ray sources, Betatron X-ray radiation, with femtosecond pulse duration, provides a new technique to diagnose femtosecond to picosecond transitions in the atomic structure. The X-ray probe system consists of an adjustable Kirkpatrick-Baez (KB) microscope for focusing the Betatron emission to a small probe spot on the sample being measured, and a flat Potassium

*The contents of this chapter have been published in the article: M.Z. Mo, et al., Rev. Sci. Instrum. **84**, 123106 (2013).

Acid Phthalate (KAP) Bragg crystal spectrometer to measure the transmitted X-ray spectrum in the region of the aluminum K-edge absorption lines. An X-ray focal spot size of around 50 um was achieved after reflection from the Platinum-coated 10-cm-long KB microscope mirrors. Shot to shot positioning stability of the Betatron radiation was measured resulting in an rms shot to shot variation in spatial pointing on the sample of 16 μm. The entire probe setup, had a spectral resolution $\sim$ 1.5 eV, a detection bandwidth of $\sim$ 24 eV and an overall photon throughput efficiency on the order of 10^{-5}. Approximately 10 photons were detected by the X-ray CCD per laser shot within the spectrally resolved detection band. Thus it is expected that hundreds of shots will be required per data point to clearly observe the K-shell absorption features expected from the ionization states of the warm dense aluminum.

9.1 Introduction

The Warm Dense Matter (WDM) regime lies between the condensed matter state and the ideal plasma state, and is characterized by temperatures of $\sim 1 - 20$ eV and near solid densities. Although it is challenging to theoretically describe the WDM state due to the fact that its temperature is comparable to the Fermi energy and its ion-ion coupling parameter exceeds unity[158], the interest in understanding the properties of WDM is growing rapidly due to its significance in a large number of areas such as shock physics [158], astrophysics[159], and inertial confinement fusion[160].

One approach to producing a WDM state in the laboratory is to use intense femtosecond laser pulse to isochorically and uniformly heat ultrathin metallic foils [161]. The WDM state created in such a way usually has a short lifetime and requires ultrashort probe diagnostics in order to characterize it. In previous studies of warm dense matter [161, 162, 163, 164, 165, 166], a second ultrafast optical beam was used to probe the transient material properties. However,

one disadvantage of using optical probing is the limited penetration depth of the optical beam into WDM with mass density close to solid. Also, the optical probe pulse interacts with the electrons near the conduction band or free electrons, and cannot readily provide information about the atomic structure. To solve this problem, ultrafast X-ray absorption spectroscopy has been proposed and successfully applied to study the dynamic properties of warm dense aluminum [148] and warm dense copper[167].

In warm dense matter generated by femtosecond laser pulse, the laser energy is coupled to the electrons first while the ions typically remain cold for the first picosecond or more. The ionization state of material in this non-equilibrium warm dense matter regime is not well understood yet. Measurements of the ionization states in non-equilibrium WDM aluminum created with X-ray free-electron laser have been conducted by Vinko and his colleagues using X-ray emission spectroscopy[168]. However, this technique relies on the availability of a high brightness tunable ultrafast X-ray pulse to generate the WDM and the average ionization state is analyzed by observing the time integrated emission spectra. Recently a new source of ultrashort X-ray radiation has become available in the form of Betatron radiation from laser wakefield accelerated electrons[58]. While the brightness of the Betatron radiation is not sufficient to form WDM states, it can be used as a probe to diagnose the ionization states of WDM.

The ionization states of materials under equilibrium condition can be theoretically calculated. Fig.9.1 shows the simulated K-shell absorptions lines for different equilibrium temperatures as predicted by PrismSPECT software [169] for 50-nm-thick aluminum at solid density. The simulated spectra indicate that K-shell absorption depends on the number of excited charge states which increases with the target temperature. These predicted K-shell absorption features can be experimentally observed using ultrafast X-ray absorption spectroscopy provided that sufficient spectral and temporal resolution is avail-

able. Although these absorption spectra are calculated for equilibrium states, they provide guidance to investigate the ionization states in the non-equilibrium condition using the Betatron radiation where similar features are expected.

Betatron radiation is produced as part of the laser wakefield acceleration process where electrons are accelerated by the longitudinal electric field formed inside a laser driven wakefield cavity[6]. Electron beams with energy of the order of a GeV produced in underdense plasma of the order of a centimetre in length have been demonstrated by many research groups. [20, 45, 46, 47, 51] As the electrons are accelerated inside the wakefield cavity, they undergo transverse (betatron) oscillations due to the restoring force exerted by the space charge residing in the middle of the cavity [58, 21]. The frequency of the betatron oscillation is given by $\omega_\beta = \omega_p/\sqrt{2\gamma}$, where ω_p is the plasma frequency and γ is the Lorentz factor associated with the electron motion along the plasma channel. The accelerating charges then radiate electromagnetic waves. The resultant radiation spectrum from the oscillating electrons is characterized by the betatron strength parameter [59], namely

$$K = \gamma r_\beta \omega_\beta / c = 1.33 \times 10^{-10} \sqrt{\gamma n_e [cm^{-3}]} r_\beta [\mu m] \tag{9.1}$$

where the r_β is the oscillation amplitude, c is the speed of light, and n_e is the electron density. The radiation spectrum becomes broadband if K becomes large ($K \gg 1$), and the on-axis spectral intensity can be described by the synchrotron radiation function [60, 61]:

$$\frac{dI}{dE} \cong \frac{1}{4\pi\epsilon_0} \sqrt{3} \frac{e^2}{c} \gamma \frac{E}{E_c} \int_\xi^\infty K_{5/3}(\xi')\, d\xi' \tag{9.2}$$

where $\xi = E/E_c$, and $E_c(keV) \cong 5 \times 10^{-24} \gamma^2 n_e(cm^{-3}) r_\beta(\mu m)$ is the critical energy [59] and $K_{5/3}$ is a modified Bessel function of the second kind. Half of the energy will be radiated below E_c and half above E_c. Because of the strongly relativistic motion of the electrons, the betatron radiation is confined

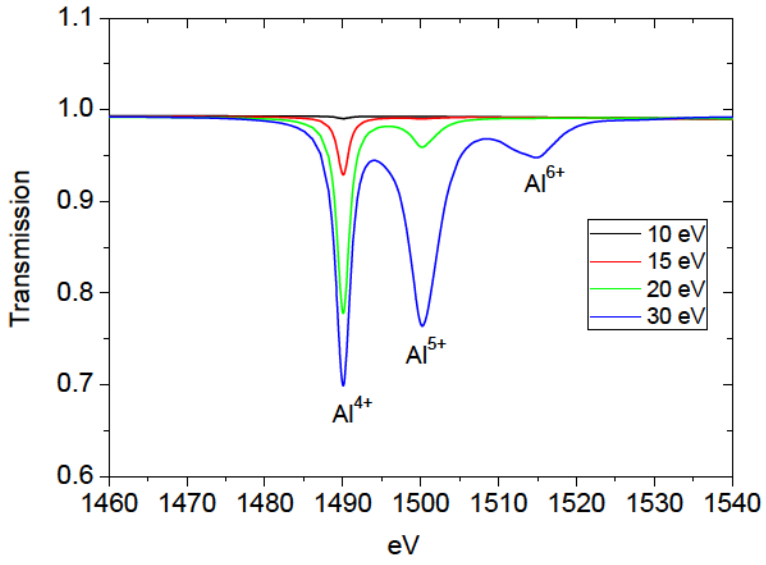

Figure 9.1: Simulated K-shell absorption lines versus different temperatures for 50-nm-thick Aluminum at solid density.

to a narrow cone angle with opening angle $\theta \simeq K/\gamma$. The Betatron radiation has approximately the same temporal duration as the laser excited electron bunch. In principle, its pulse duration can be as short as a few femtoseconds,[13] making Betatron radiation an ideal probe for measuring phenomena on the time scale of femtoseconds. Another advantage of the Betatron radiation is its temporal synchronization with the source laser pulse. This allows one to precisely synchronize the X-ray with an optical pulse which can be used to create the WDM state.

Because of these potential advantages, we have started to develop betatron radiation as a spectroscopic probe source to directly measure the temporal evolution of the ionization states in warm dense aluminum. This requires an X-ray microscope system to capture and refocus the X-rays to a small probe spot to pass through the WDM region under study and a spectral dispersion system to analyze the absorption spectrum. Such a system has been developed, and the design and the characterization of this system are described in the present paper.

In our design, as shown in Fig.9.2, we use an adjustable Kirkpatrick-Baez (KB) Microscope to focus the radiation around the 1.5 keV photon energy range onto an ultrathin free-standing aluminum foil that is heated by a synchronized 800 nm 30-fs laser pump pulse. The K-shell absorption spectra in this range is spectrally analyzed using a flat Potassium Acid Phthalate (KAP) Bragg crystal spectrometer. By measuring the absorption dips in the transmitted spectra, we will be able to determine the ionization state of aluminum as a function of time and heating pulse fluence. In this chapter we report the results on the development of such a system. In the following sections we outline details of the Betatron source, the X-ray imaging system and dispersive elements, together with an analysis of the expected system performance. A series of experimental measurements have been carried out to verify that the required performance specifications can be achieved.

9.2 Experimental Design

The experiments were conducted at the Advanced Laser Light Source (ALLS) facility located at INRS, Varennes [85]. As depicted in Fig.9.2, the layout of the system consists of three major parts: Betatron radiation generation, X-ray focusing and X-ray spectrometer system. To create the plasma wakefield that generates the Betatron radiation, linearly polarized 800nm laser pulses

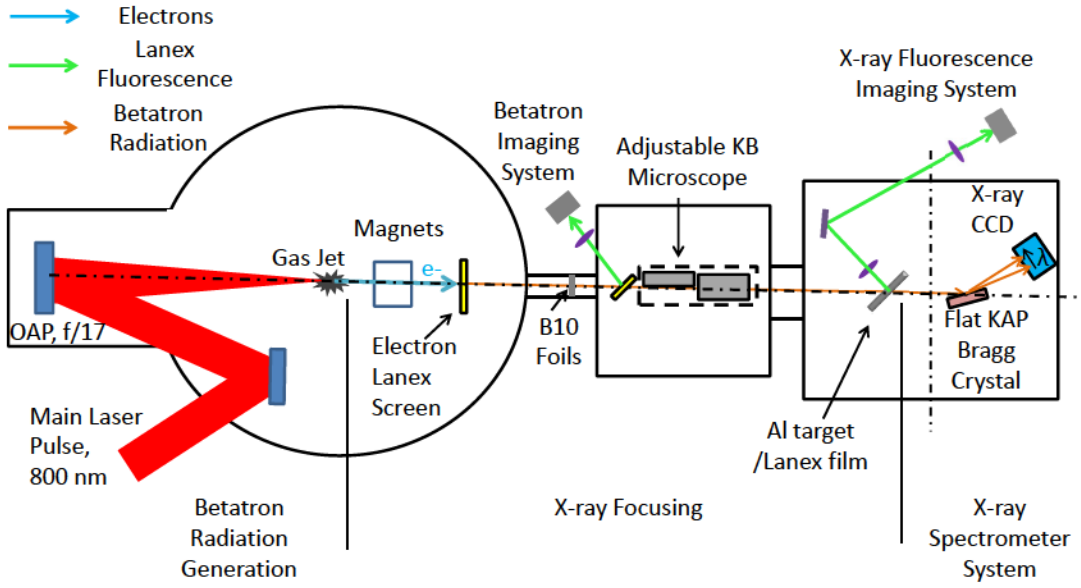

Figure 9.2: Schematic diagram showing the Betatron X-ray probe system layout. The entire setup except the optical imaging systems is situated in vacuum. Lens systems for collecting and imaging the electron fluorescence from the Lanex fluorescent screen are omitted here.

with energy of 2.4 J and pulse duration of 30 fs (FWHM) were focused by an f/17 off-axis parabola (OAP) onto a gas jet target. The FWHM of the vacuum focal spot was measured to be 24 μm and the peak vacuum intensity was approximate $7.0 \times 10^{18}\ W/cm^2$. Helium was used as the gas target and was pulsed from a commercial Parker Valve (Model 009-0496-010-003) connected to a 1-cm-diameter supersonic conical nozzle.

The generated electron beams were measured by an electron spectrometer that is composed of two separate dipole magnets in succession with magnetic field strengths of 1.12 T and 0.84 T. Along the Betatron propagation axis, at 1.23 m away from the gas jet center, there is a Lanex (Kodak Fine series) fluorescent screen angled at 45 degrees with respect to the beam axis to look at the Betatron far-field beam profile as well as to monitor the shot to shot intensity variation. To prevent the main laser pulse from entering the optical systems and from damaging the Lanex film at this position, B10 filter foils, consisting of a 2 μm polyester film coated with 200-nm-thick aluminum, were used as light-proof filters inserted in the beam path in the tube connecting the gas jet chamber and the KB Microscope chamber.

The Betatron signal was optimized by scanning the laser focal positions inside the gas jet and the backing pressure of the gas. Under the optimum conditions, the average flux of the generated X-ray photons at 1.5 keV during the experiments was estimated to be on the order of $10^8\ photons/srad/0.1\%BW/shot$ by comparing the Lanex emission intensity with the previous measurements, in which the Lanex signal was calibrated to a photon counting X-ray CCD signal [66]. The average divergence of the Betatron emission under the present conditions was measured to be approximately 24 $mrad \times 12\ mrad$ $(H \times V)$. A rectangular aperture with the width of 5 mm was cut in the center of the fluorescent screen in order to let the center of the radiation pass through to the remainder of the measurement system.

To assure adequate X-ray photon flux for detecting the absorption dips of

the warm dense aluminum, the Betatron X-ray emission was focused by an adjustable KB Microscope onto the aluminum target. The KB Microscope was set at a demagnification of twofold to give an incident probe cone angle which would result in a spectral width of $\sim 24\ eV$ when analyzed using a KAP crystal. The two 10-cm-length KB mirrors were cylindrically curved and were coated with 15 nm of Platinum. The mirror pair of the KB microscope is arranged such that the first mirror focuses the X-rays in the horizontal plane while the second one focuses in the vertical plane. For convenience and clarity, we name the first mirror as horizontal focusing mirror and the second one as vertical focusing mirror hereafter. The radius of curvature (ROC) of the each mirror is adjustable in one dimension by applying a variable force individually at each end of the mirror strip through two spring metal plates that are connected to piezo-driven motors. To measure the two-dimensional X-ray focal spot from the KB Microscope, a Lanex fluorescent screen (Kodak Medium series) was placed at the sample target position. The fluorescence emitted from the screen was collected by an f/2.5 lens system and imaged to a sensitive electron multiplier CCD (EMCCD) camera. The X-rays could be focused at the target plane by adjusting the ROC of the KB mirrors while observing the X-ray fluorescent spot on the fluorescent screen. More details on the focusing of the X-rays are given in Section 9.2.1. Ray trace calculations of the KB microscope system have indicated a temporal stretching of the x-ray pulse due to aberrations in the imaging system of the order of a femtosecond at the sample test position. Thus aberrations in the x-ray imaging system should not cause significant stretching of the Betatron probe pulse.

A flat KAP Bragg crystal spectrometer was employed to resolve the spectrum of the transmitted X-rays after the interaction plane. The KAP Bragg crystal is a synthetic crystal that has a 2d spacing of 26.63 $\AA$, which corresponds to a Bragg angle θ_B of 18.09^o at 1.5 keV when used in its 1st diffraction order. The crystal has an active area of $5\ cm \times 2\ cm$ and was mounted on a

motorized rotational stage to have one degree of freedom to adjust the incident angle of the X-rays. An X-Ray CCD (Princeton Instruments, PI MTE: 1300B) was used as the detector for the spectrometer system. It is a vacuum compatible back-illuminated CCD without AR coating for sensitive detection of low energy X-rays. The compactness and the vacuum compatibility of this model of CCD allowed us to fit the entire spectrometer setup inside the vacuum chamber.

9.2.1 X-ray Focusing using bendable Kirkpatrick-Baez Microscope

It is well known that KB Microscope is an achromatic X-ray instrument in that the high-Z coated mirror reflects whatever X-ray energy is incident but with a reflectivity that falls off with photon energy above a certain critical energy. The cutoff photon energy is given by the energy that has a critical angle for total internal reflection equal to the incident grazing angle. In other words, by selecting a proper grazing angle and proper input filters, one can select a certain bandwidth of X-rays which are transmitted by the KB Microscope.

Fig.9.3 plots the theoretical reflectivity of 1.5 keV X-ray as a function of the grazing angle for platinum obtained from Fresnel reflection theory using scattering factors from NIST tables [153]. For comparison, the reflectivity computed with the X-ray Oriented Programs (XOP) software[170] is also plotted on the same graph. For this case, the X-ray scattering factors were taken from the built-in database of XOP so-called DABAX[170]. Note that in both calculations, the roughness of the mirror coating is not considered, which may cause some degree of reduction in reflectivity depending on how well the platinum is coated [157]. Less than 10% of deviation is observed between the two curves, which mainly comes from the slight difference of the atomic scattering factors that are used in each calculation. The throughput of a single mirror, i.e., the

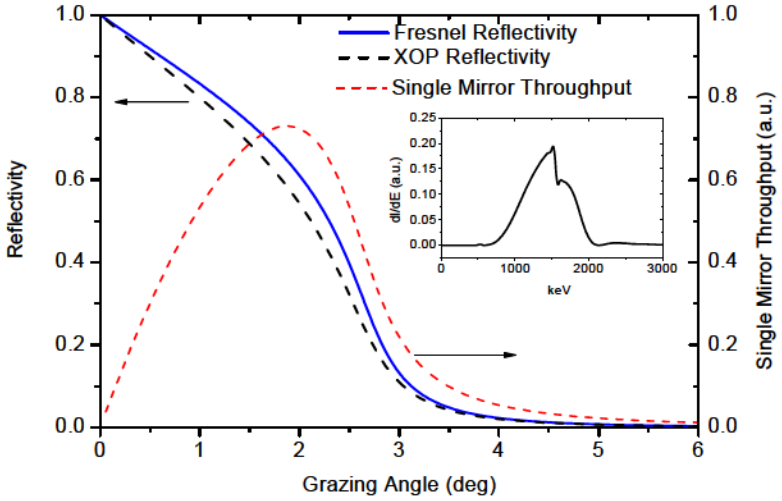

Figure 9.3: Theoretical reflectivity of Platinum at 1.5 keV versus grazing angle. The blue solid (black dashed) curve represents the reflectivity obtained from Fresnel theory using scattering factors from NIST tables (XOP calculations using scattering factors generated from its built-in database so-called DABAX). The red dashed curve represents the theoretical throughput of 1.5 keV photons for a single 10 cm KB mirror versus grazing angle of incidence that is positioned the same distance relative to gas jet center as in the experiment. The inset shows the Betatron spectrum after two KB mirrors for a grazing angle of incidence of 2^o and after the B10 filter foils that were used in the experiments.

product of the reflectivity and the aperture angle spanned by the mirror strip relative to the gas jet center, is also shown in Fig.9.3 based on the Fresnel reflectivity. As indicated by the curve, a region of maximum throughput is reached with grazing angle ranging from 1.7^o to 2.1^o for a throughput above 95%. In our experiments, the critical energy E_c of the Betatron source was estimated to be around 13 keV, close to the value of $E_c = 12.3$ keV that was previously reported in Ref.[66]. Therefore, in computing the reflected spectrum of the Betatron radiation by the two KB mirrors with grazing angle of 2 degrees, the Betatron source was assumed to have a E_c of 13 keV and the result is presented in the inset of Fig.9.3. Note that the X-ray transmittance of the total of 3 layers of B10 foils that were used in the experiments is already taken into account in computing the reflected spectrum. The reflected Betatron spectrum indicates that an X-ray pulse centering at 1.5 keV with a bandwidth of $\sim 700\ eV$ (FWHM) is selected from the broadband Betatron spectrum by the KB microscope together with B10 filters. Note that the sharp edge observed in the spectrum is the K-edge of aluminum that is coated on both sides of the B10 foils.

The incident angle of X-rays on each mirror of the KB Microscope was set to the optimum range for 1.5 keV by using the same method of measuring the separation between the 1D focused line images and the 2D focal spot image as used in Ref.[157]. The final grazing angles of the horizontal and the vertical mirrors were measured to be $1.96^o \pm 0.02^o$ and $1.81^o \pm 0.03^o$ respectively. The grazing angles were fixed for the entire experiment and the focal spot was optimized by adjusting the ROC's of the two mirrors as mentioned earlier. Initial measurements of the ROC's of both mirrors were carried out offline by measuring the distance relative to the KB mirror of the intercept of two parallel HeNe beams focused by the KB mirror at close to normal incidence. The measurements demonstrated that the ROC of the KB mirror could be bent from infinity all the way down to 16 m, corresponding to a focal length range

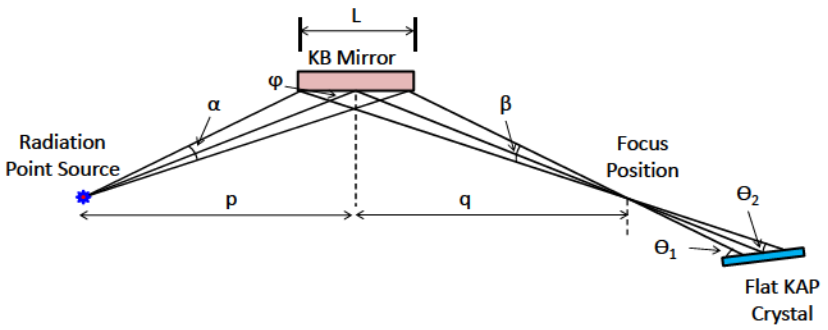

Figure 9.4: Sketch that shows the definition of variables for computing the angular range of X-ray at KAP crystal.

of 28 cm to infinity for a grazing angle of 2^o.

9.2.2 X-ray Spectrometry with flat KAP Bragg crystal

The performance of a Bragg crystal spectrometer is mainly determined by the detection bandwidth, spectral resolution and its reflectivity in the desired X-ray wavelength range. These three parameters will be evaluated in this section for our system.

Detection Bandwidth

The Bragg crystal reflects X-rays according to the Bragg diffraction condition:

$$2dsin\theta_B = n\lambda \tag{9.3}$$

where d is the lattice spacing, θ_B is grazing angle, n is an integer representing the diffraction order and λ is the wavelength of the incident X-rays. The Bragg

condition implies that each X-ray wavelength is reflected at a specified angle for a given diffraction order, hence, to estimate the bandwidth of a Bragg crystal spectrometer, one has to know the angular range of the X-rays that reach the crystal. The observed bandwidth of our Bragg crystal spectrometer can be derived by analyzing the geometry of our X-ray imaging system.

For simplicity, we assume an ideal radiation point source and a perfect line focus that is formed by a single KB mirror. Since the X-ray spectrum is dispersed in one dimension by the crystal, we only consider the horizontal focusing mirror in our KB system that focuses the X-rays in the meridional plane, i.e., the X-ray dispersion plane. We assume, as is the case here, that the length of the region employed for dispersion on the KAP crystal is much smaller than the length of the crystal. As indicated in Fig.9.4, the angle spanned by the KB mirror relative to the source is α, the grazing angle at the center of the mirror is denoted by φ and the angle subtended by the KB mirror relative to the focus by β. The upper and lower bounds of the grazing angles at the KAP crystal are given by θ_1 and θ_2 respectively. The distance from the source to KB mirror is represented by p and the distance from the mirror to focus by q. From the geometric layout, one can derive that:

$$\beta = \theta_1 - \theta_2 = \Delta\theta \tag{9.4}$$

And after a bit of algebra, one can determine an equation for β:

$$\beta = \arctan(\frac{q * tan(\varphi)}{q - L/2}) - \arctan(\frac{q * tan(\varphi)}{q + L/2}) \tag{9.5}$$

where L is the length of the mirror. Substituting $q = Mp$ into Eqn.9.5, where M is the magnification ratio given by q/p, gives:

$$\beta = \arctan(\frac{pM * tan(\varphi)}{pM - L/2}) - \arctan(\frac{pM * tan(\varphi)}{pM + L/2}) \tag{9.6}$$

Substituting λ by hc/E into Eqn.9.3, where E is the X-ray energy whose Bragg angle is θ_B at diffraction order of n, h is the Planck constant and c is the speed of light in vacuum, taking the derivatives on both sides and solving for ΔE, gives:

$$\Delta E = \frac{2d\ cos\theta_B\ E^2}{nhc}\Delta\theta = \frac{2d\ cos\theta_B\ E^2}{nhc}\beta \tag{9.7}$$

In practical units for d=1.3315 nm and n=1, Eqn.9.7 can be rewritten as:

$$\Delta E(eV) = 2.148\ cos\theta_B\ E^2(keV)\ \Delta\theta\ (mrad) \tag{9.8}$$

Eqn.9.8 together with Eqn.9.6 will give the detection bandwidth of our Bragg crystal spectrometer. For instance, given our experimental parameters for the KB Microscope, i.e.: $p = 130\ cm$, $M = 0.5$, $L = 10\ cm$ and $\varphi = 1.96^o$, Eqn.9.6 yields $\beta = \Delta\theta \simeq 5.25\ mrad$. Substituting $\Delta\theta = 5.25\ mrad$ into Eqn.9.8 along with other parameters, i.e.: $\theta_B = 18.09^o$ and $E = 1.5\ keV$ gives $\Delta E \simeq 24\ eV$, which is adequate to cover the absorption dips for two charge states of aluminum, as presented in Fig.9.1, by viewing a window from 1483 to 1507 eV. This spectral window can be expanded if desired by increasing the subtended angle of the X-rays by increasing the KB demagnification ratio. However, the brightness of the signal will decrease proportionately.

Spectral Resolution

The total spectral resolution of the Bragg crystal spectrometer is limited by the following factors:

1) The intrinsic resolving power of the crystal which is mainly attributed to the imperfections in the crystalline lattice. As shown experimentally in Ref.[171], the resolving power, $\lambda/\Delta\lambda$, of KAP crystal in the first order of diffraction for wavelength between 1.54 $\AA$ and 23.7 $\AA$ can reach above 2000, which suggests that the spectral resolution of the KAP crystal is of the order of 0.75 eV near the Al $K\alpha$ line.

2) The pixel size of the X-ray CCD that defines the spatial resolution of the detector. The pixel size of the CCD in our experiments is 20 μm. The spectral width corresponding to this pixel size is estimated to be 0.35 ± 0.01 eV for a detector at 13 cm away from the KAP crystal for the first order of diffraction based on the spatial shifts of the X-rays on the CCD when rotating the KAP crystal.

3) The spatial broadening due to the Betatron source size and the aberration of the KB microscope system. These two effects were simulated using the SHADOW X-ray tracing program [172] that is an extension package to the XOP software. In the SHADOW simulations, reflectivities of the two KB mirrors and the rocking curve of the KAP crystal were taken into account. The transverse size of the Betatron radiation has been measured in Ref.[66] to be around 2 μm using the knife-edge technique. The SHADOW simulation tends to indicate a negligible effect from this small source size on the spatial broadening. It is worthwhile mentioning that the Betatron radiation may have a longitudinal extension of hundreds of micron that depends on the plasma density and conditions[173]. Nonetheless, thanks to the small aperture angle ($\sim$ 2.6 $mrad$) of the KB mirror relative to the source, the effect due to this magnitude of the longitudinal extension on the spatial broadening is equivalent to a transverse size of 1-2 μm at the source position, which again is negligible. On the other hand, as indicated in Fig.9.5, the SHADOW simulation shows that at the best focus condition of the KB microscope, the line broadening in the dispersion direction due to the aberration of the two KB mirrors is approximately 43 μm at the detector position, corresponding to a spectral width of 0.75 eV.

4) Since multiple shots will typically be required to record spectra there is also a contribution from shot to shot variations of source position. The shot to shot variations of the source position consequently lead to the spatial motion of the probe spot at the target position, which was measured to be around 16

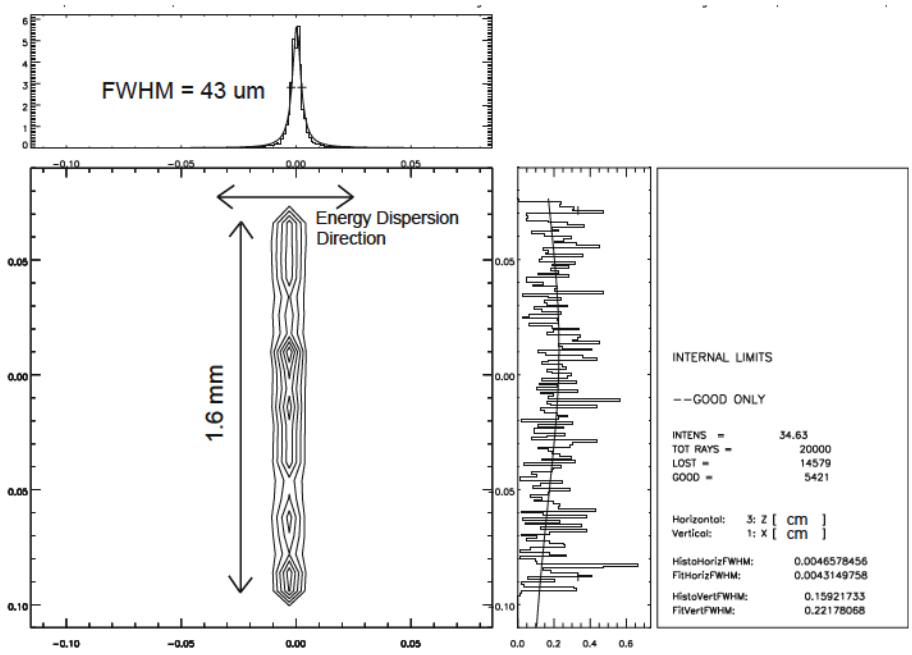

Figure 9.5: Contour plot of the simulated broadened Al Kα line at X-ray CCD position using SHADOW program. This is achieved with the KB microscope at the best focus condition. A Lorentzian fit to the horizontal lineout of the Al Kα line shows a FWHM of 43 um. The intensity distribution in vertical direction is rather uniform with a length of $\sim$ 1.6 mm. The simulated geometric layout is the same as that in Fig.9.2. The input parameters for the source are as follows: (1) photon energy and number of ray : 1.487 keV and 20,000; (2) transverse spatial distribution: Gaussian with FWHM size of 2 μm in both horizontal and vertical directions; (3) longitudinal spatial distribution: uniform with length of 400 μm; (4) angular distribution: Gaussian with FWHM angle of 4 mrad in both horizontal and vertical directions.

μm by taking the standard deviation of the image spot centroid positions for a series of data shots. The influence of the variation of the probe spot position on the spectral blurring can be simulated by taking a 64 μm (FWHM) effective source spot size (due to the 2X demagnification of the KB microscope system). When this is done the effective width on the CCD detector becomes ~ 50 μm, which corresponds to a spectral width of 0.88 eV.

From the above analysis, one can see that the resolution of our system is limited primarily by resolving power of the crystal, the aberration of the KB microscope and the shot to shot variations in source spot position. Assuming the final resolution is the quadratic combination of the above four widths, one can obtain the total resolution of our system of ~ 1.4 eV or a resolving power of ~ 1100 near the Al $K\alpha$ line.

Reflectivity

The reflectivity of the KAP crystal was calculated using the built-in Xcrystal function of XOP, which is specified to compute the reflectivity for perfect and mosaic crystals. In calculating the X-ray reflectivity, XOP utilizes the DABAX database to define the crystal structure and to retrieve the scattering factors to build the crystal structure factors. Input parameters to Xcrystal are given as follows: the KAP crystal was assumed perfect with Miller indices of (001), the temperature factor was set to unity and the Mosaic crystal was turned off, the crystal was treated in Bragg geometry and the beam intensity was calculated in the diffracted direction, the Rocking curve was centered at zero degrees, the X-ray energy was fixed at the Al Kα line, i.e.: 1.487 keV (8.34 $\mathring{A}$), and the asymmetry angle of the crystallines and the thickness of the crystal were set to zero and 3 mm respectively. The program automatically considers the absorption of the X-rays by the crystal and also automatically separates the results for p-polarization and s-polarization. Results of the reflectivities for p and s polarizations are presented together in Fig.9.6. The integrated

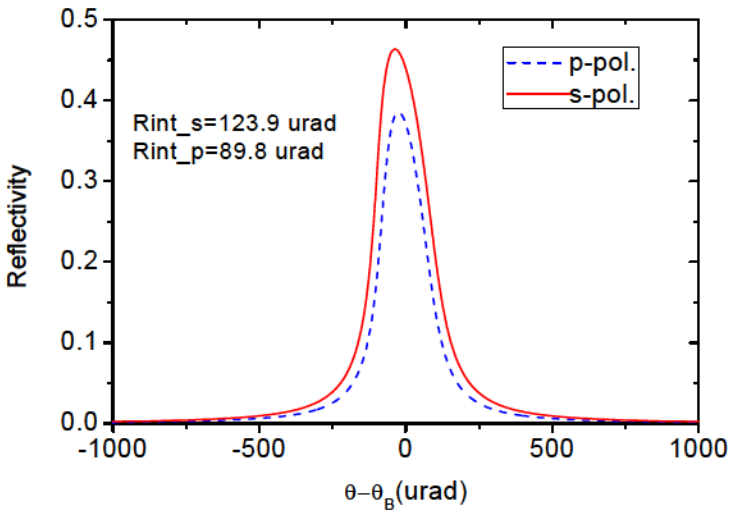

Figure 9.6: Rocking curve of flat perfect KAP crystal at 1.487 keV achieved with XOP. Solid curve: s-polarized light, dashed curve: p-polarized light.

reflectivity, peak reflectivity and FWHM angle of the calculated Rocking curve for KAP crystal are 89.8 (123.9) urad, 0.386 (0.463) and 174.6 (205.2) urad for p (s) polarization light respectively. By comparing to the measured integrated reflectivities for unpolarized Al Kα light as reported in Ref.[174] ($\sim$ 83 urad) and Ref.[175] ($\sim$ 86 urad), one finds that the unpolarized integrated reflectivity, average of the p and s polarizations, achieved by the XOP is higher by $\sim$ 30% due to the ideal nature of the simulated crystal. Thus, to be more realistic, we chose the p-polarized Rocking curve to represent the actual behavior of the KAP crystal for any SHADOW simulations that are described in this paper.

9.2.3 Measurement Efficiency of the Integrated Setup

The measurement efficiency of our setup is defined as the ratio of the number of X-ray photons of interest within a bandwidth of ΔE collected by the X-ray CCD after the KAP crystal to the total of all the emitted same energy X-ray photons generated by the Betatron oscillations in laser wakefield cavity. For a given flux of $N_e(\nu)$ photons per steradian per $0.1\%BW$ per shot, the number of X-ray photons per shot within a certain bandwidth ΔE at the energy of interest that are detected by the CCD chip $N_d(\nu)$ can be given by:

$$N_d(\nu) \simeq N_e(\nu)\frac{\Delta E}{0.1\%BW}\{\Omega_{kb}R_{kb}(\nu)\}\{\frac{W_cR_p}{\Delta\theta}\}QE(\nu)T(\nu) \tag{9.9}$$

Here we assume ΔE is relatively small such that the photon flux per unit energy can be treated as a constant within this range. Inside the first bracket are the KB microscope parameters, with Ω_{kb} representing the solid angle and $R_{kb}(\nu)$ the total combined reflectivity of two KB mirrors. Inside the second bracket is the effective reflectance of the KAP crystal, with W_c the FWHM angle of the rocking curve, $\Delta\theta$ the angular width of all the imaged rays striking the KAP crystal surface, and R_p the peak reflectivity of the rocking curve. $QE(\nu)$ is the quantum efficiency of the X-ray CCD and the $T(\nu)$ is the transmission of the overall filters set in the beam path.

Dividing Eqn.9.9 by the total emitted photons of interest $N_e(\nu)\Omega_e\Delta E/0.1\%BW$, with Ω_e the betatron emission solid angle, one can obtain the overall detection efficiency η of our system, which is given by:

$$\eta \simeq \{\frac{\Omega_{kb}}{\Omega e}R_{kb}(\nu)\}\{\frac{W_cR_p}{\Delta\theta}\}QE(\nu)T(\nu) \tag{9.10}$$

For example, we can estimate the efficiency for the 1.5 keV photons that we are interested in using to measure the ionization states of the warm dense aluminum. To first order, we assume $QE = 1$ and $T = 1$; Substituting our experimental conditions into Eqn.9.10, i.e.: $\Omega_{kb} \simeq 4.3\ \mu srad$, $\Omega_e \simeq 288\ \mu srad$,

$R_{kb} \simeq 0.6^2$, $\Delta\theta \simeq 5.25\ mrad$, along with XOP simulated Rocking curve parameters of the KAP crystal, i.e.: $W_c \simeq 174.6\ \mu rad$ and $R_p = 0.386$, gives $\eta \sim 7 \times 10^{-5}$.

To verify the derived detection efficiency, SHADOW simulation was implemented. All the input parameters are the same as those used in the simulation that produces the result shown in Fig.9.5 except the divergence angle of the source was changed to the measured result of 24 $mrad \times 12\ mrad$. Note that no filters were inserted into the simulated layout in order to compare with the above estimation, and the detector at the CCD position is assumed to be a perfect detector with a quantum efficiency of unity. Multiple runs of the simulation yield a total ray intensity of 2.2 was detected at the CCD position for a total input intensity of 25,000 of the source rays, which gives a simulated detector efficiency $\eta_s \sim 9 \times 10^{-5}$. Note that the SHADOW program assumes the intensity of each ray is one at the source and 25,000 is the maximum number of the input rays. Thus, there is agreement between the simulation and calculated result which allows us to predict the number of photons of interest detected by the CCD chip.

9.3 Results

9.3.1 X-ray Focus Measurement

A typical single shot image of the KB image spot for the Betatron radiation for a given combination of the ROC's for the two grazing incident mirrors is shown in Image (a) of Fig.9.7. As clearly indicated by the lineouts plotted in (c) and (d), in the horizontal direction, the spot has a much gentler falling edge on the left, which manifests itself as a sloping tail as shown in (a), and in the vertical direction it has a shoulder downwards. The FWHM of the spot in horizontal and vertical directions for this ROC condition is measured to be 67±6 um and 63 ± 6 um by averaging over 14 consecutive shots, with the error bar being the

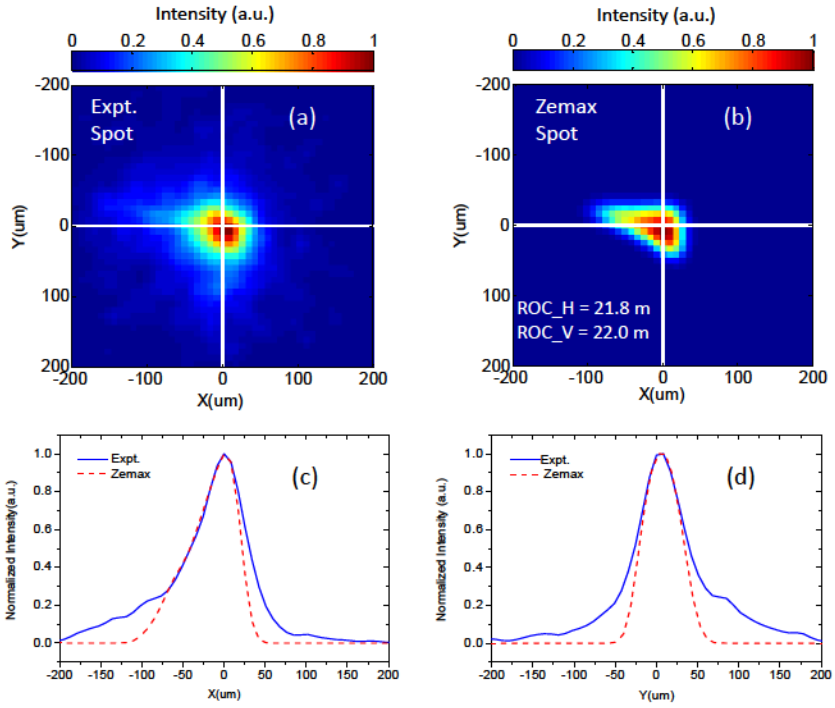

Figure 9.7: Images of the Betatron radiation at the WDM target position observed using the fluorescent screen imaging system for a given combination of ROC's for the two KB mirrors. (a) is the measured single shot focal spot and (b) is the Zemax simulated spot that is found to best match the measured one shown in (a). Intensities of both images are normalized to unity for comparison. The horizontal lineouts of spot (a) and (b) are plotted in (c), while the vertical are shown in (d). Lineout positions are indicated by the white lines in (a) and (b), and the linewidths are set identically to 60 um such that it is adequately wide to cover the asymmetric features observed in both spots.

standard deviation of the measurements. To assese the experimental focal spot results, a ray tracing program called Zemax [176] was applied to model our KB microscope setup.

Non-sequential mode was used for the Zemax simulations, and the major input settings are described below: the source was defined as a circular source with a full width of 2 um in both X and Y axes. Here we omitted the longitudinal extension of the betatron source in the Z direction since the effect is negligible as described previously. Rays from the source are emitted in a Gaussian distribution with the FWHM divergence angle of 4 mrad for both horizontal and vertical directions, which is wider than the acceptance angles of both KB mirrors. The angle of each KB mirror relative to the propagation axis was fixed at the same angle as that set in the experiments. The ROC's of the two KB mirrors are the two chief variables that were adjusted to match the focal spots with those achieved from the experiments. The pixel size of the detector was set smaller than the instrumental resolution of the imaging system, and the default smoothing method on the spot image was turned off. The raw simulated focal spot was convolved with a 2-D Gaussian instrumental function with FWHM of 15 um estimated as the approximate resolution of the system used to image the X-ray fluorescent spot. An example of the processed spot obtained from the ray tracing simulation is presented in image (b) of Fig.9.7. This spot was achieved with the ROCs of 21.8 m and 22.0 m for the horizontal and vertical focusing mirrors respectively and is found to best match the experimental spot as shown in (a). While the general widths of the spots are matched fairly well, discrepancies are noticed between the simulated and measured spots in the wings of the profile. For instance, in the vertical direction, the simulation does not see the pedestal shoulders as seen in experiment. Furthermore, the horizontal lineout of the simulated spot falls off faster on the lefthand side than the experimental one. The aforementioned disparities may be caused by the following two factors: a) the possible non-uniformity of

the ROC across the KB mirror and b) scattering of light in the diffuse layer of the Lanex screen. As mentioned early, there are two motors, one at each end of the mirror, to bend the 10-cm-long mirror. Hence it is possible that one can bend the mirror non-uniformly and a certain amount of non-uniformity of ROC may exist across the mirror in the experiments. This non-uniformity may contribute to the extra shoulder features seen in the experiment. The scattering of generated optical photons within the Lanex screen may also play a role in blurring and producing a diffuse halo spot around the initial spot. In contrast, the Zemax simulation assumes perfectly curved mirrors and a perfect detector where no scattering effect is present.

9.3.2 X-ray CCD Image Processing

From the estimated detection efficiency of 7×10^{-5} and expected source brightness of 1×10^{8} $photons/srad/0.1\%BW$, we only expect to detect a handful of photons per laser shot at the detector. Fig.9.8(a) shows a cropped region of the raw X-ray CCD image in which the signal of the KAP crystal is located. As shown, due to background hard X-rays hitting the detector from the wakefield electron source, the raw image is quite noisy such that the actual signal reflected by the KAP crystal is hard to see in the image. The background arises from the energetic wakefield electrons generating γ radiation upon impacting materials which in turn produce secondary radiation throughout the laboratory area for each laser shot. Nonetheless, as we know the CCD brightness response is essentially a pulse height response proportional to photon energy, in principle we can isolate the signal pixel events for photons of a particular energy from those at other energies caused by the spurious background at random energies. An algorithm known as single-pixel event [177, 178] was implemented to reconstruct the Bragg crystal spectrum. Prior to the algorithm, a cleanup method on the background subtracted image was carried out to eliminate the multiple connected pixels which are evidently introduced by the background

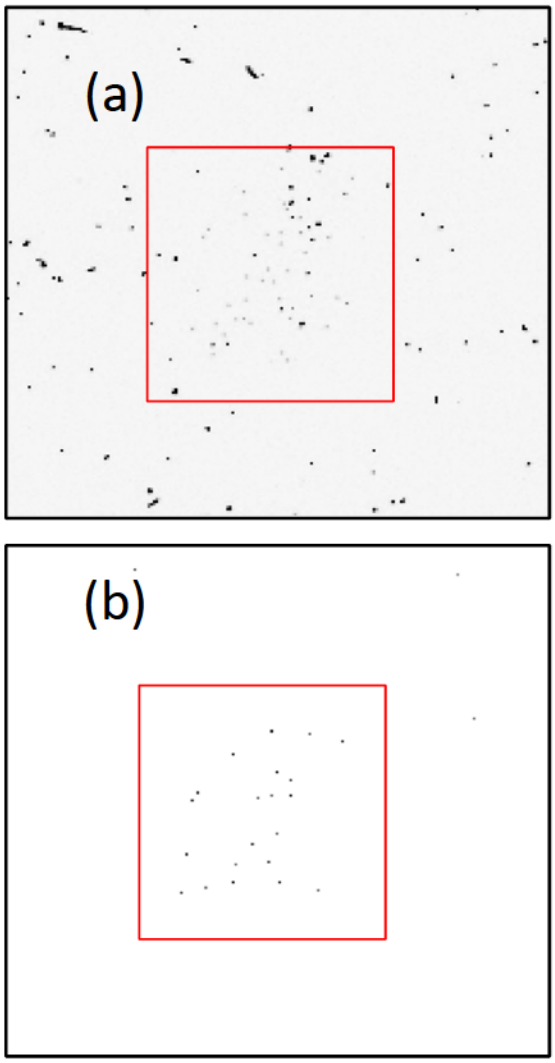

Figure 9.8: (a) Cropped image of the raw single-shot X-ray CCD image (b) Processed X-ray image using the single-pixel event algorithm for the same data of (a). Red boxes indicate the approximate region where the reflected X-rays from the KAP crystal are located.

X-rays as seen in Fig.9.8(a). As described in Ref.[177], in the single-pixel event algorithm, the ratio of each pixel to the sum of it and the adjacent 8 pixels was used a criterion to determine the single-pixel event. In our case, this ratio is 61% by setting the pixel value as 3 times of the CCD noise level for all adjacent 8 pixels. Furthermore, for simplicity, after the algorithm, we only keep the pixels within 1 to 2 keV pulse height range. From previous calibrations we know that 150 counts approximately corresponds to 1.5 keV. As an example, the processed image using the above approach is shown in Fig.9.8(b), whose raw image is depicted in Fig.9.8(a). As indicated in Fig.9.8(b), after the single-pixel event algorithm, there is a clear cluster of bright pixels that are situated in the middle of the processed image. In addition, the location of the cluster agrees with what we expect based on the incident angle of KAP crystal, implying that this cluster of bright pixels of the correct energy is the X-ray signal that is reflected by the KAP crystal. The total transmission of the overall filters that were used in this data shot is approximately 0.5 at 1.5 keV, and the quantum efficiency QE of our CCD chip is around 73.5% at 1.5 keV according to the manufacturer's specifications. Substituting these two parameters into Eqn.9.9, and using the estimated detection efficiency of 7×10^{-5}, one can obtain the corrected overall detection efficiency of 2.6×10^{-5} for our system. This detection efficiency gives the number of 1.5 keV photons that we expect to be detected by the CCD chip as $N_d \simeq 12$ for the detection bandwidth ΔE of 24 eV and an average source fluence of 10^8 $photons/srad/0.1\%BW$. This estimated number of photons is close to what we observe in Fig.9.8(b) where around 19 X-ray photons are detected after background subtraction for a particular bright spot.

9.3.3 X-ray Wavelength Tuning

The fact that in a single shot only a dozen of 1.5 keV photons manage to reach the CCD chip necessitates multiple-shot operation in order to observe enough photons to statistically measure the absorption features as shown in Fig.9.1.

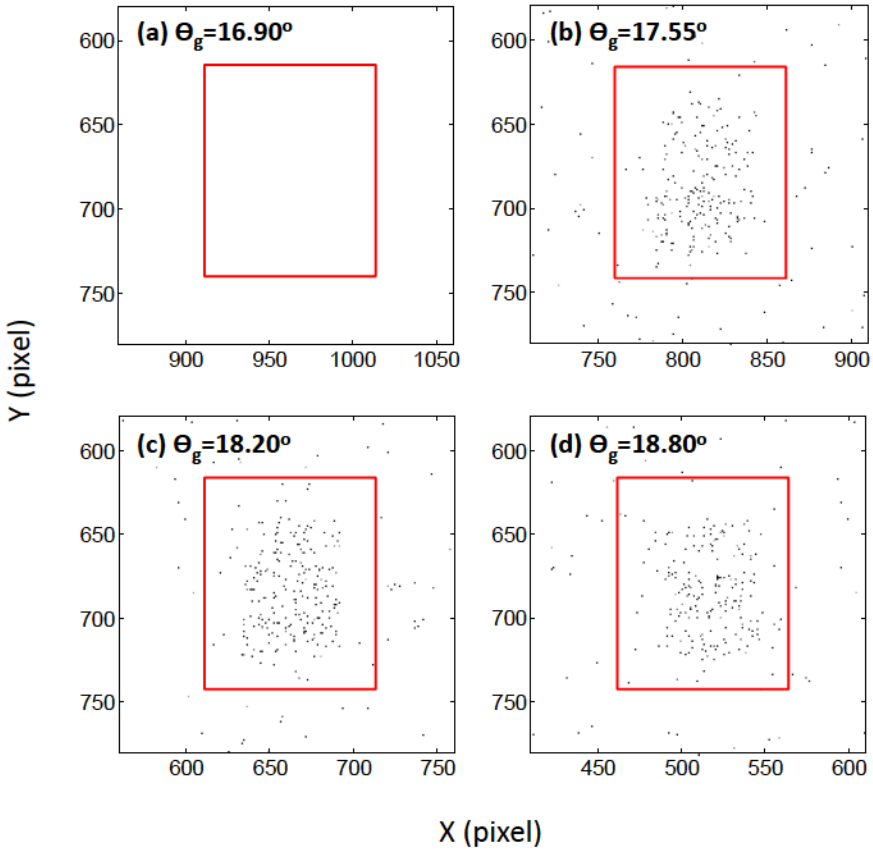

Figure 9.9: Accumulated X-ray CCD images for different grazing angles of the KAP crystal. The number of accumulated shots at each angle varied from 20 to 30 shots. Note that no WDM target was fielded in these measurements and the X-ray filters applied here are identical to those used in Fig.9.8. Red boxes hightlight the approximate signal regions for the different angles.

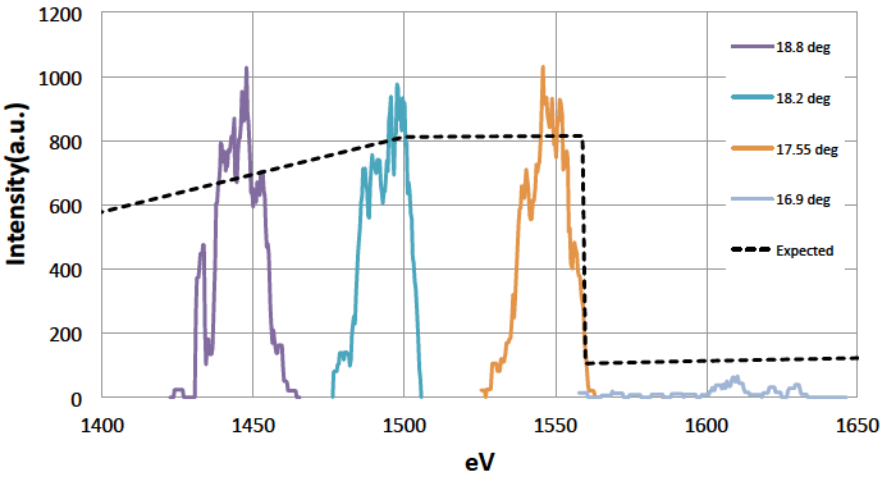

Figure 9.10: X-ray wavelength tuning of the KAP crystal. The dashed black line is the expected X-ray transmission curve after taking into account all the X-ray filters in the beam path. Solid curves are the detected X-ray spectra corresponding to the accumulated images as shown in Fig.9.9; The intensity of each spectrum was normalized to the total measured X-ray input for a given number of accumulated shots. Note that spectral curves shown here are the smoothed results of raw lineouts using a 3.5 eV smoothing window.

For instance, to distinguish a 10% absorption dip, a minimum signal level of approximate one thousand photons within the spectral linewidth ($\sim 4eV$) is required to give 3% standard deviation leading to a signal measurement at a confidence level of 3 standard deviations.

The accumulations of post-processed CCD images for a given number of shots at four different grazing angles of the KAP crystal were carried out and the results are depicted in Fig.9.9. In these images, the horizontal direction is the energy dispersion direction whereas the vertical is the transverse spatial dimension. Looking at the last three images, (b)-(d), where clear clusters of photons are seen, one finds that the vertical height of the signal region is around 1.7 mm after converting the pixel number (20 um/pixel) into mm, which matches well with what the SHADOW simulation shown in Fig.9.5. Also an average of 10 photons per shot was found for these three angles, again agreeing well with what we predicted. In image (a), the number of observed photons decreases significantly due to the fact the spectrum at this particular Bragg angle is shifted into the absorption region of the Aluminum K-edge, as indicated in Fig.9.10. Taking the horizontal lineouts for the images as shown in Fig.9.9, and converting the pixel units into eV, one can reconstruct the X-ray spectra selected by the KAP crystal, and the results are plotted in Fig.9.10. Also plotted in the graph is the X-ray transmission curve after considering all the filters that were inserted in the beam path of our system. As depicted in the graph, the trend of the measured intensities of X-ray pulses at different energy ranges matches well with the predicted transmission curve. Furthermore, the average spectral width of the measured x-ray pulses is (23 ± 2) eV, which is in good agreement with the predicted width of 24 eV. However, one can clearly see from the spectral curves large fluctuation in the measured spectral signal, indicating that many more data shots must be taken in order to reduce the noise and allow observation of the K-shell absorption lines of warm dense heated Aluminum as we wish to measure. If we accept a measurement bandwidth of

4 eV and require an rms measurement error of 3.3% within this bandwidth, approximately 1000 photons must be detected within this interval leading to 6000 photons detected over our entire 24 eV bandwidth. Given a detection efficiency of $\sim$ 10 photons/shot would require 600 shots per measured spectrum.

9.4 Conclusion

In conclusion, we have developed a femtosecond time scale X-ray probe for time-resolved measurements of the ionization states of the warm dense heated aluminum. The X-ray probe is based on the Betatron oscillations occurring in a laser driven wakefield cavity. A systematic characterization to the X-ray probe setup has been carried out both theoretically and experimentally, indicating that the source is suitable for carrying out high spectral resolution time resolved X-ray probing in the 1.5 keV X-ray range. An overall X-ray efficiency of 2.6×10^{-5} is achieved leading to the detection of $\sim$ 10 X-ray photons in the 24 eV measurement window per shot. Thus, high sensitivity X-ray measurement will require hundreds of shots per measured spectra which in principle is achievable given the 10 Hz repetition rate of the actual source laser. In the next chapter, we combine this probe with the optical heating of thin targets to obtain the absorption spectra of the warm dense aluminum.

Chapter 10

Measurements of Ionization States in Warm Dense Aluminum with Femtosecond Betatron Radiation

In Chapter 9, we have presented the results of characterizing the laser wakefield generated X-ray probe for measuring the ionization states of warm dense aluminum. In this chapter, we present the results of integrating this X-ray probe with an optical heating laser pulse for creating warm dense aluminum and the results of the first-time measurement of ionization states of warm dense aluminum with such integrated setup.

10.1 Physics Background

In the introduction of Chapter 9, we have underlined the significance of studying the ionization states of WDM, described the technique of K-shell line absorption spectroscopy for measuring the ionization states of WDM and emphasized that femtosecond Betatron radiation generated from the laser wakefield

acceleration is an ideal tool for measuring such phenomena on the time scale of femtoseconds. In this section we turn our attention to the calculation of opacity that accounts for radiation absorption in the technique of K-shell absorption spectroscopy. The goal of this work is to develop a simple model which can be incorporated as a post processor for hydrodynamic simulations of the plasma expansion to predict the line of sight integrated x-ray line absorption for any given plasma density and temperature profile.

Knowledge about the opacity of materials is of great importance in the study of stellar interiors. As such, most of models for calculating the opacity in materials were developed by astrophysicists and can be traced back to the early 1900s. However, in the 1980s, the interest in this subject was aroused again by the research on hot and dense plasmas generated by intense laser or particle beams interacting with matter. The conditions of plasma produced in this way are similar to those existing in stellar interiors. Under these conditions, transport of energy relies in part on the radiation that in turn affects the hydrodynamic behavior of the plasma.

Computing the opacity or photoabsorption coefficient with a high degree of accuracy is not trivial as it requires rather sophisticated computer codes. The main difficulties lie in accurate determination of energy levels for a given ionic configuration, treatment of a large number of excited states and line transitions associated with diverse ion species, as well as the computation of the spectral line profiles. To avoid those difficulties for the accurate calculation of opacity, we resort to an approximate method for computing opacities in hot and dense plasmas demonstrated by Tsakiris et al. [179]. This method is based on the average ion model for calculating the occupation numbers of various electronic levels of a fictitious average ion [180], assuming Local Thermodynamic Equilibrium (LTE) conditions. Subsequent photoabsorption coefficients were computed in the hydrogenic approximation and then were appropriately averaged to obtain the mean opacities. As indicated in the paper, the opaci-

ties calculated with this approximate method show reasonable agreement with those from other detailed and more elaborate calculations, in addition, the ranges of mass density and plasma temperatures for calculating the opacities cover the region of our interest, i.e.: warm dense matter regime, therefore, it is worthwhile for us to employ this scheme to compute the opacity of warm dense aluminum.

10.1.1 The Average Ion Model

The average ion (AI) model is an approximate atomic model to describe complex atoms (with more than one electron) that are embedded in plasma environment. The basic idea of the AI model is to make use of the known hydrogen-like results as much as possible. In the AI model, the ion of interest is treated as a fictitious ion with 10 shells of electrons surrounding the nucleus. The fractional occupation number, P_n, up to 10 shells are derived from the following set of nonlinear equations [179, 181]:

$$P_n = \frac{2n^2 d_n}{1 + (317A/\rho Z_i)T^{3/2} exp(E_n/T)} \tag{10.1}$$

$$Z_i = Z - \sum_n P_n \tag{10.2}$$

$$Z_n = Z - \sum_{m \neq n} P_m \sigma_{nm} - P_n \sigma_{nn}[1 - (1/2n^2)] \tag{10.3}$$

$$E_n = -13.6 \times 10^{-3}(Z_n/n)^2 + \Delta E_n \tag{10.4}$$

where the electrons are distributed in different energy levels according to the Fermi-Dirac distribution. The principle quantum number of each level is denoted by n (n=1,2,..,10). The material is characterized by atomic number Z and weight A, the temperature T (keV), and the density ρ (g/cm^3). The ionization state Z_i is simply the difference between the atomic number and the total bound electrons given by $\sum_n P_n$ in Eqn.10.2. The screened nuclear charge Z_n at the position of the nth shell is given in Eqn.10.3. The screening

Table 10.1: Screening constants σ_{nm} as given by Mayer (1947).

m \ n	1	2	3	4	5	6	7	8	9	10
1	0.6250	0.9383	0.9811	0.9870	0.9940	0.9970	0.9990	1.0000	1.0000	1.0000
2	0.2346	0.6895	0.8932	0.9400	0.9700	0.9840	0.9900	0.9930	0.9950	1.0000
3	0.1090	0.3970	0.7018	0.8500	0.9200	0.9550	0.9700	0.9800	0.9900	1.0000
4	0.0617	0.2350	0.4781	0.7050	0.8300	0.9000	0.9500	0.9700	0.9800	0.9900
5	0.0398	0.1552	0.3312	0.5310	0.7200	0.8300	0.9000	0.9500	0.9700	0.9800
6	0.0277	0.1093	0.2388	0.4000	0.8540	0.7350	0.8300	0.9000	0.9500	0.9700
7	0.0204	0.0808	0.1782	0.3102	0.4590	0.6100	0.7450	0.8300	0.9000	0.9500
8	0.0156	0.0625	0.1378	0.2425	0.3710	0.5060	0.6350	0.7500	0.8300	0.9000
9	0.0123	0.0494	0.1106	0.1936	0.2990	0.4310	0.5440	0.6560	0.7600	0.8300
10	0.0100	0.0400	0.0900	0.1584	0.2450	0.3530	0.4660	0.5760	0.6700	0.7650

constants σ_{nm} are taken from Ref.[180] and listed in Table 10.1. The screening constants essentially describe the degree of shielding of the nuclear charge due to an electron in the mth shell as seen by an electron in the nth shell.

Using the screened charges, the energy of each level E_n (keV) is given by Eqn.10.4. The first term of Eqn.10.4 is the standard expression for isolated hydrogenic atomic levels but with nuclear charge replaced by the screened charge at level n as given by Eqn.10.3, whereas the second term ΔE_n represents the energy shift due to continuum lowering [26], which describes the pertubation of energy levels due to the coulomb interaction of the host ion with free electrons and other ions in the plasma. The expression for this energy shift is given by [179]:

$$\Delta E_n(keV) = 9.805 \times 10^{-3} Z_i [3.6(\rho/A)^{1/3} - 0.13(7 + 5/n^2)\rho/A] \qquad (10.5)$$

Generally, this energy shift is a small modification to the inner shell energy levels but it becomes important when the principle number is higher.

In addition, the AI model takes into account the pressure ionization[182], a phenomenon illustrating the change of the ionization potentials of bound states and the level occupation numbers due to the screening effects of neighboring electrons and ions occurring when atoms are pushed closer together in a high

density plasma. This effect is included by the factor d_n in Eqn.10.1 and is given by: $d_n = 1/[1 + (\alpha R_n^0/R_0)^\beta]$, where $R_0 = (3Am_p/4\pi\rho)^{1/3}$ is the ion sphere radius and $R_n^0 = 0.529 \times 10^{-8} n^2/Z_n^0$ the free atom orbit radius of the nth shell with Z_n^0 the screened charge at the nth shell for a neutral atom. α and β are two free parameters that can be determined by comparing AI with other plasma models.

The AI model neglects the energy splitting of major n shells into n, l subshells and only considers the energy levels corresponding to the principle quantum numbers. As found in Ref.[179], this approximation leads to rather large errors in ionization potential (IP) calculation for high-Z ions such as gold ion, however, for the low-Z ions such as aluminum, satisfactory agreement was achieved by comparing the calculated IP from the AI model with other experimental results. While acceptable for IP calculation, the approximation employed in the AI model must be refined for calculation of an emission or absorption spectra. To achieve this, a quantum defect factor Δ_{nl} that accounts for the subshell splittings is introduced into the Eqn.10.4 as given [183]:

$$E_{nl} = -13.6 \times 10^{-3} (\frac{Z_n}{n - \Delta_{nl}})^2 + \Delta E_n. \tag{10.6}$$

Δ_{nl} can be determined by comparing the calculated line position with other plasma spectroscopic codes that take into account the subshell splitting such as UBCAM [184] and PrismSpect [169]. For example, for the 1s-2p absorption lines of Al^{4+} and Al^{5+} ions, Δ_{nl} was determined to be 0.027 and 0.017 respectively by comparing the line positions (1.49 keV for Al^{4+} and 1.50 keV for Al^{5+}) calculated with PrismSpect .

The averaged ionization states $\langle Z \rangle$ calculated with the AI model using $\alpha = 2$ and $\beta = 8$ as a function of plasma temperature for aluminum at a mass density of 2.7 g/cm^3 are given in Fig.10.1. For comparison, ionization states at the same mass density calculated with other models such as UB-

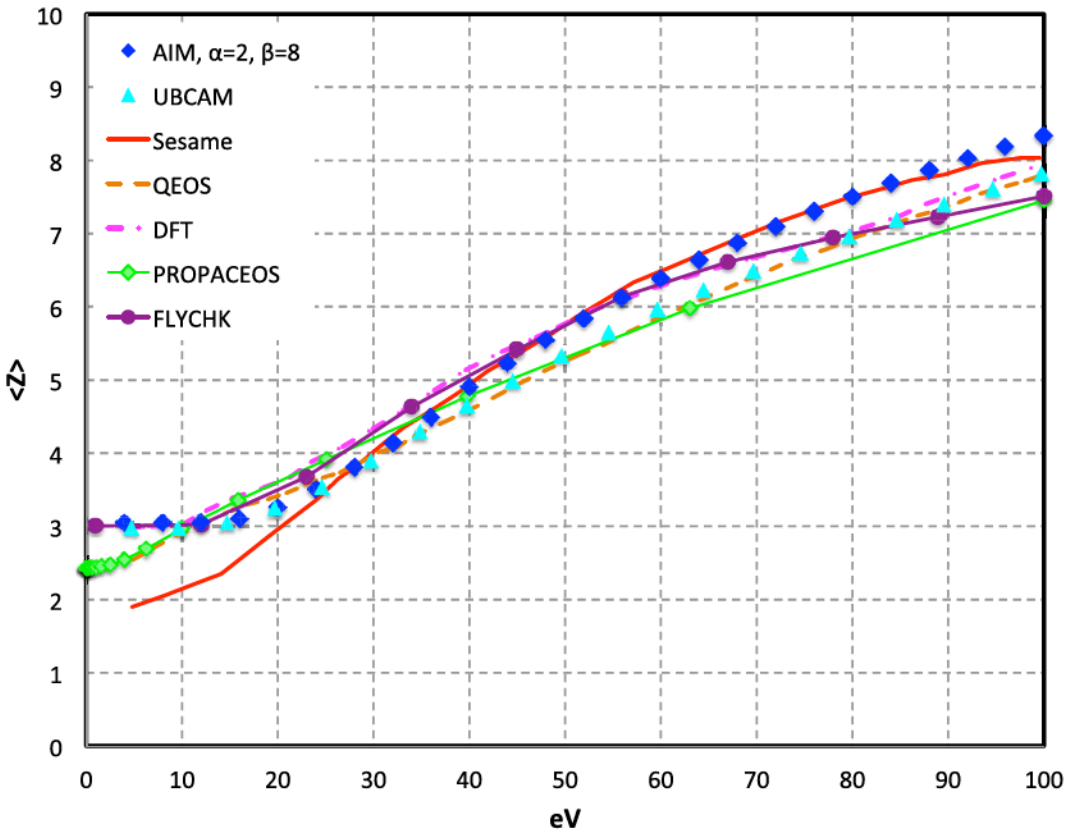

Figure 10.1: The average ionization states of aluminum as a function of plasma temperature at a density of 2.7 g/cm^3 obtained with various models. The curves of ionization states for UBCAM, Sesame, QEOS and DFT were digitized from Figure 1 in Ref.[184].

CAM [184], Sesame[185], quotidian equation of states (QEOS)[186], density-functional-theory (DFT)[187], PROPACEOS [188] and FLYCHK[1] are also plotted in Fig.10.1. As shown in Fig.10.1, the ionization states calculated with the AI model with $\alpha = 2$ and $\beta = 8$ show a good agreement with the results obtained by other models except Sesame below 20 eV.

[1]FLYCHK[189] is an online computer code provided by NIST that is able to compute the ionization and level population distributions of plasmas in zero dimension.

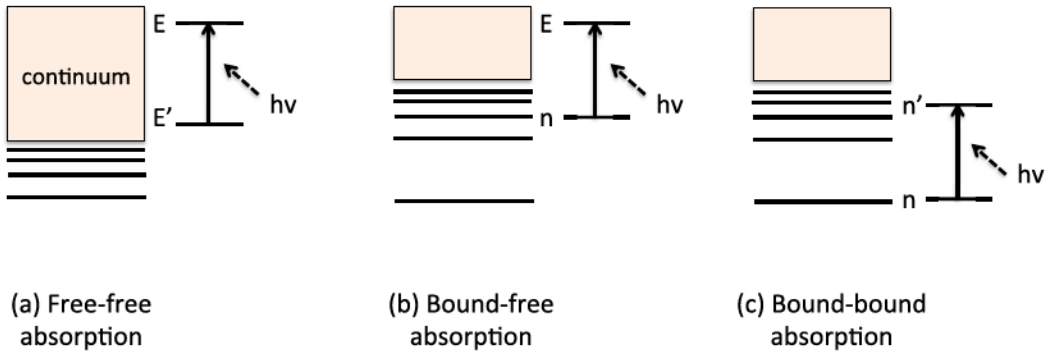

Figure 10.2: Schematic diagrams showing different photo-absorption processes. (a) inverse Bremsstrahlung or free-free absorption, (b) photoionization or bound-free absorption, (c) atomic line or bound-bound absorption.

10.1.2 The Opacity Coefficients

Photoabsorption mechanisms in plasma include the inverse Bremsstrahlung absorption, photoionization absorption and atomic line absorption. Fig.10.2 sketches the principles of these three absorption processes.

As shown in Fig.10.2, inverse Bremsstrahlung absorption involves the transition of electrons occurring in the continuum region, in which the energy states of electrons are positive and electrons are free electrons. Since the final and initial energy states are both positive, Bremsstrahlung absorption is also refereed to as free-free (f-f) absorption. Photoionization absorption, refereed to as bound-free (b-f) absorption, involves bound-free transitions, in which the electron in a bound state (energy state is negative) makes a transition to a free state after absorbing a photon energy $h\nu$. The transition in atomic line absorption occurs between two bound states and is normally refereed as bound-bound (b-b) absorption.

Detailed derivations of the photoabsorption or opacity coefficients for these three atomic processes using the screened hydrogenic approximation [180] can be found in textbook authored by Stefano Atzeni [26]. The expressions for those coefficients are listed as bellowed.

(a) The inverse bremsstrahlung (f-f) opacity coefficient is

$$\kappa_\nu^{ff} = 2.78 \frac{Z_i^3 \rho}{A^2 \sqrt{T_e} (h\nu)^3} \ cm^2/g \tag{10.7}$$

where Z_i is the ion charge, ρ is the mass density of the material in g/cm^3, A is the atomic weight of the material, T_e is the plasma temperature in keV, and $h\nu$ is photon energy in keV. Notice that the ff opacity κ_ν depends on ρ and that the optical thickness $\kappa_\nu \rho R$, where R is the thickness of the plasma, of a given plasma layer scales as $\rho^2 R$.

(b) The photoionization (b-f) opacity coefficient for electrons starting in the nth shell is

$$\kappa_\nu^{bf} = 12.0 \frac{Z_n^4 P_n}{A n^5 (h\nu)^3} \ cm^2/g \tag{10.8}$$

where Z_n is the screened charge as given in Eqn.10.3, P_n is the occupation number of electrons in the nth shell.

(c) The atomic line (b-b) opacity coefficient is

$$\kappa_\nu^{bb} = \frac{6.6 \times 10^4 f(n \to n')}{A} L(h\nu) \ cm^2/g \tag{10.9}$$

In the above equation, $f(n \to n')$ is the oscillator strength and is given by:

$$f(n \to n') = \frac{32}{3\pi\sqrt{3}} \frac{Z_n^4 Z_{n'}^2}{n^5 n'^3} \left(\frac{E_A/2}{E_{n'} - E_n} \right)^3 \tag{10.10}$$

where E_A is the atomic energy unit and is given by $E_A = e^2/a_B = 27.2\,eV$ where a_B is the Bohr radius equal to 0.529 $\AA$. $L(h\nu)$ is the normalized line-shape function ($\int L(h\nu)d(h\nu) = 1$) in units of keV^{-1}.

The line-shape function $L(h\nu)$ in Eqn.10.9 is for characterizing the spectral line broadening associated with the bound-bound transitions. Line broadening mechanisms have been well established in the area of atomic spectroscopy and consist of natural broadening, collisional broadening, Doppler broadening and Stark broadening [190]. The natural broadening arises from the uncertainty of determining precisely the energy level due to the finite life time of the excited energy state. The collisional broadening is due to the fact that the energies of the absorbing or emitting ion are perturbed when the ion suffers frequent collisions with other atoms or ions. The Doppler broadening is a result of the thermal motion of the emitting or absorbing ions. The Stark broadening is caused by electric fields of adjacent electrons and ions perturbing the absorbing or emitting ions. The final line width is the combination of all of the widths caused by the above four broadening mechanisms. For plasma states close to solid density as studied here, line broadening due to the Stark effect is generally dominant over other broadening mechanisms [26]. However, computing Stark broadening is quite complex and is beyond the study of this thesis. To estimate the spectral line width, we resort to a commercial plasma spectroscopic code, PrismSpect[169], which takes into account all of the broadening mechanisms that are discussed here. With the help of PrismSpect, we computed the widths of the 1s - 2p transition line for Al^{4+} and Al^{5+} ions for different mass densities and plasma temperatures, as illustrated in Fig.10.3.

The total photoabsorption coefficient is written as [26]:

$$\kappa_\nu^{tot} = (\kappa_\nu^{ff} + \kappa_\nu^{bf} + \kappa_\nu^{bb})[1 - exp(-h\nu/T_e)] \tag{10.11}$$

including the stimulated emission correction $1 - exp(-h\nu/T_e)$, which reduces

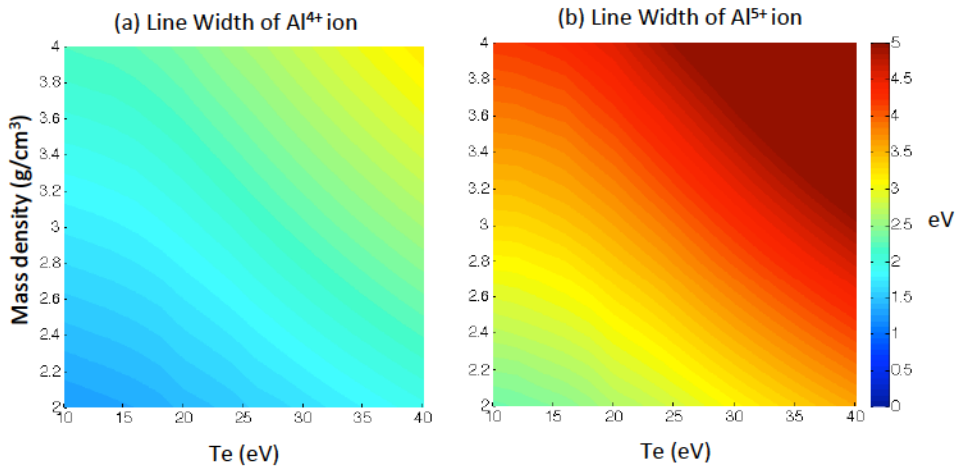

Figure 10.3: 2D contour plots of the calculated line width (in eV) of 1s - 2p transition for Al^{4+} (a) and Al^{5+} (b) ions as a function of mass density and plasma temperature. The calculations were done with PrismSpect [169].

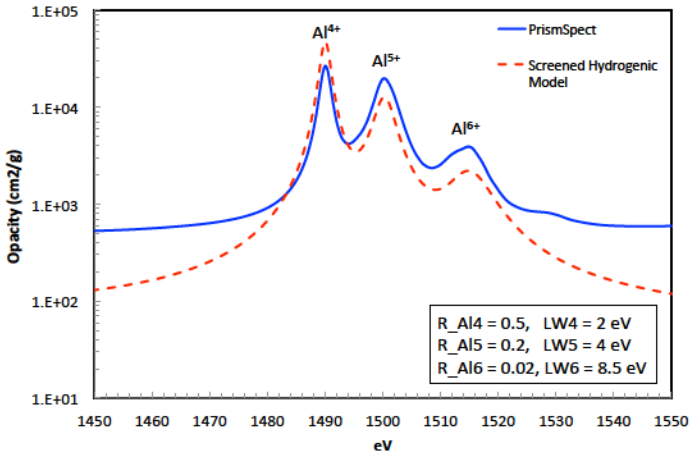

Figure 10.4: Comparison of the opacities of aluminum plasma calculated with the screened hydrogenic (SH) model (dashed red line) and PrismSpect (solid blue line). The plasma is at solid density of 2.7 g/cm^3 and temperature of 30 eV. The opacity peaks from left to right are attributed to the b-b transitions of Al^{4+}, Al^{5+} and Al^{6+} ions respectively. In the SH model, the mass ratios of these three ions and their line widths corresponding to the 1s - 2p transitions are set identical to those calculated by PrismSpect. Mass ratios (line widths) of these three ions are listed on the left (right) column in the textbox at the bottom of the graph. Note that the rest of mass (0.28) is in the form of Al^{3+} ion under this plasma condition according to PrismSpect simulation. The line shape profile for each ion species in the SH model was assumed to be a Lorentzian function with a FWHM equal to the line width achieved by PrismSpect.

the absorption in the equation.

An example of the opacity coefficient for aluminum plasma based on the screened hydrogenic (SH) model described here is plotted in Fig.10.4. For comparison, the opacity for the same plasma calculated with PrismSpect was also presented. In the SH model, the mass ratios of the absorbing ions (Al^{4+} to Al^{6+}) and their line widths corresponding to the 1s - 2p transitions are set identical to those calculated by PrismSpect at the same plasma conditions. As indicated, for the b-b opacities, shown as three peaks in the graph, the differences between the SH calculation and the PrismSpect calculation are within a factor of two. Note that on the two sides of the opacity curve, a factor of 5 in difference is found between the SH and PrismSpect calculations. The discrepancies observed here are probably due to the contribution of other subshell levels not included in the SH model calculation, which might lead to a different screened charge at each shell from that obtained in the PrismSpect that includes the subshell splitting. In the two shoulder regions of the opacity curves, the magnitudes of the opacity are relatively small, only a few hundreds, the final transmission coefficient, given by $T = exp(-\kappa_\nu^{tot}\rho R)$, varies by less than a percent due to such a difference between SH and Prismspect for ρR on the order of 10^{-5} g/cm^2 corresponding to the areal density of the warm dense aluminum studied in this thesis. For the absorbing peaks, the discrepancies in the opacity between the SH and PrismSpect under this plasma condition (2.7 g/cm^3 and 30 eV) would give around 50% difference in the final absorption coefficient for ρR on the order of 10^{-5} g/cm^2. These discrepancies in the opacity calculation indicate that the SH model is an approximate model to compute the plasma opacity. For more accurate results, opacity models that take into account the subshell splitting and more detailed physics calculations should be employed. Prismspect is such a model. In Prismspect, the atomic level population and ionic abundance in a given plasma are calculated based on the collisional-radiative (CR) plasma model incorporating the results of detailed

atomic structures from the Detail Configuration Accounting (DCA) atomic model [191]. The DCA model treats all the ionization stages of the atom to be studied together with all the possible excited states including the states due to the subshell splitting. The atomic level energies, transition energies, oscillator strengths and other atomic data are obtained from Hartree-Fock calculations [192]. The continuum lowering effect is included in PrismSpect using an occupation probability model [193], supplemented by the ionization potential depression formalism of More [194]. In the occupation probability model, the effective statistical weights of energy levels decrease with density, making it difficult for the relatively high-n states to be populated at high densities. The ionization energy thresholds are depressed using the More model, which results in an enhancement of ionization rates and a shift in the location of bound-free edges in computed spectra.

10.2 Integrated Pump-Probe Setup

In Chapter 9, we have described in detail the layout of the Betatron X-ray probe for measuring the ionization states of warm dense aluminum. Here we present the other part of the integrated setup, i.e.: the pump laser or heater pulse for generating the warm dense aluminum. Fig.10.5 shows the schematic diagram of the integrated pump-probe setup, in which the Betatron X-ray probe is identical to the one described in Chapter 9. As shown, the heater pulse was picked off in the wakefield chamber by a half-inch mirror from the main laser pulse that drives the wakefields. After the pickup mirror, the heater pulse was sent to a delay stage that can be motorized from outside the vacuum chamber. After the delay stage, the heater pulse was relayed to the KB chamber by a few mirrors via a second vacuum tube that connects the wakefield chamber and KB chamber. Inside the KB chamber, a pair of thin film polarizers (Altechna, 2-UFP-0800-2060-R1/R2) in combination with a half-wave plate made of 2-mm-

thick Quartz were inserted into the heater beam line to act as an energy adjuster for the heater beam. With this energy adjuster, the energy of the heater pulse at target can vary from zero to $\sim$ 10 mJ. After the energy adjuster, the heater pulse passed through a 1-mm-thick CaF_2 plate that was installed at a small angle with respected to the heater propagation axis. A few percent of the heater energy was reflected by the CaF_2 glass plate and the reflected light was sent to a photodiode (PD) located outside the chamber to monitor the shot-to-shot energy variation of the heater. After entering into the pump-probe chamber, the heater pulse was imaged onto a 50-nm free-standing aluminum foil, with a flat-top profile to ensure uniform heating of the target. This was done by imaging the optical wavefront from an 8-mm-diameter iris in the wakefield chamber onto the target using a CaF_2 lens (2 mm in central thickness) with focal length of 8 cm. The angle of incidence for the heater is 40 ± 1 degrees, as compared to 38.5 ± 1 degrees of the angle of incidence for the Betatron probe. The reflection of the heater pulse after interacting the aluminum target was collected by a lens system and its energy was measured by a photodiode detector installed at the image point of the lens system. The transmitted light through the foil was also collected and monitored by a photodiode detector.

Photodiode calibrations were done before the experiments. The input PD was cross calibrated with a calorimeter (Gentec,QE25-SP) that measured the pulse energy at the target position. The reflection PD and the transmission PD were then cross calibrated with the input PD. When calibrating the reflection PD, a dielectric mirror with reflectivity of 98% at 800 nm was mounted in the target position to reflect the laser pulse to the collecting system. The signals of the PD's were read out at 100 μs after the laser pulse using a 500 MHz bandwidth oscilloscope (Tektronix 5054B) with $1M\Omega$ internal impedance setting. This time delay in measurement was employed to avoid interference from the electrical noise from the laser firing at t=0.

A typical image of the heater beam profile at the target position is shown

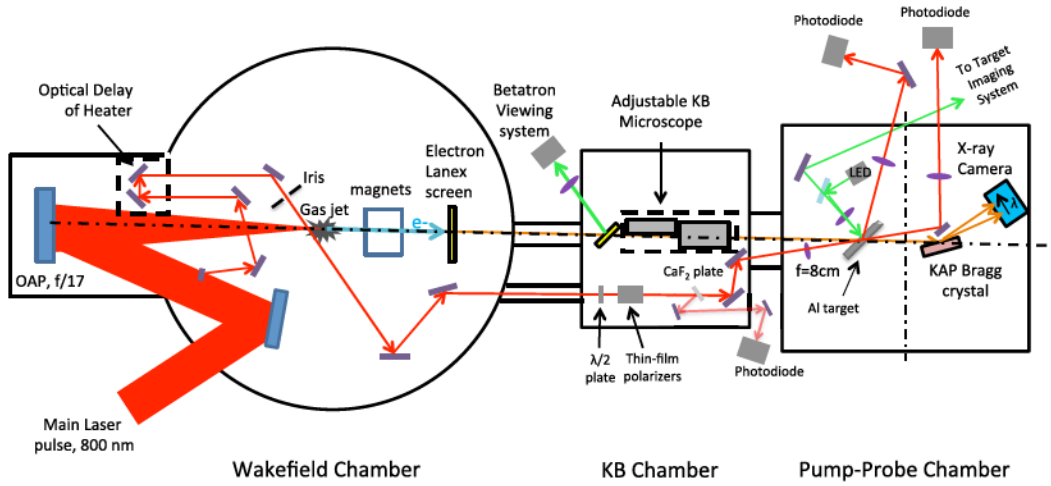

Figure 10.5: Schematic diagram showing the pump-probe setup for Betatron ionization experiments.

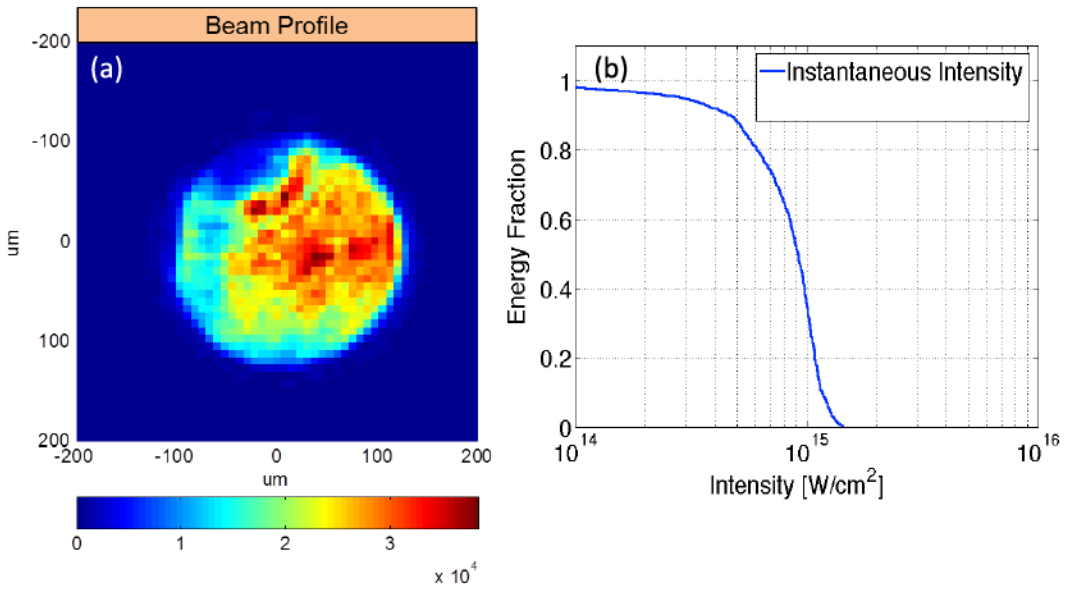

Figure 10.6: (a) Typical intensity image of the heater profile at target position in the 2013 November ALLS Campaign (arbitrary units). (b) Energy fraction versus instantaneuous intensity for the focal spot shown in (a) that was normalized to 10 mJ and 30 fs.

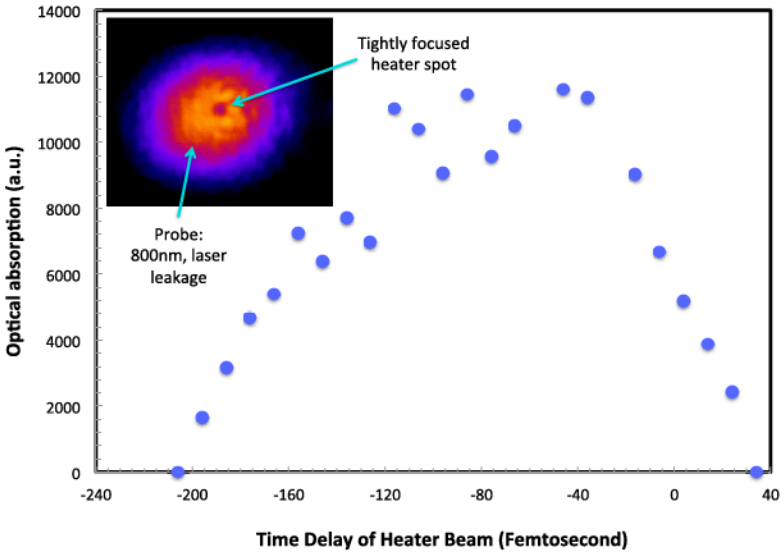

Figure 10.7: Optical absorption in the heater spot versus delay time of the heater pulse to measure the synchronization of the heater pulse with respect to the probe laser pulse. The inset is a typical image of the probe laser spot at the target position when the two laser pulses are synchronized. Positive delay means that the heater beam comes later than the probe beam.

in Fig.10.6 (a). A histogram of the intensity distribution of this laser spot is given in Fig.10.6 (b). As indicated in image (a), the heater beam profile is a quasi flat top with a diameter of approximately 230 μm. It is shown in (b) that 50% and 25% of the energy in the focal spot was contained above intensities of $8.5 \times 10^{14}\ W/cm^2$ and $9.5 \times 10^{14}\ W/cm^2$ respectively, as compared to the peak intensity of approximately $1.3 \times 10^{15}\ W/cm^2$.

Synchronization of the Betatron X-ray probe and the optical heater beam is critical to the experiments. It is difficult to directly synchronize an X-ray and optical beam. However, since the Betatron radiation is known to be synchronized with the laser pulse that drives the wakefield, one can synchronize the heater beam with the leakage of the probe laser in order to synchronize it with the Betatron X-ray. To synchronize these two optical beams, we used an approach of free-carrier induced absorption in glass. This method is described as followed: the heater was tightly focused onto a thin glass plate. Here the

focused heater intensity was controlled just below the damage threshold of the glass to maximize the number of free electrons excited by multi-photon absorption while not damaging the glass. The wakefield generation optical probe pulse was allowed to propagate in vacuum through the KB imaging system to hit the glass plate forming an 800 μm diameter optical spot at that position. A simple lens imaging system was set up to observe an image of the transmitted probe pulse in the glass plate. When the heater pulse proceeded the probe laser, a dark spot in the transmitted probe light is observed at the position where the heater is spatially overlapped with the probe laser, as indicated in the inset of Fig.10.7. This dark spot is a result of inverse Bremsstrahlung photoabsorption by the generated free electrons. The darkness of the absorbing spot is proportional to the number of free electrons existing at the instant when the probe laser arrives at the glass plate, therefore it reflects the synchronization information of the two laser pulses. Synchronization of the heater pulse with the probe laser pulse achieved with the above method is shown in Fig.10.7. The rising edge on the right represents the onset of the absorption from the focused heater beam. The half-max point of the rising edge is defined as the time zero at which time the peaks of the two pulses overlaps. Following the rising edge is a plateau, i.e.: from -40 fs to -120 fs, where the excitation and recombination of the free electrons are balanced. After the plateau, the absorption starts to fall off, which indicates that the recombination process for the free electrons dominates in this period. As indicated in Fig.10.7, the resolution of this synchronization method is of the order of 10 fs, which corresponds to the step size of the motion stage chosen for scanning the delay of the heater. It is estimated that the residual errors relative to the true X-ray pulse timing are of the order of 30 fs. Accurate timing can be established in the end by measuring the rapid rise in ionization in the WDM target itself at the leading edge of the laser heater pulse.

10.3 Experimental Results and Discussions

Fig.10.8 (a) and Fig.10.9 (a) show the raw X-ray spectra measured at 0.5 ps and 1 ps after the Al target was heated. For reference, the X-ray spectra for cold or unheated Al target were also taken, as indicated in Fig.10.8 (b) and Fig.10.9 (b). For convenience, we define the spectrum achieved with pump and probe together as full-shot spectrum, and the one without pump as reference spectrum. The pixel number labeled in the horizontal axes of all the spectra represents the X-ray energy, which increases with the pixel number. The total number of shots acquired for these two data points are 174 and 150 respectively. The incident energy of the pump laser for heating the aluminum target was measured to be approximately 10 mJ. As indicated, it is difficult to distinguish the K-shell absorption dips from the raw full-shot spectrum as it is noisy due to the finite number of X-ray photons arriving at the detector. However, after smoothing the raw spectra with a Gaussian smoothing function, the absorption dips become conspicuous when comparing with the corresponding reference spectra. For both delays, as shown in Fig.10.8 (a) and Fig.10.9 (a), the dip on the left of full-shot spectrum is a result of the photoabsorption by Al^{4+} ion, and the one on the right is by the Al^{5+} ion. Note that for both delays, the spectral intensity of the full-shot spectrum differs from that of the reference spectrum, which is due to the shot-to-shot instability of the intensity of the Betatron radiation generated in the laser wakefield cavities. This has to be taken into account when deriving the final transmission curve of the X-ray through the heated Al target.

Dividing the full-shot spectrum by the reference spectrum, one can obtain the X-ray transmission curve of warm dense aluminum, shown as solid green curves in Fig.10.10. Here the pixel number in the horizontal axes have already been converted to keV using the calibration method of the spectrometer as described in Chapter 9. The measured X-ray transmission curve was normalized

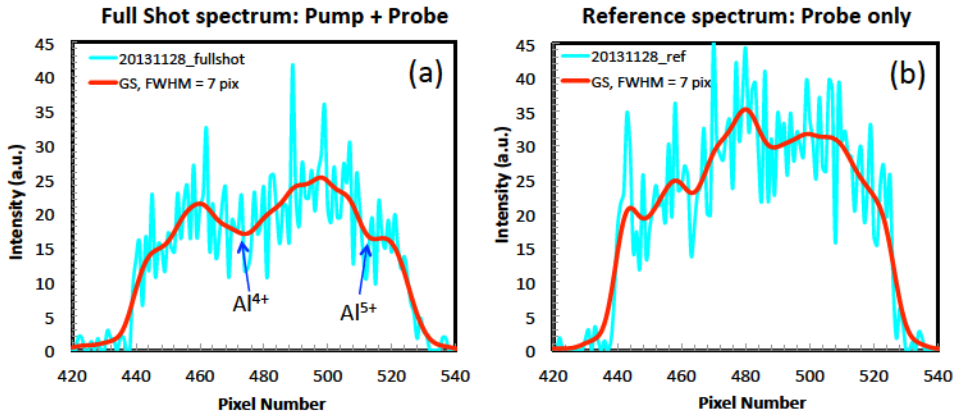

Figure 10.8: (a) Measured X-ray spectrum (cyan) at 0.5 ps after the Al target was heated and corresponding gaussian-smoothed curve (red). (b) Reference X-ray spectrum of (a) in which the pump for heating the Al target was switched off. The Gaussian smoothing functions used for (a) and (b) are identical and have the same FWHM of 7 pixels, corresponding to 2.1 eV in the final energy spectrum. A total number of 174 shots were accumulated respectively to achieve these two spectra. The measured energy of the pump laser at target was 10 mJ.

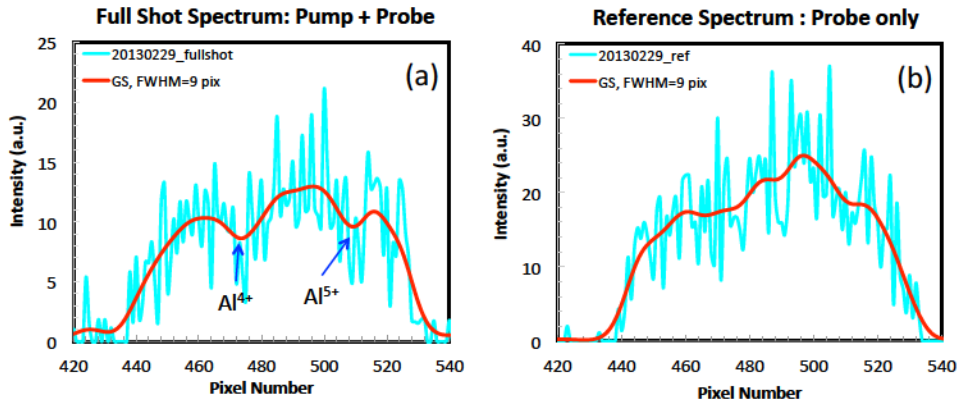

Figure 10.9: Same as Fig.10.8 but at a time delay of 1 ps. The Gaussian smoothing function used here has a FWHM of 9 pixels, corresponding to 2.7 eV in the final energy spectrum. The total number of shots for this data is 150.

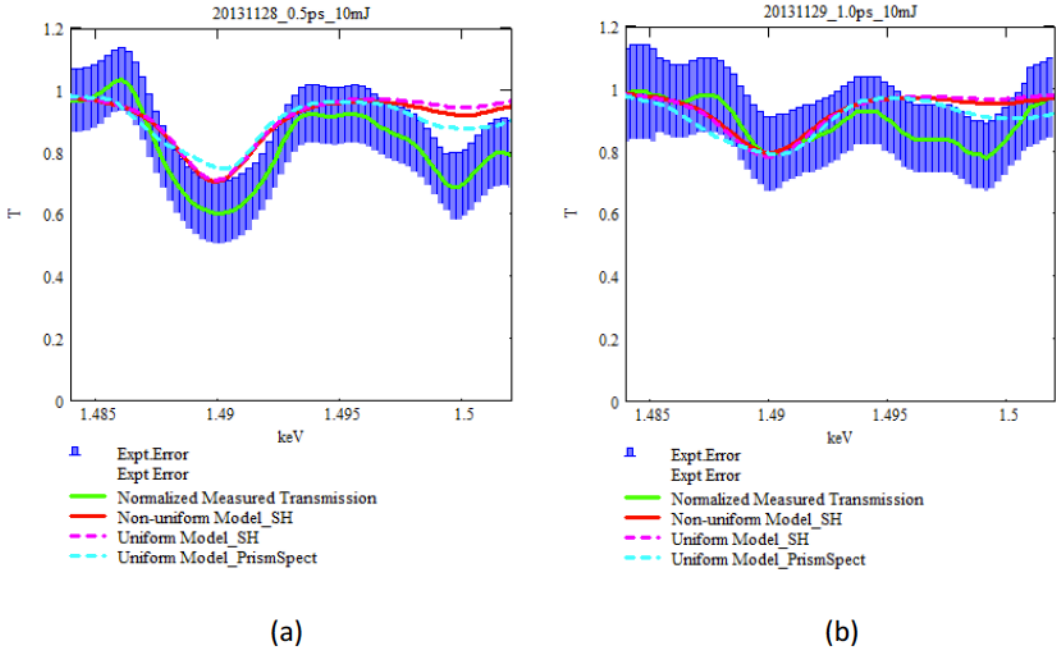

Figure 10.10: (a) Comparison of the measured transmission curve at delay of 0.5 ps with the simulated transmission curves obtained with different models. The measured transmission curve (green solid curve) was achieved by diving the two smoothed spectra as indicated in Fig.10.8 and was normalized to compare with the simulations. The blue bars are the experimental errors with the measured transmission curve. For the simulations, the red solid curve represents the result based on the screened hydrogenic (SH) model assuming a non-uniform slab; the pink dashed curved represents the result based on the SH model assuming a uniform slab; the cyan dashed curve represents the result achieved with PrismSpect assuming a uniform slab. (b) Same as (a) but for the data point achieved at delay of 1 ps, corresponding to the spectra shown in Fig.10.9. For the two uniform slab models, the equivalent electron temperature, mass density and thickness used in calculating the X-ray transmission for the measurement achieved at 0.5 ps (1 ps) are 24 eV (22.5 eV), 2.5 g/cm^3 (2.0 g/cm^3) and 59 nm (68 nm) respectively. The thicknesses shown here have taken into account the angle of incidence of the laser.

in order to compare with the simulations. The error bar of the measurement was achieved by taking the inverse square root of the number of the photons within a certain bin width. For the measurements at delay of 0.5 ps and 1 ps, this bin width was set to 4.5 eV and 5.5 eV respectively. A slightly bigger bin width was chosen for the latter case due to the higher noise level associated with the measurement. From the measured X-ray transmission curves, firstly, one can find that there are two absorption dips, one nearby 1.49 keV and the other one nearby 1.50 keV. The measured positions of these two dips agree well with the positions of the K-shell absorption dips for the Al^{4+} and Al^{5+} ions as calculated by PrismSpect, which is shown in Fig.10.4. Secondly, the time dependence of the ion abundance is resolved. At the delay of 0.5 ps, as indicated in Fig.10.10 (a), the dip caused by Al^{4+} ions is deeper than that caused by Al^{5+} ions, indicating the abundance of Al^{4+} ions is relatively higher that of Al^{5+} ions inside the warm dense aluminum at this particular moment. As the time goes on, the warm dense aluminum cools down and the ions recombine with the free electrons, resulting in a decrease of the ion abundance. This is seen by the shallower dips of Al^{4+} and Al^{5+} in Fig.10.10 (b).

10.4 Simulations and Discussions

To understand the ionized charge distributions leading to the measured K-shell absorption dips at these two time delays, 1D hydrodynamic simulations with MULTI-fs [195] and plasma spectroscopic simulations were employed. The MULTI-fs simulation was conducted to understand the hydrodynamic expansion after a period of 1 ps of the ultra-thin solid-density aluminum irradiated by the 30 fs ultra-short laser pulse. An example of the MULTI-fs simulation is shown in Fig.10.12. The simulated physical states, such as the mass density and electron temperature, of the heated aluminum at the time of interest, were employed as initial conditions for the plasma spectroscopic simulation

to compute the X-ray transmission coefficients. By comparing the simulated X-ray transmission coefficients with the measured ones, one can infer the underlying ionization fraction with the measured K-shell absorption dips. For the plasma spectroscopic simulations, both uniform slab model and non-uniform slab model were assumed to compute the final X-ray transmission coefficients. The opacity calculations were done based on the screened hydrogenic (SH) model as described before or were done with the PrismSpect software. In principle, there are four combinations of the algorithm to compute the X-ray transmission coefficients depending on the selection of slab model and the opacity model. However, due to the expensive computational cost and the complicated data post-processing, the non-uniform slab model with PrismSpect Opacity was not considered here. Details of these three models are given in Appendix C. Here we only give brief overview of each of model.

The flowcharts in Fig.10.11 show the algorithms used in the three models to compute the X-ray transmission curve of the warm dense aluminum. For the non-uniform slab model with SH opacity, as indicated in Flowchart (a), the MULTI-fs code was first used to simulate the hydrodynamic expansion of the solid-density aluminum. The simulated spatial distribution of the electron temperature $T_e(r,t)$ and mass density $\rho(r,t)$ were then used as initial conditions for the FLYCHK to compute the ionized charge distribution at each coordinate r. The generated ionized charge distribution together with the electron temperature, mass density, and spatial coordinates, were substituted into the SH model to compute the opacities of the non-uniform plasma and the final transmission coefficients. Flowchart (b) breaks down the procedures followed in the uniform slab model with SH opacity. Just as in the non-uniform model, a MULTI-fs simulation was carried out first. From the MULTI-fs simulation, the total internal energy $E_{internal}$ of the plasma system was calculated by subtracting the kinetic energy contained in the system that contributes to the hydrodynamic expansion from the total absorbed laser energy. Assuming this amount of in-

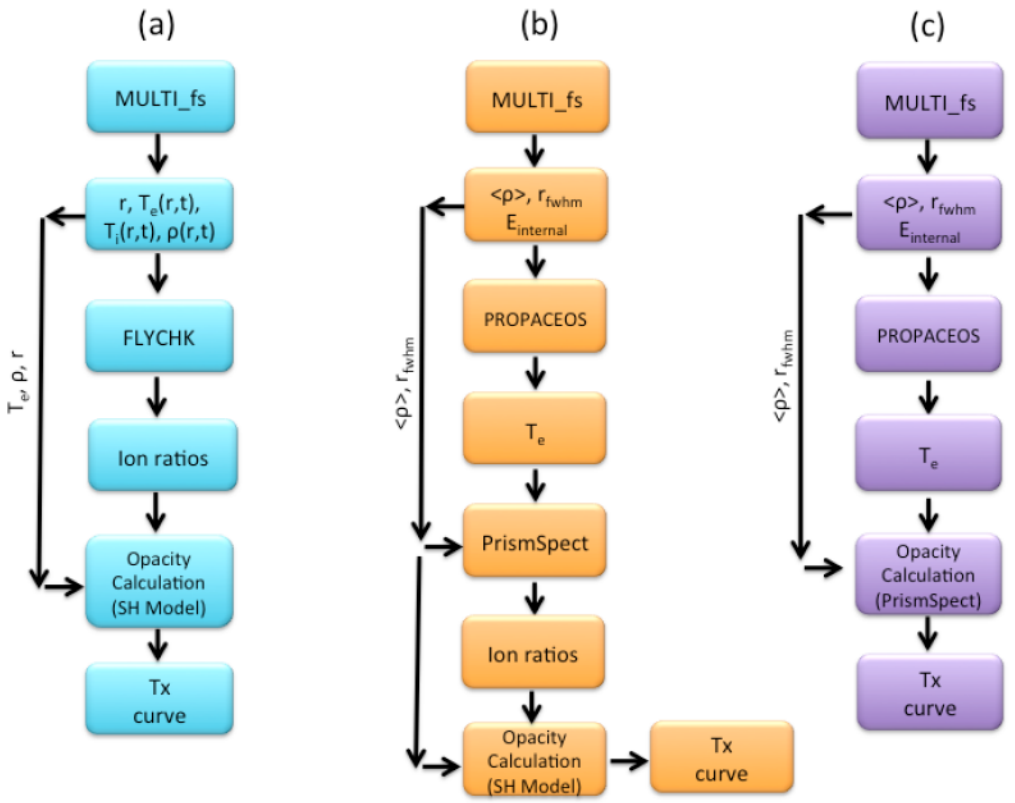

Figure 10.11: Flowcharts showing different models to compute the X-ray transmission curve of the warm dense aluminum. (a) Non-uniform slab model with opacity calculation from SH model. (b) Uniform slab model with opacity calculation from SH model. (c) Uniform slab model with opacity calculation from PrismSpect.

ternal energy $E_{internal}$ was contained in a fictitious uniform slab with known size and mass density, one can calculate the electron temperature by looking up EOS tables. The mass density of the uniform slab was achieved by taking the average mass density $\langle\rho\rangle$ of the region spanned by the two half maximum of the peak density weighted by the cell-size. The size of the fictitious slab was assumed equal to the FWHM $r_{fwhm}$of the mass density profile from the MULTI-fs simulation. Knowing the the mass density $\langle\rho\rangle$ and the total internal energy $E_{internal}$, the T_e was then found by looking up the EOS table from the PROPACEOS, which is available in our laboratory. Given the laser intensity range in our experiments, the MULTI-fs simulation show that, within the time period of 1 ps, the ions are relatively cold and their contribution to the internal energy is small. Therefore, the total internal energy $E_{internal}$ obtained here should be considered as the electron internal energy when looking up the T_e. The next step is to calculate the ionized charge distribution of the uniform slab characterized by the mass density $\langle\rho\rangle$, plasma temperature T_e and size r_{fwhm}. This was done by using the Prismspect software. The remaining step is to calculate the opacity and the corresponding transmission curve with the SH model. Flowchart (c) shows the uniform slab model but with opacities from PrismSpect software. The assumed uniform slab is achieved in the same way as shown in Flowchart (b). The opacity and transmission curve in this case are directly calculated from the PrismSpect code.

Note that in the uniform model, only the center mass of the expanded plasma is taken to compute the opacity. This essentially underestimates to some degree the final X-ray transmission coefficient and requires some assessment on the contribution from the unaccounted mass to the final X-ray transmission. This was done and the details are given in Appendix C. The assessment shows that the unaccounted mass will add only a few percent on the absorption dips of the Al^{4+} and Al^{5+} for the uniform models, indicating that the uniform model is a reasonable assumption to simulate the X-ray transmis-

sion in the expanded plasma with absorption dips on the order of a few tens of percent.

It is apparent that the MULTI-fs simulation plays a significant role in computing the opacity for the three methods described above. Therefore, it is necessary to have the simulations benchmarked with experimental results in order to examine the validity of models employed in the simulations. MULTI-fs has already been compared to femtosecond interaction experiments in Ref.[196]. We have also carried out our own benchmark experiment. This was done by an offline experiment in which the self-reflectivity of an 130 fs, 800 nm laser pulse irradiating 50-nm-thick aluminum foils with oblique incidence was measured as a function of laser intensity. In addition, the self-reflectivity measurements taken during the betatron ionization experiments give another data point to benchmark the MULTI-fs simulation for an interacting laser pulse with a pulse duration of 30 fs. The detail of these two self-reflectivity measurements are described in Appendix D. Overall, the MULTI-fs simulations show a reasonable agreement with the self-reflectivity measurements, allowing us to study the hydrodynamic expansion of solid-density aluminum irradiated by ultra-short laser pulse.

Fig.10.12 and Fig.10.13 show MULTI-fs simulation results of a 50 nm Al foil irradiated by a p-pol, 800 nm laser pulse with pulse duration (FWHM) of 30 fs and peak intensity of $1.3 \times 10^{15}\ W/cm^2$. The laser intensity used here is the peak intensity of the pump laser during the Betatron ionization experiments. The angle of incidence of the laser pulse is 40 degrees, the same as that in the experiments. In the simulation, an artificial layer, 30 nm, of aluminum vapor with ρ of $2 \times 10^{-3}\ g/cm^3$ was added at the back of the target to observe the rear expansion. The time evolution of the target can be followed in Fig.10.12.(a) and (b), and Fig.10.13 (a) and (b) that display mass density, average charge state, electron temperature and ion temperature, as functions of time and spatial coordinate respectively. The spatial lineouts of these variables at time = 0, 250

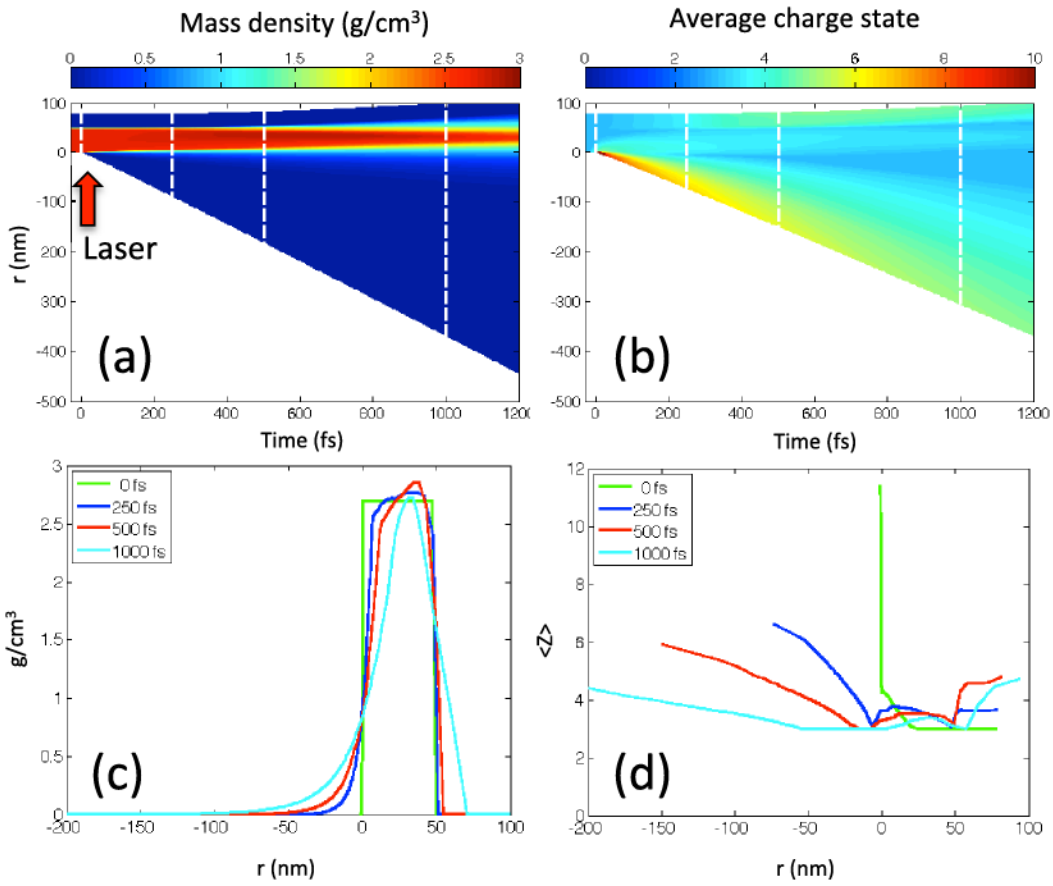

Figure 10.12: (a) Contour plot of the simulated (MULTI−fs) mass density $\rho(r,t)$ of a 50 nm Al foil irradiated by a 30 fs, 1.3×10^{15} W/cm^2 laser pulse at wavelength of 800 nm. The laser impinges on the target from the bottom, as indicated by the arrow in the graph, with angle of incidence of 40 degree and p polarization. The corresponding lineouts for four different times are plotted in (c) with the laser peak defined as time zero. (b) and (d) are the same as (a) and (c) but for average charge state $\langle Z \rangle(r,t)$.

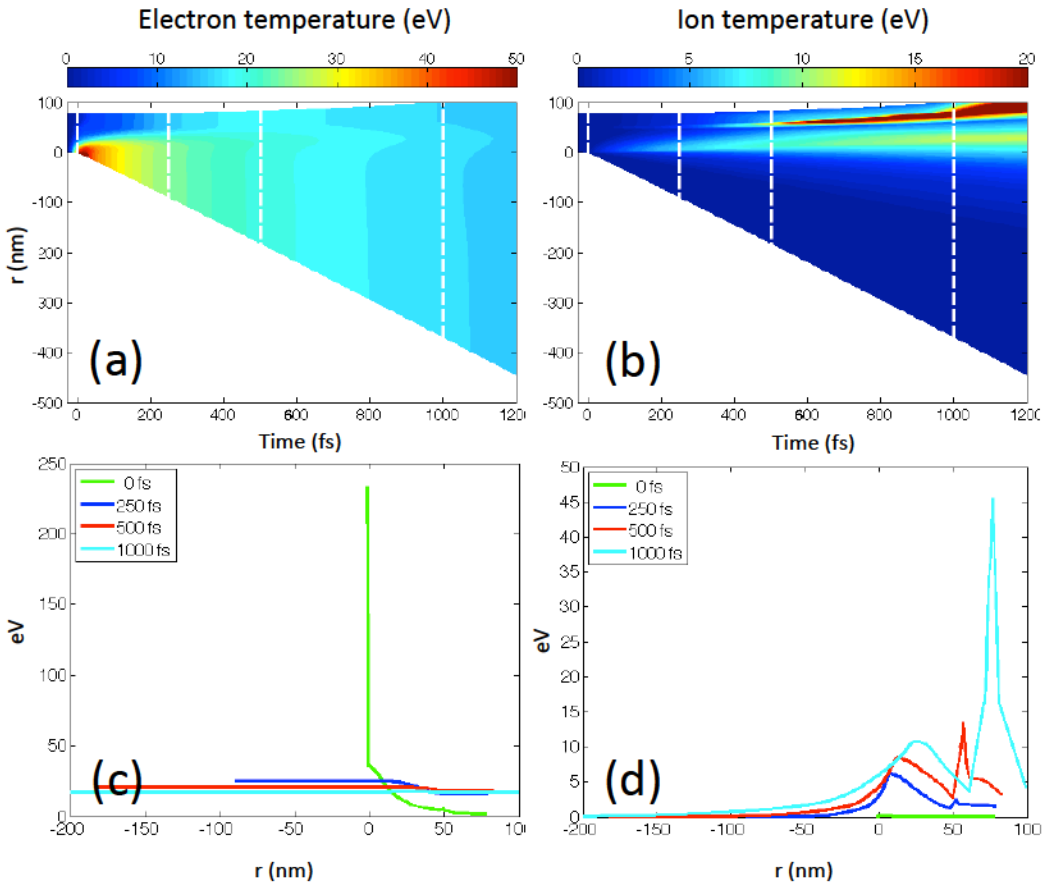

Figure 10.13: Same as in Fig.10.12 but for electron temperature $T_e(r,t)$, indicated by (a) and (c), and for ion temperature $T_i(r,t)$, indicated by (b) and (d). In the simulation, an artificial layer of aluminum vapor with ρ of 2×10^{-3} g/cm^3 was added at the back of the target to observe the rear expansion, mainly for the mass density. This artificial layer is so dilute such that it does not affect the mass expansion from the rear side significantly.

fs, 500 fs and 1000 fs are shown in Fig.10.12(c) and (d), and Fig.10.13 (c) and (d) respectively. Here time zero is defined as the time when peak of the laser arrives at the target. At time zero, the target is still intact. As a consequence, the laser energy is deposited at solid density. The absorbed energy ($\sim$ 17%) resides predominantly in the thermal energy of electrons, which are heated up to almost 250 eV. The kinetic energy at this time is less than 1% of the thermal energy, which is negligible and explains the intact spatial profile of the target. The spatial profile of the T_e extends over a larger range compared to the laser deposition region that penetrates only a few nm into the front interface of the target. The inward heating indicates a nonlinear heat wave has propagated into the solid. On the other hand, the ions remain cold, less than 0.3 eV, due to the slow electron-ion equilibration time, which is normally in range of 10 - 20 ps for cold solid aluminum [196]. After the laser pulse is turned off, the front layer of the target expands into the vacuum rapidly, resulting in an inward motion of deeper layers that compresses the target. The compression increases with the time and after a few hundred femtoseconds a weak shock wave is developed close to the rear side of the target, as demonstrated by the density lineout at time of 500 fs in Fig.10.12 (c). Meanwhile, as this weak shock develops, the rear end of target starts to expand due to the thermal heating by the heat wave that arrived prior to the shock wave. This rear expansion creates a backward-propagating rarefaction wave which weakens the front of the forward propagating shock wave. At the time of 1 ps, the concurrence of backward propagating rarefaction wave and the forward propagating shock wave causes a density spike in the middle of the target which has a value close to the initial density of aluminum. At the same time, the flat T_e profile indicates a fairly uniform heating across the entire target. The ions at this time are already heated up with a peak temperature of 10 eV nearby the middle of the target, which is around half of the electron temperature. The kinetic energy at 1 ps increases to 27% of the total absorbed laser energy ($\sim$ 35%) , as compared

to 67% for electron internal energy and 6% for ion internal energy. Note that there are temperature spikes residing behind the target ($r > 50\,nm$) for T_i profiles after 250 fs. The reasons are that the rear expansion of the target after 250 fs drives a small shock wave (too small to be observable for the y-scale used in 10.12 (c)) into the vapor region. In the shock front, the ions are heated such that they are hotter than adjacent ions and could be even hotter than the electrons if sufficient heating is provided. However, these spikes do not exist in reality since there is no aluminum vapor after the target in the real experiments.

With the MULTI-fs simulation results as discussed above, which are achieved under the peak intensity ($1.3 \times 10^{15}\ W/cm^2$) of the laser employed in the experiments, one can compute the theoretical X-ray transmission curves for the warm dense aluminum using the three methods as shown in Fig.10.11. Note that in the above MULTI-fs simulation, the measured laser peak intensity instead of the average laser intensity over the probe area was used. As presented in Appendix C, the simulated integrated laser absorption coefficient is 35%, which corresponds to an absorbed intensity of $4.55 \times 10^{14}\ Wcm^{-2}$ given the peak intensity used here. This absorbed intensity is in line with the measured average absorbed intensity of $4.55 \times 10^{14}\ Wcm^{-2}$ in the probed region of the target (top 20% energy range).

The results of these three methods for calculating the absorption spectra are shown in Fig.10.10. Note that the linewidths (FWHM) for the Al^{4+} and Al^{5+} dips in the simulation were set constantly to 2.5 eV and 3.5 eV respectively, which represent a combination of the theoretical broadened linewidth and the instrumental resolution of the spectrometer. For the 0.5 ps data point, as shown in Fig.10.10 (a), at the Al^{4+} absorption dip position (1.49 keV), the non-uniform slab model and uniform SH model predict a similar absorption coefficient, which touches the upper boundary of the measurement error bar. The uniform slab model with Prismspect opacity gives a slightly lower absorption

coefficient, which falls above the measured absorption dip. At the Al^{5+} absorption dip position (1.50 keV), all of the three models appear to underestimate the absorption coefficient. For the 1 ps data point, at the Al^{4+} position, the values calculated from the three models are in a good agreement with the measured absorption coefficient, however, at the Al^{5+} position, these three models again underestimate the absorption coefficient. Overall for Al^{4+}, the absorption coefficients predicted with the three models agree with the measurements within one error bar at the two delays. However, at the Al^{5+} position, all of the models fail to match with the experiment, particularly at 0.5 ps, where the discrepancy is on the order of twice the estimated error bars.

The reasons behind these discrepancies could be due to (a) the electron temperature being underestimated by the MULTI-fs, which could be due to the electron heat capacity that was used in the simulation. For a given electron internal energy, higher heat capacity leads to a lower electron temperature. (b) the ionization model used in the simulation underestimates the ionization fractions for Al^{4+} and Al^{5+}. As indicated by Fig.10.1, for a given electron temperature, different EOS models and ionization models predict different average ionization states. A small difference in the average ionization state may correspond to a significant difference in ion abundance that can impact the X-ray transmission coefficient. (c) the uncertainties of the experimentally measured absorption peaks due to the small number of photons captured within the spectral window. The error bar shown in Fig.10.1 is achieved by taking the inverse square root of the total number of photon residing within a bin width of approximately 5 eV, close to the full width of the dips indicated in the Fig.10.1. Thus effectively the comparison is primarily comparing the area under the curve for the experiment versus simulation. (d) the ionization potential depression (IPD) effect being underestimated by the PrismSpect and FLYCHK, which were used to calculate the ionization fractions in the uniform and non-uniform models respectively. In a recent experiment [197] in which the IPD in dense Al plasmas

was measured by means of K-edge measurements in the Linac Coherent Light Source (LCLS) facility, it was found that the More's model (or the Ion Sphere (IS) model as quoted in Ref.[197]) and the Stewart-Pyatt (SP) model [198] for IPD predict a lesser amount of IPD than the measured one corresponding to different Al charge states. An ab initio calculation based on the density functional theory that accounts for the IPD effect [199] was found to be better than the IS and SP models and showed excellent agreement with the experimental results as reported in Ref.[197]. In PrismSpect and FLYCHK, the IS and SP models were used to simulate the IPD effect for ions embedded in a plasma environment respectively. The fact that these two models underestimate the IPD effect will essentially lead to a relatively lower ionization state for the aluminum in the simulations, which may explain the lower fractions of Al^{5+} ions calculated by PrismSpect and FLYCHK as employed in the uniform and non-uniform models.

It should be noted that the heater pulses in our experiments were subject to pulse stretching due to the dispersion from the three transmissive optical elements (2-mm-thick Quartz for the half wave-plate, 1-mm-thick CaF_2 beam splitter and the 2-mm-thick CaF_2 lens) that the heater pulses propagate through before arriving at the targets. This pulse stretching effect is not included in the MULTI-fs simulation. Calculation shows that the dispersion from the above three optics causes approximately 3 fs of pulse stretching in total. According to MULTI-fs simulations, the absorbed laser energy for the stretched laser pulse of 33 fs is almost identical to that of the original pulse width of 30 fs given that the input pulse energy and other conditions are the same. Therefore the pulse stretching effect in our experiments is not the source for the discrepancies observed here.

Another way of fitting the measured absorption dips is by using the ion fraction as a free parameter in order to figure out the best-fit ion fraction. This can be done with the SH model in which the ion fractions are free parameters

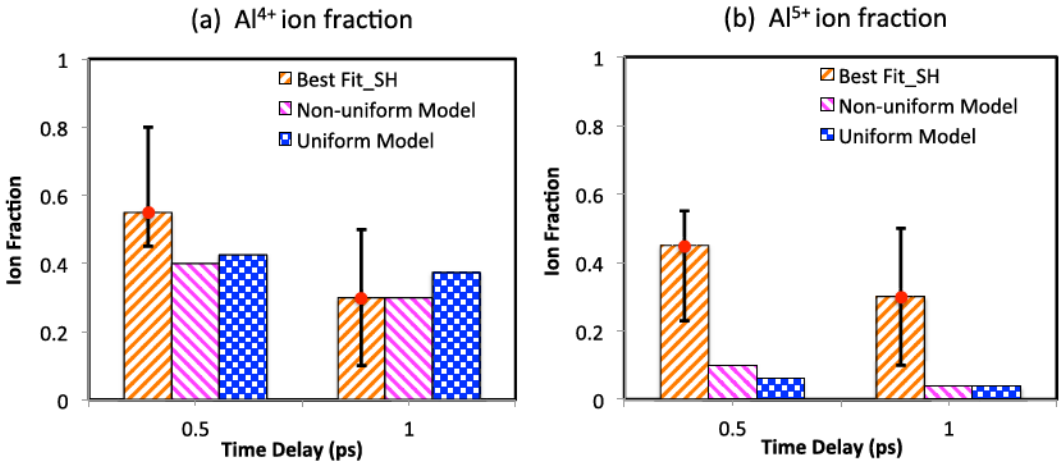

Figure 10.14: (a) Derived fraction of Al^{4+} ion as a function of time using different methods. The bar with orange upward diagonals represents the best fit ratio using the SH model assuming a uniform slab; The bar with pink downward diagonals represents the effective ratio from the simulation based on non-uniform slab model. The bar with blue check-board pattern represents the results from the calculation based on the the uniform slab model. (b) Same as (a) but for Al^{5+} ion.

when calculating the opacity. However, the pitfall with this method is that one has to assume the target is uniformly heated, which would give constant ion fraction for each ion species across the whole target. To calculate the line absorption coefficient, in addition to the opacity, the other necessary parameters are the mass density ρ and thickness R. According to the MULTI-fs simulations, the target at the time of 0.5 ps and 1 ps is no longer isochorically heated and the density has a spatial dependency. To first order, we use the average $\langle\rho\rangle$ and r_{fwhm} achieved in the uniform model as indicated in Fig.10.11 as our mass density and size. The electron temperature in this method is not critical as it only affects the bound-free opacity which is much less than the bound-bound opacity.

The best-fit results of the ion fractions using the above method for the two measurements at delay of 0.5 ps and 1 ps are shown in Fig.10.14. For comparison, the effective ion fractions from the simulation based on non-uniform

slab mode and the ion fractions from the simulation based on uniform slab model are plotted in the same graph. The error bars for the fitting results are achieved by fitting the upper and lower boundary of the error bars of the measured absorption dips as indicated in Fig.10.10. Again, the large error bars with best-fit ratios are due to the high noise level induced by the lack of signal photons. For Al^{4+} ion, at 0.5 ps, the non-uniform model and uniform model give similar ion fractions that are slightly lower than one standard deviation of the best fit value. At 1 ps, these three results are in a good agreement. All the three results show that the ion fraction decreases with time. For Al^{5+} ion, large discrepancies are found between the simulation results and the best-fit results, the reasons of which have been discussed previously.

10.5 Conclusion

In summary, we have demonstrated the results of direct measurements of the ionization states of warm dense aluminum probed by femtosecond Betatron radiation generated from laser wakefield accelerated electrons. The warm dense aluminum was formed by a 800 nm, 30 fs laser pulse with energy of 10 mJ interacting with a 50-nm free-standing aluminum foil. The ionization states of the warm dense aluminum were measured at delays of 0.5 ps and 1 ps using the technique of K-shell absorption spectroscopy. Absorption dips in the transmitted X-ray spectrum caused by the Al^{4+} and Al^{5+} ions were clearly seen during the experiments. To interpret the ionized charge distributions from the measured K-shell absorption lines, 1D hydrodynamic simulations associated with plasma spectroscopic modeling were carried out. The 1D hydrodynamic simulations with MULTI-fs indicate that the target is subject to some degree of hydrodynamic expansion at the times of 0.5 ps and 1 ps, necessitating a non-uniform model for the analysis. Three models were implemented to conduct the plasma spectroscopic simulations, including non-uniform slab model

with screened-hydrogenic opacity, uniform slab model with screened-hydrogenic opacity and uniform slab model with opacity from PrismSpect. The absorption coefficients predicted from the three models agree reasonably well with the measured ones for the Al^{4+} ions at the two delays, however, conspicuous discrepancies were found between the simulations and the experiments for the Al^{5+} ions. Factors that can contribute to this have been discussed and perhaps the recent re-evaluation of the IPD models indicating a stronger depression of the ionization potential than assumed in the present analysis could explain a large part of the discrepancy. At present the error bars on the Al^{5+} peak measurement are quite large and thus final conclusions on this discrepancy would require a more accurate measurement of this absorption peak. This can be improved in the future by accumulating more photons by taking a larger number of shots. Despite there being some discrepancies between the simulations and experiments, the successful measurements of the ionization states of the warm dense aluminum indicates that Betatron radiation from laser wakefield acceleration is a powerful tool for time resolved absorption spectroscopy over a broad wavelength range.

Chapter 11

Resistive effect of target material on hot electron transport relevant to Fast Ignition

11.1 Introduction

In Fast Ignition, energy from the short pulse laser deposition zone is transported by hot electrons to the dense core region where the ignition of the fusion reaction occurs. However, the hot electrons are subject to large angular divergence while traveling in overdense plasma [200, 201, 202], which poses significant design constraints on Fast Ignition. To achieve ignition, hot electrons must be able to deposit at least $\sim$ 20 kJ energy within $\sim$ 20 ps in a small fuel region, called the hot spot, with a diameter of 40 μm and areal density of $\sim$ 0.6 g/cm^2 [67]. These requirements constrain the maximum divergence allowed with the hot electron beam and restrict the standoff distance from the electron source to the fuel region to the order of 100 μm. It is apparent that the divergence of hot electrons propagating in overdense plasma plays a significant

role in determining the success of fast ignition approach and therefore should be minimized.

Cone-guided fast ignition, where a hollow cone is inserted into the fuel shell to provide a clear passage for the ignition laser pulse, has been demonstrated as an easier approach to implement for initial experiments than the original fast ignition approach using laser hole boring [203]. In such cone-in-shell design, a high-Z material such as gold is normally coated at the cone tip to shield the inside of the cone from X-rays that will create preplasma and to generate copious electrons. However, the high-Z material at the cone tip has the potential to affect the electron transport over the duration of the laser pulse through scattering, absorption or resistive collimation [204]. Recently, the work done by Chawla et al. [205] demonstrated that a high-Z transport layer embeded in a low-Z layer is capable of collimating the hot electron beam without imposing a significant loss in the central forward-going electron energy flux. 2D collisional particle-in-cell simulation results showed excellent agreement with the experiments and indicated that the initially divergent hot electron beam was modified by the strong resistive magnetic field formed in the high-Z transport targets. The self-generated resistive magnetic field is given by:

$$\frac{\partial \mathbf{B}}{\partial t} = -\nabla \times \mathbf{E} = -(\eta \cdot \nabla \times \mathbf{J}_R + (\nabla \eta) \times \mathbf{J}_R) \tag{11.1}$$

where $\mathbf{E}$ is the inhibition electric field resulting from the finite resistivity of the background plasma, given by $\mathbf{E} = \eta \cdot \mathbf{J}_R$, where η is the resistivity and $\mathbf{J}_R$ is the return current generated to neutralize the hot current $\mathbf{J}$. The magnetic field generated from the resistivity gradient, second term on the RHS, pushes the electrons towards the higher resistivity region. Therefore by introducing a resistivity gradient into the target, one can in principle collimate the hot electrons with the help of the enhanced magnetic field as demonstrated in Ref.[205].

Here we present the experimental results of an investigation of the resistive effect of target material on the hot electron transport using the Titan 2ω laser. This is a follow-up experiment to the one conducted at 1ω wavelength in Ref.[205] where the second-harmonic of the Titan laser pulse was used instead of the fundamental wave to create the hot electron beam. The 2ω laser pulse was used to minimize the preplasma effect on the laser matter interaction.

11.2 Experimental Setup

The experiments[1] were conducted with the Titan laser beamline at the Jupiter Laser Facility that is located at the Lawrence Livermore National Laboratory. The setup is shown in Fig.11.1(c). To minimize the intrinsic prepulse resulting from the amplification of spontaneous emission (ASE) occurring in the front end of the laser system, the 1.054 μm main laser pulse was frequency doubled to green light (527 nm) before being sent to the target chamber. The green laser pulses with FWHM pulse length of 700 fs were focused by a f/3 off-axis parabola inside the vacuum chamber onto the target front surface with an incident angle of $\sim 14^o$. As introduced in Chapter 4, the best focus at the target plane in vacuum was achieved by optimizing the alignment of the off-axis parabola at the beginning of the experiments using millijoule laser light provided from the OPCPA module located in the laser front end. With this method, the typical shape of the focal spot in vacuum was measured to be an ellipse, with FWHM sizes of 3.5 μm by 8.0 μm in the vertical and horizontal directions. Based on the OPCPA focal spots, the focused peak intensities were estimated to range from $3 \times 10^{19}\ W/cm^2$ to $6 \times 10^{19}\ W/cm^2$ as the laser energies on target varied from 30 J to 60 J from shot to shot. In addition, an equivalent plane monitor (EPM) was set up to monitor the shot-to-shot equivalent plane focal spot at

[1]The experiments were done in collaboration with the researchers from the Lawrence Livermore National Laboratory, the University of California at San Diego, the Ohio State University, the Imperial College London and General Atomics.

TCC by using the leakage light through the last turning mirror. The EPM focal spots were measured to be larger than those achieved from the OPCPA light, in large part due to the extra B-integral of the 2ω light passing through thick optical elements in the diagnostic beampath line. A typical EPM focal spot is shown in Chapter 4 with FWHM of 7.7 μm by 15.3 μm in vertical and horizontal directions. The impact of preplasma on the hot electron generation was also studied. This was done by injecting colinearly an extra long pulse with energy of 3 mJ over a few ns prior to the main pulse.

To simulate the material effect in cone-guided Fast Ignition, planar multilayered targets were adopted in our experiments. We used two types of planar multilayered targets: the first type, as shown in Fig.11.1(a), is with a thin (10um) gold layer buried in an aluminum slab, while in the second type, Fig.11.1(b), the same thickness gold layer is coated in front of the aluminum slab. Both types of targets have copper tracer layers (12 μm for buried Z and 25 μm for front Z) inside the aluminum slab and a 1-mm CH plastic block at the back of the target foil to suppress the electron reflux off the back of target [206], and guarantee hot electrons traverse the copper layer only once. For comparison, each type of target has a reference target in which the gold layer is replaced by a 25 μm aluminum layer. The thicknesses of the transport layers ($10\mu m$ gold versus 25 μm aluminum) were chosen to ensure similar electron stopping power. In the buried Z design, hot electrons experience resistive gradients in opposite directions at the two sides of the gold layer. As a result, hot electrons will be pinched and diverged by the induced magnetic fields as given in Eqn.11.1 at the front and back interfaces of the gold layer with the aluminum respectively. The competition between the pinching and diverging determines the final resistive effect on the divergence of the hot electron beam. On the other hand, for the front Z design, the gold layer not only plays a role of modifying the divergence of hot electron beam but also acts as the hot electron source.

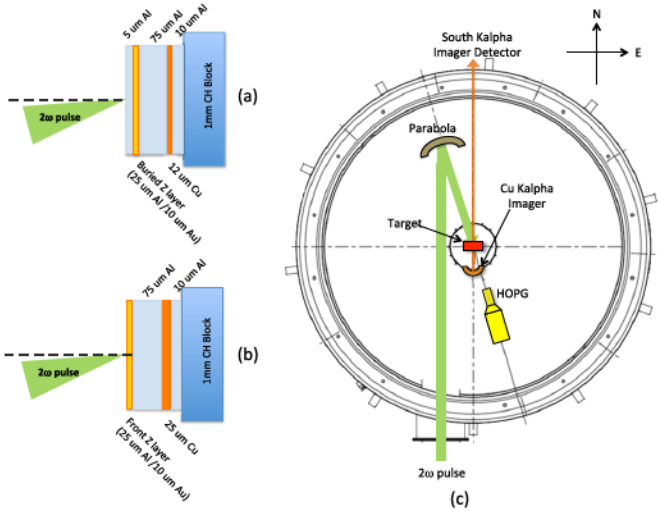

Figure 11.1: Layouts of planar targets with buried Z layer (a) and front Z layer (b). (c) Schematic diagram showing the laser, target and X-ray diagnostics. The Cu $K\alpha$ Imager was located 40 degree below the rear target normal. The HOPG spectrometer were installed in the rear side of the target with viewing direction along the laser propagation axis.

The hot electron beam was characterized by the K_α fluorescence in the copper tracer layer. As shown in Fig.11.1(c), the spot profile of fluorescence was imaged by the Cu Kα Bragg crystal imager located at the rear side of the target. The spatially integrated total Cu Kα yield was measured by an absolutely calibrated HOPG spectrometer [207] that was installed behind the target with viewing direction along the laser propagation axis.

11.3 Experimental Results and Discussions

Fig.11.2 shows two typical $K\alpha$ images achieved from the buried Z targets with Z = Au (a) and Z = Al (b) when there is no injected prepulse. These two images are reconstructed images of which the viewing angle is parallel to the target normal. This was done by using a Matlab script written by my colleague Shaun Kerr, in which the geometry of the crystal imager and the target was

used in transforming the raw images. The FWHM sizes of the two spots are 150 ± 10 μm and 154 ± 10 μm respectively. The error bar of 10 μm is from the astigmatism-limited spatial resolution of the crystal imager [208, 95]. From the two similar spot sizes, it appears that there is no obvious evidence that the resistive collimation from the buried gold layer plays a significant role in guiding the hot electron beam under our experimental conditions. Similar trends were observed for the same type of target with injected prepulse and the front-Z targets with and without injected prepules, as indicated in Fig.11.3 (a). The spot sizes corresponding to the buried-Z and front-Z targets achieved with and without injected prepulse are shown in Fig.11.3 (a). Each data point represents the average size of two images with error bar being the quadratic combination of the standard deviation of the measured sizes and the spatial resolution of the crystal imager. Clearly, there is no obvious reduction of the spot sizes due to the either the resistive effect or the preplasma effect for both buried and front Z targets. This is in contrast to the observed 36% reduction in spot size for buried gold targets obtained with the 1ω Titan laser as demonstrated in Ref.[205]. 2D Hybrid PIC simulation was conducted to understand the physics behind the unchanged divergence observed in our experiments and the details will be given later in Sec.11.4.

Fig.11.3(b) presents the measured Cu Kα yield normalized to laser energy and solid angle for the same targets as shown in (a). For the buried Z targets, a reduction in Kα yield is observed for the buried Au target. However, the difference of the Kα yield between the Au and Al targets is within the error bar of the measurements independent of the injected prepulse, therefore, further experiments are required to establish the true drop in Kα yield when the gold layer is introduced. In Ref.[205], a factor of two in Kα yield was measured for the buried gold targets, which was claimed to be due to the resistive stopping of the hot electrons by the strong resistive E fields and B-field trapping. For the front Z targets, a small reduction in the Kα yield is observed for the Au target

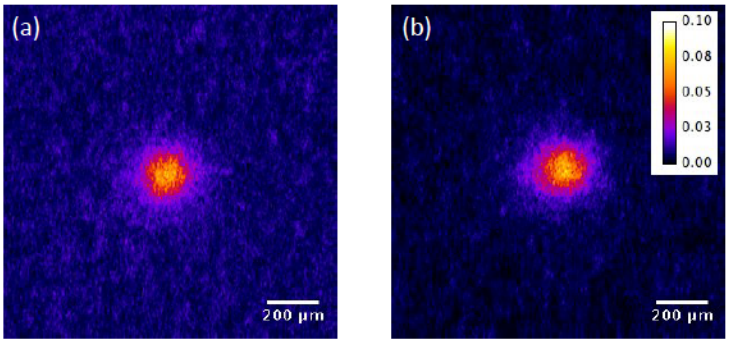

Figure 11.2: Typical Cu $K\alpha$ images (a) and (b) from Z = Au and Z = Al of the buried-Z targets respectively when there is no injected prepulse. These two images are reconstructed images of which the viewing angle is parallel to the target normal, which was done by transforming the raw images according to the geometry of viewing axis of the crystal imager relative to target normal. The averaged FWHM size of spot (a) is 150 ± 10 μm, as compared to 154 ± 10 μm of the FWHM size of spot (b).

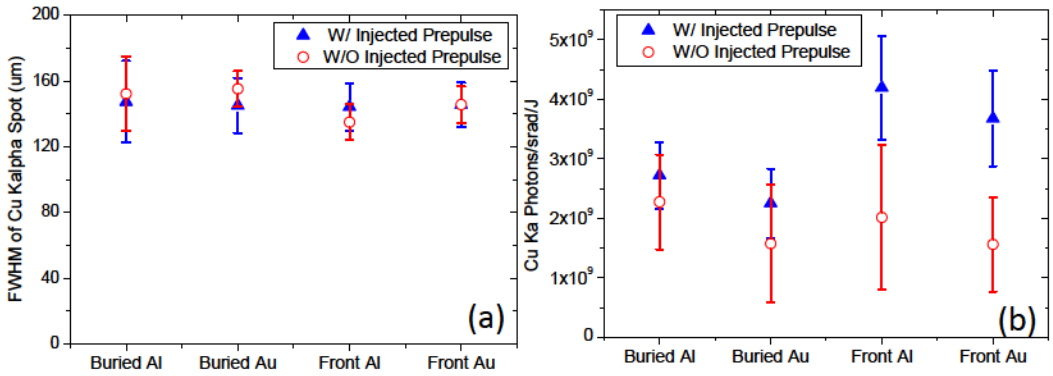

Figure 11.3: (a) Measured Cu Kα spot sizes achieved from Cu Kα imager for targets of buried gold, front gold and their references under condition of with injected prepulse (solid triangles) and without injected prepulse (empty circles). (b) Corresponding normalized yields of the Cu Kα X ray from HOPG spectrometer.

but this is well within the error bars and no strong conclusion can be drawn. However, when the prepulse is introduced, some degree of enhancement of Kα yield was observed, indicating the hot electron generation is more efficient in the presence of preplasma. Recall that the spot sizes for front-Z targets were measured to be consistent independent of injected prepulse. What this means is that the enhanced number of hot electrons does not cause any large modification to the beam divergence.

11.4 Simulations and Discussions

To understand the underlying physics in this experiment, kinetic electron transport code simulations were performed with the code developed by J.J. Honrubia and his colleagues [209]. These simulations were conducted by J.J. Honrubia. Because the laser plasma interaction cannot be described by this hybrid code, the hot electron transport was calculated using a prescribed electron source. In this multigroup kinetic transport code, the relativistic electron beam is treated by 3D multigroup (energy and angle) electron transport including collisional energy loss, while the high-density background plasma is modelled by resistive MHD equations including hydrodynamic motion to describe magnetic field suppression by plasma return currents [209]. The initial energy distribution of the injected beam electrons is assumed to be one-dimensional relativistic Maxwellian of the form $dN/dE \sim \gamma\sqrt{\gamma^2-1}\,exp(-E/kT_h)$ with kT_h of 0.5 MeV. This temperature was estimated using the Beg's scaling law [75] based on the $I\lambda^2$ of $\sim 1.5\times10^{19}\ Wcm^{-2}\mu m^2$ corresponding to our experimental condition. The hot electron beam was injected at a plane that is 1 μm inside the front target surface, and had a Gaussian spatial distribution with FWHM of 8 μm, which is the geometric average of the OPCPA and EPM focal spots. The full divergence of the hot electron beam consists of two components, the global angular divergence of 30^o (HWHM) and the local angular spread of 55^o

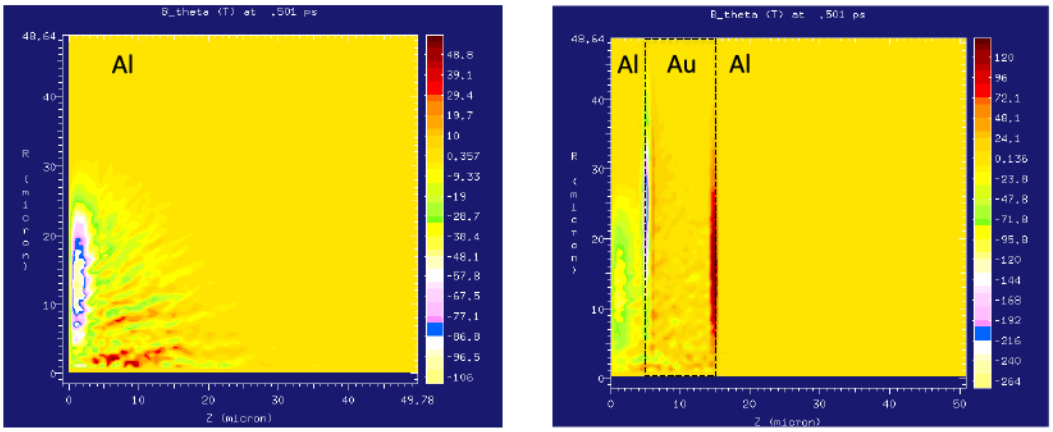

Figure 11.4: (a) Contour plot of the azimuthal magnetic fields formed in the buried Al target at time = 0.5 ps. (b) The same as (a) but for buried Au target.

(HWHM) of the electron distribution in the laser plasma interaction region [210]. The local divergence is due to the hot electron scattering in the stochastic magnetic fields generated by the Weibel instability coupled to the laser fields[211], whereas the global angular spread is determined by the electron deviation in transverse direction due to the laser transverse ponderomotive force and propagation effects in the preplasma. When the preplasma is present, the global angular spread can become comparable to the local angular divergence [210]. Therefore, the full divergence set in the simulation has taken into account the preplasma effect on initial divergence of the hot electron beam. The temporal profile of the electron source is a Gaussian function with pulse duration (FWHM) of 700 fs and peak current density of $\sim 1.5 \times 10^{13}\ A/cm^2$. To first order, the hot electron transport in the buried Z targets was modeled without the presence of preplasma as the preplasma does not appear to affect the hot electron transport.

We first examine the self-generated magnetic fields during the hot electron propagating through the buried Z targets, which are shown in Fig.11.4 with time = 500 fs. A relativistic electron beam propagating through a charge and

current neutralizing plasma background is subject to the resistive filamentation instability [212]. Because of this instability, the local current neutralization was destroyed and the initial current beam was forced to break up to multiple filaments. Similar filamented features are expected with the magnetic fields as they follow closely with the currents. These are confirmed by the numerous channels of magnetic fields as observed in Fig.11.4 (a) for the buried Al target. On the other hand, for the buried Au target, the magnetic channels are washed out in the Au layer, indicating that the resistive filamentation instability appears to be suppressed in an inhomogeneous plasma where steep resistivity differences are present in the propagation direction of the hot electrons.

As predicted by Eqn.11.1, magnetic fields can be generated by the resistivity gradient seen by the divergent hot electron beam. This is clearly seen in Fig.11.4 (b), in which two opposite magnetic interface fields are formed along the front and rear interfaces of the gold layer. At the front interface, the resistive magnetic field reaches as high as 250 T. With this magnitude of magnetic field, the Larmor radius, $r_L(um) \simeq 3(E/keV)/(B/Tesla)$ for 0.5 MeV electrons is approximately 6 μm, which is comparable to thickness of the gold layer. As such, no strong guiding or collimation of the hot electrons from the magnetic fields will be expected, agreeing with the observation of no evident magnetic filaments penetrating into the gold layer. In Ref.[205], strong hot-electron guiding was observed in their PIC simulations, in which the generated magnetic fields are on the order of a few thousands of Tesla for the buried gold target. Therefore, one tends to conclude that in order to have evident resistive collimation of hot electrons, self-generated magnetic fields on the order of 1000's T are required, which however is not the case in our experiments due to the much lower current density.

Note that the simulations show that the resistive magnetic fields (beyond the injection plane that is 1 um inside the target front surface) formed in the buried Al target are relatively weaker than those in the buried Au target,

which agrees with what was observed in the PIC simulations conducted in Ref.[205]. The reason for that is given as follows[205]: for the buried aluminum target, the resistivity, scaling as $\eta \propto kT_e^{-3/2}$ (Spitzer behavior), is lower in the center region where the plasma temperature is higher due to heating by the high density current. In our 2D cylindrical simulation geometry, the dominant terms for the azimuthal B-field generation are given by:

$$\partial \mathbf{B}_\theta / \partial t = \eta(\partial \mathbf{J}_z / \partial r) + (\partial \eta / \partial r)\mathbf{J}_z \tag{11.2}$$

where $\mathbf{J}_z$ is the z component of the hot electron current. Because of the opposite signs of the transverse resistivity gradient and the transverse current density gradient with the Al plasma, the two components on the right hand side of the above equation act against each other, therefore limiting the field growth. For the buried gold target, firstly, the transverse resistivity gradient in the gold layer is negligible due to the much higher heat capacity [205]. As such, the contribution from the second term on the right side of Eqn.11.2 is not comparable to that from the first term, causing less inhibition on the growth of the magnetic fields. Secondly, at the two interfaces of the gold layer, the second term in Eqn.11.2, changed to $(\partial \eta / \partial z)\mathbf{J}_r$, is dominant in contributing to the B-field generation due to the large resistivity gradient, resulting in a significant growth of B-field at the two interfaces.

Fig.11.5 shows the time-integrated Kα spots and corresponding lineouts from the two buried-Z targets. From the lineout plot, it is clear that the two spot size are identical, indicating that there is no evident resistive collimation of the hot electrons due to the gold material. This is in good agreement with what we found from analyzing the B-fields developed in the buried gold target and is in agreement with what we observed during the experiments. From the two spots, one can tell that the intensity of the X-ray from the buried aluminum target is relatively higher than that of buried gold target. Analysis shows that

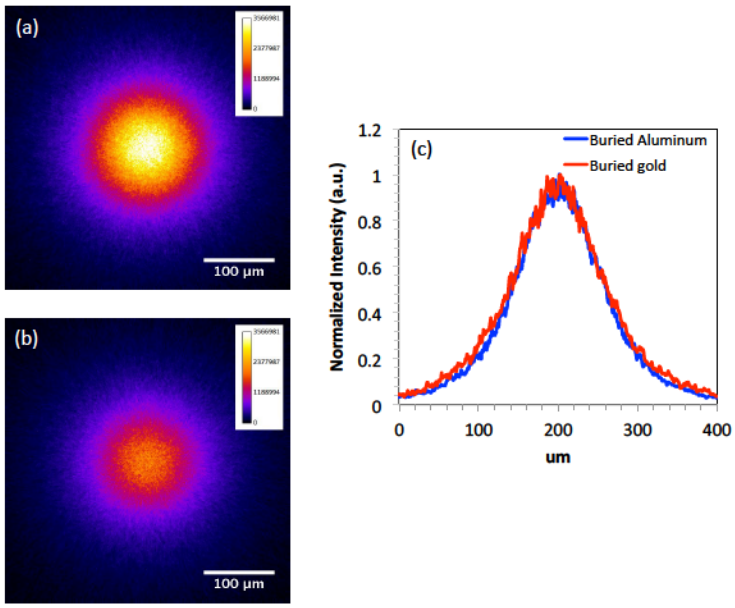

Figure 11.5: (a)Simulated time-integrated Cu Kα spot formed in the buried Al target. (b)Simulated time-integrated Cu Kα spot formed in the buried Au target. (a) and (b) are displayed in the same color scale. (c) The normalized lineouts of the two Cu Kα spots, red curve for buried Au and blue for buried Al.

the simulated total Kα yield from the buried aluminum is 1.5 times higher that that from the buried gold target. This difference agrees reasonably with the measured difference between the averaged yields of buried Al and buried gold as shown in Fig.11.3(b). However, this measured difference has a fairly large error bar.

11.5 Conclusion

In this chapter, we have presented the results of hot-electron transport inside solid targets with buried and front high-Z material. Our experimental results indicate no evident resistive collimation of the hot electrons due to the high-Z material, indicated by the unchanged size of the fluorescent spots from the copper tracer layer inserted in the targets with high-Z and low-Z materials. 2D PIC simulation results are in good agreement with the experiments and show that the generated B-fields in our experiments are relatively weak due to low current density and therefore not sufficient to guide or collimate the hot electrons.

Acknowledgments

We gratefully acknowledge all the hard work from the experimental campaign team including A. Link, G.E. Kemp, C. Mcguffey, J. Peebles, H. Nakamura, M.S. Wei, D. Wertepny, Y. Ping, F. Beg, R.R. Freeman, L.D. Van Woerkom, R.B Stephens, H.S. McLean, P. Patel. We would like to thank J.J. Honrubia for conducting the kinetic electron transport simulations for this experiment. We also would like to thank the Jupiter Laser Facility staff for their assistance and technical expertise throughout the experiment.

Chapter 12

Conclusions and Future Work

12.1 Conclusions

In conclusion, we have studied the electron acceleration and Betatron radiation from laser wakefield acceleration as well as successfully measured the ionization states of warm dense aluminum with Betatron radiation. In addition, hot electron transport in solid targets with a high-Z material layer related to Fast Ignition was investigated.

In pursuit of GeV electron generation from LWFA, we have performed a series of experiments in which the 80 TW laser pulses from ALLS were employed to interact with different gas-jet targets. Overall, the experimental results revealed new regimes of operation and are summarized as followed:

1. We demonstrated the generation of electron bunches with peak energies as high as GeV, which are approximately double those from analytical laser bubble wakefield scaling laws in an experiment with a 5-mm-long pure helium gas jet. This energy enhancement phenomena is explained as a laser wakefield process followed by a plasma wakefield process. The characteristics of this two stage process are clearly identified in the 3D PIC simulations under conditions similar to those of the experiment. The key components of the process include the creation of a large primary

electron charge bunch, a pump depletion length approximately equal to the dephasing length so that the primary bunch of electrons can take over driving the plasma wake just as the laser pulse loses its driving strength and sufficient remaining plasma length for the plasma wakefield acceleration to boost a second smaller bunch of electrons up to GeV energies. These conditions can be met within a range of densities which in the case of the current experiment is approximately $8 \times 10^{18}\ cm^{-3}$ to $2 \times 10^{19}\ cm^{-3}$. The present results indicate that attainment of energies approximately double those from LWFA alone can be achievable under well controlled conditions.

2. We demonstrated that it is possible to use a pure nitrogen gas jet. In a 10 mm long interaction region, we showed that quasimonoenergetic electron beams with peak energies > 0.5 GeV and divergence as low as 2 mrad can be achieved at a plasma density of $4.3 \times 10^{18}\ cm^{-3}$. Long-tail features were observed in the electron beams due to continuous injection. The measured peak electron energy decreased with the increasing plasma density, which agrees with the predicted maximum energy gain scaling for electrons. Experiments also show a threshold density of $3 \times 10^{18}\ cm^{-3}$ for self-trapping. Our experiments suggest that by using higher laser power and lower densities, pure Nitrogen is a potential candidate gas to achieve GeV level monoenergetic electrons in the ionization induced trapping scheme for laser wakefield acceleration.

3. We investigated ionization injection seeding of the LWFA process using CO_2 as the electron seed source in He gas. In the experiment with 5-mm-long gas jet of helium seeded with CO_2, electron bunches with average energies of the order of 500 MeV have been produced with ionization induced injection under the self-guiding condition of laser wakefield acceleration. These results are in approximate agreement with the bubble

wakefield scaling laws, particularly at densities above $6 \times 10^{18}\ cm^{-3}$. The use of ionization injection leads to improved performance in regards to increased electron charge, by a factor of two, lower injection threshold electron densities of $4 \times 10^{18}\ cm^{-3}$ as compared to $7 \times 10^{18}\ cm^{-3}$ for pure helium alone under the same conditions and much higher probability of producing electrons above 500 MeV as compared to self injection in He gas alone under the same conditions. These results were obtained with shorter acceleration lengths and higher densities than typically reported previously. In a few shots, energies of approximately double the average values, up to the GeV energy range, were obtained indicative of an additional acceleration mechanism, which was identified as a transition to PWFA after the laser pulse depletion as in the case of pure helium as discussed above.

We then characterized the Betatron radiation, where we have developed a new approach to measure the average critical energy E_c, an important parameter in determining the spectrum of Betatron radiation, based on the technique of Reflection off a Grazing Incidence Mirror. In this approach a grazing incidence mirror with high-Z coating reflects the Betatron X-ray radiation at different grazing angles. Assuming a synchrotron-like spectrum of the Betatron radiation, one can determine the value of E_c for the Betatron radiation from every single shot. This measurement was carried out with several grazing angles in the range of 0.3^o to 0.7^o for a Pt mirror and an average value of E_c of 7.5 ± 1.3 keV was determined. This E_c is in reasonable agreement with the value measured with a photon-counting X-ray CCD under the same experimental conditions, indicating a uniform synchrotron-like spectrum over a large photon energy range of a few keV to 25 keV. Such a grazing incidence mirror measurement can be used as an online E_c monitor in Betatron application experiments by sampling a small part of the beam where a simple fluorescent screen together with CCD camera readout can be used. Specifically, for KB

microscope applications the straight through radiation and single mirror reflection radiation could be used for this measurement without interfering with the main image spot of the KB microscope.

We developed a Betatron X-ray probe beamline based on the technique of K-shell absorption spectroscopy to directly measure the temporal evolution of the ionization states of warm dense aluminum. The X-ray probe system consists of an adjustable Kirkpatrick-Baez (KB) microscope for focusing the Betatron emission to a small probe spot on the sample being measured, and a flat Potassium Acid Phthalate (KAP) Bragg crystal spectrometer to measure the transmitted X-ray spectrum in the region of the aluminum K-edge absorption lines. A systematic characterization of the X-ray probe setup has been carried out both theoretically and experimentally, indicating that the source is suitable for carrying out high spectral resolution time resolved X-ray probing in the 1.5 keV X-ray range. An overall X-ray efficiency of 2.6×10^{-5} is achieved leading to the detection of ~ 10 X-ray photons in the 24 eV measurement window per shot. Thus, high sensitivity X-ray measurement will require hundreds of shots per measured spectra which in principle is achievable given the 10 Hz repetition rate of the actual source laser.

With the well characterized Betatron X-ray probe, we demonstrated the results of first-time direct measurements of the ionization states of warm dense aluminum. The warm dense aluminum was formed by a 800 nm, 30 fs laser pulse with energy of 10 mJ interacting with a 50-nm free-standing aluminum foil. The ionization states of the warm dense aluminum were measured at delays of 0.5 ps and 1 ps using the technique of K-shell absorption spectroscopy. Absorption dips in the transmitted X-ray spectrum caused by the Al^{4+} and Al^{5+} ions were clearly seen during the experiments. To interpret the ionized charge distributions from the measured K-shell absorption lines, a plasma spectroscopic absorption model was developed and 1D hydrodynamic simulations were carried out. The 1D hydrodynamic simulations with MULTI-fs indicated

that the target is subject to a modest degree of hydrodynamic expansion at the time of 0.5 ps and 1 ps, necessitating a non-uniform model for detailed analysis. Three models were implemented to conduct the plasma spectroscopic simulations, including a non-uniform slab model with screened-hydrogenic opacity, a uniform slab model with screened-hydrogenic opacity and a uniform slab model with opacity from PrismSpect. Comparison with the experiments indicates that the simulation based on the non-uniform model agrees better with the measurements. The absorption coefficients predicted from the non-uniform simulations agree reasonably well with the measured ones for the Al^{4+} ions at the two delays, however, conspicuous discrepancies were found between the simulations and the experiments for the Al^{5+} ions. The limited number of photons that were captured during the experiment leads to large error bars on the Al^{5+} measurement and thus improved measurements would be required before drawing any strong conclusions. However this can be improved in the future by accumulating more photons by taking a larger number of shots. Despite there being some discrepancies between the simulations and experiments, the successful measurements of the ionization states of the warm dense aluminum indicates that Betatron radiation from laser wakefield acceleration is a powerful tool for time resolved absorption spectroscopy over a broad wavelength range.

Apart from the above LWFA and Betatron studies, we have conducted an experimental study to understand the resistive effect from target materials on electron transport relevant to Fast Ignition. The experiment was conducted using the second harmonic pulse from the Titan laser at the Jupiter Laser Facility located at the Lawrence Livermore National Laboratory. To study this effect, the ultra-short high intensity laser pulses (700 fs, $\sim 5 \times 10^{19}\, W/cm^2$, 527 nm) were used to irradiate multi-layer solid aluminum targets with a buried or front Au layer and a buried copper tracer layer, backed with a plastic get-lost layer to minimize the electron refluxing. Our experimental results indicate no evident resistive collimation of the hot electrons due to the high-Z Au layer,

as indicated by the unchanged size of the fluorescent spots from the copper tracer layers when comparing with the reference target where the gold layer is replaced by Al. 2D electron kinetic transport simulation results are in good agreement with the experiments and show that the B-fields generated at the layer interfaces in our experiments were relatively weak due to the low current density and therefore not sufficient to guide or collimate the hot electrons. An increase in the absorption of electron energy was observed in the case of the Au layers in the target.

12.2 Future work

As the major part of this thesis study, we have attempted to produce high-quality GeV electrons through LWFA and to employ the Betatron radiation to study the warm dense matter.

In the experiment with pure helium, we have found a transition mechanism from LWFA to PWFA that explains the observed electron energy enhancement in relatively high plasma density. This transition mechanism, often neglected by LWFA community, offers a possibility to achieve higher energy electrons with the laser driven wakefield accelerator. Simulation results show a good agreement with the experimental results. However, to fully understand the detailed characteristics of this two-stage process, further theoretical and experimental work is required. For instance, our current simulation shows that the tail of the laser E-field is trapped inside the bubble at the second stage when the primary electron bunch drives the wakefield. This trapped radiation is subject to a pulse stretching effect such that its oscillation frequency is decreased. This trapped radiation could be playing a role together with the primary electron bunch in modifying the secondary acceleration process. More theoretical analysis should be conducted to understand this residual E-field trapped inside the bubble, and experimental measurements should be made of these strongly

shifted field components. Furthermore, for any practical applications with the energetic electron beam, a sufficient charge is necessary. However, the charge of the GeV bunch obtained from this transition mechanism is on the order of a few pC, which may not be enough for some applications. Therefore, increasing the beam loading efficiency of the secondary bunch is necessary and again would require more theoretical and experimental studies.

In the experiments with pure nitrogen and pure helium mixed with CO_2, we only reported experimental studies in achieving 500 Mev to GeV electrons and identified some advantages of using these two types of gas targets. However, to fully understand the underlying physics and to control the generation of energetic electrons, theoretical modeling including ionization dynamics is required. In all the LWFA experiments, it is critical to have very reproducible laser pulse conditions (wave-front and pulse shape) in order to stabilize the high energy electron generation. Further work in improving the quality of the laser pules is required in the future.

Regarding the experiment of probing the ionization states of warm dense aluminum with Betatron radiation, we have successfully measured the ionization states of warm dense aluminum via the technique of K-shell absorption spectroscopy. However, the error bar of the measurement is significant due to the limited number of X-ray photons acquired during the experiments. This should be improved in the future by taking a larger number of shots. The laser already operates at 10 Hz and thus a higher shot rate could be obtained by installing a differential vacuum pumping system for the pulse gas jet and a high speed thin film target alignment system. With improved accuracy of the measurements, the quantitative information of the ionized charge distribution for the warm dense aluminum under non-equilibrium condition will become more accurate. The other issue with this experiments is the non-uniform heating of the target from the 30-fs laser pulse with the peak intensity of interest. This non-uniformity of the target conditions made the data analysis and interpre-

tation more difficult and less accurate. One way to improve this is to use a short-pulse proton beam to produce the warm dense matter, which has already been proven to be a good way to uniformly and isochorically heat ultra-thin targets[148]. However, more work has to be done to generate the proton source with desired energies and to integrate that source with the Betatron X-ray probe.

The secondary part of this thesis was to study the electron transport relevant to Fast Ignition. As indicated by our experiments and the simulations, the resistive layer did not collimate the hot electrons at our current densities. Further studies should extend these investigation to higher current density using second harmonic pulses. However, the problem studied here is just a small part of the FI process. The relativistic laser absorption and fast electron transport in a full-scale integrated FI experiment is more complex. Therefore a good deal of effort is still needed in order to better understand the hot electron generation and transport process.

Bibliography

[1] T. H. Maiman. Stimulated Optical Radiation in Ruby. *Nature*, 187:493, 1960.

[2] S. Harold. Mode-locked laser. *US Patent 3613028*, 1971.

[3] P. Maine, D. Strickland, P. Bado, M. Pessot, and G. Mourou. Generation of ultrahigh peak power pulses by chirped pulse amplification. *IEEE Journal of Quantum Electronics*, 24:398, 1988.

[4] G. Mourou. The ultrahigh-peak-power laser: present and future. *Applied Physics B*, 65:205, 1997.

[5] M. Tabak, J. Hammer, M. E. Glinsky, W. L. Kruer, S. C. Wilks, J. Woodworth, E. M. Campbell, M. D. Perry, and R. J. Mason. Ignition and high gain with ultrapowerful lasers. *Physics of Plasmas*, 1:1626, 1994.

[6] T. Tajima and J. M. Dawson. Laser Electron Accelerator. *Physical Review Letters*, 4:267, 1979.

[7] P. V. Nickles, V. N. Shlyaptsev, M. Kalachnikov, M. Schnürer, I. Will, and W. Sandner. Short Pulse X-Ray Laser at 32.6 nm Based on Transient Gain in Ne-like Titanium. *Physical Review Letters*, 78:2748, 1997.

[8] F. Ewald, H. Schwoerer, and R. Sauerbrey. Kα-radiation from relativistic laser-produced plasmas. *Europhysics Letters*, 60:710, 2002.

[9] R. W. Hamm and M. E. Hamm. *Industrial Accelerators and Their Applications*. World Scientific Press, Singapore, 2012.

[10] W. P. Levin, H. Kooy, J. S. Loeffler, and T. F. DeLaney. Proton beam therapy. *British Journal of Cancer*, 93:849, 2005.

[11] E. Esarey, P. Sprangle, S. Member, J. Krall, and A. Ting. Overview of Plasma-Based Accelerator Concepts. *IEEE Transactions on Plasma Science*, 24:252, 1996.

[12] E. Esarey, C. Schroeder, and W. Leemans. Physics of laser-driven plasma-based electron accelerators. *Reviews of Modern Physics*, 81:1229, 2009.

[13] O. Lundh, J. Lim, C. Rechatin, L. Ammoura, A. Ben-Ismaïl, X. Davoine, G. Gallot, J.-P. Goddet, E. Lefebvre, V. Malka, and J. Faure. Few femtosecond, few kiloampere electron bunch produced by a laserplasma accelerator. *Nature Physics*, 7:219, 2011.

[14] J. Osterhoff, A. Popp, Z. Major, B. Marx, T. P. Rowlands-Rees, M. Fuchs, M. Geissler, R. Hörlein, B. Hidding, S. Becker, E. A. Peralta, U. Schramm, F. Grüner, D. Habs, F. Krausz, S. M. Hooker, and S. Karsch. Generation of stable, low-divergence electron beams by laser-wakefield acceleration in a steady-state-flow gas cell. *Physical Review Letters*, 101:085002, 2008.

[15] R. Weingartner, S. Raith, A. Popp, S. Chou, J. Wenz, K. Khrennikov, M. Heigoldt, A. R. Maier, N. Kajumba, M. Fuchs, B. Zeitler, F. Krausz, S. Karsch, and F. Grüner. Ultralow emittance electron beams from a laser-wakefield accelerator. *Physical Review Special Topics - Accelerators and Beams*, 15:111302, 2012.

[16] P. Brijesh, C. Thaury, K. T. Phuoc, S. Corde, G. Lambert, V. Malka, S. P. D. Mangles, M. Bloom, and S. Kneip. Tuning the electron energy by

controlling the density perturbation position in laser plasma accelerators. *Physics of Plasmas*, 19:063104, 2012.

[17] A. Buck, J. Wenz, J. Xu, K. Khrennikov, K. Schmid, M. Heigoldt, J. M. Mikhailova, M. Geissler, B. Shen, F. Krausz, S. Karsch, and L. Veisz. Shock-Front Injector for High-Quality Laser-Plasma Acceleration. *Physical Review Letters*, 110:185006, 2013.

[18] X. Wang, R. Zgadzaj, N. Fazel, Z. Li, S. A. Yi, X. Zhang, W. Henderson, Y.-Y. Chang, R. Korzekwa, H.-E. Tsai, C.-H. Pai, H. Quevedo, G. Dyer, E. Gaul, M. Martinez, A. C. Bernstein, T. Borger, M. Spinks, M. Donovan, V. Khudik, G. Shvets, T. Ditmire, and M. C. Downer. Quasi-monoenergetic laser-plasma acceleration of electrons to 2 GeV. *Nature Communications*, 4:1988, 2013.

[19] W. P. Leemans, A. J. Gonsalves, H. Mao, K. Nakamura, C. Benedetti, C. B. Schroeder, C. Tóth, J. Daniels, D. E. Mittelberger, S. S. Bulanov, J. Vay, C. G. R. Geddes, and E. Esarey. Multi-GeV Electron Beams from Capillary-Discharge-Guided Subpetawatt Laser Pulses in the Self-Trapping Regime. *Physical Review Letters*, 113:245002, 2014.

[20] C. Clayton, J. Ralph, F. Albert, R. Fonseca, S. Glenzer, C. Joshi, W. Lu, K. Marsh, S. Martins, W. Mori, A. Pak, F. Tsung, B. Pollock, J. Ross, L. Silva, and D. Froula. Self-Guided Laser Wakefield Acceleration beyond 1 GeV Using Ionization-Induced Injection. *Physical Review Letters*, 105: 105003, 2010.

[21] S. Corde, K. Ta Phuoc, G. Lambert, R. Fitour, V. Malka, A. Rousse, A. Beck, and E. Lefebvre. Femtosecond x rays from laser-plasma accelerators. *Reviews of Modern Physics*, 85:1, 2013.

[22] N. D. Powers, I. Ghebregziabher, G. Golovin, C. Liu, S. Chen, S. Banerjee, J. Zhang, and D. P. Umstadter. Quasi-monoenergetic and tunable

X-rays from a laser-driven Compton light source. *Nature Photonics*, 8: 28, 2013.

[23] J. M. Boone and S. J. Anthony. A Figure of Merit Comparison between Bremsstrahlung and Monoenergetic X-Ray Sources for Angiography. *Journal of X-ray Science and Technology*, 5:334, 1994.

[24] D. J. Brenner, R. Doll, D. T. Goodhead, E. J. Hall, C. E. Land, J. B. Little, J. H. Lubin, D. L. Preston, R. J. Preston, J. S. Puskin, E. Ron, R. K. Sachs, J. M. Samet, R. B. Setlow, and M. Zaider. Cancer risks attributable to low doses of ionizing radiation: assessing what we really know. *Proceedings of the National Academy of Sciences of the United States of America*, 100:13761, 2003.

[25] A. Rousse, K. Ta Phuoc, R. Shah, R. Fitour, and F. Albert. Scaling of betatron X-ray radiation. *European Physical Journal D*, 45:391, 2007.

[26] S. Atzeni and J. Meyer-Ter-Vehn. *The Physics of Inertial Fusion*. Oxford Science Publications, Oxford, 2004.

[27] L. A. Artsimovich. Tokamak devices. *Nuclear Fusion*, 12:215, 1972.

[28] L. Spitzer. The stellarator concept. *Physics of Fluids*, 1:253, 1958.

[29] J. D. Lawson. Some Criteria for a Power Producing Thermonuclear Reactor. *Proceedings of the Physical Society*, 70:6, 1956.

[30] M. Honda, J. Meyer-ter Vehn, and A. Pukhov. Collective stopping and ion heating in relativistic-electron-beam transport for fast ignition. *Physical Review Letters*, 85:2128, 2000.

[31] C. McGuffey, G. R. Thomas, W. Schumaker, T. Matsuoka, V. Chvykov, F. J. Dollar, G. Kalintchenko, V. Yanovsky, A. Maksimchuk, K. Krushelnick, V. Yu. Bychenkov, I. V. Glazyrin, and V. Karpeev. Ionization

Induced Trapping in a Laser Wakefield Accelerator. *Physical Review Letters*, 104:025004, 2010.

[32] C. D. Decker, W. B. Mori, K.-C. Tzeng, and T. Katsouleas. The evolution of ultra-intense, short-pulse lasers in underdense plasmas. *Physics of Plasmas*, 3:2047, 1996.

[33] F. F. Chen. *Introduction to Plasma Physics and Controlled Fusion, Volume 1: Plasma Physics.* Springer, 2nd Ed., 1983.

[34] W. Lu, M. Tzoufras, C. Joshi, F. Tsung, W. Mori, J. Vieira, R. Fonseca, and L. Silva. Generating multi-GeV electron bunches using single stage laser wakefield acceleration in a 3D nonlinear regime. *Physical Review Special Topics - Accelerators and Beams*, 10:061301, 2007.

[35] J. M. Dawson. Nonlinear Electron Oscillations in a Cold Plasma. *The Physical Review*, 113:383, 1959.

[36] E. Esarey and M. Pilloff. Trapping and acceleration in nonlinear plasma waves. *Physics of Plasmas*, 2:1432, 1995.

[37] S. P. D. Mangles, G. Genoud, M. S. Bloom, M. Burza, Z. Najmudin, A. Persson, K. Svensson, A. G. R. Thomas, and C.-G. Wahlström. Self-injection threshold in self-guided laser wakefield accelerators. *Physical Review Special Topics - Accelerators and Beams*, 15:011302, 2012.

[38] F. S. Tsung, R. Narang, W. B. Mori, C. Joshi, R. A. Fonseca, and L.O. Silva. Near-GeV-Energy Laser-Wakeeld Acceleration of Self-Injected Electrons in a centimeter-scale plasma channel. *Physical Review Letters*, 93:185002, 2004.

[39] D. H. Froula, C. E. Clayton, T. Döppner, K. A. Marsh, C. P. J. Barty, L. Divol, R. A. Fonseca, S. H. Glenzer, C. Joshi, W. Lu, S. F. Martins, P. Michel, W. B. Mori, J. P. Palastro, B. B. Pollock, A. Pak, J. E. Ralph,

J. S. Ross, C. W. Siders, L. O. Silva, and T. Wang. Measurements of the Critical Power for Self-Injection of Electrons in a Laser Wakefield Accelerator. *Physical Review Letters*, 103:215006, 2009.

[40] A. G. R. Thomas. Scalings for radiation from plasma bubbles. *Physics of Plasmas*, 17:056708, 2010.

[41] S. P. D. Mangles, A. G. R. Thomas, O. Lundh, F. Lindau, M. C. Kaluza, A. Persson, C.-G. Wahlstrom, K. Krushelnick, and Z. Najmudin. On the stability of laser wakefield electron accelerators in the monoenergetic regime. *Physics of Plasmas*, 14:056702, 2007.

[42] A. Pak, K. A. Marsh, S. F. Martins, W. Lu, W. B. Mori, and C. Joshi. Injection and Trapping of Tunnel-Ionized Electrons into Laser-Produced Wakes. *Physical Review Letters*, 104:025003, 2010.

[43] P. Gibbon. *Short Pulse Laser Interactions with Matter*. Imprerial College Press, London, 2005.

[44] J. Faure, Y. Glinec, A. Pukhov, S. Kiselev, E. Gordienko, S.and Lefebvre, J.-P. Rousseau, F. Burgy, and V. Malka. A laser-plasma accelerator producing monoenergetic electron beams. *Nature*, 431:541, 2004.

[45] W. P. Leemans, B. Nagler, A. J. Gonsalves, Cs. Tóth, K. Nakamura, C. G. R. Geddes, E. Esarey, C. B. Schroeder, and S. M. Hooker. GeV electron beams from a centimetre-scale accelerator. *Nature Physics*, 2: 696, 2006.

[46] N. A. M. Hafz, T. M. Jeong, I. W. Choi, S. K. Lee, K. H. Pae, V. V. Kulagin, J. H. Sung, T. J. Yu, K-. H. Hong, T. Hosokai, J. R. Cary, D.-K. Ko, and J. Lee. Stable generation of GeV-class electron beams from self-guided laser plasma channels. *Nature Photonics*, 2:571, 2008.

[47] S. Kneip, S. Nagel, S. Martins, S. Mangles, C. Bellei, O. Chekhlov, R. Clarke, N. Delerue, E. Divall, G. Doucas, K. Ertel, F. Fiuza, R. Fonseca, P. Foster, S. Hawkes, C. Hooker, K. Krushelnick, W. Mori, C. Palmer, K. Phuoc, P. Rajeev, J. Schreiber, M. Streeter, D. Urner, J. Vieira, L. Silva, and Z. Najmudin. Near-GeV Acceleration of Electrons by a Nonlinear Plasma Wave Driven by a Self-Guided Laser Pulse. *Physical Review Letters*, 103:035002, 2009.

[48] J. E. Ralph, C. E. Clayton, F. Albert, B. B. Pollock, S. F. Martins, A. E. Pak, K. A. Marsh, J. L. Shaw, A. Till, J. P. Palastro, W. Lu, S. H. Glenzer, L. O. Silva, W. B. Mori, C. Joshi, and D. H. Froula. Laser wakefield acceleration at reduced density in the self-guided regime. *Physics of Plasmas*, 17:056709, 2010.

[49] J. S. Liu, C. Q. Xia, W. T. Wang, H. Y. Lu, Ch. Wang, A. H. Deng, W. T. Li, H. Zhang, X. Y. Liang, Y. X. Leng, X. M. Lu, C. Wang, J. Z. Wang, K. Nakajima, R. X. Li, and Z. Z. Xu. All-Optical Cascaded Laser Wakefield Accelerator Using Ionization-Induced Injection. *Physical Review Letters*, 107:035001, 2011.

[50] M. Z. Mo, A. Ali, S. Fourmaux, P. Lassonde, J. C. Kieffer and R. Fedosejevs. Quasimonoenergetic electron beams from laser wakefield acceleration in pure nitrogen. *Applied Physics Letters*, 100:074101, 2012.

[51] M. Z. Mo, A. Ali, S. Fourmaux, P. Lassonde, J. C. Kieffer, and R. Fedosejevs. Generation of 500 MeV - GeV energy electrons from laser wakefield acceleration via ionization induced injection using CO_2 mixed in He. *Applied Physics Letters*, 102:134102, 2013.

[52] P. Chen, J. M. Dawson, and T. Huff, R. W.and Katsouleas. Acceleration of Electrons by the Interaction of a bunched Electron Beam with a Plasma. *Physical Review Letters*, 54:693, 1985.

[53] P. Muggli, B. Blue, C. Clayton, S. Deng, F.-J. Decker, M. Hogan, C. Huang, R. Iverson, C. Joshi, T. Katsouleas, S. Lee, W. Lu, K. Marsh, W. Mori, C. O'Connell, P. Raimondi, R. Siemann, and D. Walz. Meter-Scale Plasma-Wakefield Accelerator Driven by a Matched Electron Beam. *Physical Review Letters*, 93:014802, 2004.

[54] T. Katsouleas, S. Wilks, P. Chen, J. M. Dawson, and J. J. Su. Beam Loading In Plasma Accelerators. *Particle Accelerators*, 22:81, 1987.

[55] S. Gordienko and A. Pukhov. Scalings for ultrarelativistic laser plasmas and quasimonoenergetic electrons. *Physics of Plasmas*, 12:043109, 2005.

[56] M. Tzoufras, W. Lu, F. Tsung, C. Huang, W. Mori, T. Katsouleas, J. Vieira, R. Fonseca, and L. Silva. Beam Loading in the Nonlinear Regime of Plasma-Based Acceleration. *Physical Review Letters*, 101: 145002, 2008.

[57] I. Blumenfeld, C. E. Clayton, F.-J. Decker, M. J. Hogan, C. Huang, R. Ischebeck, R. Iverson, C. Joshi, T. Katsouleas, N. Kirby, W. Lu, K. A. Marsh, W. B. Mori, P. Muggli, E. Oz, R. H. Siemann, D. Walz, and M. Zhou. Energy doubling of 42 GeV electrons in a metre-scale plasma wakefield accelerator. *Nature*, 445:741, 2007.

[58] E. Esarey, B. A. Shadwick, P. Catravas, and W. P. Leemans. Synchrotron radiation from electron beams in plasma-focusing channels. *Physical Review*, 65:056505, 2002.

[59] F. Albert, R. Shah, K. T. Phuoc, R. Fitour, F. Burgy, J.-P. Rousseau, A. Tafzi, D. Douillet, T. Lefrou, and A. Rousse. Betatron oscillations of electrons accelerated in laser wakefields characterized by spectral X-ray analysis. *Physical Review E*, 77:056402, 2008.

[60] J. D. Jackson. *Classical Electromagnetics.* John Wiley and Sons, 3rd Ed., New York, 2001.

[61] K. Phuoc, S. Corde, R. Shah, F. Albert, R. Fitour, J.-P. Rousseau, F. Burgy, B. Mercier, and A. Rousse. Imaging Electron Trajectories in a Laser-Wakefield Cavity Using Betatron X-Ray Radiation. *Physical Review Letters*, 97:225002, 2006.

[62] F. Albert, B. B. Pollock, J. L. Shaw, K. A. Marsh, J. E. Ralph, Y. Chen, D. Alessi, A. Pak, C. E. Clayton, S. H. Glenzer, and C. Joshi. Angular Dependence of Betatron X-Ray Spectra from a Laser-Wakefield Accelerator. *Physical Review Letters*, 111:235004, 2013.

[63] I. Kostyukov, S. Kiselev, and A. Pukhov. X-ray generation in an ion channel. *Physics of Plasmas*, 10:4818, 2003.

[64] S. Kneip, C. Mcguffey, J. L. Martins, S. F. Martins, C. Bellei, V. Chvykov, F. Dollar, R. Fonseca, C. Huntington, G. Kalintchenko, A. Maksimchuk, S. P. D. Mangles, T. Matsuoka, S. R. Nagel, C. A. J. Palmer, J. Schreiber, K. T. Phuoc, A. G. R. Thomas, V. Yanovsky, L. O. Silva, K. Krushelnick, and Z. Najmudin. Bright spatially coherent synchrotron X-rays from a table-top source. *Nature Physics*, 6:980, 2010.

[65] W. Ackermann, G. Asova, and et al. Operation of a free-electron laser from the extreme ultraviolet to the water window. *Nature Photonics*, 1: 336, 2007.

[66] S. Fourmaux, S. Corde, K. T. Phuoc, P. Lassonde, G. Lebrun, S. Payeur, F. Martin, S. Sebban, V. Malka, A. Rousse, and J. C. Kieffer. Single shot phase contrast imaging using laser-produced Betatron x-ray beams. *Optics Letters*, 36:2426, 2011.

[67] S. Atzeni. Inertial fusion fast ignitor: Igniting pulse parameter window

vs the penetration depth of the heating particles and the density of the precompressed fuel. *Physics of Plasmas*, 6:3316, 1999.

[68] C. Li and R. Petrasso. Stopping of directed energetic electrons in high-temperature hydrogenic plasmas. *Physical Review E*, 70:067401, 2004.

[69] J. C. Kieffer, P. Audebert, M. Chaker, J. P. Matte, H. Pepin, and T. W. Johnston. Short-Pulse Laser Absorption in Very Steep Plasma Density Gradients. *Physical Review Letters*, 62:760, 1989.

[70] J.P. Freidberg, R. W. Mitchell, R. L. Morse, and L. I. Rudsinski. Resonant Absorption of Laser Light by Plasma Targets. *Physical Review Letters*, 28:795, 1972.

[71] D.W. Forslund, J. M. Kindel, K. Lee, E. L. Lindman, and R. L. Morse. Theory and simulation of resonant absorption in a hot plasma. *Physical Review A*, 11:679, 1975.

[72] F. Brunel. Not-So-Resonant,Resonant Absorption. *Physical Review Letters*, 59:6, 1987.

[73] P. Gibbon and A. R. Bell. Collisionless absorption in sharp-edged plasmas. *Physical Review Letters*, 68:1535, 1992.

[74] W. L. Kruer and K. Estabrook. JB heating by very intense laser light. *Physics of Fluids*, 28:430, 1985.

[75] F. N. Beg, A. R. Bell, A. E. Dangor, C. N. Danson, A. P. Fews, M. E. Glinsky, B. A. Hammel, P. Lee, P. A. Norreys, and M. Tatarakis. A study of picosecond lasersolid interactions up to 10^{19} W/cm^2. *Physics of Plasmas*, 4:447, 1997.

[76] S. C. Wilks, W. L. Kruer, M. Tabak, and A. B. Langdon. Absorption of ultra-intense laser pulses. *Physical Review Letters*, 69:1383, 1992.

[77] M. Haines, M. Wei, F. Beg, and R. Stephens. Hot-electron temperature and laser-light absorption in fast ignition. *Physical Review Letters*, 102: 045008, 2009.

[78] A. G. MacPhee, K. U. Akli, F. N. Beg, C. D. Chen, H. Chen, R. Clarke, D. S. Hey, R. R. Freeman, A. J. Kemp, M. H. Key, J. A. King, S. Le Pape, A. Link, T. Y. Ma, H. Nakamura, D. T. Offermann, V. M. Ovchinnikov, P. K. Patel, T. W. Phillips, R. B. Stephens, R. Town, Y. Y. Tsui, M. S. Wei, L. D. Van Woerkom, and A. J. MacKinnon. Diagnostics for fast ignition science. *Review of Scientific Instruments*, 79:10F302, 2008.

[79] C. D. Chen, J. A. King, M. H. Key, K. U. Akli, F. N. Beg, H. Chen, R. R. Freeman, A. Link, A. J. MacKinnon, A. G. MacPhee, P. K. Patel, M. Porkolab, R. B. Stephens, and L. D. Van Woerkom. A Bremsstrahlung spectrometer using k-edge and differential filters with image plate dosimeters. *Review of Scientific Instruments*, 79:10E305, 2008.

[80] C. D. Chen. *Spectrum and Conversion Efficiency Measurements of Suprathermal Electrons From Relativistic Laser Plasma Interactions.* PhD thesis, Massachusetts Institute of Technology, 2009.

[81] B. Westover, C. D. Chen, P. K. Patel, H. McLean, and F. N. Beg. Characterization of the fast electrons distribution produced in a high intensity laser target interaction. *Physics of Plasmas*, 21:031212, 2014.

[82] A. R. Bell, J. R. Davies, S. Guerin, and H Ruhl. Fast-electron transport in high-intensity short-pulse laser-solid experiments. *Plasma Physics and Controlled Fusion*, 39:653, 1997.

[83] Y. T. Lee and R. M. More. An electron conductivity model for dense plasmas. *Physics of Fluids*, 27:1273, 1984.

[84] R. Harrach and R. Kidder. Simple model of energy deposition by

suprathermal electrons in laser-irradiated targets. *Physical Review A*, 23:887, 1981.

[85] S. Fourmaux, S. Payeur, A. Alexandrov, C. Serbanescu, F. Martin, T. Ozaki, A. Kudryashov, and J. C. Kieffer. Laser beam wavefront correction for ultra high intensities with the 200 tw laser system at the advanced laser light source. *Optics Express*, 16:11987, 2008.

[86] S. Fourmaux, S. Payeur, S. Buffechoux, P. Lassonde, C. St-Pierre, F. Martin, and J. C. Kieffer. Pedestal cleaning for high laser pulse contrast ratio with a 100 tw class laser system. *Optics Express*, 19:8486, 2011.

[87] https://jlf.llnl.gov/html/facilities/titan/titan.php.

[88] S. Semushin and V. Malka. High density gas jet nozzle design for laser target production. *Review of Scientific Instruments*, 72:2961, 2001.

[89] R. Benattar, C. Popovics, and R. Siger. Polarized light interferometer for laser fusion studies. *Review of Scientific Instruments*, 50:1583, 1979.

[90] K. Bockasten. Transformation of Observed Radiances into Radial Distribution of the Emission of a Plasma. *Journal of the Optical Society of America*, 51:943, 1961.

[91] R. Fedosejevs. *Critical Density Profiles of Plasmas Produced by Nanosecond Gigawatt CO2 Laser Pulses*. PhD thesis, University of Toronto, 1979.

[92] N. Gottardi. Evaluation of electron density profiles in plasmas from integrated measurements. *Journal of Applied Physics*, 50:2647, 1979.

[93] R. A. Baumgartner and R. Byer. Optical Parametric Amplification. *IEEE Journal of Quantum Electronics*, 15:432, 1979.

[94] W. L. Bragg. The diffraction of short electromagnetic waves by a crystal. *Proceedings of the Cambridge Philosophical Society*, 17:43, 1913.

[95] K. U. Akli, M. H. Key, H. K. Chung, S. B. Hansen, R. R. Freeman, M. H. Chen, G. Gregori, S. Hatchett, D. Hey, N. Izumi, J. King, J. Kuba, P. Norreys, A. J. Mackinnon, C. D. Murphy, R. Snavely, R. B. Stephens, C. Stoeckel, W. Theobald, and B. Zhang. Temperature sensitivity of Cu K imaging efficiency using a spherical Bragg reflecting crystal. *Physics of Plasmas*, 14:023102, 2007.

[96] H. Legall, H. Stiel, V. Arkadiev, and A. A. Bjeoumikhov. High spectral resolution x-ray optics with highly oriented pyrolytic graphite. *Optics Express*, 14:4570, 2006.

[97] A. V. Baez and P. Kirkpatrick. Formation of Optical Images by X-Rays. *Journal of the Optical Society of America*, 6:766, 1948.

[98] A. Modena, Z. Najmudin, A. E. Dangor, C. E. Clayton, K. A. Marsh, C. Joshi, V. Malka, C.B. Darrow, C. N. Danson, D. Neely, and F.N. Walsh. Electron acceleration from the breaking of relativistic plasma waves. *Nature*, 377:606, 1995.

[99] D. Umstadter, S.-Y. Chen, A. Maksimchuk, G. Mourou, and R. Wagner. Nonlinear optics in relativistic plasmas and laser wake field acceleration of electrons. *Science*, 273:472, 1996.

[100] S. P. D. Mangles, C. D. Murphy, Z. Najmudin, A. G. R. Thomas, J. L. Collier, A. E. Dangor, E. J. Divall, P. S. Foster, J. G. Gallacher, C. J. Hooker, D. A. Jaroszynski, A. J. Langley, W. B. Mori, P. A. Norreys, F. S. Tsung, R. Viskup, B. R. Walton, and K. Krushelnick. Monoenergetic beams of relativistic electrons from intense laser-plasma interactions. *Nature*, 43:535, 2004.

[101] C. G. R. Geddes, J. V. Tilborg, E. Esarey, C. B. Schroeder, D. Bruhwiler, C. Nieter, J. Cary, and W. P. Leemans. High-quality electron beams from

a laser wakefield accelerator using plasma-channel guiding. *Nature*, 431: 538, 2004.

[102] A. Thomas, Z. Najmudin, S. Mangles, C. Murphy, A. Dangor, C. Kamperidis, K. Lancaster, W. Mori, P. Norreys, W. Rozmus, and K. Krushelnick. Effect of laser-focusing conditions on propagation and monoenergetic electron production in laser-wakefield accelerators. *Physical Review Letters*, 98:095004, 2007.

[103] C. McGuffey, T. Matsuoka, S. Kneip, W. Schumaker, F. Dollar, C. Zulick, V. Chvykov, G. Kalintchenko, V. Yanovsky, A. Maksimchuk, A. G. R. Thomas, K. Krushelnick, and Z. Najmudin. Experimental laser wakefield acceleration scalings exceeding 100tw. *Physics of Plasmas*, 19:063113, 2012.

[104] P. Mora and T. Antonsen. Electron cavitation and acceleration in the wake of an ultraintense, self-focused laser pulse. *Physical Review E*, 53: R2068, 1996.

[105] A. Pukhov and J. Meyer-ter Vehn. Laser wake field acceleration: the highly non-linear broken-wave regime. *Applied Physics B*, 74:355, 2002.

[106] W. Lu, C. Huang, M. Zhou, M. Tzoufras, F. S. Tsung, W. B. Mori, and T. Katsouleas. A nonlinear theory for multidimensional relativistic plasma wave wakefieldsa. *Physics of Plasmas*, 13:056709, 2006.

[107] S. Kalmykov, S. Yi, V. Khudik, and G. Shvets. Electron self-injection and trapping into an evolving plasma bubble. *Physical Review Letters*, 103:135004, 2009.

[108] S. Y. Kalmykov, A. Beck, S. A. Yi, V. N. Khudik, M. C. Downer, E. Lefebvre, B. A. Shadwick, and D. P. Umstadter. Electron self-injection into an

evolving plasma bubble: Quasi-monoenergetic laser-plasma acceleration in the blowout regimea. *Physics of Plasmas*, 18:056704, 2011.

[109] J. B. Rosenzweig, B. Breizman, T. Katsouleas, and J. J. Su. Acceleration and focusing of electrons in two-dimensional nonlinear plasma wake fields. *Physical Review A*, 44:R6189, 1991.

[110] M. Hogan, C. Barnes, C. Clayton, F. Decker, S. Deng, P. Emma, C. Huang, R. Iverson, D. Johnson, C. Joshi, T. Katsouleas, P. Krejcik, W. Lu, K. Marsh, W. Mori, P. Muggli, C. O'Connell, E. Oz, R. Siemann, and D. Walz. Multi-GeV Energy Gain in a Plasma-Wakefield Accelerator. *Physical Review Letters*, 95:054802, 2005.

[111] D. Gordon, K. Tzeng, C. Clayton, A. Dangor, V. Malka, K. Marsh, A. Modena, W. Mori, P. Muggli, Z. Najmudin, D. Neely, C. Danson, and C. Joshi. Observation of Electron Energies Beyond the Linear Dephasing Limit from a Laser-Excited Relativistic Plasma Wave. *Physical Review Letters*, 80:2133, 1998.

[112] C. M. Huntington, A. G R Thomas, C. McGuffey, T. Matsuoka, V. Chvykov, G. Kalintchenko, S. Kneip, Z. Najmudin, C. Palmer, V. Yanovsky, A. Maksimchuk, R. P. Drake, T. Katsouleas, and K. Krushelnick. Current filamentation instability in laser wakefield accelerators. *Physical Review Letters*, 106:105001, 2011.

[113] B. Hidding, T. Königstein, J. Osterholz, S. Karsch, O. Willi, and G. Pretzler. Monoenergetic Energy Doubling in a Hybrid Laser-Plasma Wakefield Accelerator. *Physical Review Letters*, 104:195002, 2010.

[114] K. H. Pae, I. W. Choi, and J. Lee. Self-mode-transition from laser wakefield accelerator to plasma wakefield accelerator of laser-driven plasma-based electron acceleration. *Physics of Plasmas*, 17:123104, 2010.

[115] W. Li, J. Liu, W. Wang, Z. Zhang, Q. Chen, Y. Tian, R. Qi, C. Yu, C. Wang, T. Tajima, R. Li, and Z. Xu. The phase-lock dynamics of the laser wakefield acceleration with an intensity-decaying laser pulse. *Applied Physics Letters*, 104:093510, 2014.

[116] S. Fourmaux, K. Ta Phuoc, P. Lassonde, S. Corde, G. Lebrun, V. Malka, A. Rousse, and J. C. Kieffer. Quasi-monoenergetic electron beams production in a sharp density transition. *Applied Physics Letters*, 101:111106, 2012.

[117] P. Gibbon, F. Jakober, P. Monot, and T. Auguste. Experimental study of relativistic self-focuing and Self-channeling of an Intense Laser. *IEEE Transactions on Plasma Science*, 24:343, 1996.

[118] J. E. Ralph, K. A. Marsh, A. E. Pak, W. Lu, C. E. Clayton, F. Fang, W. B. Mori, and C. Joshi. Self-Guiding of Ultrashort, Relativistically Intense Laser Pulses through Underdense Plasmas in the Blowout Regime. *Physical Review Letters*, 102:175003, 2009.

[119] A. G. R. Thomas, S. P. D. Mangles, Z. Najmudin, M. C. Kaluza, C. D. Murphy, and K. Krushelnick. Measurements of wave-breaking radiation from a laser-wakefield accelerator. *Physical Review Letters*, 98:054802, 2007.

[120] T. Matsuoka, C. McGuffey, P. G. Cummings, Y. Horovitz, F. Dollar, V. Chvykov, G. Kalintchenko, P. Rousseau, V. Yanovsky, S. S. Bulanov, A. G R Thomas, A. Maksimchuk, and K. Krushelnick. Stimulated Raman side scattering in laser wakefield acceleration. *Physical Review Letters*, 105:034801, 2010.

[121] K. I. Popov, V. Yu. Bychenkov, W. Rozmus, R. D. Sydora, and S. S. Bulanov. Vacuum electron acceleration by tightly focused laser pulses with nanoscale targets. *Physics of Plasmas*, 16:053106, 2009.

[122] D. Romanov, V. Bychenkov, W. Rozmus, C. Capjack, and R. Fedosejevs. Self-Organization of a Plasma due to 3D Evolution of the Weibel Instability. *Physical Review Letters*, 93:215004, 2004.

[123] A. G. Mordovanakis, P.-E. Masson-Laborde, J. Easter, K. Popov, B. Hou, G. Mourou, W. Rozmus, M. G. Haines, J. Nees, and K. Krushelnick. Temperature scaling of hot electrons produced by a tightly focused relativistic-intensity laser at 0.5 kHz repetition rate. *Applied Physics Letters*, 96: 071109, 2010.

[124] A. K. Upadhyay, S. Arun Samant, and S. Krishnagopal. Role of the laser pulse-length in producing high-quality electron beams in a homogenous plasma. *Physics of Plasmas*, 19:073110, 2012.

[125] N. Vafaei-Najafabadi, K. A. Marsh, C. E. Clayton, W. An, W. B. Mori, C. Joshi, W. Lu, E. Adli, S. Corde, M. Litos, S. Li, S. Gessner, J. Frederico, A. S. Fisher, Z. Wu, D. Walz, R. J. England, J. P. Delahaye, C. I. Clarke, M. J. Hogan, and P. Muggli. Beam Loading by Distributed Injection of Electrons in a Plasma Wakefield Accelerator. *Physical Review Letters*, 112:025001, 2014.

[126] A. Oguchi, A. Zhidkov, K. Takano, E. Hotta, K. Nemoto, and K. Nakajima. Multiple self-injection in the acceleration of monoenergetic electrons by a laser wake field. *Physics of Plasmas*, 15:043102, 2008.

[127] P. Sprangle, E. Esarey, and A. Ting. Nonlinear interaction of intense laser pulses in plasmas. *Physical Review A*, 41:4463, 1990.

[128] B. A. Shadwick, C. B. Schroeder, and E. Esarey. Nonlinear laser energy depletion in laser-plasma accelerators. *Physics of Plasmas*, 16:056704, 2009.

[129] C. Decker and W.B. Mori. Group velocity of large-amplitude electromagnetic waves in a plasma. *Physical Review Letters*, 72:490, 1994.

[130] C. D. Decker and W. B. Mori. Group velocity of large-amplitude electromagnetic waves in a plasma. *Physical Review E*, 51:1364, 1995.

[131] W. Zhu, J. P. Palastro, and T. M. Antonsen. Pulsed mid-infrared radiation from spectral broadening in laser wakefield simulations. *Physics of Plasmas*, 20:073103, 2013.

[132] S. Kiselev, A. Pukhov, and I. Kostyukov. X-ray Generation in Strongly Nonlinear Plasma Waves. *Physical Review Letters*, 93:135004, 2004.

[133] A. Rousse, K. Phuoc, R. Shah, A. Pukhov, E. Lefebvre, V. Malka, S. Kiselev, F. Burgy, J.-P. Rousseau, D. Umstadter, and D. Hulin. Production of a keV X-Ray Beam from Synchrotron Radiation in Relativistic Laser-Plasma Interaction. *Physical Review Letters*, 93:135005, 2004.

[134] A. Popp, J. Vieira, J. Osterhoff, Zs. Major, R. Hörlein, M. Fuchs, R. Weingartner, T. P. Rowlands-Rees, M. Marti, R. A. Fonseca, S. F. Martins, L. O. Silva, S. M. Hooker, F. Krausz, F. Grüner, and S. Karsch. All-Optical Steering of Laser-Wakefield-Accelerated Electron Beams. *Physical Review Letters*, 105:215001, 2010.

[135] M. Schnell, A. Sävert, I. Uschmann, M. Reuter, M. Nicolai, T. Kämpfer, B. Landgraf, O. Jäckel, O. Jansen, A. Pukhov, M. C. Kaluza, and C. Spielmann. Optical control of hard X-ray polarization by electron injection in a laser wakefield accelerator. *Nature Communications*, 4: 2421, 2013.

[136] D. Strickland and G. Mourou. Compression of amplified chirped optical pulses. *Optics Communications*, 55:447, 1985.

[137] E. Oz, S. Deng, T. Katsouleas, P. Muggli, C. Barnes, I. Blumenfeld, F. Decker, P. Emma, M. Hogan, R. Ischebeck, R. Iverson, N. Kirby, P. Krejcik, C. O?Connell, R. Siemann, D. Walz, D. Auerbach, C. Clayton, C. Huang, D. Johnson, C. Joshi, W. Lu, K. Marsh, W. Mori, and M. Zhou. Ionization-Induced Electron Trapping in Ultrarelativistic Plasma Wakes. *Physical Review Letters*, 98:084801, 2007.

[138] T. P. Rowlands-Rees, C. Kamperidis, S. Kneip, A. J. Gonsalves, S. P. D. Mangles, J. G. Gallacher, E. Brunetti, T. Ibbotson, C. D. Murphy, P. S. Foster, M. J. V. Streeter, F. Budde, P. A. Norreys, D. A. Jaroszynski, K. Krushelnick, Z. Najmudin, and S. M. Hooker. Laser-Driven Acceleration of Electrons in a Partially Ionized Plasma Channel. *Physical Review Letters*, 100:105005, 2008.

[139] F. V. Hartemann, D. J. Gibson, W. J. Brown, A. Rousse, K. Ta Phuoc, V. Mallka, J. Faure, and A. Pukhov. Compton scattering x-ray sources driven by laser wakefield acceleration. *Physical Review Special Topics - Accelerators and Beams*, 10:011301, 2007.

[140] S. P. D. Mangles, G. Genoud, S. Kneip, M. Burza, K. Cassou, B. Cros, N. P. Dover, C. Kamperidis, Z. Najmudin, A. Persson, J. Schreiber, F. Wojda, and C.-G. Wahlstrm. Controlling the spectrum of x-rays generated in a laser-plasma accelerator by tailoring the laser wavefront. *Applied Physics Letters*, 95:181106, 2009.

[141] R. Fedosejevs, X. F. Wang, and G. D. Tsakiris. Onset of relativistic self-focusing in high density gas jet targets. *Physical Review E*, 56:4615, 1997.

[142] M. Adachi, E. Miura, S. Kato, K. Koyama, S. Masuda, T. Watanabe, A. Ogata, H. Okamoto, and M. Tanimoto. Monoenergetic electron beam

generation in a laser-driven plasma acceleration. *Laser Physics Letters*, 3:79, 2006.

[143] H. Kotaki, Y. Hayashi, K. Kawase, M. Mori, M. Kando, T. Homma, J. K. Koga, H. Daido, and S. V. Bulanov. Manipulation and electron-oscillation-measurement of laser accelerated electron beams. *Plasma Physics and Controlled Fusion*, 53:014009, 2011.

[144] N. Hafz, G. H. Kim, C. Kim, and H. Suk. Generation of good-quality relativistic electron b e a m from self-modulated laser wakefield acceleration. *International Journal of Modern Physics B*, 21:398, 2007.

[145] A. F. Lifschitz and V. Malka. Optical phase effects in electron wakefield acceleration using few-cycle laser pulses. *New Journal of Physics*, 14: 053045, 2012.

[146] K. P. Singh and V. Sajal. Quasimonoenergic collimated electrons from the ionization of nitrogen by a chirped intense laser pulse. *Physics of Plasmas*, 16:043113, 2009.

[147] T. Auguste, P Monot, L.-A. Lompr, G. Mainfray, and C Manus. Defocusing effects of a picosecond terawatt laser pulse in an underdense plasma. *Optics Communications*, 89:145, 1992.

[148] A. Mancic, A. Levy, M. Harmand, M. Nakatsutsumi, P. Antici, P. Audebert, P. Combis, S. Fourmaux, S. Mazevet, O. Peyrusse, V. Recoules, P. Renaudin, J. Robiche, F. Dorchies, and J. Fuchs. Picosecond short-range disordering in isochorically heated aluminum at solid density. *Physical Review Letters*, 104:035002, 2010.

[149] D. Milathianaki, S. Boutet, G. J. Williams, A. Higginbotham, D. Ratner, A. E. Gleason, M. Messerschmidt, M. M. Seibert, D. C. Swift, P. Hering,

J. Robinson, W. E. White, and J. S. Wark. Femtosecond visualization of lattice dynamics in shock-compressed matter. *Science*, 342:220, 2013.

[150] S. Kneip, S. Nagel, C. Bellei, N. Bourgeois, A. Dangor, A. Gopal, R. Heathcote, S. Mangles, J. Marquès, A. Maksimchuk, P. Nilson, K. Phuoc, S. Reed, M. Tzoufras, F. Tsung, L. Willingale, W. Mori, A. Rousse, K. Krushelnick, and Z. Najmudin. Observation of Synchrotron Radiation from Electrons Accelerated in a Petawatt-Laser-Generated Plasma Cavity. *Physical Review Letters*, 100:105006, 2008.

[151] S. Fourmaux, S. Corde, K. Ta Phuoc, P. M. Leguay, S. Payeur, P. Lassonde, S. Gnedyuk, G. Lebrun, C. Fourment, V. Malka, S. Sebban, A. Rousse, and J. C. Kieffer. Demonstration of the synchrotron-type spectrum of laser-produced betatron radiation. *New Journal of Physics*, 13:033017, 2011.

[152] M. Z. Mo, Z. Chen, S. Fourmaux, A. Saraf, K. Otani, J. C. Kieffer, Y. Y. Tsui, A. Ng, and R. Fedosejevs. Laser wakefield generated x-ray probe for femtosecond time-resolved measurements of ionization states of warm dense aluminum. *Review of Scientific Instruments*, 84:123106, 2013.

[153] National Institute of Standards, Attenuation Technology, X-ray Form factor, and Scattering Tables. http://physics.nist.gov/PhysRefData/FFast/html/form.html.

[154] D. P. Trauernicht and R. V. Metter. The measurement of conversion noise in x-ray intensifying screens. *Proceeding of SPIE*, 914:100, 1988.

[155] H. E. Bennett and J. O. Porteus. Relation between surface roughness and specular reflectance at normal incidence. *Journal of the Optical Society of America*, 51:123, 1961.

[156] H. Davies. The reflection of electromagnetic waves from a rough surface. *Monograph: Radio Sec.*, 90:209, 1954.

[157] H. Friesen, H. F. Tiedje, D. S. Hey, M. Z. Mo, A. Beaudry, R. Fedosejevs, Y. Y. Tsui, A. Mackinnon, H. S. McLean, and P. K. Patel. Kirkpatrick-baez microscope for hard x-ray imaging of fast ignition experiments. *Review of Scientific Instruments*, 84:023704, 2013.

[158] A. Ng, T. Ao, F. Perrot, M. W. C. Dharma-Wardana, and M. E. Foord. Idealized slab plasma approach for the study of warm dense matter. *Laser and Particle Beams*, 23:527, 2005.

[159] D. Saumon, G. Chabrier, D. J. Wagner, and X. Xie. Modeling pressure-ionization of hydrogen in the context of astrophysics. *High Pressure Research*, 16:331, 2000.

[160] T. R. Dittrich, S. W. Haan, M. M. Marinak, S. M. Pollaine, D. E. Hinkel, D. H. Munro, C. P. Verdon, G. L. Strobel, R. McEachern, R. C. Cook, C. C. Roberts, D. C. Wilson, P. A. Bradley, L. R. Foreman, and W. S. Varnum. Review of indirect-drive ignition design options for the national ignition facility. *Physics of Plasmas*, 6:2164, 1999.

[161] A. Forsman, A. Ng, G. Chiu, and R. M. More. Interaction of femtosecond laser pulses with ultrathin foils. *Physical Review E*, 58:R1248, 1998.

[162] K. Widmann, T. Ao, M. E. Foord, D. F. Price, A. D. Ellis, P. T. Springer, and A. Ng. Single-state measurement of electrical conductivity of warm dense gold. *Physical Review Letters*, 92:125002, 2004.

[163] T. Ao, Y. Ping, K. Widmann, D. F. Price, E. Lee, H. Tam, P. T. Springer, and A. Ng. Optical properties in nonequilibrium phase transitions. *Physical Review Letters*, 96:055001, 2006.

[164] Y. Ping, D. Hanson, I. Koslow, T. Ogitsu, D. Prendergast, E. Schwegler, G. Collins, and A. Ng. Broadband dielectric function of nonequilibrium warm dense gold. *Physical Review Letters*, 96:255003, 2006.

[165] Z. Chen, V. Sametoglu, Y. Y. Tsui, T. Ao, and A. Ng. Flux-limited nonequilibrium electron energy transport inwarm dense gold. *Physical Review Letters*, 108:165001, 2012.

[166] Z. Chen, B. Holst, S. E. Kirkwood, V. Sametoglu, M. Reid, Y. Y. Tsui, V. Recoules, and A. Ng. Evolution of ac conductivity in nonequilibrium warm dense gold. *Physical Review Letters*, 110:135001, 2013.

[167] B. I. Cho, K. Engelhorn, A. A. Correa, T. Ogitsu, C. P. Weber, H. J. Lee, J. Feng, P. A. Ni, Y. Ping, A. J. Nelson, D. Prendergast, R. W. Lee, R. W. Falcone, and P. A. Heimann. Electronic structure of warm dense copper studied by ultrafast x-ray absorption spectroscopy. *Physical Review Letters*, 106:167601, 2011.

[168] S. M. Vinko, O. Ciricosta, B. I. Cho, K. Engelhorn, H. K. Chung, C. R. D. Brown, T. Burian, J. Chalupsky, R. W. Falcone, C. Graves, V. Hajkova, A. Higginbotham, L. Juha, J. Krzywinski, H. J. Lee, M. Messerschmidt, C. D. Murphy, Y. Ping, A. Scherz, W. Schlotter, S. Toleikis, J. J. Turner, L. Vysin, T. Wang, B. Wu, U. Zastrau, D. Zhu, R. W. Lee, P. A. Heimann, B. Nagler, and J. S. Wark. Creation and diagnosis of a solid-density plasma with an x-ray free-electron laser. *Nature*, 482:10746, 2012.

[169] J. J. Macfarlane, I. E. Golovkin, P. R. Woodruff, D. R. Welch, B. V. Oliver, T. A. Mehlhorn, and R. B. Campbell. Simulation of the ionization dynamics of aluminum irradiated by intense short-pulse lasers. In *Proceedings of Inertial Fusion and Science Applications*, La Grange Park, IL, 2003.

[170] M. S. del Rio and R. J. Dejus. Xop: A multiplatform graphical user interface for synchrotron radiation spectral and optics calculations. *Proceeding of SPIE*, 3152:148, 1997.

[171] D. Chopra. X-ray spectrometric characteristics of potassium acid phthalate crystals. *Review of Scientific Instruments*, 41:1004, 1970.

[172] M. S. del Rio, N. Canestrari, F. Jiang, and F. Cerrina. Shadow3: a new version of the synchrotron x-ray optics modelling package. *Journal of Synchrotron Radiation*, 18:708, 2011.

[173] S. Corde, C. Thaury, K. Phuoc, A. Lifschitz, G. Lambert, J. Faure, O. Lundh, E. Benveniste, A. Ben-Ismail, L. Arantchuk, A. Marciniak, A. Stordeur, P. Brijesh, A. Rousse, A. Specka, and V. Malka. Mapping the X-Ray Emission Region in a Laser-Plasma Accelerator. *Physical Review Letters*, 107:215004, 2011.

[174] B. L. Henke, E. M. Gullikson, and J. C. Davis. X-ray interactions - photoabsorption, scattering, transmission, and reflection at e=50-30,000 ev, z=1-92. *Atomic Data and Nuclear Data Tables*, 54:181, 1993.

[175] A. J. Burek, D. M. Barrus, and R. L. Blake. Spectrometric properties of crystals for x-ray astronomy. *Astrophysical Journal*, 191:533–543, 1974.

[176] http://www.radiantzemax.com/.

[177] B. R. Maddox, H. S. Park, B. A. Remington, and M. McKernan. Calibration and characterization of single photon counting cameras for short-pulse laser experiments. *The Review of scientific instruments*, 79:10E924, 2008.

[178] C. Fourment, N. Arazam, C. Bonte, T. Caillaud, D. Descamps, F. Dorchies, M. Harmand, S. Hulin, S. Petit, and J. J. Santos. Broadband, high dynamics and high resolution charge coupled device-based

spectrometer in dynamic mode for multi-kev repetitive x-ray sources. *Review of Scientific Instruments*, 80:083505, 2009.

[179] G. D. Tsakiris and K. Eidmann. An approximate method for calculating Planck and Rosseland mean opacities in hot, dense plasmas. *Journal of Quantitative Spectroscopy and Radiative Transfer*, 38:353, 1987.

[180] H. Mayer. Methods of opacity calculations. *Los Alamos Scientific Laboratory Report, LA-647, Los Alamos, N.M.*, 1947.

[181] G. C. Pomraning. *The Equations of Radiation Hydrodynamics*. Pergamon Press Ltd., Oxford, 1973.

[182] G. B. Zimmerman and R. M. More. Pressure Ionization in Laser-fusion target simulation. *Journal of Quantitative Spectroscopy and Radiative Transfer*, 23:517, 1979.

[183] R. M. More. Electronic energy-levels in dense plasmas. *Journal of Quantitative Spectroscopy and Radiative Transfer*, 27:345, 1982.

[184] G. Chiu and A. Ng. Pressure ionization in dense plasmas. *Physical Review E*, 59:1024, 1999.

[185] Sesame Data Table, Los Alamos National Laboratory, Material Number 23715.

[186] R. M. More, K. H. Warren, D. A. Young, and G. B. Zimmerman. A new quotidian equation of state (QEOS) for hot dense matter. *Physics of Fluids*, 31:3059, 1988.

[187] F. Perrot and M. W. C. Dharma-Wardana. Equation of state and transport properties of an interaction multispecies plasma: application to multiply ionization Al plasma. *Physical Review E*, 52:5352, 1995.

[188] http://www.prism cs.com/Software/PROPACEOS/PROPACEOS.htm.

[189] http://nlte.nist.gov/FLY/.

[190] G. C. Junkel, M. A. Gunderson, C. F. Hooper, and D. A. Haynes. Full Coulomb calculation of Stark broadened spectra from multielectron ions: A focus on the dense plasma line shift. *Physical Review E*, 62:5584, 2000.

[191] J. J. Macfarlane, I. E. Golovkin, P. R. Woodruff, D. R. Welch, B. V. Oliver, T. A. Mehlhorn, and R. B. Campbell. Simulation of the ionization dynamics of aluminum irradiated by intense short-pulse lasers. In *Proceedings of Inertial Fusion and Science Applications*, La Grange Park, IL, 2003.

[192] D.R. Hartree. *The Calculation of Atomic Structures.* John Wiley and Sons, New York, 1957.

[193] D. G. Hummer and D. Mihalas. The Equation of State for Stellar Envelopes. An Occupation Probability Formulism For the Truncation of Internal Partition Functions. *The Astrophysical Journal*, 331:794, 1988.

[194] R. M. More. *Applied Atomic Collision Physics.* Academic Press, New York, 1982.

[195] R. Ramis, K. Eidmann, J. Meyer-ter Vehn, and S. Hüller. MULTI-fs—A computer code for laser plasma interaction in the femtosecond regime. *Computer Physics Communications*, 183:637, 2011.

[196] K. Eidmann, J. Meyer-ter Vehn, T. Schlegel, and S. Hüller. Hydrodynamic simulation of subpicosecond laser interaction with solid-density matter. *Physical Review E*, 62:1202, 2000.

[197] O. Ciricosta, S. M. Vinko, H.-K. Chung, B.-I. Cho, C. R. D. Brown, T. Burian, J. Chalupský, K. Engelhorn, R. W. Falcone, C. Graves, V. Hájková, A. Higginbotham, L. Juha, J. Krzywinski, H. J. Lee, M. Messerschmidt, C. D. Murphy, Y. Ping, D. S. Rackstraw, A. Scherz,

W. Schlotter, S. Toleikis, J. J. Turner, L. Vysin, T. Wang, B. Wu, U. Zastrau, D. Zhu, R. W. Lee, P. Heimann, B. Nagler, and J. S. Wark. Direct Measurements of the Ionization Potential Depression in a Dense Plasma. *Physical Review Letters*, 109:065002, 2012.

[198] J. C. Stewart and K. D. Pyatt. Lowering of ionization potentials in plasmas. *Astrophysical Journals*, 144:1203, 1966.

[199] S. M. Vinko, O. Ciricosta, and J. S. Wark. Density functional theory calculations of continuum lowering in strongly coupled plasmas. *Nature Communications*, 5:3533, 2014.

[200] R. B. Stephens, R. A. Snavely, Y. Aglitskiy, F. Amiranoff, C. Andersen, D. Batani, S. D. Baton, T. Cowan, R. R. Freeman, T. Hall, S. P. Hatchett, J. M. Hill, M. H. Key, J. a. King, J. A. Koch, M. Koenig, A. J. MacKinnon, K. L. Lancaster, E. Martinolli, P. Norreys, E. Perelli-Cippo, M. Rabec Le Gloahec, C. Rousseaux, J. J. Santos, and F. Scianitti. Kα fluorescence measurement of relativistic electron transport in the context of fast ignition. *Physical Review E*, 69:066414, 2004.

[201] K. L. Lancaster, J. S. Green, D. S. Hey, K. U. Akli, J. R. Davies, R. J. Clarke, R. R. Freeman, H. Habara, M. H. Key, R. Kodama, K. Krushelnick, C. D. Murphy, M. Nakatsutsumi, P. Simpson, R. Stephens, C. Stoeckl, T. Yabuuchi, M. Zepf, and P. A. Norreys. Measurements of energy transport patterns in solid density laser plasma interactions at intensities of 5×10^{20} W/cm^2. *Physical Review Letters*, 98:125002, 2007.

[202] J. Green, V. Ovchinnikov, R. Evans, K. Akli, H. Azechi, F. Beg, C. Bellei, R. Freeman, H. Habara, R. Heathcote, M. Key, J. King, K. Lancaster, N. Lopes, T. Ma, A. MacKinnon, K. Markey, A. McPhee, Z. Najmudin, P. Nilson, R. Onofrei, R. Stephens, K. Takeda, K. Tanaka, W. Theobald, T. Tanimoto, J. Waugh, L. Van Woerkom, N. Woolsey,

M. Zepf, J. Davies, and P. Norreys. Effect of Laser Intensity on Fast-Electron-Beam Divergence in Solid-Density Plasmas. *Physical Review Letters*, 100:015003, 2008.

[203] R. Kodama, P. A. Norreys, K. Mima, A. E. Dangor, R. G. Evans, H. Fujita, Y. Kitagawa, K. Krushelnick, T. Miyakoshi, N. Miyanaga, T. Norimatsu, S. J. Rose, T. Shozaki, K. Shigemori, A. Sunahara, M. Tampo, K. A. Tanaka, Y. Toyama, T. Yamanaka, and M. Zepf. Fast heating of ultrahigh-density plasma as a step towards laser fusion ignition. *Nature*, 412:798, 2001.

[204] A. Bell and R. Kingham. Resistive Collimation of Electron Beams in Laser-Produced Plasmas. *Physical Review Letters*, 91:035003, 2003.

[205] S. Chawla, M. Wei, R. Mishra, K. Akli, C. Chen, H. McLean, A. Morace, P. Patel, H. Sawada, Y. Sentoku, R. Stephens, and F. Beg. Effect of Target Material on Fast-Electron Transport and Resistive Collimation. *Physical Review Letters*, 110:025001, 2013.

[206] K. Wharton, S. Hatchett, S. Wilks, M. Key, J. Moody, V. Yanovsky, A. Offenberger, B. Hammel, M. Perry, and C. Joshi. Experimental Measurements of Hot Electrons Generated by Ultraintense ($> 10^{19}$ $W/cm2$) Laser-Plasma Interactions on Solid-Density Targets. *Physical Review Letters*, 81:822, 1998.

[207] K. U. Akli, P. K. Patel, R. V. Maren, R. B. Stephens, M. H. Key, D. P. Higginson, B. Westover, C. D. Chen, A. J. Mackinnon, T. Bartal, F. N. Beg, S. Chawla, R. Fedosejevs, R. R. Freeman, D. S. Hey, G. E. Kemp, S. LePape, A. Link, T. Ma, A. G. MacPhee, H. S. McLean, Y. Ping, Y. Y. Tsui, L. D. V. Woerkom, M. S. Wei, T. Yabuuchi, and S. Yuspeh. A dual channel X-ray spectrometer for fast ignition research. *Journal of Instrumentation*, 5:P07008, 2010.

[208] J. A. Koch, Y. Aglitskiy, C. Brown, T. Cowan, R. Freeman, S. Hatchett, G. Holland, M. Key, A. MacKinnon, J. Seely, R. Snavely, and R. Stephens. 4.5- and 8-keV emission and absorption x-ray imaging using spherically bent quartz 203 and 211 crystals (invited). *Review of Scientific Instruments*, 74:2130, 2003.

[209] J. J. Honrubia and J. Meyer-ter Vehn. Fast ignition of fusion targets by laser-driven electrons. *Plasma Physics and Controlled Fusion*, 51:014008, 2009.

[210] A. Debayle, J. J. Honrubia, E. DHumières, and V. T. Tikhonchuk. Divergence of laser-driven relativistic electron beams. *Physical Review E*, 82:036405, 2010.

[211] J. C. Adam, A. Héron, and G. Laval. Dispersion and transport of energetic particles due to the interaction of intense laser pulses with overdense plasmas. *Physical Review Letters*, 97:205006, 2006.

[212] L. Gremillet, G. Bonnaud, and F. Amiranoff. Filamented transport of laser-generated relativistic electrons penetrating a solid target. *Physics of Plasmas*, 9:941, 2002.

[213] A. J. Kemp and J. Meyer-ter Vehn. An equation of state code for hot dense matter, based on the QEOS description. *Nuclear Instruments and Methods in Physics Research, Section A: Accelerators, Spectrometers, Detectors and Associated Equipment*, 415:674, 1998.

[214] K. Eidmann. Radiation transport and atomic physics modeling in high-energy-density laser-produced plasmas. *Laser and Particle Beams*, 12: 223, 1994.

[215] J. Meyer-Ter-Vehn, A. Tronnier, and Y. Cang. Physical Collision Fre-

quency for Metals and Warm Dense Matter. In *35th EPS Conference on Plasma Phys. Hersonissos*, volume 32D, page 2, 2008.

[216] V. P. Krainov. Inverse stimulated bremsstrahlung of slow electrons under Coulomb scattering. *Journal of Physics B: Atomic, Molecular and Optical Physics*, 33:1585, 2000.

[217] Spectra-Physics, Inc., 1335 Terra Bella Ave., Mountain View, CA 94039, USA.

[218] J. H. Weaver and H. P. R. Frederikse. Optical properties of selected elements. *CRC handbook of Chemistry and Physics, 82nd edition, p12-120*, 2001.

[219] H. M. Michberg, R. R. Freeman, S. C. Davey, and R. M. More. Resistivity of a Simple Metal from Room Temperature to 10^6 K. *Physical Review Letters*, 61:2364, 1988.

[220] R. Fedosejevs, R. Ottman, R. Sigel, G. Kuhnle, S. Szatmari, and F.P. Schafer. Absorption of Femtosecond Laser Pulses in High-Density Plasma. *Physical Review Letters*, 64:1250, 1990.

Appendix A

Frinedit - A matlab GUI APP for processing optical interferograms for the LWFA experiments

In LWFA experiments, the plasma density is normally measured by interferometry such as Mach-Zehnder interferometry or Nomarski interferometry. To derive the plasma density from the measured interferogram, the Abel inversion algorithm is normally employed and its details have been given in Chapter 4. Frinedit is a software package developed for calculating the plasma density from an interferogram based on the Abel inversion algorithm. The Frinedit program uses the matlab graphical user interface (GUI) platform and its user interface is shown in Fig.A.1.

Flowchart A.2 shows the processes of analyzing the fringe image by the Frinedit software. The loaded image is first converted to the correct spatial scale, normally from pixel number to μm. After that, an edge function is employed to trace the fringes and display the traced fringes on top of the image. The traced fringes are displayed as a number of line segments connected by

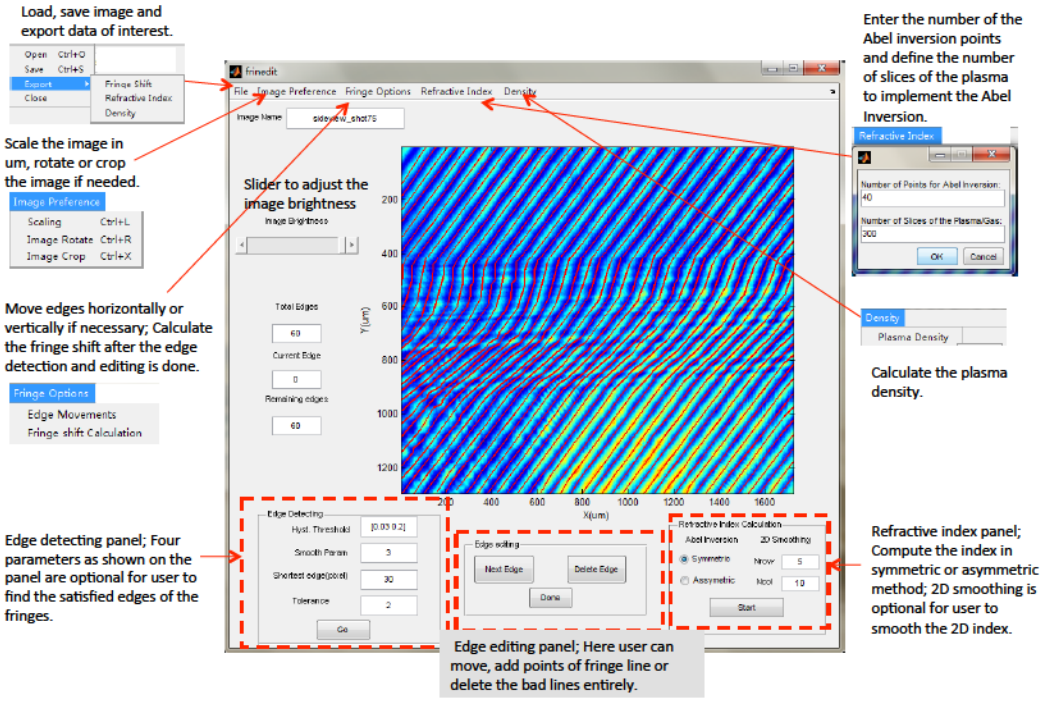

Figure A.1: The user interface of the Frinedit software.

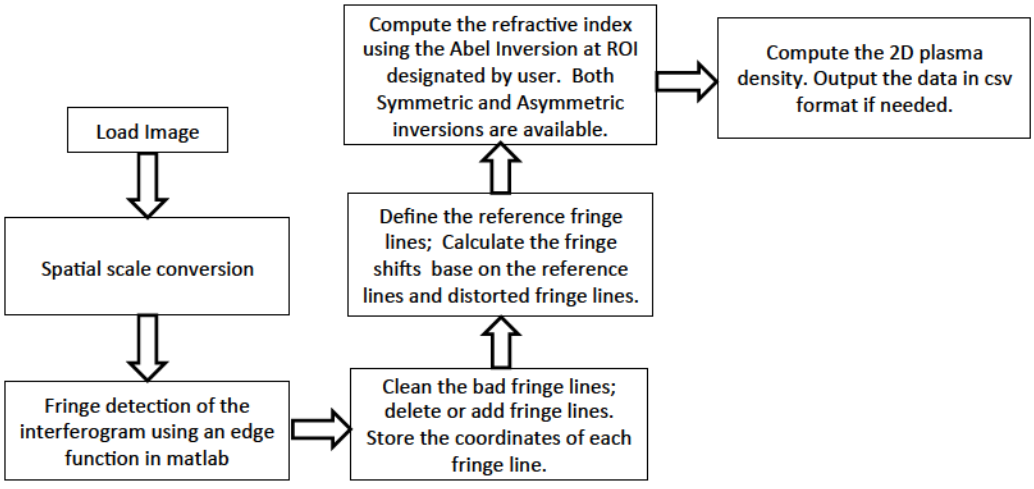

Figure A.2: Flowchart illustrating the workflow for analyzing the optical fringes by Frinedit. In this flowchart, only the major steps are listed.

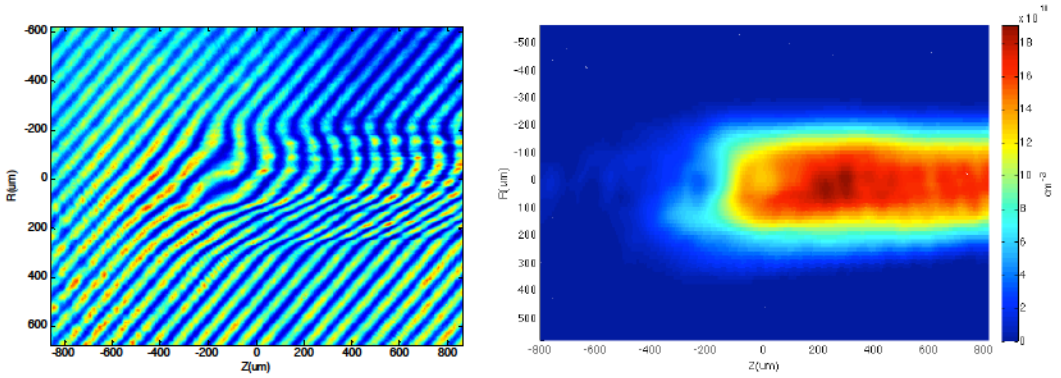

Figure A.3: (a) An interferogram taken in one of the ALLS experimental campaigns showing the leading front of the laser pulse propagating in the underdense plasma. The laser propagated from right to left. The gas target for this data shot was pure helium obtained with the backing pressure of 700 psi. (b) The corresponding 2D plasma density profile achieved with the Frinedit program using the asymmetric inversion technique.

draggable vertices. Depending on the clarity of the original fringes, sometimes there are some bad traced fringes that may not follow exactly the original fringes. In these cases, some correction of the coordinates of the incorrectly traced fringe lines can be carried out by manually dragging the off-track vertices back to the original fringes. In this step, the user can delete undesired fringes or add new fringe lines if necessary. The final coordinates of the fringes are then stored before proceeding to the next step in which the reference fringe lines are defined and the fringe shifts are calculated accordingly. After obtaining the fringe shift from the interferogram, the spatial distribution of the refractive index within the region of interest (ROI) is calculated using the symmetric or asymmetric Abel inversion algorithm as described in Chapter 4. The final step is converting the refractive index to plasma density using Equations 4.8 - 4.10 as shown in Chapter 4.

Fig.A.3 shows an example of a 2D plasma density profile calculated with the Frinedit software and its original interferogram.

Appendix B

MULTI-fs simulation code

The code MULTI-fs is a numerical tool for studying the interaction of ultra-short (fs - ps time scale) laser pulses with matter in the intensity range of 10^{11} to 10^{17} W/cm^2. The hydrodynamic motion together with laser energy deposition, thermal conduction and radiation emission and transport is solved in one-dimensional geometry using a fractional step scheme. Fluid motion and heat diffusion are solved by using an implicit Langrangian method. Thermal conduction and radiation as well as electron-ion energy coupling are treated in a two-temperature model (TTM) covering the wide range from solid state to high temperature plasma. Laser energy deposition is calculated by one-dimensional Maxwell equations. The electron-ion collision frequency, which determines the laser absorption, is treated with two different plasma models that can cover the regime of warm dense matter (WDM) between the solid state and plasma regimes. The equation-of-state of the matter to be studied is interpolated from tables generated from the MPQeos code [213], whereas the opacities and ionization are interpolated from tables generated from the SNOP code[214].

A detailed description of the MULTI-fs code can be found in Ref.[195]. Here only the two plasma models for calculating the electron ion collision frequency that can cover the warm dense matter regime are described. The following two

sections are based on the descriptions given in Ref.[195].

B.1 The Electron-Phonon model

In an ideal plasma, the electron-ion collision frequency can be calculated using Spitzer's formula and is given by:

$$\nu_{Spitzer} = \frac{4\sqrt{2\pi}}{3} \frac{\ln(\Lambda) e^4 Z n_e}{m_e^{1/2} (kT_e)^{3/2}} \tag{B.1}$$

where e is the electron charge, Z is the ionization state, T_e is the electron temperature, n_e is the plasma density, m_e is the electron mass, k_B is the Boltzmann constant, and $\ln(\Lambda)$ is the Coulomb logarithm, where $\Lambda = 12\pi n_e \lambda_D^3$ [33] with λ_D the Debye length given by $\lambda_D = (\epsilon_0 k_B T_e / n_e e^2)^{1/2}$.

In the limit of cold solid with temperature below the Fermi temperature, the plasma approaches metal-like states, in which the ions are distributed in lattice-like order and are embedded in a sea of degenerate electrons. The electrons that are responsible for the electric and thermal transport are moving with velocities on the order of the Fermi velocity of $\upsilon_F = (3\pi^2 n_e)^{1/3} \hbar / m_e$, and are subject to scattering from the thermal ion fluctuations or phonons. In the MULTI-fs code, the electron-ion collision frequency ν_{ep} due to the electron-phonon interaction is obtained as:

$$\nu_{ep} = K_{wdm} \frac{e^2}{\hbar \upsilon_F} \frac{k_B T_i}{\hbar} \tag{B.2}$$

where $\hbar$ is the reduced Planck constant, T_i is the ion temperature and K_{wdm} is an empirical parameter to be adjusted to fit experimentally observed data. In MULTI-fs code, the value of K_{wdm} is set to be equal to 18.8 for aluminum by comparing to the experimental reflectivity of 400 nm light [195].

As indicated by Eqn.B.2, the collision frequency based on electron-phonon model increases linearly with ion temperature, which is in contrast to the high temperature plasma regime, in which the collision frequency follows the Spitzer

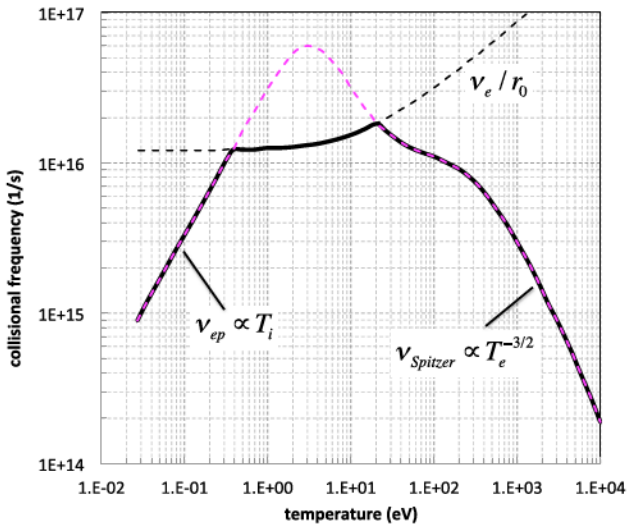

Figure B.1: Collision frequency of solid Al ($\rho = 2.7\ g/cm^3$) as a function of plasma temperature (black solid line) calculated with the electron-phonon model employed in MULTI-fs code. The magenta dashed line represents the results achieved from Eqn.B.3 and the black dashed line is the upper limit of the collision frequency given by requirement $\lambda_e > r_0$. Note that the results of collision frequency shown here were taken from Fig.1 of Ref.[196]. In calculating these results, as quoted in Ref.[196], it was assumed that the electrons and ions are in thermal equilibrium, i.e.: $T_e = T_i$. The average ionization state of aluminum required for computing the Spitzer collision frequency was achieved with a Thomas-Fermi model assuming local thermodynamic equilibrium (LTE) condition.

behavior and scales like $\nu_{Spitzer} \propto T_e^{-3/2}$ as shown in Eqn.B.1. In the electron-phonon model as employed in MULTI-fs, the gap between metal and plasma regimes is bridged by ad hoc interpolation as given by:

$$\nu_{wdm} = \frac{1}{1/\nu_{ep} + 1/\nu_{Spitzer}}. \tag{B.3}$$

The electron-ion collision frequency as a function of the plasma temperature for solid Al achieved with the above interpolation is given in Fig.B.1, as indicated by the magenta dashed line. As shown, the collision frequency increases linearly at low temperature, reaches a maximum at a temperature ($\sim$ 3 eV) below the Fermi temperature (11.7 eV for Al), and then merges into plasma behavior $\propto T_e^{-3/2}$. Examining the electron mean free path $\lambda_e = \sqrt{v_{th}^2 + v_F^2}/\nu_e$, where $v_{th} = (kT_e/m_e)^{1/2}$ is the thermal velocity, it is found that around the maximum of ν_e, λ_e is considerably below the interatomic distance $r_0 = (4\pi n_e/3Z)^{-1/3}$. To avoid this non-physical behavior, in MULTI-fs code, the actual collision frequency is taken as:

$$\nu_e = min(\nu_{wdm}, \sqrt{v_{th}^2 + v_F^2}/r_0). \tag{B.4}$$

The results of the collision frequency based on the above equation for solid Al is indicated by the solid black line in Fig.B.1. As indicated, in the temperature range of (1 - 100) eV, the collision frequency shows a weak dependency on the plasma temperature and has a maximum nearby the Fermi temperature.

The electron-phonon model has been compared with the experimental results of 150 fs laser pulses irradiating aluminum foils over a wide range of intensities from 10^{12} to 10^{17} W/cm^2 [196]. Although it was found to be useful in modeling the femtosecond experiments, the electron-phonon model appears to underestimate significantly the collisionality of metals and warm dense matter [195]. A different and more physical approach based on the Drude-Sommerfeld (DS) model was therefore developed to circumvent this problem and is available

in the MULTI-fs code.

B.2 The Drude-Sommerfeld model

In the description of the electron ion collision based on the Drude-Sommerfeld model [215], the dominant part of the collision frequency is due to the electron-ion collisions, as in the case of a classical plasma, but now it takes into account the electron degeneracy in WDM regime and the modifications to the Coulomb scattering [216] for slow electrons defined by $Ze^2/\hbar v \gg 1$, where the v is the velocity of the electrons. In this way, the dynamical collision frequency $\nu_e(T_e, \omega)$ required for laser collisional absorption, where ω is the light frequency, is described reasonably well in comparison with the experimental data [215].

Two important features of this new approach should be noted. The first feature is that the collision frequency for slow electrons scales with electron velocity $\propto 1/v$, which allows a finite value of collision frequency when averaging over the electron distribution [216]. This is in contrast to the fast-electron high-temperature regime in which the collision frequency scales $\propto 1/v^3$. The second feature is that, $\nu_e(T_e, \omega)$ decreases with both the T_e and ω for temperatures below the Fermi temperature due to the effect of the electron degeneracy. This second feature was found to be in a good agreement with experimental data [215].

In the WDM regime $mv_{th}^3/(Ze^2\omega) < 1$, the collision frequency is given by:

$$\nu_{wdm} = \frac{4\pi^2 2^{2/3}\Gamma(1/3)}{15\, 3^{5/6}\Gamma(2/3)} \frac{Ze^4 n_e}{m_e^2 v_{th}^3} \left(\frac{m_e v_{th}^3}{Ze^2\tilde{\omega}}\right)^{2/3} \left\langle \frac{v_{th}}{v} \right\rangle, \tag{B.5}$$

where $\Gamma(x)$ is the gamma function evaluated at x, $\tilde{\omega} = max(\omega, \omega_p)$. The brackets denote the averaging over the Fermi distribution function $f(\epsilon) = (1 +$

$exp[(\epsilon-\mu)/kT_e])$, where μ is the chemical potential, including Pauli blocking:

$$\langle\frac{\upsilon_{th}}{\upsilon}\rangle=\frac{3\nu_{th}}{m\nu_F^3}\int_0^\infty f(\epsilon)(1-f(\epsilon+\hbar\omega))d\epsilon=3(\frac{\nu_{th}}{\nu_F})^3\ln(\frac{1+e^y}{1+e^{y-z}})\frac{1}{1-e^{-z}}, \quad \text{(B.6)}$$

with $y=\mu/kT_e$ and $z=\hbar\omega/kT_e$. The chemical potential μ is defined implicitly by the electron density n_e and can be obtained in good approximation by:

$$y=-\frac{3}{2}\ln\frac{T_e}{T_F}+\ln\frac{4}{3\sqrt{\pi}}+\frac{A(\frac{T_e}{T_F})^{-(b+1)}+B(\frac{T_e}{T_F})^{-(b+1)/2}}{1+A(\frac{T_e}{T_F})^{-b}}, \quad \text{(B.7)}$$

where the constants are $A=0.25054$, $B=0.072$ and $b=0.858$.

The gap between the WDM regime and the Spitzer regime $mv_{th}^3/(Ze^2\omega)>1$ is connected by a smooth interpolation, which takes the form of:

$$\nu_e(T_e,\omega)\simeq 2\sqrt{2\pi}\frac{Ze^4n_e}{m_e^{1/2}(kT_e)^{3/2}}\ln[1+K_{ds}\frac{1.32}{\sqrt{2\pi}}\frac{kT_e}{(m_e^{1/2}Ze^2\tilde{\omega})^{2/3}}]F(T_e,\hbar\omega). \quad \text{(B.8)}$$

In the above equation, K_{ds} is a free parameter and is defaulted to be unity in the MULTI-fs code. $F(T_e,\hbar\omega)=\sqrt{\pi/2}\langle\frac{\upsilon_{th}}{\upsilon}\rangle$ is the Fermi factor and asymptotically takes the forms:

$$F(T_e,\hbar\omega)\rightarrow\begin{cases}\frac{3}{4}\sqrt{\pi/2}\frac{\upsilon_{th}}{\upsilon_F}\min(\hbar\omega/kT_F,1) & \text{for } T_e\rightarrow 0,\\ 1 & \text{for } T_e\rightarrow\infty.\end{cases} \quad \text{(B.9)}$$

The effective collision frequency $\nu_e(T_e,\omega)$ as a function of electron temperature T_e and photon energy $\hbar\omega$ is shown in Fig.B.2 for the case of aluminum at solid density. As indicated, ν_e reaches maximum values of approximately 10^{16} s^{-1} at temperatures in the region of 10-100 eV and also at photon energies of $\sim$ 50 eV. Below these values of T_e and $\hbar\omega$, the collision frequency decreases almost linearly, which is due to the Fermi factor $F(T_e,\hbar\omega)$ that reduces the number of electrons available for scattering in a degenerate plasma.

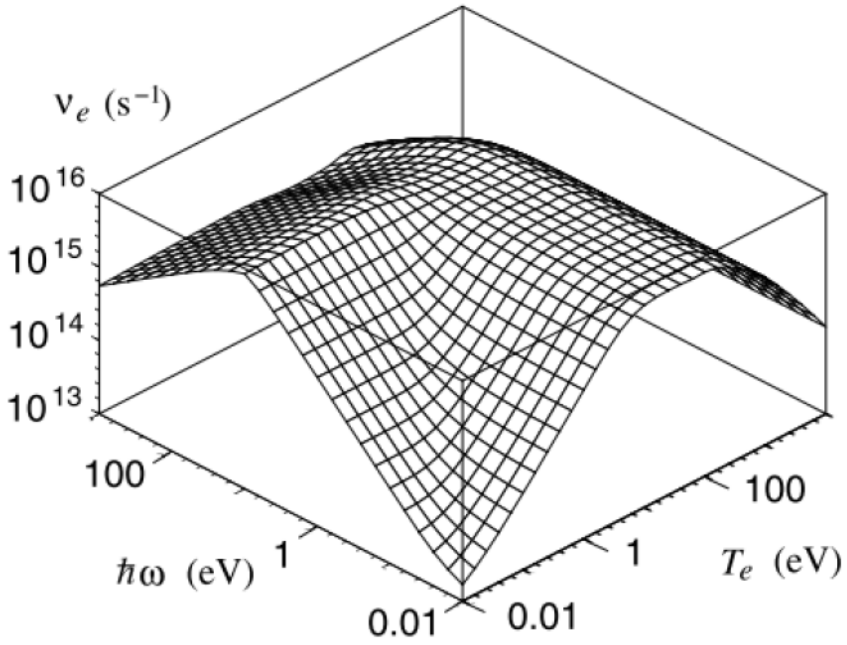

Figure B.2: Effective collision frequency $\nu_e(T_e, \omega)$ given by Eqn.B.8 as a function of electron temperature T_e and photon energy $\hbar\omega$ for aluminum at solid density $\rho = 2.7\ g/cm^3$ and $K_{ds} = 1$. Figure taken from Ref.[195].

Appendix C

Plasma spectroscopic models for computing the X-ray transmission of warm dense aluminum

In Chapter 10, three plasma spectroscopic models were used to calculate the X-ray transmission of warm dense aluminum and an overview of these three plasma models has been given in that chapter. Here, more details on these three models will be given.

C.1 Non-uniform model

In the non-uniform model, the spatial distribution of electron temperature $T_e(r,t)$ and mass density $\rho(r,t)$ at given time t obtained from the MULTI-fs simulation were plugged into the FLYCHK code to compute the ionized charge distribution at each spatial coordinate r. The generated ionized charge distribution together with the electron temperature, mass density, and spatial coordinates, were then substituted into the screened hydrogenic model to

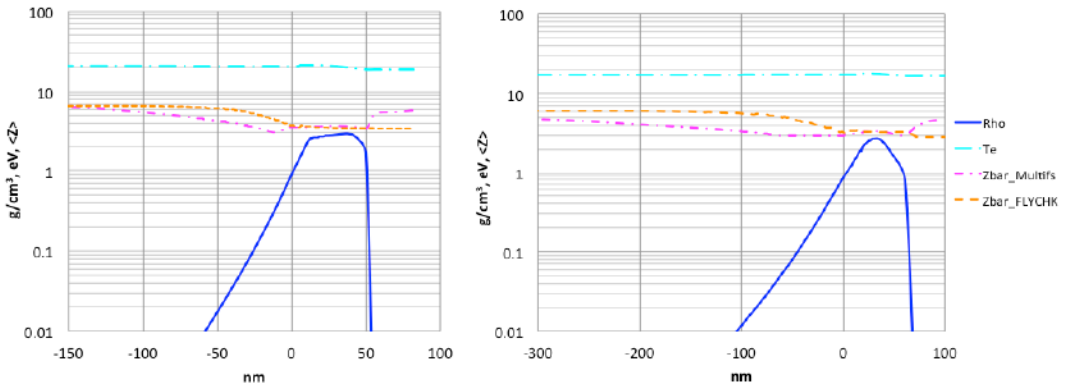

Figure C.1: (a) MULTI-fs simulated spatial dependence of mass density ρ (blue line), electron temperature T_e (cyan line), average ionization state $\langle Z \rangle$ (magenta line) at the time of 0.5 ps after the laser peak arrives at the target for the case in which a 800nm, 30 fs, laser pulse with peak intensity of 1.3×10^{15} W/cm^2 irradiating 50nm aluminum foil at 40 degrees angle of incidence. Note that in the simulation the laser pulse comes from the left. The average ionization state $\langle Z \rangle$ calculated from FLYCHK (orange line) with the input parameters (ρ, T_e) as plotted here. (b) The same as (a) but for simulation time of 1 ps after the laser peak arrives at the target.

compute the opacities of the non-uniform plasma and the final transmission coefficients.

Fig.C.1 shows the spatial distribution of $T_e(r,t)$ and $\rho(r,t)$ at the time of 0.5 ps (a) and 1 ps (b) after the peak of the laser pulse arrives at the target for the simulation case as discussed in Chapter 10. Based on these physical quantities, the ionization state distribution at each r was calculated from the FLYCHK. For comparison, the average ionization state $\langle Z \rangle$ as a function of r obtained from the FLYCHK and the MULTI-fs simulation are plotted in Fig.C.1 for the two simulation times. As indicated, within the bulk of the target in which the major mass is contained, e.g. $0 < r < 50$ nm in (a), the results from the FLYCHK agree reasonably well with those generated from the MULTI-fs simulation. However, in the corona plasma region $r < 0$, the FLYCHK appears to predict a relatively higher ionization state than the MULTI-fs simulation.

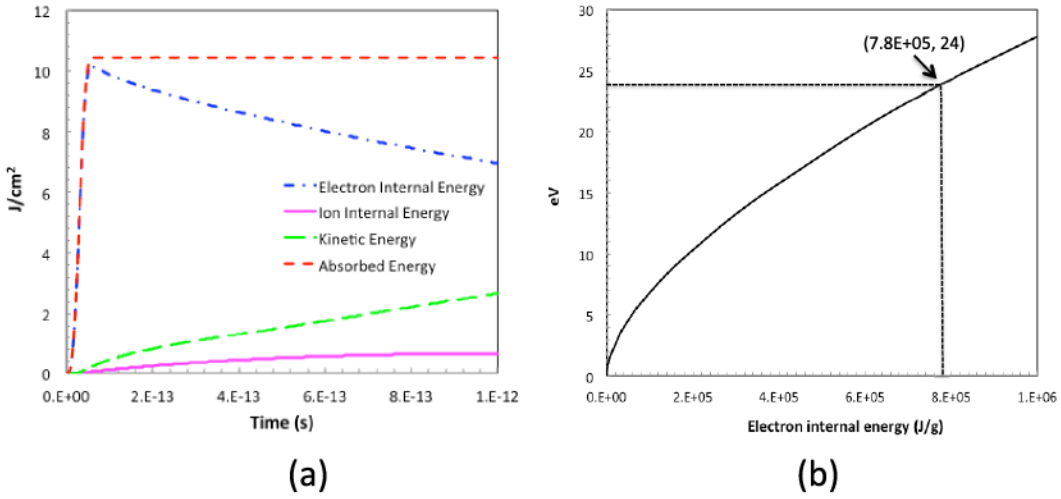

Figure C.2: (a) Time evolution of the absorbed energy (red line), electron internal energy (blue line), ion internal energy (magenta line) and kinetic energy (green line) for the simulation case as shown in Fig.C.1 (a). (b) PROPACEOS estimated electron temperature versus the electron internal energy for aluminum with mass density of 2.5 g/cm^3.

C.2 Uniform model

In the uniform model, a fictitious uniform plasma slab is assumed. The size of this fictitious uniform slab was assumed equal to the FWHM r_{fwhm} of the mass density profile from the MULTI-fs simulation, and its mass density was achieved by taking the average mass density $\langle\rho\rangle$ within the FWHM of MULTI-fs simulated density profile weighted by the cell-size. The plasma temperature of this uniform slab is determined by looking up the EOS table generated by PROPACEOS based on the total internal energy $E_{internal}$ obtained from the MULTI-fs simulation. The total electron internal energy $E_{internal}$ was achieved by subtracting the kinetic energy contained in the plasma system from the total absorbed laser energy in the MULTI-fs simulation.

The following shows an example of calculating such a uniform slab for the expanded target at the time of 0.5 ps.

Fig.C.2 (a) shows the time evolution of the absorbed laser energy, electron internal energy, ion internal energy and kinetic energy from the simulation case

as shown in Fig.C.1 (a). Based on these results, one can obtain the $E_{internal}$ of $\sim 8.8\ J/cm^2$ by subtracting the the kinetic energy from the absorbed laser energy at the time of 0.5 ps. From the mass density profile as shown in Fig.C.1 (a), r_{fwhm} along with $\langle\rho\rangle$ and the total areal density within FWHM region are obtained as 45 nm, 2.5 g/cm^3 and $1.1 \times 10^{-5}\ g/cm^2$ respectively. Dividing the $E_{internal}$ by the total areal density gives an energy density of $7.8 \times 10^5\ J/g$. Knowing the the energy density and the mass density, an electron temperature of 24 eV was obtained by looking up the electron internal energy versus electron temperature from the PROPACEOS, as shown in Fig.C.2 (b). Here, $E_{internal}$ is assumed to be equal to the electron internal energy when finding the electron temperature since the ions at this time scale are relatively cold.

The same procedures were applied to achieve a uniform plasma slab for the expanded target at the time of 1 ps. The final T_e, ρ, $E_{internal}$ and r were calculated to be 22.5 eV, 2.0 g/cm^3, $7.3 \times 10^5\ J/g$ and 52 nm respectively.

Note that in the uniform model, only the mass within the FWHM of the expanded plasma is taken to compute the opacity. This essentially underestimates to some degree the X-ray absorption coefficient at the Al^{4+} and Al^{+5} positions. Therefore, assessment is required to estimate the contribution from the unaccounted mass, mainly in the front of the target, to the final X-ray absorption.

Here we show two ways to assess the effect from the unaccounted mass in the front of the target. As an example, we consider the expanded target at the time of 0.5 ps.

The first way is by assuming the ionization state as 5+ for the unaccounted high-temperature corona plasma in the front of the target. This sets up an upper limit for the unaccounted X-ray absorption. From the mass density lineout at the time of 0.5 ps as shown in Fig.C.1(a), the total areal density ρr before the half density peak is found to be $1.5 \times 10^{-6}\ g/cm^2$. For the opacity, to first order, the peak opacity κ of $7 \times 10^4\ cm^2/g$ corresponding to the Al^{5+}

absorption line with linewidth of 3.5 eV calculated from the SH model was used. Taking into account the incident angle θ of 40 degrees for the heater laser, the final transmission coefficient $T = exp(-\kappa\rho r/cos(\theta))$ is calculated to be ~ 0.87.

The second way is by using the ion fraction numbers achieved from FLYCHK in the non-uniform model to calculate the opacity with the SH model. This was carried out and the X-ray transmission at the Al^{4+} and Al^{5+} positions are calculated to be 0.96 and 0.97 respectively. The estimate done in this way does not take into account the fact that the ionization states calculated in the expanding plasma are not accurate since they will typically freeze out at higher ionization states. However, the final effect on the fractional ionization states can only be determined by a time dependent solution of the ionization and recombination rate equations. It is expected that only a fraction of the ions on front of the target would be in the Al^{5+} state and, thus, it is expected that the true contribution to the final absorption from the unaccounted mass in front of the target would be closer to the FLYCHK estimate. Such a correction would only add a few percent to the final absorption coefficient at the Al^{4+} and Al^{5+} positions. The same procedures were applied to the 1 ps case, and the contribution to the final absorption from the unaccounted mass was found to be on the similar order to that of the 0.5 ps case.

Appendix D

Self-reflectivity measurement of femtosecond laser pulses interacting with solid aluminum targets with peak intensity up to $10^{15}\ W/cm^2$

The purpose of this self-reflectivity measurement was to benchmark the MULTI-fs simulation, which was used to model the target expansion for the experiment of probing the ionization states of warm dense aluminum with Betatron radiation as presented in Chapter 10. The experiment was performed with a commercial regeneratively amplified Ti:sapphire laser system [217] located at the Electrical and Computer Engineering Department of the University of Alberta. This laser operates at a center wavelength of 800 nm with pulse width (FWHM) of 130 fs and pulse energy of up to 500 μJ.

Fig.D.1 shows the experimental setup for the reflectivity measurement. The 800 nm, 130 fs, p-polarized laser pulses with diameter of $\sim$ 1 cm were focused onto the targets with incident angle of 45 degrees by a 5-cm focal length achro-

mat lens with anti-reflection (AR) coating for IR light. A 50 nm aluminum thin film sputtered onto a glass plate was used as the target, which was mounted on a commercial 3D motorized translation stage. The focal spots of the laser pulses at the target plane after interacting with the targets were recorded by a lens imaging system that consisted of an objective (Vickers G9928, 3X/NA0.1) and a CCD camera. The input focal spots at the target plane were also measured by this lens system by lowering the laser intensity below the damage threshold of the aluminum. A two-lens imaging system was set up to view the target front surface to make sure the area of the target plate for interaction was always at the focal plane of the 800 nm laser pulse. The light source for this two-lens imaging system was generated from a green LED that was located outside the chamber. The pulse energy was controlled by a combination of a half-wave plate followed by a Glan polarizer at the output of the laser. The pulse energy was measured at a kilohertz repetition rate with a power meter (Spectra-Physics Model 407A) placed at the target position to calibrate the photodiode PD1. This calibrated photodiode was subsequently used for shot-to-shot energy measurement of the incident laser pulse. The maximum pulse energy at target was measured to be approximately 250 μJ. The reflected energy of the laser pulse was measured by another photodiode PD2, which was calibrated with the photodiode PD1 by mounting a 98% dielectric mirror at the target position. The output of the PDs were read out at 100 μs after the laser pulse using a 100 MHz bandwidth oscilloscope (Tektronix TDS200) with $1M\Omega$ internal impedance setting. This time delay in measurement was employed to avoid interference from the electrical noise from the laser firing at t=0. In this experiment, we ignored the transmission of the 800 nm light through the 50 nm aluminum foil, which was found to be negligible in a previous ALLS experimental campaign.

Fig.D.2(a) shows a typical image of the focal spot profile at the target position. Presented in (b) is the histogram of the intensity distribution for

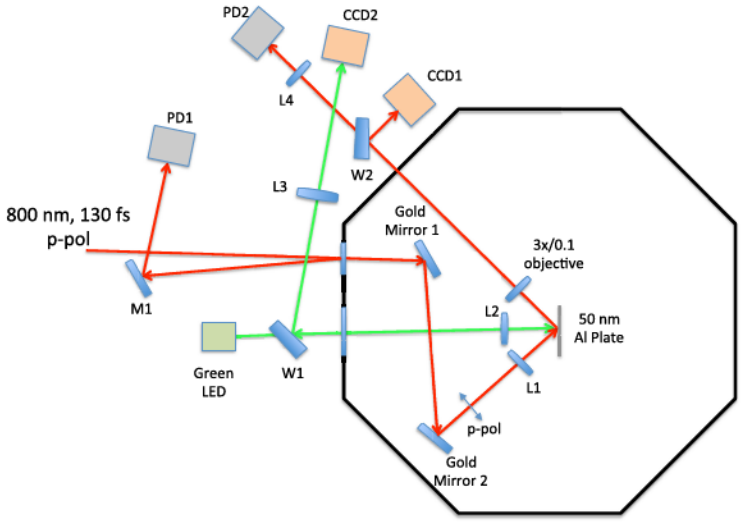

Figure D.1: Schematic diagram showing the experimental setup for the reflectivity measurement at the University of Alberta. The 800nm, 130 fs, p-polarized laser pulses with diameter of $\sim$ 1 cm entered the vacuum chamber from the left. The entrance window was tilted at a small angle to reflect a few percent of the laser energy to a photodiode system (M1 and PD1) to monitor the input laser energy. The laser pulses were focused onto the 50 nm Al target plate by 5cm focal length lens. The focal spot reflected from the target plane was imaged by a lens system consisting of a 3X/NA0.1 objective, wedge W2 and CCD (CCD1). The reflected laser light transmitted through the wedge W2 was refocused onto a photodiode (PD2) to monitor the reflected energy of the laser pulse after interacting with the Al target. A lens imaging system consisted of lens L2 (f=7.5 cm), wedge W1, lens L3 (f=30 cm) and detector CCD2 was set up to view the target front surface to make sure the area of the target plate for interaction was at the focal plane of the 800 nm laser pulse. The light source for this lens imaging system was a green LED that was located outside the chamber.

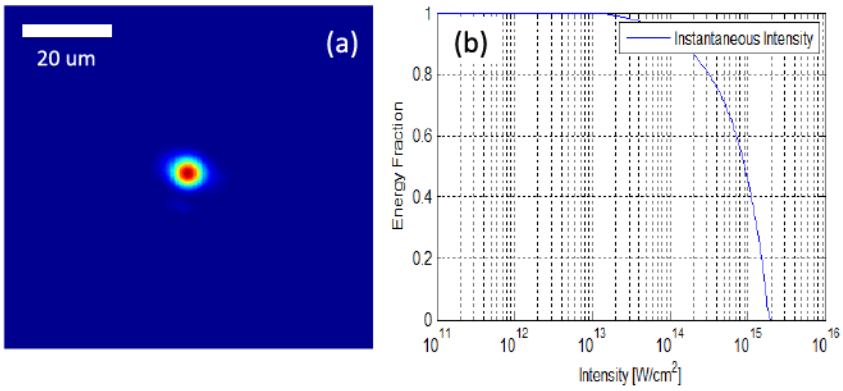

Figure D.2: (a) Typical intensity contour image of the focal spot at the target position for the reflectivity measurement. Energy fraction versus instantaneous intensity for the focal spot (a) is shown in (b). In graph (b), the curve was achieved by normalizing the focal spot to 100 μJ and 130 fs.

this focal spot that was normalized to 100 μJ and 130 fs. As indicated, the focal spot is a Gaussian spot with FWHM of approximately 6 μm. It was determined that 20% and 50% of the available energy was delivered above $1.6 \times 10^{15}\ W/cm^2$ and $9.7 \times 10^{14}\ W/cm^2$ respectively. The peak intensity is approximately $2.0 \times 10^{15}\ W/cm^2$ for this particular energy.

Knowing the total energy and spatial distribution of the input and reflected focal spots, the reflectivity corresponding to a given laser peak intensity can be calculated. This reflectivity can be achieved by dividing the peak intensity of the input focal spot image by the peak intensity of the reflected focal spot image. For a given focal spot, the top three intensity pixels were averaged to represent the final peak intensity. The reflectivity achieved in this way differs from the one that is achieved by simply dividing the input energy by the reflected energy in that the latter one is essentially an integrated reflectivity in which the 2D spatial distribution of focal spot has to be taken into account. As such, for the latter case, the reflectivity is normally described as a function of laser fluence.

The measured reflectivity as a function of laser peak intensity is shown by the green solid circles in Fig.D.3. As indicated, the measurements show

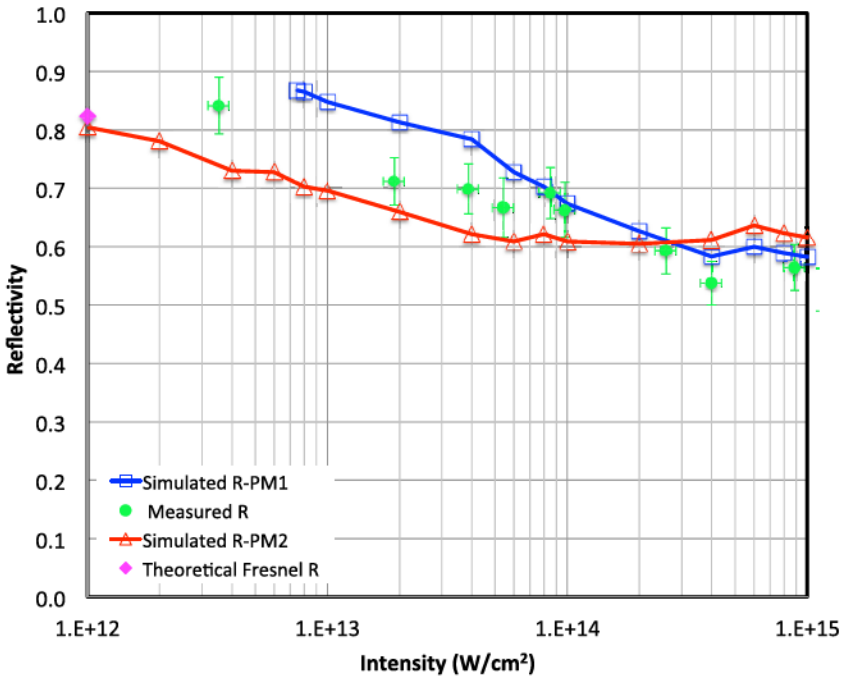

Figure D.3: Reflectivity as a function of incident peak intensity for 130 fs, 800nm, p-pol light irradiating 50 nm aluminum films on glass at 45 degrees angle of incidence. The green solid circles represent the experimental data, while the blue empty squares connected by a blue line represent the results of MULTI-fs simulation with plasma model 1: electron-phonon model and the red empty triangles connected by red line for MULTI-fs simulation with plasma model 2: Drude-Sommerfeld model. The details on these two models are given Appendix B. Note that under the intensity condition corresponding to the measured data point below $1 \times 10^{13}\ W/cm^2$, the aluminum target was not damaged. For comparison, the theoretical reflectivity based on Fresnel equations for 800nm, p-polarized light irradiating aluminum with 45 degrees angle of incidence is shown as a cyan diamond in the graph. The real and imaginary parts of the complex index of refraction used in computing the theoretical Fresnel reflectivity were interpolated from the data given in Ref.[218] and were obtained as 2.7 and 8.4 respectively.

that the reflectivity gradually decreases with the intensity and then reaches a plateau when the intensity is approximately above $3 \times 10^{14}\ W/cm^2$. MULTI-fs simulations [195] were conducted to interpret and compare with these measured reflectivities. The laser parameters set in the MULTI-fs simulations are the same as those in the experiments: 130 fs (FWHM), 800 nm, p-polarization, 45 degrees of incidence. The laser pulse shape in the simulation is a sine-squared function with the form of $I(t) = I_{max} sin^2(\frac{\pi}{2}\frac{t}{\tau})$, where I_{max} is the peak intensity, τ is the FWHM pulse duration. The target is 50 nm solid aluminum with mass density of $2.7\ g/cm^3$ and is initially at room temperature $T_e = T_i = 0.0258\, eV$. The target in the simulation has a finer cell size toward the irradiated side, where most of the laser plasma interaction takes place. In the simulation, the EOS tables were generated by MPQeos code[213], and the opacities and ionization tables were generated by the SNOP code[214] assuming local thermodynamic equilibrium (LTE). The heat flux inhibition parameter was set to free streaming limit $f = 0.6$. Two different plasma conductivity models were employed for the simulations, i.e.: the electron-phonon model and the Drude-Sommerfeld model. The details of these two plasma models have been given in Appendix B. The simulated reflectivities versus laser peak intensities are shown in Fig.D.3, with the blue empty squares representing the results from the electron-phonon model and red empty triangles from Drude-Sommerfeld model.

As shown in Fig.D.3, the reflectivities simulated by the two plasma models follow a trend similar to that of the experimental measurements, i.e.: decrease gently at first and become flat after a certain intensity. For the electron-phonon model, this transition intensity falls between $(2-4) \times 10^{14}\ W/cm^2$ whereas it falls between $(4-6) \times 10^{13}\ W/cm^2$ for Drude-Sommerfeld model. The falling parts of the simulated and measured reflectivity curves are due to the linear increase of the plasma collision frequency with the plasma temperature T_e when $T_e << T_F$, where T_F is the Fermi temperature of the material, leading

to an enhanced laser absorption. In the electron-phonon model, the increasing collision frequency is due to the heating of the ions which enhances the electron-phonon interactions. In the Drude-Sommerfeld model, the increasing collision frequency is due to the increase in the number of electrons available for Coulomb scattering in a degenerate plasma. When the plasma temperature keeps increasing, the collision frequency reaches a nearly flat region where the collision frequency is maximum before it falls off in a classical plasma behavior $\propto T_e^{-3/2}$ (Spitzer collision model). In this flat region, the laser absorption would remain approximately constant, which explains what we observed when the laser peak intensity is above $3 \times 10^{14}\ W/cm^2$. However, as shown by the simulation results, it appears that the starting intensity for this maximum-collision-frequency flat region is different for the two plasma models.

In the intensity region below $10^{14}\ W/cm^2$, the electron-phonon model somewhat underestimates the laser absorption, whereas the Drude-Sommerfeld model appears to overestimate the absorption. In Ref.[196], the MULTI-fs simulations with electron-phonon model were also compared with experimental results for p-polarized light interacting with solid aluminum in 45-degree incidence. However, the experimental results used for comparison were achieved with laser pulses with shorter wavelength(308 nm for Michlberg [219] and 248 nm for Fedosejevs [220]) and longer pulse duration (400 fs for Michlberg and 250 fs for Fedosejevs). What was found from the comparison is that the laser absorption is sensitive to the electron-ion relaxation time at low intensity, because it determines the ion temperature which in turn affects the collision frequency. The sensitivity of the laser absorption to the electron-ion relaxation time at low intensity may explain the discrepancy we observed here for the electron-phonon model. However, for the Drude-Sommerfeld model, the collision frequency is independent of ion temperature but scales with the average ionization state $\propto Z^{1/3}$ at low intensity. As shown in Ref.[196], the ionization model based on LTE assumption used in MULTI-fs tends to overestimate the ionization, which

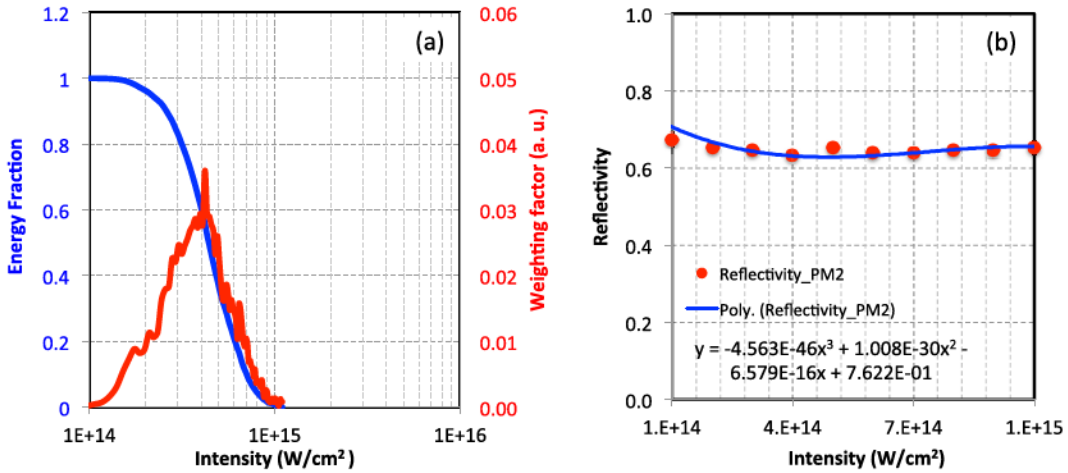

Figure D.4: (a) The blue curve is the energy fraction above a given intensity as a function of intensity for a typical heater focal spot measured in the ALLS 2014 January campaign. The focal spot was normalized to 6 mJ and 30 fs. The red curve is the weighting factor or energy fraction for each intensity component in the focal spot. This weighting factor curve was used to compute the effective reflectivity of the focal spot. (b) MULTI-fs simulated reflectivity with plasma model 2 as a function of laser peak intensity. The simulation layout is the same as the experimental one, i.e.: 800 nm, 30 fs, p-pol laser pulses with various intensities irradiating a 50 nm aluminum target at 40 degrees angle of incidence. The blue line is the fitted curve to the discrete simulation points (red solid circles).

would enhance the collision frequency in the Drude-Sommerfeld model and the absorption accordingly. For the region above 10^{14} W/cm^2, the results from the two plasma models seem to merge together, and show a reasonable agreement with the experimental results.

In addition to the above experimental results achieved at the UofA, we have performed another reflectivity measurement in one of the ALLS campaigns for the Betatron ionization experiments. This reflectivity measurement can be also used to benchmark the MULTI-fs simulation for interaction laser pulse with shorter pulse duration, i.e.: 30 fs.

The experimental setup for the reflectivity measurement has been described in Chapter 10. In this experiment, only the input focal spots together with

the input and reflected pulse energies were recorded. Therefore, the intensity distribution of focal spot has to be taken into account in order to match the measured integrated reflectivity which is achieved by dividing the input pulse energy by the reflected pulse energy. Fig.D.4 (a) shows the histogram of the intensity distribution of a typical heater focal spot measured during the ALLS 2014 January experimental campaign. The energy fraction of each intensity component in the focal spot was used as the weighting factor for computing the final integrated reflectivity and is shown in Fig.D.4 (a) as well. For the MULTI-fs simulation, the Drude-Sommerfeld model was selected to simulate the laser absorption under the intensity range of the measured focal spots since it matches better with the experiment with laser pulse duration of 30 fs. The simulation layout is the same as the experimental one, i.e.: 800 nm, 30 fs, p-pol laser pulses irradiating a 50 nm aluminum target at 40 degrees angle of incidence. The simulated reflectivity as a function of laser peak intensity is show in Fig.D.4 (b). With these simulation reflectivities, the theoretical integrated reflectivity from the MULTI-fs simulation corresponding to the laser focal spot of interest can be calculated, and the equation for that is given by:

$$R_{th} = \sum_{i=1}^{n} r_i W_i \tag{D.1}$$

where r_i is the MULTI-fs reflectivity for the ith laser intensity in the histogram of the focal spot intensity distribution, W_i is the weighting factor of the ith intensity component as shown in Fig.D.4 (a), n is the total number of bins in making the histogram for the intensity distribution of the focal spot. Here, for computational convenience, the equation of a third-order polynomial fit to the MULTI-fs simulated reflectivities, as show in Fig.D.4 (b), was used to estimate r_i. Fig.D.5 shows the R_{th} calculated with the above method together with the measured reflectivities achieved for four consecutive shots. From the graph, the simulated reflectivities using the Drude-Sommerfeld model indicate

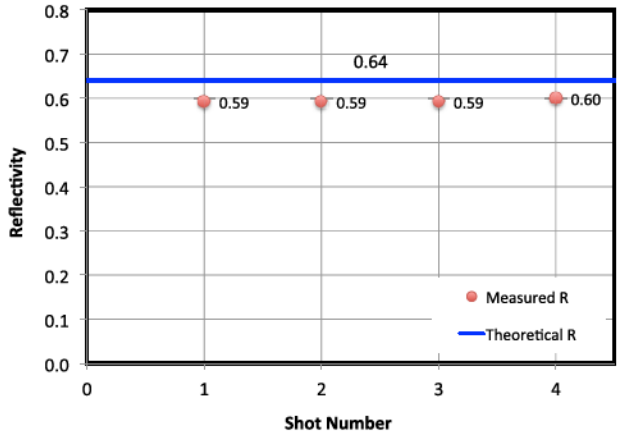

Figure D.5: Measured reflectivities (red solid circles) versus the MULTI-fs simulated reflectivity (blue line) achieved with the method described in this text. The measured reflectivities were simply achieved by dividing the input pulse energy by the reflected pulse energy.

a reasonable agreement with the measured reflectivities.

To conclude, we have conducted two experiments to benchmark the MULTI-fs simulation by comparing the measured and calculated self-reflectivities of the interaction laser pulses irradiating 50-nm-thick aluminum foils at oblique incidence. In comparing with the measured results obtained with 130 fs laser pulses, the MULTI-fs simulation is able to predict the behavior of the laser absorption versus laser peak intensity as observed in experiment. However, at low intensity, discrepancies in the laser absorption between the simulations and experiments were clearly seen, with the experimental results falling in between the two models. At relatively high intensity (above 10^{14} W/cm^2), the simulations with both plasma models (electron-phonon and Drude-Sommerfeld) merged together and showed a reasonable agreement with the experimental results. For a second set of measurements with 30 fs laser pulses in which the laser intensities ranged from 10^{14} W/cm^2 to 10^{15} W/cm^2, the reflectivity result from the MULTI-fs simulation with Drude-Sommerfeld plasma model was found to agree the best with the experimental result.